Lecture Notes in Electrical Engineering 446

M.C. Bhuvaneswari
Jayashree Saxena
Editors

Intelligent and Efficient Electrical Systems

Selected Proceedings of ICIEES'17

Springer

Lecture Notes in Electrical Engineering

Volume 446

"Lecture Notes in Electrical Engineering (LNEE)" is a book series which reports the latest research and developments in Electrical Engineering, namely:

- Communication, Networks, and Information Theory
- Computer Engineering
- Signal, Image, Speech and Information Processing
- Circuits and Systems
- Bioengineering

LNEE publishes authored monographs and contributed volumes which present cutting edge research information as well as new perspectives on classical fields, while maintaining Springer's high standards of academic excellence. Also considered for publication are lecture materials, proceedings, and other related materials of exceptionally high quality and interest. The subject matter should be original and timely, reporting the latest research and developments in all areas of electrical engineering.

The audience for the books in LNEE consists of advanced level students, researchers, and industry professionals working at the forefront of their fields. Much like Springer's other Lecture Notes series, LNEE will be distributed through Springer's print and electronic publishing channels.

More information about this series at http://www.springer.com/series/7818

M.C. Bhuvaneswari · Jayashree Saxena
Editors

Intelligent and Efficient Electrical Systems

Selected Proceedings of ICIEES'17

Springer

Editors
M.C. Bhuvaneswari
Electrical and Electronics Engineering
PSG College of Technology
Coimbatore, Tamil Nadu
India

Jayashree Saxena
Anora LLC
Plano, TX
USA

ISSN 1876-1100 ISSN 1876-1119 (electronic)
Lecture Notes in Electrical Engineering
ISBN 978-981-10-4851-7 ISBN 978-981-10-4852-4 (eBook)
https://doi.org/10.1007/978-981-10-4852-4

Library of Congress Control Number: 2017940536

Printed on acid-free paper

This Springer imprint is published by Springer Nature
The registered company is Springer Nature Singapore Pte Ltd.
The registered company address is: 152 Beach Road, #21-01/04 Gateway East, Singapore 189721, Singapore

Preface

Intelligent and efficient electrical systems have been the topic of discussion and intense debate among electrical engineering professionals and academics worldwide. This edited volume on "Intelligent and Efficient Electrical Systems" is an outcome of the selected papers presented in the Second International Conference on Intelligent and Efficient Electrical Systems, (ICIEES'17) held on 20–21 January 2017 in Coimbatore, Tamil Nadu, India. This conference organized by the department of Electrical and Electronics Engineering, PSG College of Technology since 2001, occurs every four years. This conference brings together researchers in industry and academia to exchange their ideas, applications and innovative techniques in the area of intelligent and efficient electrical systems.

This year's conference had three keynote addresses and six technical paper sessions. The technical paper sessions were on Smart Grid Systems, Power Converters and Drives, Power Systems, Data Communication & Signal Processing, Renewable Energy Systems and Embedded & Control Systems.

Chapter "Multi-Objective Optimization of Stand-alone Renewable Energy Hybrid System" focuses on multi-objective optimization algorithm for hybrid systems that uses solar, wind, diesel energy systems along with battery and inverter.

Chapter "Wind Farm Power Prediction Based on Wind Speed and Power Curve Models" deals with a combined power prediction models of nonlinear auto regressive wind speed model together with the wind turbine power curve model for very short-term forecasting of wind power.

Chapter "Integration of Wind Power Generators for the Enhancement of Profit by Optimal Allocation of SVC" presents an optimal allocation of static VAR compensator (SVC) for wind power generators with IEEE 6 bus system, and a Grey Wolf Optimizer (GWO) algorithm is used to solve optimal power flow (OPF) problem.

Chapter "Block-Random Access Memory-Based Digital Pulse Modulator Architecture for DC–DC Converters" deals with digital pulse mode architecture using FPGA to control the DC–DC converters with high degree of resolution to provide accurate output voltage.

Chapter "Fractional-Order Controller Design and Analysis for SEPIC Converter" focuses on the optimized genetic algorithm-based fractional-order PI (FOPI) controller for a single-ended primary inductance converter (SEPIC) to get better transient performance.

Chapter "Advanced Energy Management of a Micro-grid Using Arduino and Multi-agent System" presents the optimization of distributed energy management of solar micro-grid system with a multi-agent system approach using Java Agent Development Environment.

Chapter "Sustain the Critical Load in Blackout Using Virtual Instrumentation" deals with blackout power system restoration process to handle critical loads using LabVIEW.

Chapter "Optimal Single and Multiple DG Installation in Radial Distribution Network Using SLPSO Algorithm" deals with an efficient social learning particle swarm optimization (SLPSO) algorithm for sizing and location of distributed generation (DG) units in radial distribution network.

Chapter "Dynamic Modeling and Control of Utility Interactive Microgrid Using Fuzzy Logic Controller" deals with the application of fuzzy logic-based PQ control technique for micro-grid system consisting of photovoltaic (PV) and solid oxide fuel cell (SOFC).

Chapter "A Novel Method of Power Quality Improvement in BLDC Motor Using Cascaded H-Bridge MLI Topology" presents a modelling and simulation of BLDC motor using cascaded H-bridge multi-level inverter (MLI).

Chapter "Tuning of Fractional Order Proportional Integral Derivative Controller for Speed Control of Sensorless BLDC Motor using Artificial Bee Colony Optimization Technique" deals with a GA and a novel Artificial Bee Colony (ABC)-based tuning methods of fractional-order proportional integral derivative (FOPID) controller for BLDC motor.

Chapter "Torque Ripple Minimization of a FOC-Fed PMSM with MRAS Using Popov's Hyper-Stability Criterion" presents a Popov's hyper-stability criterion-based model reference adaptive control system (MRAS) for torque and flux ripples reduction technique in PMSM.

Chapter "Effectual Particle Swarm Optimization Algorithm for the Solution of Non-convex Economic Load Dispatch Problem" deals with effectual particle swarm optimization EPSO to solve the convex and non-convex economic load dispatch (ELD) problems.

Chapter "Differential Evolution with Parameter Adaptation Strategy to Economic Dispatch Incorporating Wind" presents an efficient, reliable and powerful population-based real parameter optimization algorithm for economic load dispatch of wind forms.

Chapter "Application of Cuckoo Search Algorithm in Deregulated Economic Load Dispatch" deals with the economic load dispatch problems in deregulated power system network using meta-heuristic and stochastic search methods.

Chapter "An Investigation of Small-Signal Stability of IEEE 14 Bus System with AVR, PSS and Performance Comparison with FACTS Devices" focuses to improve transient stability margin, increased power transfer capability, real and reactive power

compensation and good power oscillation damping using FACTS devices like SVC and UPFC.

Chapter "Investigation on the Properties of Natural Esters Blended with Mineral Oil and Pyrolysis Oil as Liquid Insulation for High Voltage Transformers" explains the investigation methods to develop and analyze the properties for the applications in high voltage transformers as alternate liquid insulation using natural esters and blended oil for high voltage transformers.

Chapter "A Novel Approach to Using Energy-Efficient LED-Based Visible Light Communication in Hospitals" presents a novel approach in the transmission of healthcare information using the up-and-coming wireless visible light communication technology.

Chapter "Implementation of Mesh Network Using Bluetooth Low Energy Devices" focuses on developing BLE mesh network for the wireless environment to implement the data transfer in the BLE devices.

Chapter "Online Static Security Assessment Module Using Radial Basis Neural Network Trained with Particle Swarm Optimization" deals with modelling of online static security analysis module with neural network for contingency analysis of IEEE-30 bus system.

Chapter "Ocular Artifact Suppression in Single Trial EEG Using DWT-Combined ANC" presents an effective ocular artefact suppression using discrete wavelet transform (DWT) combined recursive least square (RLS) adaptive noise canceller (ANC) method for the signal obtained in the fronto-polar region where the ocular artifact is dominant.

Chapter "Egomotion Estimation Using Background Feature Point Matching in OpenCV Environment" describes an algorithm of feature based high frame rate ego-motion estimation with Gradient projection and Gabor wavelet transform, which is capable of computing real-time computer vision applications.

Chapter "Performance Analysis of Wavelet Function Using Denoising for Clinical Database" reports various wavelet filter coefficients for image de noising suitable for clinical database image processing.

Chapter "Influence of PWM Waveform on Breakdown in Twisted Pairs" reports the effect of PWM converter switching frequency on the life of the motor winding insulation.

Chapter "Diagnosis of Cardiovascular Diseases (CVD) Using Medical Images" deals with Support Vector Machine (SVM) and Radial Basis Function (RBF) based classifier in image processing methods for ultrasound images.

We wish to place on record our sincere thanks and appreciation to all the experts and contributions to these selected proceedings of ICIEES'17. We wish to thank Springer for publishing these proceedings in the area of intelligent and efficient electrical systems.

Coimbatore, India — M.C. Bhuvaneswari
Plano, USA — Jayashree Saxena

Organizing Committee

Chief Patron

Shri. L. Gopalakrishnan, Managing Trustee, PSG & Sons' Charities

Patron

Dr. R. Rudramoorthy, Principal, PSG College of Technology

Convener

Dr. P. Navaneethan, Professor & Head, Department of EEE, PSG College of Technology

Organizing Secretary

Dr. M.C. Bhuvaneswari, Associate Professor, Department of EEE, PSG College of Technology

Joint Organizing Secretaries

Mr. A. Natarajan, Assistant Professor, Department of EEE, PSG College of Technology
Mr. J. Chelladurai, Assistant Professor, Department of EEE, PSG College of Technology

Coordinators

Ms. A. Gunasundari, Assistant Professor, Department of EEE, PSG College of Technology
Mr. P. Sivakumar, Assistant Professor, Department of EEE, PSG College of Technology
Mr. A. Angamuthu, Assistant Professor, Department of EEE, PSG College of Technology

Contents

Editors and Contributors

About the Editors

Dr. M.C. Bhuvaneswari received her B.E. degree in Electronics and Communication Engineering from the Government College of Technology, Coimbatore, in 1985; M.E. degree in Applied Electronics in 1989 and Ph.D. degree in the area of Very Large Scale Integration (VLSI) testing in 2002 from PSG College of Technology, Coimbatore. She is currently an associate professor at the Department of Electrical and Electronics Engineering at the same college. Her research interests include VLSI testing, VLSI CAD, embedded system design, evolutionary algorithms and multi-objective optimization. She has published 65 papers on these topics in journals and conferences. She has 26 years of teaching experience and was the recipient of the 2010 Dakshinamoorthy Award for Teaching Excellence, instituted by PSG College of Technology.

Dr. Jayashree Saxena received her Ph.D. in Electrical and Computer Engineering from the University of Massachusetts, Amherst in 1993. She is currently a business unit manager at Anora LLC in Plano, Texas where she is responsible for design-for-test (DFT) services. Prior to that, she worked at Texas Instruments, Dallas from 1993 to 2013, where she served in various roles ranging from management to technical leadership in the DFT area. She received the most Significant Paper award at the International Test Conference (ITC) 2013 for the ITC 2003 paper "A Case-study of IR drop in Structured At-Speed Testing". She also served on the Technical Program Committee of ITC from 2005 to 2013.

Contributors

B. Anitha Vijayalakshmi Kings Engineering College, Chennai, Tamil Nadu, India

R. Arulraj Department of Electrical Engineering, FEAT, Annamalai University, Chidambaram, Tamil Nadu, India

S. Arunkumar Kumaraguru College of Technology, Coimbatore, India

M. Bakrutheen Department of Electrical and Electronics Engineering, National Engineering College, Kovilpatti, Tamil Nadu, India

S. Balakiruthiha Department of Electrical and Electronics Engineering, National Engineering College, Kovilpatti, India

K. Baskaran Department of Electrical and Electronics Engineering, Government College of Technology, Coimbatore, India

Nedumaran Damodaran Central Instrumentation and Service Laboratory, University of Madras, Chennai, India

G. Edwin Prem Kumar Department of Computer Sciences Technology, Karunya University, Coimbatore, India

K. Elanseralathan Department of EEE, Pondicherry Engineering College, Pillaichavadi, Puducherry, India

Karthick Ganesan Anna University, Chennai, Tamil Nadu, India

B. Geethalakshmi Pondicherry Engineering College, Puducherry, India

P. Gomathinayagam Sri Ramakrishna Engineering College, Coimbatore, Tamil Nadu, India

R. Hariharan Saveetha School of Engineering, Saveetha University, Chennai, India

A. Immanuel Selvakumar Department of Electrical Technology, Karunya University, Coimbatore, India

R. Indumathi K. Ramakrishnan College of Engineering, Tiruchirappalli, India

S. Jayanthy Sri Ramakrishna Engineering College, Coimbatore, Tamil Nadu, India

S. Jeyasudha Pondicherry Engineering College, Puducherry, India

T. Kesavamurthy Department of Electronics and Communication Engineering, PSG College of Technology, Coimbatore, India

N. Krishna Kumari EEE Department, VNR VJIET, Hyderabad, Telangana, India

N. Kumarappan Department of Electrical Engineering, FEAT, Annamalai University, Chidambaram, Tamil Nadu, India

M. Lekshmi Jain University, Bangalore, India

M. Lydia Department of Electrical Technology, Karunya University, Coimbatore, India

J. Mahadevan Department of Electrical and Electronics Engineering, Dhanalakshmi Srinivasan College of Engineering and Technology, Chennai, India

Krishnan Mahadevan Department of Electrical and Electronics Engineering, PSNA College of Engineering and Technology, Dindigul, Tamil Nadu, India

M. Maheswari Department of ECE, K. Ramakrishnan College of Engineering, Tiruchirappalli, India

R.S. Milton Department of Computer Science and Engineering, SSN College of Engineering, Chennai, Tamil Nadu, India

N. Mohana Sundaram Kumaraguru College of Technology, Coimbatore, India

Antony Amalraj Morais Department of Electrical and Electronics Engineering, SSN College of Engineering, Chennai, Tamil Nadu, India

P. Muthu Kannan Saveetha School of Engineering, Saveetha University, Chennai, India

S. Nagalakshmi Department of Electrical & Electronics Engineering, Sethu Institute of Technology, Kariapatti, India

M.S. Nagaraj Department of EEE, Acharya Institute of Technology, Bangalore, India

S. Narasimha Rao Department of EEE, Pondicherry Engineering College, Pillaichavadi, Puducherry, India

M. Nesa Sudha Karunya University, Coimbatore, Tamil Nadu, India

J. Pearly Catherine J.K.K. Nattraja College of Engineering and Technology, Kumarapalayam, India

A.J. Pinto Pius NMAMIT, Udupi District, Karnataka, India

P. Prema Department of Biomedical Engineering, PSG College of Technology, Coimbatore, India

V. Radhika Department of Electronics and Instrumentation Engineering, Sri Ramakrishna Engineering College, Coimbatore, India

Harikumar Rajaguru Bannari Amman Institute of Technology, Erode, Tamil Nadu, India

Leo Raju Department of Electrical and Electronics Engineering, SSN College of Engineering, Chennai, Tamil Nadu, India

K. Ramadoss Department of Neurology, PSG Institute of Medical Sciences and Research, Coimbatore, India

Rani Thottungal Kumaraguru College of Technology, Coimbatore, India

Rajendran Joseph Rathish Department of Electrical and Electronics Engineering, PSNA College of Engineering and Technology, Dindigul, Tamil Nadu, India

D. Ravi Kumar EEE Department, VNR VJIET, Hyderabad, Telangana, India

R. Rengaraj Department of Electrical and Electronics Engineering, SSN College of Engineering, Chennai, India

R.C. Rohini Department of Electrical & Electronics Engineering, Kamaraj College of Engineering & Technology, Virudhunagar, India

S. Senthil Kumar Department of Electrical and Electronics Engineering, National Engineering College, Kovilpatti, Tamil Nadu, India

Sharmila Bakthavachalam Central Instrumentation and Service Laboratory, University of Madras, Chennai, India

Smrithi Radhakrishnan Department of Electrical and Electronics Engineering, Karpagam College of Engineering, Coimbatore, India

S. Suresh Kumar Department of Electronics & Communication, Dr. NGP Institute of Technology, Coimbatore, India

C. Udhayashankar Kumaraguru College of Technology, Coimbatore, India

P. Usha Rani R.M.D. Engineering College, Chennai, India

John Valder PA College of Engineering, Mangalore, Karnataka, India

K.R. Valluvan Velalar College of Engineering and Technology, Erode, Tamil Nadu, India

K. Vanchinathan Velalar College of Engineering and Technology, Erode, Tamil Nadu, India

M. Vanitha Department of Electrical Power, Al Musanna College of Technology, Muscat, Oman

G.R. Venkatakrishnan Department of Electrical and Electronics Engineering, SSN College of Engineering, Chennai, India

T. Vigneysh Department of Electrical Engineering, Annamalai University, Chidambaram, Tamil Nadu, India

M. Willjuice Iruthayarajan Department of Electrical and Electronics Engineering, National Engineering College, Kovilpatti, Tamil Nadu, India

Multi-Objective Optimization of Stand-alone Renewable Energy Hybrid System

Rajendran Joseph Rathish and Krishnan Mahadevan

Abstract This paper shows the complete analysis of optimal configuration of hybrid system that uses solar, wind, diesel energy system along with battery and inverter. These systems are gaining popularity due to increasing energy costs and decreasing costs of wind turbines and solar panels. The only drawback of this system is their outputs depend on climatic conditions. The main goal is to optimize the configuration of the system as well as the control strategy that minimizes the total cost and emissions. This must be achieved through the useful life of the installation to meet the desired consumption and/or the pollutant emissions. Strength Pareto Evolutionary Algorithm to the multi-objective optimization of a stand-alone PV–wind–diesel system with batteries storage and inverter is applied. The objectives to be minimized are net present cost, CO_2 emissions, and unmet load. Results show that hybrid renewable energy technology is the best suitable for stand-alone system.

Keywords Multi-objective optimization · Hybrid systems · Stand-alone systems Wind · Photovoltaic · Diesel

1 Introduction

Stand-alone hybrid grids are more economical than the systems that use single source of energy [1]. Hybrid PV–wind or PV–wind–diesel system with battery storage has been studied elaborately in the technical literature [2–7]. Hybrid systems which include diesel generator are often cheaper than the systems which include photovoltaic (PV) and wind systems. Climate can make one type of hybrid

R.J. Rathish (✉) · K. Mahadevan
Department of Electrical and Electronics Engineering, PSNA College of Engineering and Technology, Kothandaraman Nagar, Dindigul, Tamil Nadu, India
e-mail: josepheee@psnacet.edu.in

K. Mahadevan
e-mail: mahadevan@psnacet.edu.in

M.C. Bhuvaneswari and J. Saxena (eds.), *Intelligent and Efficient Electrical Systems*, Lecture Notes in Electrical Engineering 446,
https://doi.org/10.1007/978-981-10-4852-4_1

system more profitable than another type, like PV–battery–diesel system is ideal in warm countries [8]. Systems with low cost of energy usually include diesel generator, but CO_2 emissions are more [9]. Surplus electricity generated from hybrid systems can be sold to grid [10]. Different types of tools for hybrid system have been discussed [11].

This paper applies Strength Pareto Evolutionary Algorithm (SPEA) for multi-objective optimization of stand-alone PV–wind–diesel system with battery storage and inverters. The objectives to be minimized are net preset cost (NPC), CO_2 emissions, and unmet load. Optimization is achieved using improved Hybrid Optimization using Genetic Algorithms (iHOGA), which serves as a design tool.

2 Simulation and Optimization

The considered system is given in Fig. 1. It consists of PV panels and wind turbines. Generator (diesel) with a battery bank and an inverter is included as part of backup and storage system. The main advantage of hybrid systems is that they utilize different types of renewable energy systems. PV panels are able to generate electricity whenever solar illumination is available. Wind turbines are able to generate electric power when the wind speed is greater than cut-in speed. The ultimate goal of independent power system using renewable energy system is the proper selection of energy mix and proper control of the system. System components must be determined so as to:

- Minimize the cost of production of electricity (€/kWh) and
- Meet the energy demand by consumers.

The mathematical design problem involves lot of variables [9]. When the number of variables and possible solutions is high, the classic optimization

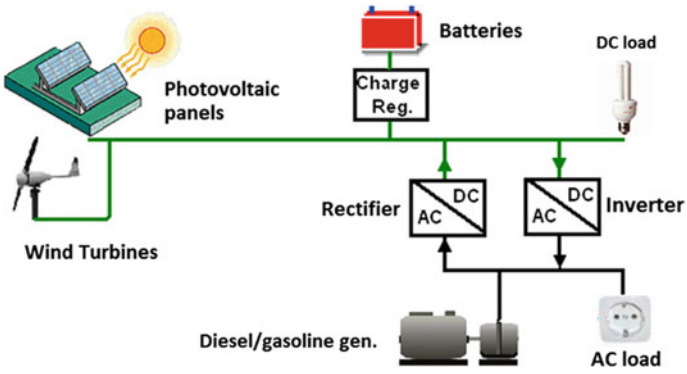

Fig. 1 PV–wind–diesel–batteries hybrid system

techniques are not able to provide the best solution. In such complicated design problems, heuristic techniques have been applied successfully [12]. One of the most commonly used heuristic techniques is based on genetic algorithms [13].

The design posed an optimization problem. The solution allows the attainment of the optimum configuration of the system by simultaneously minimizing net present cost, CO_2 emissions, and unmet load. This task is achieved using iHOGA that uses Multi-Objective Evolutionary Algorithms (MOEAs). This has been already applied in numerous research studies [14].

Some of the most important concepts that should be taken into account while applying MOEAs can be observed graphically. Figure 2 shows a set of possible solutions to a multi-objective optimization problem of minimization considering two objectives (F1 and F2). The solutions "a", "b", "c", "d", "e", and "f" are non-dominated solutions, as none of them has both lower F1 and lower F2 than any other of them. The non-dominated solutions are into the Pareto front. The solutions "1", "2", "3", and "4" are dominated solutions. For example, solution "1" is dominated by "b" and "c" (both "b" and "c" have lower F1 and lower F2 than "1"), solution "4" is dominated by "b", "c", "d", "1", and "2", and so on. Therefore, the only solutions of interest are the non-dominated solutions.

At the end of the optimization process (when the last generation of the MOEA is evaluated), the non-dominated solutions of the Pareto front are the best considering, simultaneously, both objectives. This will be considered the "best Pareto front."

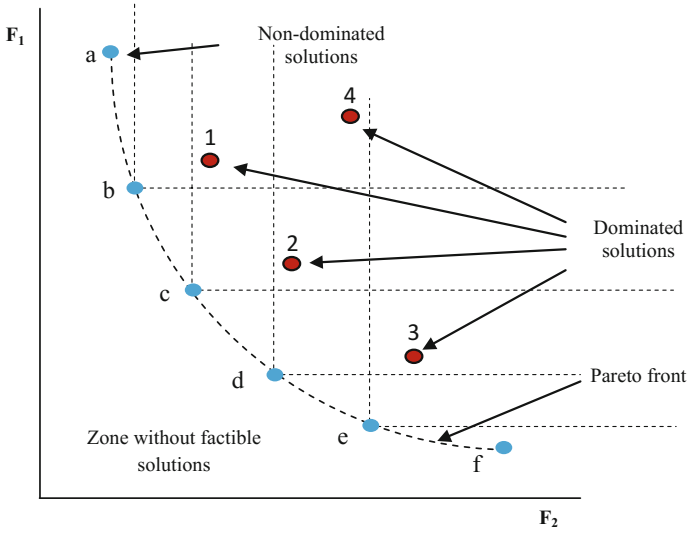

Fig. 2 Pareto front of MOEA

3 Mathematical Model

3.1 Load Profile

The load profile that has been considered is as shown in Fig. 3. Different types of loads are considered. The load used in the analysis is AC-only, but design tool allows for DC-only or AC and DC loads simultaneously.

3.2 Current from the PV Generator

Hourly solar irradiation is needed for proper selection of PV panels. These values can be calculated from the average monthly data [15]. By using this model [15], hourly solar irradiation on the PV generator can be calculated G_h (kWh/m^2) considering both azimuth and tilt angles. For each hour h of 8760 h of year, the power produced by the photovoltaic generator (W) is given by

$$P_{PV_h} = P_{peak_{PV}} \times G_h \times F_{loss} \tag{1}$$

where $P_{peak_{PV}}$ (W_p) is the nominal peak power of the generator and F_{loss} is the factor that considers the losses of power given by photovoltaic panels due to dirt, shadows, temperature, etc.

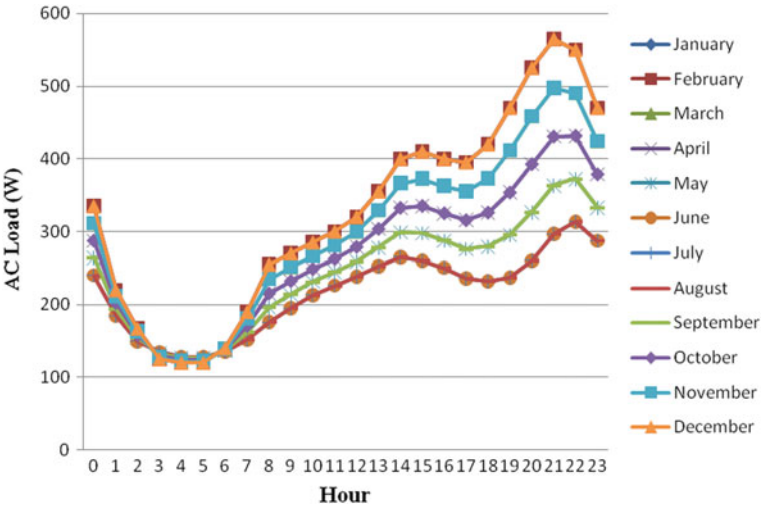

Fig. 3 Daily load profiles used in optimization

3.3 Current from Wind Turbine

Power curves are needed for calculating the power generated by the wind turbine. Current generated by the wind turbine is calculated from these power curves supplied by the manufacturer [16]. Figure 4 shows the curve of this kind. Hourly values needed for calculation of wind speed are similar to those applied in HOMER program [17].

3.4 Batteries

Proper selection of battery is needed for storing the generated electric power and to supply the demand when needed. This depends on charge condition of the battery and the maximum admissible currents. Many models are available to calculate it such as Ah model [18] and KiBaM model [19]. Life span calculation of batteries is as crucial, as it influences the net cost of the system. Life of battery can be calculated as follows:

$$\text{Life}_{\text{bat}} = \frac{1}{\sum_{i=1}^{m} \left(\frac{N_i}{\text{CF}_i}\right)} \tag{2}$$

where m represents intervals, N_i number of cycles of depth of discharge (DOD), and CF_i represents cycle of failure obtained from Fig. 5.

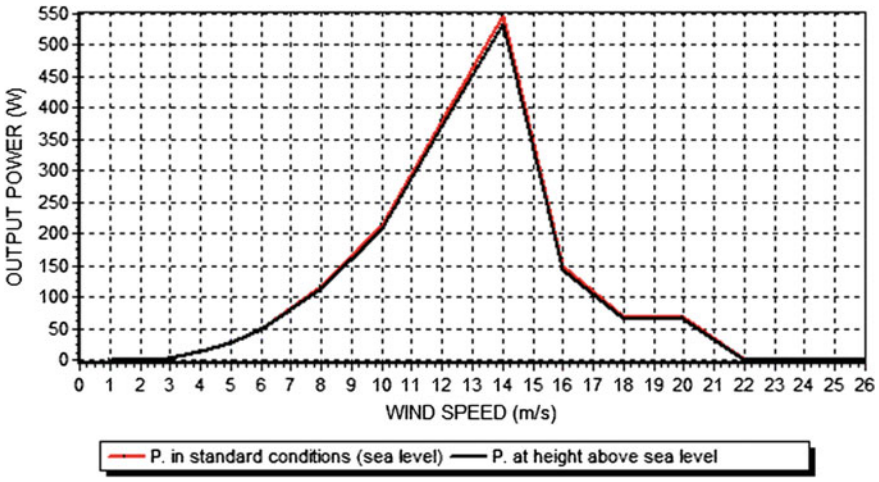

Fig. 4 Power curve of a wind turbine

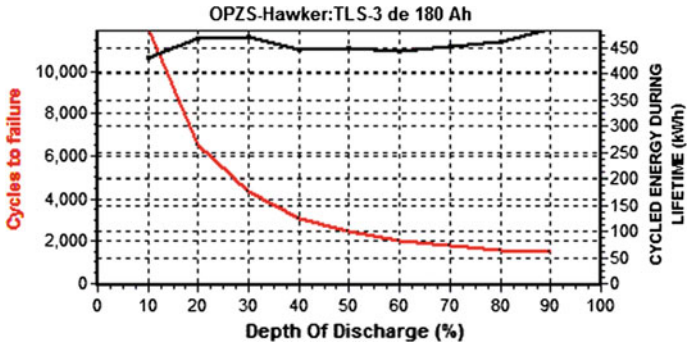

Fig. 5 Battery cycle life versus DOD

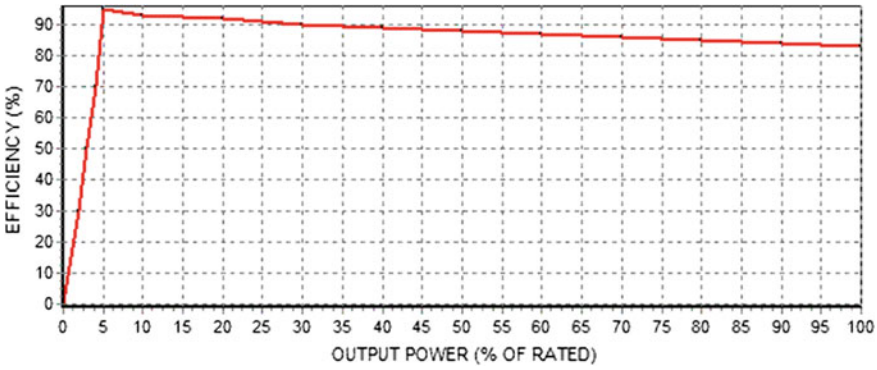

Fig. 6 Inverter efficiency

3.5 Inverter

Inverter has been modeled, considering efficiency variable as a function of apparent power output as shown in Fig. 6.

4 Solar and Wind Data

The location that is considered for the analysis is Dindigul (latitude 10.4747 N, longitude 77.8367 E, height above sea level 268 m)

- Monthly average daily irradiation over horizontal surface (Fig. 7) is obtained from NASA Web [20], daily average irradiation is 4.44 kWh/m^2 and total annual irradiation is 1620.77 kWh/m^2.
- Monthly average wind speed (Fig. 8) is obtained from NASA Web [20].

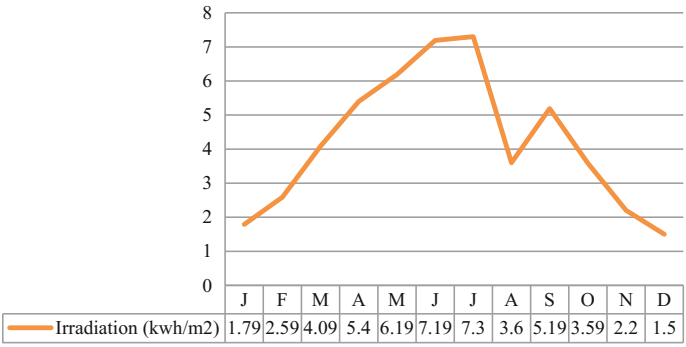

Fig. 7 Hourly irradiation values

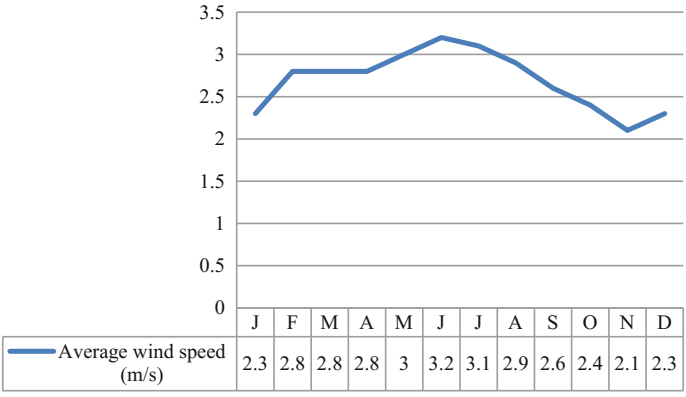

Fig. 8 Hourly wind speed

5 Objective Functions

Total net present cost (NPC) is the cost objective function which is given by

$$\begin{aligned}\text{Totalcost} = &\left\{\begin{array}{c}\text{purchasing cost of PV panels, wind turbine, batteries, inverters, charge regulators} \\ \text{and diesel generator}\end{array}\right\} \\ &+ \{\text{maintenance cost PV panels, wind turbines, batteries}\} \\ &+ \{\text{replacing cost of batteries, inverters, charge regulators, wind turbine}\} \\ &+ \{\text{operation and maintenance cost of diesel genertor}\} \\ &+ \{\text{fuel consumed during life time}\}\end{aligned}$$

Some of the costs depend on control strategy. Strategies considered are as explained in [21].

5.1 Cost of Supplying Energy with Batteries

The cost of supplying power from the batteries (€/kWh) can be calculated using the following equation:

$$C_{\text{sup\_}P_{\text{batt}}} = \frac{C_{\text{bat}}1000}{C_N N_{\text{batt\_p}} V_{\text{DC}} N_{\text{cycles\_eq}} \sqrt{\eta_{\text{global\_batt}}}} \tag{3}$$

where $C_{\text{bat}}1000$ is the bank acquisition cost (€), C_N is the nominal capacity of one battery (Ah),

$N_{\text{batt\_p}}$ is the number of batteries in parallel, V_{DC} is the DC voltage, $N_{\text{cycles\_eq}}$ is the average of equivalent full cycles of battery life, and $\eta_{\text{global\_batt}}$ is the overall efficiency of the battery.

5.2 Cost of Supplying Energy with Diesel Generator

The average cost of power P during 1 h with the diesel generator is, in (€):

$$C_{P_{\text{gen}}} = C_{\text{fixed}_{\text{gen}}} + \frac{\text{AP}_{r_{\text{fuel}}} P}{\eta_{\text{AC/DC}} \text{Factor}_{\text{DC}} + (1 - \text{Factor}_{\text{DC}})} \tag{4}$$

$$C_{\text{fixed}_{\text{gen}}} = C_{\text{O\&M}_{\text{gen}}} + \frac{C_{\text{gen}}}{\text{Life}_{\text{gen}}} + \text{BP}_{\text{N\_gen}} P_{\text{r\_fuel}} \tag{5}$$

where $P_{\text{N\_gen}}$ is the nominal power of the diesel generator (kW), $P_{\text{r\_fuel}}$ is the fuel price (€/l), C_{gen} is the cost of acquisition of the diesel generator in €, Life_{gen} is the estimated life span of the diesel generator (hour), $\eta_{\text{AC/DC}}$ is the efficiency of AC/DC converter, and $C_{\text{fixed}_{\text{gen}}}$ is the fixed cost of operation of the diesel generator (which is independent of the output power) in (€/h), A and B are fuel curve coefficients.

5.3 Unmet Load

$$\text{Unmet load}(\%) = \frac{\text{Total unmet load (kWh/year)}}{\text{total annual electric load (kWh/year)}} \times 100 \tag{6}$$

The multi-objective algorithm searches for the low NPC, low CO_2 emission, and low unmet load.

6 Hybrid System Components

The components that are considered in the hybrid system are listed in Table 1.

Table 1 Components of hybrid system

DC voltage (V)	48
AC voltage (V)	230
System life span (years)	25
Nominal annual interest rate (%)	4
Annual inflation, except for fuel (%)	2
PV panels	
Number of possible different types	10
Maximum number in parallel	17
Life span (years)	9
Tilt angle (º)	20
Azimuth angle (º)	0
F_{Loss}	1.2
O &M cost of the PV generator (€/year)	40
Batteries	
Number of possible different types	6
Maximum number in parallel	3
Model	Ah (Schuhmacher)
Floating life (years)	18
Minimum state of charge suggested by manufacturer (%)	20
O &M cost of the battery bank (€/year)	50
Wind turbines	
Number of possible different types	12
Maximum number in parallel	1
Life span (years)	15
Hub height (m)	10
O&M cost of each wind turbine (€/year)	151
Diesel generator	
Number of possible different types	3
Maximum number in parallel	2
Fuel price (€/l)	1.3
Fuel annual inflation (%)	5
Minimum output power recommended by manufacturer (%)	30
Life span (hour)	10,000
Emissions ($kgCO_2$/liter fuel)	3.5
O &M cost (€/hour)	0.14

7 Results and Discussions

Optimum system configuration and control strategy is obtained by using hybrid system. The optimization results for the hybrid system (Fig. 1) are shown in Figs. 9 and 10. The simulation software iHOGA suggested a list of feasible configurations needed for this project. Figure 9 shows the NPC against CO_2 consumed, and Fig. 10 shows NPC against unmet load, where the number of generations in the genetic algorithm is 15. It is observed that the best NPC is 32890 € Fig. 11. The obtained value is the global minimum NPC after 15 tests with the same parameter. The optimum configuration obtained is composed of four panels series and 12 panels parallel, which generates a power of 6.48 kWp; 24 batteries in series and two in parallel; AC wind turbine with nominal power of 1.66 kW at 14 m/s; inverter 900 VA; battery charge regulator with current of 149 A; and battery charger of 2913 W. The total system cost is 32,818 €, and levelized cost of energy is 0.55 €/kWh. The various other costs are as shown in Fig. 12. Figure 13 gives energy generated in year, and best combination of components is given in Fig. 14. CO_2 emissions per year are found to be 381 kg CO_2/year, and unmet load is made zero.

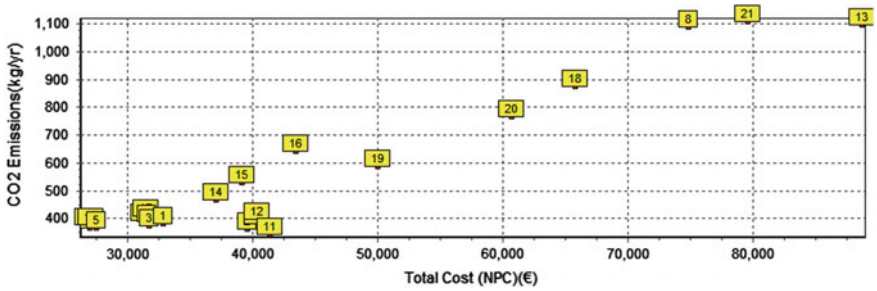

Fig. 9 Best Pareto front for CO_2 emissions and NPC for the given load

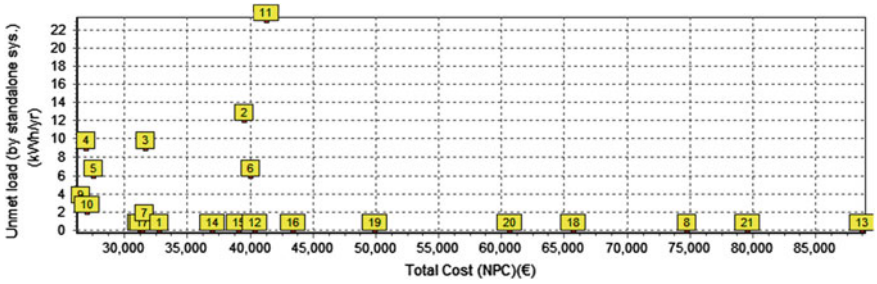

Fig. 10 Best Pareto front for unmet load and NPC for the given load

Dom. by:	Total Cost (NPC)(€)	Emission (kgCO2/yr)	Unmet (kWh/yr)	Unmet (%)	D.range	Cn(Ah)/(Isc+Idc)(A)	Ren(%)	Cost E(€/kWh)
0	32890	381	0	0	3.8	5.6	100	0.56
0	39832	364	13.6	0.6	3.8	6.2	99.4	0.68
0	31711	373	9.2	0.4	3.8	6	99.6	0.54
0	26955	366	9	0.4	3.8	5.7	99.6	0.46
0	27503	366	5.6	0.2	3.8	5.7	99.8	0.47
0	40030	380	6	0.3	3.8	5.9	99.7	0.68
0	31566	390	1.3	0.1	3.8	5.6	99.9	0.53
0	74791	1090	0	0	3.8	1.5	100	1.26
0	26525	379	3.1	0.1	3.8	5.4	99.9	0.45

Fig. 11 Optimized result of hybrid system

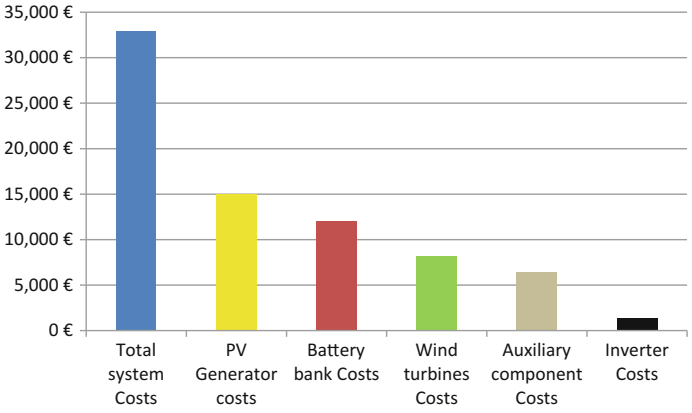

Fig. 12 NPC of the system

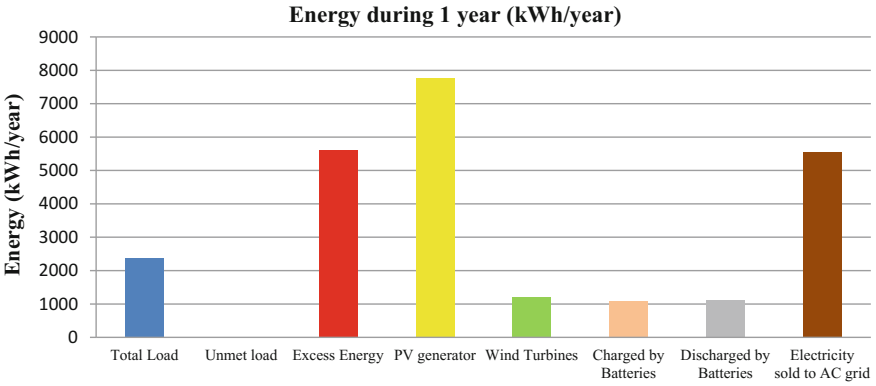

Fig. 13 Energy during 1 year

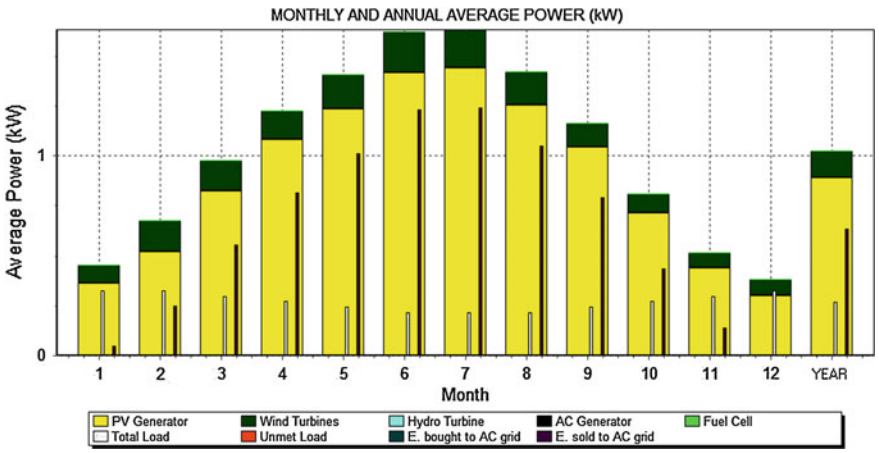

Fig. 14 Best combination of components

8 Conclusions

iHOGA software permits the multi-objective optimization (CO_2 emissions, unmet load vs. NPC) of stand-alone PV–wind–diesel system with batteries storage. Using iHOGA, the optimization of the system at the considered site and load is achieved as discussed above. Almost all of the possible solutions of the best Pareto fronts do not include diesel generator. The results also show that CO_2 emission can be minimized by using the optimized components and also it is shown that unmet load is made zero. Diesel generators may be used as backup source with the hybrid PV–wind–battery system, to guarantee the reliable supply without interruption of the load.

Acknowledgements The authors acknowledge with gratitude the software provided by Dr. Rodolfo Dufo López, Department of Electrical Engineering, University of Zaragoza, Spain.

References

1. Muselli M, Notton G, Louche A (1999) Design of hybrid-photovoltaic power generator, with optimization of energy management. Sol Energy 65(3):143–157
2. Zhou W, Lou C, Li Z, Lu L, Yang H (2010) Current status of research on optimum sizing of stand-alone hybrid solar–wind power generation systems. Appl Energy 87:380–389
3. Saheb-Koussa D, Haddadi M, Belhamel M (2009) Economic and technical study of a hybrid system (wind–photovoltaic–diesel) for rural electrification in Algeria. Appl Energy 86:1024–1030
4. Ekren O, Ekren BY (2010) Size optimization of a PV/wind hybrid energy conversion system with battery storage using simulated annealing. Appl Energy 87(2):592–598

5. Bekele G, Palm G (2010) Feasibility study for a standalone solar–wind-based hybrid energy system for application in Ethiopia. Appl Energy 87(2):487–495
6. Diaf S, Notton G, Belhamel M, Haddadi M, Louche A (2008) Design and techno economical optimization for hybrid PV/wind system under various meteorological conditions. Appl Energy 85(10):968–987
7. Kalantar M, Mousavi GSM (2010) Dynamic behavior of a stand-alone hybrid power generation system of wind turbine, micro turbine, solar array and battery storage. Appl Energy 87(10):3051–3064
8. Shaahid SM, Elhadidy MA (2003) Opportunities for utilization of stand-alone hybrid (photovoltaic + diesel + battery) power systems in hot climates. Renew Energy 28(11):1741–1753
9. Bernal-Agustín JL, Dufo-López R, Rivas-Ascaso DM (2006) Design of isolated hybrid systems minimizing costs and pollutant emissions. Renew Energy 31(14):2227–2234
10. Bernal-Agustín JL, Dufo-López R (2010) Techno-economical optimization of the production of hydrogen from PV-Wind systems connected to the electrical grid. Renew Energy 35:747–758
11. Bernal-Agustín JL, Dufo-López R (2009) Simulation and optimization of stand-alone hybrid renewable energy systems. Renew Sustain Energy Rev 13:2111–2118
12. Dufo-López R, Bernal-Agustín JL, Contreras J (2007) Optimization of control strategies for stand-alone renewable energy systems with hydrogen storage. Renew Energy 32(7):1102–1126
13. Goldberg DE (1989) Genetic algorithms in search, optimization and machine learning. Addison-Wesley, Boston, MA
14. Coello CA, Veldhuizen DAV, Lamont GB (2002) Evolutionary algorithms for solving multi-objective problems. Kluwer Academic/Plenum Publishers, New York
15. Graham VA, Hollands KGT (1990) A method to generate synthetic hourly solar radiation globally. Sol Energy 44(6):333–341
16. Manwell JF, McGowan JG, Rogers AL (2002) Wind energy explained. Wiley, New York
17. Hybrid optimization model for electric renewables (HOMER). Website: www.nrel.gov/international/homer
18. Schuhmacher J (1993) INSEL—interactive simulation of renewable electrical energy supply systems. Reference Manual, University of Oldenburg, Renewable Energy Group, Department of Physics (1993)
19. Manwell JF, McGowan JG (1993) A lead acid battery storage model for hybrid energy systems. Sol Energy 50(5):399–405
20. Surface meteorology and solar energy. A renewable energy resource web site (release 6.0). Sponsored by NASA's Earth Science Enterprise Program. http://eosweb.larc.nasa.gov/sse/RETScreen/
21. Dufo-López R, Bernal-Agustín JL (2011) Multi-objective design and control of hybrid systems minimizing costs and unmet load. Appl Energy 88:4033–4011

Wind Farm Power Prediction Based on Wind Speed and Power Curve Models

M. Lydia, S. Suresh Kumar, A. Immanuel Selvakumar and G. Edwin Prem Kumar

Abstract Accurate prediction of wind farm power is essential for increasing wind penetration in the electricity grid. It also aids the power system operators in planning unit commitment, economic scheduling, and dispatch. In this paper, combined wind farm power prediction models have been built based on wind speed prediction models and power curve models. The wind speed prediction models have been built using nonlinear autoregressive models with and without external variables. The wind turbine power curve has been modeled using parametric and nonparametric models. Parametric models are built using four- and five-parameter logistic expression, whose parameters are solved using particle swarm optimization (PSO) and differential evolution (DE). Nonparametric models were built based on data mining algorithms. Multistep prediction model for wind power forecasting has been developed for very short-term forecasting of wind power. Real-time data obtained from Sotavento Galicia Plc. has been used for testing the proposed model.

Keywords Data mining · Differential evolution · Particle swarm optimization Time-series model · Wind speed forecasting

1 Introduction

Wind power has definitely gone a long way in solving the problems of energy and environmental crisis. Though wind energy promises to be a clean and sustainable source of energy, its integration into the existing electrical supply system is a great

M. Lydia (✉) · A. Immanuel Selvakumar
Department of Electrical Technology, Karunya University, Coimbatore, India
e-mail: lydiaedwin.05@gmail.com

S. Suresh Kumar
Department of Electronics & Communication, Dr. NGP Institute of Technology, Coimbatore, India

G. Edwin Prem Kumar
Department of Computer Sciences Technology, Karunya University, Coimbatore, India

M.C. Bhuvaneswari and J. Saxena (eds.), *Intelligent and Efficient Electrical Systems*, Lecture Notes in Electrical Engineering 446,
https://doi.org/10.1007/978-981-10-4852-4_2

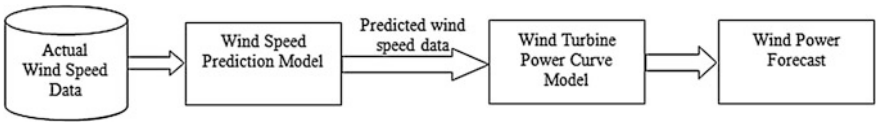

Fig. 1 Combined prediction model for wind power

challenge. Wind power prediction has been a hot area of research, and several techniques have been evolved for both onshore and offshore power prediction [1–5].

This paper presents a novel combined model for very short-term wind power forecast. It consists of the combination of a wind speed prediction model and wind turbine power curve model (Fig. 1). Many of the research works carried out earlier have built the univariate model of wind speed time-series data. In this paper, nonlinear autoregressive models (NAR1) for time-series wind speed data with and without external variables have been built. These models have been solved using data mining algorithms. Multistep prediction models for predicting wind speeds at 10 min interval up to 1 h have been built. These values are given as inputs to the wind turbine power curve models which have been built using parametric and nonparametric techniques. The parametric models of wind turbine power curve are built using the four- and five-parameter logistic expression whose variables are solved using nontraditional optimization techniques such as PSO and DE.

These techniques have the advantage of enhanced accuracy and are very easy to implement even for huge datasets. The nonparametric models are built using data mining algorithms. The combined models are used to predict the wind farm power over 10 min interval, for the next six time steps.

2 Wind Speed Prediction Model

Building an accurate model for wind speed forecasting is the first important requisite for realizing the combined prediction model shown in Fig. 1. Four different models have been built for very short-term wind speed forecasting. WS11, WS10, and WS09 refer to the 10 min averaged wind speed data of December in the years 2011, 2010, and 2009, respectively, and WD represents wind direction. The first one is a nonlinear autoregressive model (NAR1), and the remaining models are built based on exogenous variables, namely the wind direction and wind speed of the previous two years. These nonlinear models are solved using data mining algorithms, namely SMOreg, Lazy k-star, bagging, M5R, and M5P.

The defining equation for the NARX model is

$$y(t) = f(y(t-1), y(t-2), \ldots, y(t-n_y), u(t-1), u(t-2), \ldots, u(t-n_u)) \quad (1)$$

where the next value of the dependent output signal, the wind speed at a particular time $y(t)$ is regressed on previous values of the output signal and previous values of

an exogenous input signal u, n_y is the AR order, and n_u is the input order [6]. The function f can be approximated using any nonlinear algorithms such as neural networks and data mining algorithms.

2.1 NAR and NARX Models for Wind Speed

The NAR models do not have any exogenous input signal. The expression for the NAR model developed for wind speed (NAR1) using the sequential feature selection algorithm is given in Eq. 2.

$$y(t) = f(y(t-1), y(t-2), y(t-3), y(t-5)) \tag{2}$$

The wind direction and wind speeds of the corresponding time in the previous two years are the exogenous variables that have been taken into consideration.

2.1.1 Model Incorporating Wind Direction

Sensing of wind direction is essential to capture maximum power from the wind. It is usually measured in cardinal directions or in azimuth degrees and is measured using a wind vane. The nonlinear autoregressive model including wind direction (NARX1), using the sequential feature selection algorithm, is given in Eq. 3.

$$y(t) = f(y(t-1), y(t-2), y(t-3), y(t-5), u_1(t-1), u_1(t-3)) \tag{3}$$

where u_1 is the wind direction of the corresponding period.

2.1.2 Model Incorporating Annual Trends

A linear time-series-based model for forecasting wind speed and direction was proposed by relating the predicted interval to its corresponding one- and two-year old data [7]. The one-year model performed better than the two-year model for smaller prediction horizons, while the two-year models performed better for larger prediction horizons. The nonlinear autoregressive model with wind direction and wind speed of the corresponding period in the previous year (u_2) as exogenous variables (NARX2), after application of feature selection algorithm, is defined in Eq. 4.

$$y(t) = f(y(t-1), y(t-2), y(t-3), y(t-5), u_1(t-1), u_1(t-3), u_2(t-4)) \tag{4}$$

The nonlinear autoregressive model with wind direction and wind speed of the corresponding period one year before and two years before (u_3) as exogenous variables (NARX3), after application of feature selection algorithm, is defined in Eq. 5

$$y(t) = f(y(t-1), y(t-2), y(t-3), y(t-5), u_1(t-1), u_1(t-3), u_2(t-4), u_3(t-1), u_3(t-7)) \tag{5}$$

Multistep prediction up to six consecutive time steps has also been developed.

3 Wind Turbine Power Curve Model

The theoretical power captured by the rotor of a wind turbine (P) is given by

$$P = 0.5\rho\pi R^2 C_p y^3 \tag{6}$$

where ρ is the air density, R is the radius of the rotor, C_p is the power coefficient, and y is the wind speed [8]. In this paper, parametric and nonparametric models are built for the wind turbine power curve. Parametric models are built using four- and five-parameter logistic expression [9]. The parameters of these expressions are solved using PSO and DE. Nonparametric models were built using data mining algorithms.

3.1 Parametric Models

The shape of the power curve resembles the four-parameter logistic function which is defined as

$$P = a(1 + me^{-y/\tau}/1 + ne^{-y/\tau}) \tag{7}$$

where a, m, n, and τ are the vector parameters. The five-parameter logistic expression has been used for modeling the wind turbine power curve in [9]. It is defined by

$$P = d + (a - d)/\left(1 + \left(\frac{y}{c}\right)^b\right)^g \tag{8}$$

where a, b, c, d, and g are the vector parameters that are solved using PSO and DE.

3.2 Nonparametric Models

A nonparametric model for the power curve is built on the assumption that

$$P = f(y) \tag{9}$$

Nonparametric models are built using four different data mining algorithms, namely MLP, bagging, M5R, and M5P. The combined power prediction models are the major contribution of this paper. The output of the best wind speed model is given as input to the best wind turbine power curve model. Multistep prediction models for the next six consecutive time steps have been built.

4 Modeling Techniques

The nonparametric models were developed using various data mining algorithms such as SMOreg, Lazy k-star, bagging, M5R, M5P, and MLP. The optimization techniques such as PSO and DE have been employed in this paper to find the parameters of the four- and five-parameter logistic function. The optimization problem is defined as follows:

$$\text{Objective function: } \min \sum_{i=1}^{N} \left[P_e(y_i) - P_a(i)\right]^2 \tag{10}$$

where $P_e(y_i)$ is the power estimated by the logistic expressions, $P_a(i)$ is the actual power, and N is the total number of data. The constraints of the four- and five-parameter logistic expression are given in Eqs. 11 and 12, respectively.

$$\{a_{\min} \le a \le a_{\max}, m_{\min} \le m \le m_{\max}, n_{\min} \le n \le n_{\max}, \tau_{\min} \le \tau \le \tau_{\max}\} \tag{11}$$

$$\{a_{\min} \le a \le a_{\max}, b_{\min} \le b \le b_{\max}, c_{\min} \le c \le c_{\max}, d_{\min} \le d \le d_{\max}, g_{\min} \le g \le g_{\max}\} \tag{12}$$

5 Results and Analysis

The data used for this research, the results obtained, and the analysis of results have been presented in this section.

5.1 Experimental Data

The real-time data used for development of wind speed and wind power prediction models was obtained from Sotavento Galicia Plc., an experimental wind farm supported by the "Xunta de Galicia", the regional autonomous government [10]. The 10 min averaged data for the month of December 2011 has been used for the combined wind power prediction models (Fig. 2). The total number of data is 4446,

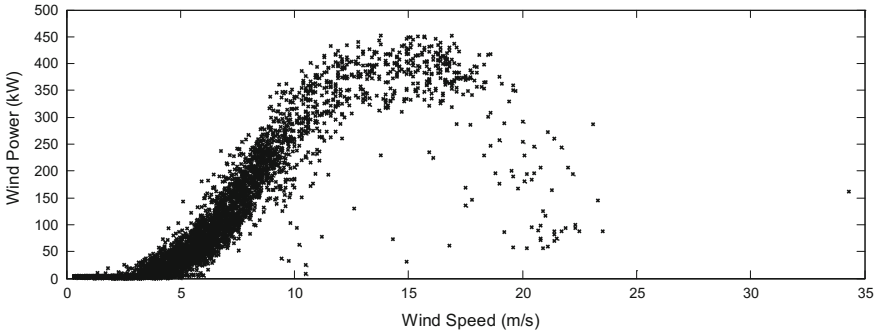

Fig. 2 Real-time data of December 2011

half of which was used for training and the other half was used for testing the data mining algorithms. The parametric algorithms which involved the application of optimization techniques were built using the entire set of data.

5.2 *Results of Wind Speed and Power Prediction Models*

As the combined model for wind power prediction is built using the best wind speed model and best wind power curve model, the performance of the various models built in this regard has been analyzed in the following section. The performance of these parametric and nonparametric models has been evaluated using the metrics mean absolute error (MAE) and root mean squared error (RMSE). If N is the total number of input data, S_e is the estimated variable, and S_a is the actual variable, MAE and RMSE are defined as follows:

$$\text{MAE} = \frac{1}{N}\sum_{i=1}^{N} |S_e(i) - S_a(i)| \tag{13}$$

$$\text{RMSE} = \sqrt{\frac{1}{N}\sum_{i=1}^{N} (S_e(i) - S_a(i))^2} \tag{14}$$

The variables can either be wind speed or power based on the model being tested.

5.2.1 Performance of Wind Speed Prediction Models

The performance of the time-series models for wind speed built using data mining algorithms was compared and the M5R algorithm performed best for the nonlinear

autoregressive model for wind speed. The M5P and bagging algorithms give the lowest MAE and RMSE, respectively, for all the other models that are built including the different external variables. The multistep prediction models were also built for wind speed using these algorithms.

5.2.2 Performance of Wind Power Prediction Models

In order to identify the best wind power prediction model, the parametric and nonparametric wind turbine power curve models are built. The data mining algorithms used for nonparametric models were developed and tested in WEKA. The optimization techniques, PSO and DE, used for solving the logistic expressions of the parametric models were built in MATLAB. The population size and maximum number of iterations of PSO and DE were selected as 50 and 100, respectively. The control parameters of PSO are $w = 0.5$, $C_1 = 2$, and $C_2 = 2$. The control parameters of DE are $F = 1$ and $C_R = 0.5$. The parameters of four-parameter logistic expression (a, m, n, τ) solved by PSO are (383.4822, −0.3050, 271.1179, 1.5341) and by DE are (384.09, −3.4636, 216.5773, 1.5634). The parameters of five-parameter logistic expression (a, b, c, d, g) solved by PSO are (395.9986, −6.31994, 9.7276, −2.7150, 0.5682) and by DE are (393.9342, −6.4761, 9.7280, −3.0050, 0.5521).

When the best wind speed prediction models are given as input to the wind power curve models, it was observed that the parametric power curve models totally outperform the nonparametric models. The wind turbine power curve built using five-parameter logistic expression whose parameters are optimized using PSO give best results for all the NARX models of wind speed. Parametric models solved using DE algorithm give the best performance for the NAR model of wind speed.

Multistep prediction models of wind power are built for the best combination of wind speed and power, and their performance is tabulated in Table 1.

5.3 Analysis of Results

The multistep prediction of the combined models of wind power has been analyzed in Table 2 using two criteria, mean and standard deviation (Std) of the errors. The mean value gives an idea about the error magnitude in every consecutive step and Std is a measure that is used to quantify the amount of variation or dispersion of a set of data values. The combination of nonlinear autoregressive wind speed model without any external variables (NAR1) built using M5R algorithm and wind turbine power curve model built using four-parameter logistic expression solved by DE algorithm registers lowest mean and standard deviation when the RMSE is considered. Though the mean of its MAE errors is higher than the other models, its standard deviation is the lowest.

Table 1 Multistep prediction of combined models of wind power

	WS model	NAR1 (M5R)	NAR1 (M5R)	NARX1 (M5P)	NARX1 (M5P)	NARX2 (M5P)	NARX2 (M5P)	NARX3 (M5P)	NARX3 (M5P)
	WP model	DE (4P)	DE (5P)	DE (4P)	PSO (5P)	DE (4P)	PSO (5P)	DE (4P)	PSO (5P)
First time step	MAE	20.7971	20.6379	20.5797	20.4825	20.5343	**20.4323**	20.5491	20.4407
	RMSE	**32.3466**	32.5559	32.6416	32.8376	32.4872	32.6725	32.4585	32.6198
Second time step	MAE	22.5446	22.4762	22.0703	22.0046	22.0344	**21.9560**	22.0813	21.9897
	RMSE	34.5132	34.8309	**33.8235**	33.9954	33.8607	34.0038	34.0114	34.1267
Third time step	MAE	24.0281	24.0235	23.9381	23.9253	23.9176	**23.8909**	23.9530	23.9258
	RMSE	**36.3888**	36.7815	36.6484	36.8099	36.7724	36.9071	36.8793	37.0102
Fourth time step	MAE	25.4151	25.4377	25.3981	25.4329	25.3087	25.3378	25.2108	**25.2568**
	RMSE	**38.1803**	38.5999	38.4410	38.6175	38.5202	38.6891	38.3307	38.5526
Fifth time step	MAE	26.6340	26.6208	26.7813	26.8438	26.5982	26.6718	26.4239	**26.5089**
	RMSE	39.5764	40.0281	40.1185	40.3744	40.0322	40.3333	**39.5346**	39.8296
Sixth time step	MAE	27.5459	27.5661	27.7663	27.8824	**27.5451**	27.6744	27.4879	27.6430
	RMSE	**40.8588**	41.3502	41.4779	41.7974	41.2307	41.5826	40.9997	41.4174

The values that are in bold represent best values
In MAE and RMSE the least values are the best values

Table 2 Analysis of multistep prediction of combined models of wind power

Combined models of wind power prediction	MAE		RMSE	
	Mean	Std	Mean	Std
NAR1 (M5R) + DE (4P)	24.49	**2.547**	**36.98**	**3.198**
NAR1 (M5R) + DE (5P)	24.46	2.608	37.36	3.298
NARX1 (M5P) + DE (4P)	24.42	2.765	37.19	3.488
NARX1 (M5P) + PSO (5P)	24.43	2.845	37.41	3.533
NARX2 (M5P) + DE (4P)	24.32	2.694	37.15	3.451
NARX2 (M5P) + PSO (5P)	24.33	2.782	37.36	3.518
NARX3 (M5P) + DE (4P)	**24.28**	2.631	37.04	3.279
NARX3 (M5P) + PSO (5P)	24.29	2.733	37.26	3.375

This model which has the lowest standard deviation augurs well for multistep prediction. Prediction of wind power based on this model would definitely give a very reliable result for very short-term horizon spanning from 10 min to 1 h.

6 Conclusion

Wind power prediction models can revolutionize electricity trading, aid the power system operators in planning and control. Combined power prediction models consisting of wind speed and wind turbine power curve models have been proposed in this paper. The combination of nonlinear auto regressive wind speed model built using M5R algorithm together with the wind turbine power curve model built using the four-parameter logistic expression, whose parameters were solved using DE, performed best. The multistep prediction of this combined model of wind power is very impressive as it records the lowest standard deviation for both the error measures, namely MAE and RMSE. These models can be effectively used to predict power for consecutive time steps, using wind speed as the only input. Development and implementation of this model will definitely go a long way in making wind-generated power more attractive, reliable, and competitive.

References

1. Munteanu I, Besancon G (2016) Identification-based prediction of wind park power generation. J Renew Energy 97:422–433
2. Dong L, Wang L, Khahro SF, Gao S, Liao X (2016) Wind power day-ahead prediction with cluster analysis of NWP. J Renew Sustain Energy Rev 60:1206–1212
3. Renani ET, Elias MFM, Rahim NA (2016) Using data-driven approach for wind power prediction: a comparative study. J Energy Convers Manage 118:193–203

4. Ouyang T, Zha X, Qin L, Xiong Y, Xia T (2016) wind power prediction method based on regime of switching kernel functions. J Wind Eng Ind Aerodyn 153:26–33
5. Heinermann J, Kramer O (2016) Machine learning ensembles for wind power prediction 89:671–679
6. Neural network toolbox, MATLAB R2008a
7. El-Fouly THM, El-Saadany EF, Salama MMA (2008) One day ahead prediction of wind speed and direction. IEEE Trans Energy Convers 23:191–201
8. Kusiak A, Zheng H, Song Z (2009) On-line monitoring of power curves. J Renew Energy 34:1487–1493
9. Lydia M, Immanuel Selvakumar A, Suresh Kumar S, Edwin Prem Kumar G (2013) Advanced algorithms for wind turbine power curve modeling. IEEE Trans Sustain Energy 4:827–835
10. http://www.sotaventogalicia.com/

Integration of Wind Power Generators for the Enhancement of Profit by Optimal Allocation of SVC

S. Nagalakshmi, R.C. Rohini and S. Balakiruthiha

Abstract Integration of wind power generators with the power grid is an alternate choice to meet out the present energy crisis. Even though wind power generators possess diverse benefits, its intermittent nature causes adverse effects to the entire system. This study proposes an approach to integrate wind power generators in order to satisfy today's energy crisis and also to enhance the profit by optimal allocation of static VAR compensator (SVC). A new population-based optimization technique grey wolf optimizer (GWO), is used to solve optimal power flow (OPF) problem that uses AC load flow equations to minimize sum of generation cost, investment cost of FACTS devices and cost of wind power generation (WPG). To validate the proposed approach, simulations are carried out on IEEE 6 bus system. The results obtained conclude that by applying GWO, profit is enhanced via optimal allocation of SVC along with the wind power generations (WPG).

Keywords Grey wolf optimizer (GWO) · Static VAR compensator (SVC) Optimal power flow (OPF) · Wind power generation (WPG)

1 Introduction

Over the past several years, the substantial progress in the energy usage results in the depletion of the conventional energy resources thus augments the need to shift from non-renewable energy resources to the renewable sources of energy. Wind

S. Nagalakshmi (✉)
Department of Electrical & Electronics Engineering,
Sethu Institute of Technology, Kariapatti, India
e-mail: snagalakshmieee@gmail.com

R.C. Rohini
Department of Electrical & Electronics Engineering,
Kamaraj College of Engineering & Technology, Virudhunagar, India

S. Balakiruthiha
Department of Electrical and Electronics Engineering,
National Engineering College, Kovilpatti, India
e-mail: balakiruthiha@gmail.com

M.C. Bhuvaneswari and J. Saxena (eds.), *Intelligent and Efficient Electrical Systems*, Lecture Notes in Electrical Engineering 446,
https://doi.org/10.1007/978-981-10-4852-4_3

energy, one of the rapidly growing alternate sources of electrical energy holds a prime position among the various renewable energy sources as it brings numerous positive benefits to the electrical network. Even though WPG possesses many assets, the integration of wind generation creates significant challenges due to the unpredictable nature of wind energy. FACTS devices provide the solution to the various dilemma caused by the renewable resources. Optimal location of FACTS devices is determined to solve steady state problem of wind penetration using GA [1]. Comprehensive review on wind integration issues is presented in [2]. A generalized approach for determination of optimal location of FACTS devices in power system is proposed by many researchers using various methods [3–11]. In [4], it is concluded that among the FACTS devices, SVC is best suited for IEEE 6 bus system.

Recently, a new population-based meta-heuristic optimization technique inspired by the social behaviour of grey wolves with less control parameters known as grey wolf optimizer (GWO) has been proposed by Mirjalili et al. in 2014 [12]. GWO is an emerging optimization algorithm among the various meta-heuristic techniques, used widely to solve many power system-related problems. GWO is capable of finding global solutions, provides fast search of large solution spaces, accounts for uncertainties in some parts of power systems and is not problem defined [12]. GWO algorithm has been used in solving economic dispatch and ORPD problems, and it provides very competitive results when compared to other algorithms [13, 14].

The main target of this work is to apply GWO to find the optimal location and settings of SVC by performing OPF on the system by integrating wind power generation for the enhancement of profit via optimal allocation of SVC. The potency of the suggested work is tested on IEEE 6 bus system, where the objective function is minimization of sum of generation cost, the hourly investment cost of SVC and cost of WPG subject to the constraints on the real and reactive power generation, bus voltage magnitude, transmission line flow and SVC settings. Among the various FACTS devices, SVC is employed in order to enhance the profit of the system. Wind generators with different capacities such as 30, 60, 100, 120, 160 and 200 kW are included in this work, and the investment cost of wind generators is considered to be 3.75 $/MWh.

2 Modelling of SVC

2.1 Static VAR Compensator (SVC)

SVC is modelled as shunt-connected static VAR generator or absorber, Q_{SVC} whose output is adjusted to exchange capacitive or inductive compensation and is inserted directly to the load bus as shown in Fig. 1.

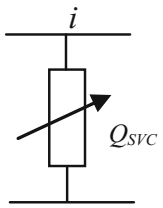

Fig. 1 Static model of SVC

3 Problem Formulation

3.1 Objective Function

Optimal power flow problem is a large scale optimization problem. The mathematical formulation of OPF is formulated as the minimization of sum of generation cost, investment cost of FACTS devices and wind generators while satisfying all the equality and inequality constraints.

$$F = \min \sum_{i=1}^{N_G} \mathrm{GC}_i(P_{gi}) + \sum_{m=1}^{N_{\mathrm{FACTS}}} HIC_{\mathrm{FACTS}}(m) + \sum_{n=1}^{\mathrm{WPG}} C_{\mathrm{WPG}}(n) \tag{1}$$

where

$$\text{Generation Fuel Cost, } \mathrm{GC}_i(P_{gi}) = a * P_{gi}^2 + b * P_{gi} + c \tag{2}$$

$$\text{Installation Cost, } \mathrm{IC}_{\mathrm{FACTS}} = 0.0003 S_c^2 - 0.3051 S_c + 127.38 \tag{3}$$

$$\text{Investment Cost, } \mathrm{InvCost}_{\mathrm{FACTS}} = (\mathrm{IC}_{\mathrm{FACTS}} \times S_c \times 1000) \tag{4}$$

$$\text{Annual Investment Cost, } \mathrm{AICost}_{\mathrm{FACTS}} = \mathrm{InvCost}_{\mathrm{FACTS}} \frac{ir(1+ir)^{\mathrm{LT}}}{(1+ir)^{\mathrm{LT}} - 1} \tag{5}$$

$$\text{Hourly Investment Cost, } \mathrm{HIC}_{\mathrm{FACTS}} = \frac{\mathrm{AICost}_{\mathrm{FACTS}}}{8760}. \tag{6}$$

GC_i	Cost curve of ith generator in \$/hr
$\mathrm{N_G}$	Number of generators
C_{WPG}	Cost of wind power generation in MW
a, b, c	Cost coefficients of the generator
P_{gi}	Real power generation at bus i in MW
$\mathrm{IC_{SVC}}$	Installation cost of SVC in \$/hr
$S_c = Q_a - Q_b$	Operating range of FACTS devices in MVAR
Q_a	Reactive power flow in the line after installing FACTS devices in MVAR

Q_b	Reactive power flow in the line before installing FACTS devices in MVAR
$\text{InvCost}_{\text{FACTS}}$	Investment cost of FACTS devices in $/hr
$\text{AICost}_{\text{FACTS}}$	Annual investment cost of FACTS in $/hr
$\text{HIC}_{\text{FACTS}}$	Hourly investment cost in $/hr
ir	Interest rate
LT	Lifetime

3.2 Equality Constraints

Power balance equation

$$\sum_{i=1}^{N_G} P_{gi} + P_{\text{WPG}} - P_{\text{loss}} - P_l = 0 \tag{7}$$

$$P_{\text{loss}} = \sum_{j=1}^{N_l} G_j \left[|V_i|^2 + |V_j|^2 - 2|V_i||V_j| \cos(\delta_i - \delta_j) \right]. \tag{8}$$

3.3 Inequality Constraint

$$\text{Voltage magnitude limits } V_i^{\min} \le V_i \le V_i^{\max} \tag{9}$$

$$\text{Phase angle limits } \phi_i^{\min} \le \phi_i \le \phi_i^{\max} \tag{10}$$

$$\text{MVA limits } S_l \le S_l^{\max} \tag{11}$$

$$\text{Real power limits } P_{gi}^{\min} \le P_{gi} \le P_{gi}^{\max} \tag{12}$$

$$\text{Reactive power limits } Q_{gi}^{\min} \le Q_{gi} \le Q_{gi}^{\max} \tag{13}$$

where

n_b	Total number of buses
N_G	Total number of generators
n_l	Total number of transmission lines
P_{di}, Q_{di}	Real and reactive power demand at bus i
P_{li}, Q_{li}	Real and reactive power losses at bus i
Q_{gi}	Reactive power generation at bus i
$P_g^{\min}$ and $P_g^{\max}$	Minimum and maximum limits of real power generation in MW

$Q_g^{\min}$ and $Q_g^{\max}$	Minimum and maximum limits of reactive power generation in MVAR
$\lvert V_i \rvert$	Voltage magnitude at bus i
$V_i^{\min}$ and $V_i^{\max}$	Minimum and maximum limits of magnitude of bus voltage in p.u
S_l	Apparent power flow in the line in MVA
$S_l^{\max}$	Maximum limit for apparent power flow in MVA
Q_{SVC}	Reactive power of SVC in MVAR.

4 Grey Wolf Optimizer (GWO)

A new population-based swarm intelligence technique known as grey wolf optimizer is proposed in this work. This technique was developed by Mirjalili et al. in 2014. Grey wolf (Canis lupus) belongs to Canidae family [12]. They are considered as the apex predators. Grey wolves are classified into four groups, namely alpha, beta, delta and omega. The three important steps employed to carry out the optimization are hunting, searching for prey, encircling the prey and attacking towards prey. Alphas are the leaders of the group, and they are the decision-makers. The second level in the hierarchy of grey wolf is beta. The lowest rank goes to omega. The wolves other than alpha, beta and omega are termed as delta.

4.1 Algorithm

Step I: *Initialization*
Initialize the bus data, upper and lower bound values, maximum number of iteration, dimension and search agents number.

Step II: *Generation*
The best score and best positions are generated randomly within the allowable limits.

Step III: *Fitness Function Calculation*
For each function, data are updated. The objective function is the minimization of cost.

Step IV: *Position Updation*
During hunting, the wolves encircle the prey. Encircling of the prey can be modelled as follows:

$$\vec{D} = \left| \vec{C} \cdot \vec{X}_p(t) - \vec{X}(t) \right| \tag{14}$$

$$\vec{X}_{(t+1)} = \vec{X}_p(t) - \vec{A} \cdot \vec{D} \tag{15}$$

The first three best (optimal) solutions obtained are stored, while the remaining agents update their positions based on the position of the best search agents.

$$\vec{D}_\alpha = \left|\vec{C}_1 \cdot \vec{X}_\alpha - \vec{X}\right| \tag{16}$$

$$\vec{D}_\beta = \left|\vec{C}_2 \cdot \vec{X}_\beta - \vec{X}\right| \tag{17}$$

$$\vec{D}_\delta = \left|\vec{C}_3 \cdot \vec{X}_\delta - \vec{X}\right| \tag{18}$$

$$\vec{X}_1 = \vec{X}_\alpha - \vec{A}_1 \cdot \left(\vec{D}_\alpha\right) \tag{19}$$

$$\vec{X}_2 = \vec{X}_\beta - \vec{A}_2 \cdot \left(\vec{D}_\beta\right) \tag{20}$$

$$\vec{X}_3 = \vec{X}_\delta - \vec{A}_3 \cdot \left(\vec{D}_\delta\right) \tag{21}$$

5 Results and Discussions

5.1 Tools and Test Systems

The effectiveness of the presented work is carried out in IEEE 6 bus system, and OPF was solved with a modified version of the MATLAB power simulation package MATPOWER [15]. Simulations are performed in computer with Intel i3 processor 2.40 GHz and 3.00 GB RAM. The proposed algorithm is implemented to find the optimal location of SVC for enhancing the profit of the system. The initial parameter of the test system and the values adopted for GWO algorithm are presented in Table 1. In this work, the interest rate and lifetime are taken as 0.05 and 20 years, respectively. In order to verify the effect of optimal location of SVC, two cases are investigated.

Case 1: without SVC and WPG in the system.
Case 2: with SVC and WPG in the system.

Table 1 Initial parameters

Test system parameters	IEEE 6 bus system	GWO parameters	Values
$V_{\max}$	1.1 p.u	Population size	30
$V_{\min}$	0.9 p.u	Number of iterations	500
$Q_{\text{SVC}}^{\max}$	100 MVAR	Number of variables	3
$Q_{\text{SVC}}^{\min}$	−100 MVAR	Convergence criteria	$1 \times e^{-6}$
WPG investment cost	3.75 $/MWh	Coefficient vectors A, C	(1, 0) and (1, 1)

5.2 IEEE 6 Bus System

The test bus system taken to validate the performance of GWO is IEEE 6 bus system. It consists of 6 buses and 11 transmission lines. In the 6 bus system, the buses 1, 2 and 3 are generator buses and the buses 4, 5 and 6 are the load bus. The real and reactive power demands of the IEEE 6 bus system are 210 MW and 210 MVAR, respectively. The single line diagram of IEEE 6 bus system is shown in Fig. 2.

5.3 Case 1: Without SVC and WPG in the System

In this case, OPF is performed without SVC and WPG in the system. In Table 2, the real, reactive and apparent power flow and generation cost without SVC and WPG are tabulated. The generation cost without SVC and WPG is found to be 3125.49 $/hr.

5.4 Case 2: With SVC and WPG in the System

In this case, OPF is performed with SVC and WPG in the system. The locations for WPG are in the load buses, 4, 5 and 6. In Table 3, the optimal generation, location and settings of SVC, total active power generation cost, hourly investment cost of SVC and investment cost of WPG, the objective function and the profit using GWO are tabulated.

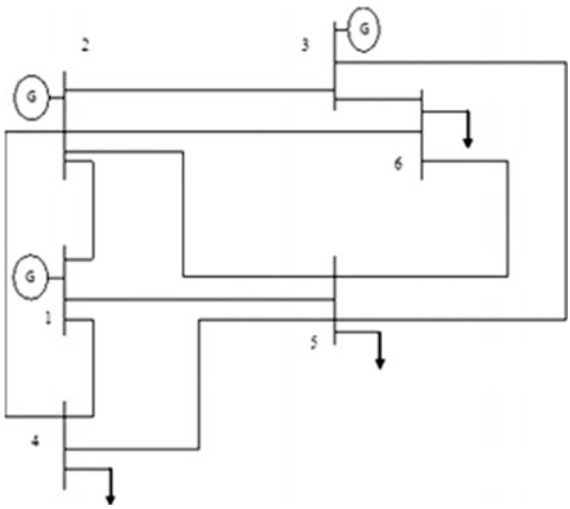

Fig. 2 Single line diagram of IEEE 6 bus system

Table 2 Transmission line power flow in IEEE 6 bus system without SVC and WPG using GWO

Line No.	Real power flow (MW)	Reactive power flow (MVAR)	Apparent power flow (MVA)	Maximum apparent power flow (MVA)	GCWF ($/hr)
1–2	0.04	0.04	0.06	**0.4**	**3125.49**
1–4	0.25	0.30	0.39	**0.6**	
1–5	0.21	0.18	0.28	**0.4**	
2–3	−0.01	−0.10	0.10	**0.4**	
2–4	0.49	0.33	0.60	**0.6**	
2–5	0.19	0.12	0.23	**0.3**	
2–6	0.24	0.12	0.27	**0.9**	
3–5	0.26	0.17	0.31	**0.7**	
3–6	0.50	0.56	0.75	**0.8**	
4–5	0.02	−0.04	0.05	**0.2**	
5–6	−0.03	−0.07	0.07	**0.4**	

Table 3 Optimal value of objective function for IEEE 6 bus system with SVC and WPG using GWO

WPG bus no.	Wind generation value (kW)	GC before SVC	Optimal location of SVC	Q_{SVC}	GC after SVC	HIC_{SVC}	WPG IC	Objective fn.	Profit
4	30	3140.23	Bus 4	−72.26	3103.25	10.40	0.11	3113.77	11.72
4	60	3149.32	Bus 4	−72.26	3103.62	10.40	0.22	3114.25	11.24
4	**100**	**3151.81**	**Bus 4**	**−72.27**	**3104.11**	**10.40**	**0.37**	**3114.89**	**10.6**
4	120	3152.21	Bus 4	−72.27	3104.36	10.40	0.45	3115.21	10.28
4	160	3160.22	Bus 4	−72.27	3104.86	10.40	0.6	3115.86	9.63
4	200	3164.93	Bus 4	−72.27	3105.35	10.39	0.75	3116.50	8.99
5	30	3140.11	Bus 4	−72.26	3103.25	10.40	0.11	3113.77	11.72
5	60	3142.33	Bus 4	−72.26	3103.62	10.40	0.22	3114.26	11.23
5	**100**	**3150.76**	**Bus 4**	**−72.26**	**3104.12**	**10.40**	**0.37**	**3114.90**	**10.59**
5	120	3160.47	Bus 4	−72.26	3104.37	10.40	0.45	3115.23	10.26
5	160	3162.87	Bus 4	−72.26	3104.87	10.40	0.6	3115.87	9.62
5	200	3163.38	Bus 4	−72.26	3105.37	10.40	0.75	3116.52	8.97
6	30	3114.23	Bus 4	−72.26	3103.24	10.40	0.11	3113.76	11.73
6	60	3132.56	Bus 4	−72.26	3103.61	10.40	0.22	3114.24	11.25
6	**100**	**3149.98**	**Bus 4**	**−72.26**	**3104.10**	**10.40**	**0.37**	**3114.88**	**10.61**
6	120	3154.21	Bus 4	−72.26	3104.35	10.40	0.45	3115.20	10.29
6	160	3159.11	Bus 4	−72.26	3104.84	10.40	0.6	3115.84	9.65
6	200	3162.28	Bus 4	−72.26	3105.32	10.40	0.75	3116.48	9.01

From Table 3, it is evident that profit decreases with the increase in the wind power generation. Hence, 100 kW of wind power generation is optimal for IEEE 6 bus system. The profit obtained with 100 kW of WPG at buses 4, 5 and 6 are 10.6, 10.59 and 10.61 $/hr, respectively. It is also found that bus 4 is the optimal location for the placement SVC in this particular IEEE 6 bus system.

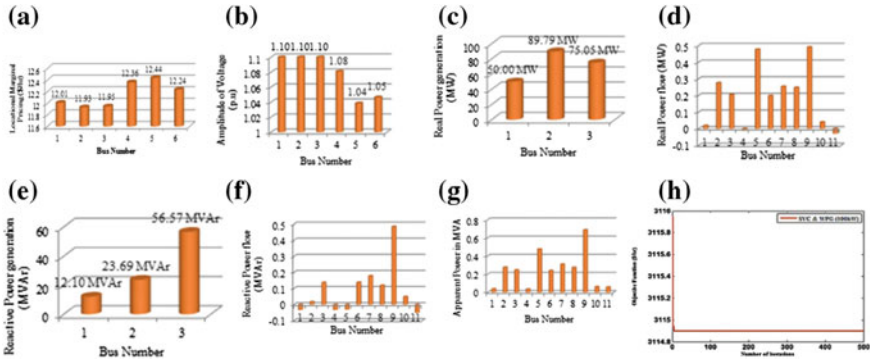

Fig. 3 **a–h** LMP, voltage profile, real power generation, reactive power generation, real power flow, reactive power flow, apparent power flow, convergence characteristics with SVC and WPG (100 kW) at bus 4 using GWO

The LMP, voltage profile, real and reactive power flows, real and reactive power generation, apparent power flows and the convergence graph with SVC in the wind-integrated IEEE 6 bus system are shown in Fig. 3a–g. The locational marginal pricing without SVC and with SVC in the wind-integrated IEEE 6 bus system is shown in Fig. 3a. It has been noted that installation of SVC can improve the LMP of the system. From Fig. 3b–g, it is observed that the voltage profile, real and reactive power generation and the branch flows are all within the upper and lower limits thus satisfying the constraints. The convergence characteristic for the proposed model is shown in Fig. 3h. From Fig. 3h, it is inferred that GWO converges faster and it shows the effectiveness of the proposed methodology in solving OPF problem.

6 Conclusion

The electric power demand has grown rapidly due to the rise in population. The substantial progress in energy demand has led to the depletion of existing energy resources. It is necessary to switch to more environmentally safe and clean resources like wind energy. The integration of wind energy into the power network causes many problems. FACTS devices are used to solve those problems and also to enhance the profit of the network. Among the various FACTS controllers, SVC is employed in this study for profit enhancement in this particular system. This paper presents a population-based meta-heuristic optimization technique, namely GWO to optimally allocate SVC in the wind-integrated system. The objective function is taken as the minimization of fuel cost and the investment cost of SVC and WPG. The numerical result reveals the potency of the proposed methodology in enhancing the profit of the system by optimally allocating SVC. From the results, it is

confirmed that SVC is best suited for profit enhancement in IEEE 6 bus system. Higher profit can be achieved with less wind power generation value. To conclude, for profit enhancement of deregulated power system with FACTS devices, GWO algorithm is considered to be the best for following reasons: (i) easy to implement, (ii) robust, (iii) minimal initial parameter settings and tuning and (iv) faster convergence. Among the FACTS devices, SVC is the best for profit enhancement of large size system.

References

1. Abdelaziz Y, El-Sharkawy MA, Attia MA, El-Saadany EF (2014) Optimal location of series FACTS to improve the performance of power system with wind penetration. In: IEEE PES general meeting/conference and exposition, July 2014, pp 1–5
2. Dowds J, Hines P, Ryan T, Buchanan W, Kirby E, Apt J, Jaramillo P (2015) A review of large-scale wind integration studies. Renew Sustain Energy Rev 768–794
3. Srinivasa Rao R, Srinivasa Rao V (2015) A generalized approach for determination of optimal location and performance analysis of FACTs devices. Int J Electr Power Energy Syst 73: 711–724
4. Nagalakshmi S, Kamaraj N (2010) Loadability enhancement for pool model with FACTS devices in transmission system using differential evolution and particle swarm optimization. In International conference on power electronics (IICPE 2010), Jan 28–30 2011, pp 1–8
5. Hingorani NG, Gyugyi L (2001) Understanding FACTS: concepts and technology of flexible AC transmission systems. IEEE Press, New York
6. Hingorani NG (1996) Role of FACTS in a deregulated market. IEEE Trans Power Syst 11 (4):1931–1936
7. Gerbex S, Cherkaoui R, Germond J (2001) Optimal location of multi-type FACTS devices in power system by means of genetic algorithms. IEEE Trans Power Syst 16(3):537–544
8. Ongsakul W, Jirapong P (2005) Optimal allocation of FACTS devices to enhance total transfer capability using evolutionary programming. IEEE In: International symposium on circuits systems ISCAS, vol 5, pp 4175–4178
9. Nagalakshmi S, Kamaraj N (2011) Secured loadability enhancement with TCSC in transmission system using computational intelligence techniques for pool and hybrid model. Appl Soft Comput 11(8):4748–4756
10. Nagalakshmi S, Kamaraj N (2012) Comparison of computational intelligence algorithms for loadability enhancement of restructured power system with FACTS devices. Swarm Evol Comput 5:17–27
11. Nagalakshmi S, Balakiruthiha S (2015) Application of gravitational search algorithm for optimal siting and sizing of FACTS devices in deregulated electricity market. Int J Appl Eng Res 10(9) ISSN: 0973–4562
12. Mirjalili S, Mirjalili SM, Lewis A (2014) Grey wolf optimizer. Adv Eng Softw 69(12):46–61
13. Wong LI, Sulaiman MH, Mohamed MR, Hong MS (2014) Grey wolf optimizer for solving economic dispatch problems. IEEE Int Conf Power Energy (PECON) 7(5):150–154
14. Sulaiman MH, Mustaffa Z, Mohamed MR, Aliman O (2015) Using the gray wolf optimizer for solving optimal reactive power dispatch problem. Appl Soft Comput 32(3):286–292
15. Zimmerman RD, Murillo-Sanchez CE, Gan D MATPOWER: MATLAB power system simulation package

Block-Random Access Memory-Based Digital Pulse Modulator Architecture for DC–DC Converters

V. Radhika and K. Baskaran

Abstract This paper proposes a new digital pulse-width modulation (DPWM) and digital frequency modulation (DPFM) architecture using block RAM (BRAM) present in the field-programmable gate arrays (FPGAs). In Xilinx FPGAs, Block RAM (BRAM) elements are available only with a synchronous reset. As the synchronous reset is used in this code, the synthesis tool implemented the code in a single BRAM element. This minimizes the decoding logic and reduces the area. Block RAM available in FPGA is used to store the desired pattern to derive the variable duty cycle and variable-frequency pulses. This DPWM/DPFM architecture can be used with switching type of DC–DC converters under both light- and heavy-load conditions. Architecture is developed with Verilog hardware language for three different control bits (4 bit, 5 bit, and 6 bit), synthesized, and implemented with Xilinx PlanAhead 14.2 tool. This proposed architecture provides higher resolution without any requirement for higher clock frequency and larger logic resources which ultimately wits the small change in output voltage produced at the output of power converter. Maximum operating frequency of 306 MHz can be achieved for 4-bit control input. For the 6-bit control input, 4096 different bit patterns are stored to derive the more precise pulses to control the DC–DC converters.

Keywords BRAM · DPFM · DPWM · Higher resolution · Spartan 3A FPGA

V. Radhika (✉)
Department of Electronics and Instrumentation Engineering, Sri Ramakrishna Engineering College, Coimbatore, India
e-mail: radhika.senthil@srec.ac.in

K. Baskaran
Department of Electrical and Electronics Engineering, Government College of Technology, Coimbatore, India
e-mail: drbaskaran@gct.ac.in

M.C. Bhuvaneswari and J. Saxena (eds.), *Intelligent and Efficient Electrical Systems*, Lecture Notes in Electrical Engineering 446,
https://doi.org/10.1007/978-981-10-4852-4_4

1 Introduction

Direct Current to Direct Current (DC–DC) converters are the back bone of portable electronic and mobile devices which are using batteries as power supply [1]. Portable devices generally hold various subcircuits each of which operates with different voltage. DC–DC converters must be able to provide these multiple supply voltages; at the same time, they must be highly efficient, area optimized, and able to provide tight voltage regulation. Controlling of converters is a critical issue in these types of applications. Traditional analog controllers cannot be used with the converters for these types of applications as the above-mentioned constraints make the analog controller circuit complex [2]. To provide a solution to these issues, digital controllers are introduced for these types of applications. Digital controllers generally have a high degree of programmability, linearity, higher efficiency, low area, less complex circuit, and less affected to parameter variations [3, 4].

Recent researches use digital pulse-width modulation (DPWM) and digital pulse-frequency modulation (DPFM) techniques realized with the FPGA for the digital control of DC–DC converters [5]. DPWM technique modifies the duty cycle of fixed-frequency square wave, whereas DPFM technique varies the frequency of square wave with constant duty cycle for controlling the switch of power converters to regulate the output voltage. DPWM provides better predictable higher operating frequency with less complex circuit but suffers from poor conversion efficiency at light-load conditions [6, 7]. DPFM provides significant advantage in light-load conditions [8]. But DPFM will not be appropriate for all types of applications so DPFM architecture combined with DPWM architecture can provide a better solution to the above-mentioned constraints of DC–DC converters.

In this paper, a new FPGA based DPWM and DPFM architecture is presented which can be used as a digital switching controller for DC–DC converters. All the traditional DPWM architectures in the literature uses the counter and other decoding mechanism to derive variable duty cycle and variable-frequency pulses to control the switch of DC–DC converters [9, 10]. However, all these types of architectures for achieving high resolution need larger logic resources and higher clock frequency which leads to higher power consumption [11, 12]. But this proposed method uses RAM-based architecture to derive the variable duty cycle or variable-frequency pulse for controlling the DC–DC converters. Xilinx FPGA consists of two columns of memory block called BRAM available with synchronous reset and can be configured with different data width [13]. In order to improve the throughput of dynamic real-time applications, BRAM blocks are used to store the bit streams [14]. Increase in throughput is linear with the number of word in BRAM [15]. In this architecture BRAM is used for storing the bit pattern to derive the pulses with variable duty cycle and variable-frequency. Depending on the value of control input, this architecture is able to provide a variable duty cycle with constant frequency or variable frequency with constant duty cycle pulses and variable-width, variable-frequency pulses. Architecture with three different bit sizes of duty cycle and frequency control bits is developed such as 4-bit duty cycle with

4-bit frequency control bit, 5-bit duty cycle with 5-bit frequency, 6-bit duty cycle with 6-bit frequency control bit. This architecture can provide higher resolution and high-frequency pulses to meet the output voltage accuracy requirement of power converters without any need for high clock frequency requirement.

Proposed architecture is developed with Verilog hardware language, synthesized, and implemented with Xilinx PlanAhead 14.2 tool.

In the next section, architecture of proposed RAM-based DPWM/DPFM is explained and in Sect. 3, simulation results obtained with Xilinx tools is discussed. Section 4 gives the experimental results, and Sect. 5 gives the conclusion.

2 RAM-based DPWM/DPFM Architechture

New proposed DPWM/DPFM architecture has a clock source, clock divider, DPWM module, DPFM module, Multiplexer A (MUX-A), Multiplexer B (MUX-B), and parallel-to-serial converter to generate variable duty cycle and variable-frequency pulses. RAM blocks are clocked with the clock signal derived from clock divider logic, and the parallel-to-serial converter works with clock signal derived from clock source. The register-transfer-level (RTL) schematic of proposed architecture is shown in Fig. 1.

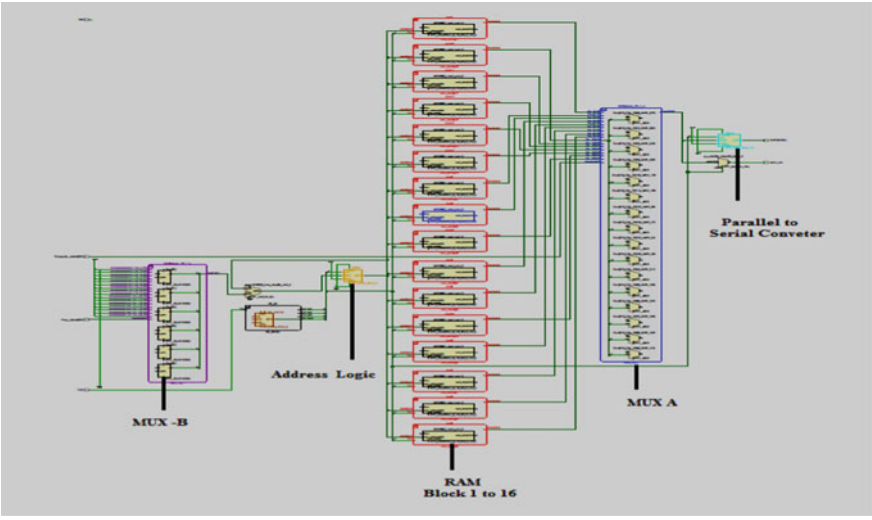

Fig. 1 RTL schematic of the proposed DPWM/DPFM architecture with 4-bit control input

2.1 Digital Pulse-Width Modulator

DPWM module is able to provide variable-width and fixed-frequency pulses for controlling the DC–DC converter switches. DPWM architecture is designed for three different duty cycle control inputs $d(n)$ that is 4-bit control input, 5-bit control input, and 6-bit control input. For n duty cycle control input, it is possible to realize 2^n number of RAM blocks. DPWM module can have 16 blocks of RAM for 4-bit control input, 32 blocks of RAM for 5-bit control input, and 64 blocks of RAM for 6-bit control input. Higher the size of duty cycle control input $d(n)$ higher the RAM blocks can be addressed, higher the resolution for PWM signal can be achieved.

RAM blocks can store binary values that represent the typical values to control the duty cycle and frequency of the pulses generated by DPWM and DPFM modules. Each RAM location in RAM block is of 16-bit wide.

Based on the duty cycle control input $d(n)$, any of the desired 2^n RAM blocks are selected with 2^n:1 multiplexer (MUX-A) to create time-varying pulses. Duty cycle ratio of pulses can be changed by connecting the suitable RAM block with different binary patterns to parallel-to-serial converter. RAM blocks are connected to the parallel-to-serial converter through the multiplexer (MUX-A) with the duty cycle control input $d(n)$ as selection input. Outputs from the RAM blocks are parallel bit patterns; these parallel bit patterns can be converted into serial pulses with parallel-to-serial converter.

RAM blocks are able to deliver 16 bits of data per clock pulse, but the parallel-to-serial converter is able to produce only one bit per clock cycle, to match the speed of serial to parallel converter with RAM block, parallel-to-serial converter works with the clock signal derived from clock source, whereas the RAM blocks are clocked with CLK-16 signal (source clock frequency divide by the constant 16) derived from clock divider logic.

2.2 Digital Pulse-Frequency Modulator

DPFM module is able to provide a variable-frequency and fixed-width pulse for controlling the power converter switches. Digital frequency modulator generates variable-frequency pulses with RAM blocks, MUX-B, MUX-A, and parallel-to-serial converter.

Each RAM location shown in Fig. 2 holds the unique value for the step change in the value. For example, RAM location $0x03_H$ holds the value 1111111111110000_b in RAM block 32 for 6-bit control input, whereas for 5-bit control input the same RAM block 32 for the same RAM location $0x03_H$ holds the value 0000000000000000_b shown in Figs. 3 and 4, respectively.

Four-bit frequency control input can address 16 RAM locations selected by the frequency control input $f(n)$ in a single RAM block through the 16:1 multiplexer (MUX-B), 5-bit frequency control input can address 32 RAM locations in a single

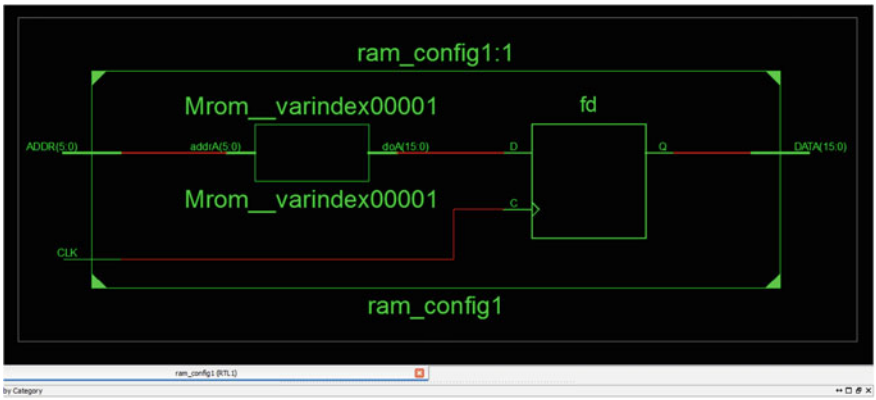

Fig. 2 RAM location 1 with 6-bit address and 16-bit data

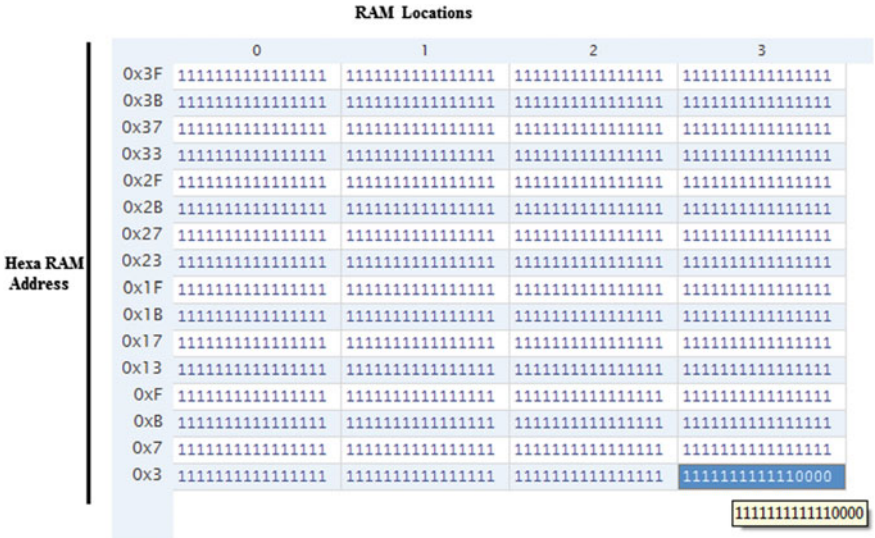

Fig. 3 RAM block 32 for 6-bit control input

RAM block through 32:1 multiplexer, where 6-bit frequency control input can address all the 64 RAM locations in a RAM block through 64:1 multiplexer.

Digital pulse-frequency modulation can be achieved by selecting the desired RAM location with 6-bit address generated from 16-bit address with the frequency control input $f(n)$ through MUX-B. Pulse-frequency modulation can be achieved by keeping $d(n)$ duty cycle control input as constant and varying-frequency control input $f(n)$. Different RAM location in a same RAM block is selected to derive the variable-frequency pulse.

The higher the size of frequency control input $f(n)$ and duty cycle control input $d(n)$, the higher the number of RAM blocks and RAM location can be addressed.

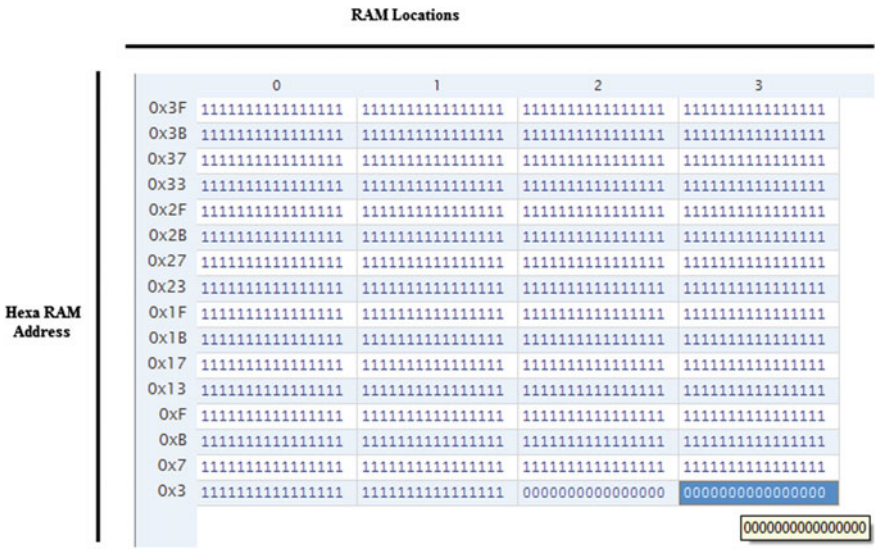

Fig. 4 RAM block 32 for 5-bit control input

With 4-bit duty cycle control input and 4-bit frequency control input, 16 different RAM blocks and 16 different RAM locations can be addressed so totally 254 different bit patterns can be addressed. Similarly, 1024-bit patterns were obtained with 5-bit control input, and 4096-bit patterns can be addressed with 6-bit control input. With the higher number of bit patterns, the DC–DC converter switches can be turned on and turned off more accurately by this type of digital controller.

2.3 Generation of PWM and PFM Signals

Proposed DPWM/DPFM architecture has duty cycle control input $d(n)$ and frequency control $f(n)$ input values from 0000_b to 1111_b for 4-bit control input, 00000_b to 11111_b for 5-bit control input, and 000000_b to 111111_b for 6-bit control input.

Duty cycle ratio of pulses can be changed by selecting suitable RAM block with the desired duty cycle control input given to the MUX-A by maintaining the frequency control input $f(n)$ as constant. Parallel bit patterns from the selected RAM block can be converted to the serial bit patterns through parallel-to-serial converter, to derive pulse-width-modulated (PWM) signal.

Frequency of the pulse can be changed by selecting suitable RAM location with frequency control input through the MUX-B by maintaining the duty cycle input $d(n)$ as constant. Parallel bits from the selected RAM locations can be converted to serial bit pattern through parallel-to-serial converter to derive frequency-modulated pulse (PFM).

3 Results and Discussion

Proposed architecture for three different sizes of control bits are designed with Verilog hardware language. Behavioral simulation results are obtained with Xilinx 14.2 tool for the functional verification of the proposed architecture, synthesized, and implemented with Xilinx PlanAhead 14.2 tool. Timing simulation results are obtained with Xilinx PlanAhead 14.2 tool for logical verification of design.

3.1 Simulation Results

Timing simulation results are obtained with PlanAhead tool for different combinations of 4-bit duty cycle and frequency select 0000_b to 1111_b, 5-bit duty cycle and frequency select 00000_b to 11111_b, and 6-bit duty cycle and frequency select 00000_b to 11111_b signals. Timing simulation results are performed for the validation of proposed design taking into account the delays of FPGA device.

Post-layout timing simulation result with variable duty cycle and frequency is shown in Figs. 5, 6 and 7.

Power estimation value of the proposed architecture with different size of control input signals can be obtained through Xilinx Xpower Analyzer tool with Xilinx Physical design file (.ncd) of the architecture. Power estimation results for different FPGA devices are tabulated in Table 1.

Table 1 shows that design with higher control bits can have higher number bit patterns and can achieve high-resolution pulses at the expense of higher power consumption. Depending on the type of application and control parameters, design with appropriate control input has to be chosen.

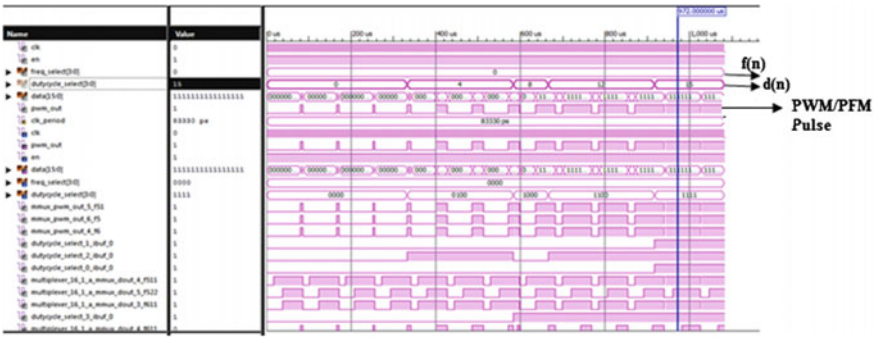

Fig. 5 Post-layout timing simulation result for 4-bit control input

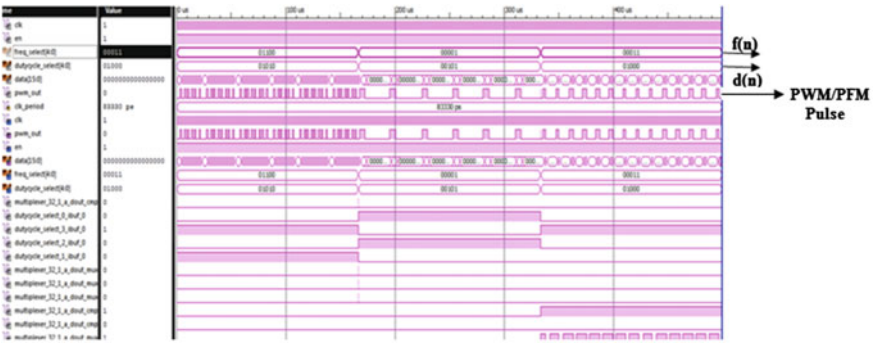

Fig. 6 Post-layout timing simulation result for 5-bit control input

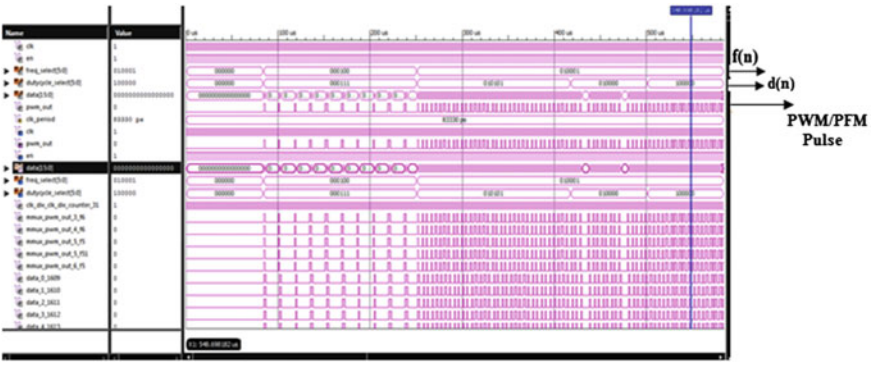

Fig. 7 Post-layout timing simulation result for 6-bit control input

Table 1 Power estimation value for Xilinx FPGA devices

Device type	Power consumption in mW		
	6-bit control input	5-bit control input	4-bit control input
xc3s50atq144-5	19.8	18.7	12.3
xc3s50atq144-4	19.3	18.6	12.2
xc3s100etq144-5	35.1	34.4	25.3
xc3s100etq144-4	34.8	34.3	25.7

4 Experimental Results

After obtaining functional and timing verification, bit stream file is generated for the proposed architecture with 4-bit duty cycle control input and 4-bit frequency control input. Generated bit stream file with the JTAG cable is moved to the target FPGA device. SPARTANXC3S50A FPGA is used for the experimental verification

of the architecture. Duty cycle and frequency control bits are given through the DIP switches present in the FPGA kit. Four switches in the FPGA kit provide duty cycle control bits, and four switches provide frequency control bits to realize 4-bit DPWM/DPFM architecture. All the combinations of DPWM control bits and DPFM control bits 0000_b to 1111_b are given through the switches to vary the duty cycle and frequency of the pulse generated. Experimental values equal the simulation values obtained through Xilinx software. Digital storage oscilloscope showing waveforms of variable duty cycle and frequency shown in Figs. 8 and 9.

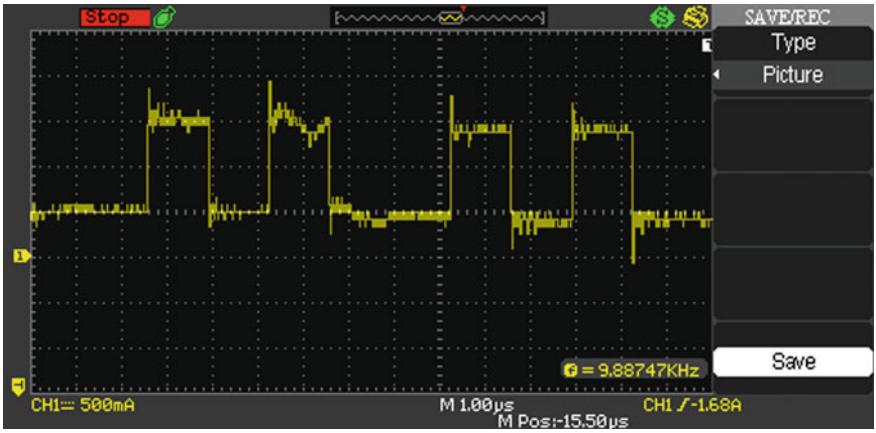

Fig. 8 Oscilloscope waveforms for duty cycle control input of $(0100)_b$ and frequency control input of $(0110)_b$

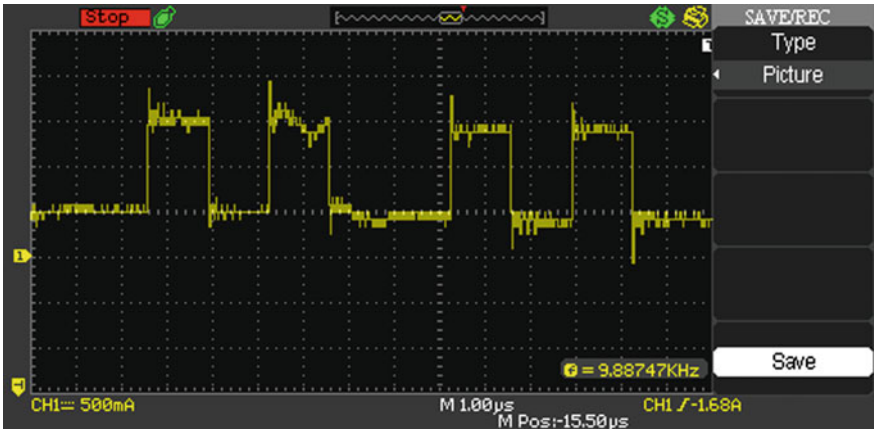

Fig. 9 Oscilloscope waveforms for duty cycle control input of $(0100)_b$ and frequency control input of $(0110)_b$

5 Conclusion and Future Work

Digital pulse-mode architecture using FPGA is designed. This architecture can derive both frequency- and duty cycle-varying pulses which can be used to control the DC–DC converters. Maximum operating frequency of 306.84 MHz is obtained with this proposed architecture for 4-bit control input which can be used with DC–DC converters for portable applications. Proposed architecture can derive pulses with high degree of resolution to provide accurate output voltage. Maximum operating frequency, power, and the logic resources utilized depends on the target FPGA device and the number of control inputs. Design with less number of control inputs can have higher maximum operating frequency and less power and consumes lesser number of logic resources but able to store less number of duty cycle and frequency control patterns. Based on the application, the design with desired control inputs can be chosen. This work can be extended further for higher bits of control inputs by simply increasing the number of RAM blocks.

References

1. Manninger M (2007) Power management for portable devices. In: 33rd European solid state circuits conference (ESSCIRC), pp 167–173
2. Ranganathan S, Sriharsha HS, Krishnan R (2015) Low cost FPGA implementation of SPWM using dynamically configurable switching frequency for three phase voltage source inverter. In: IEEE international conference on computational intelligence and computing research (ICCIC), pp 01–05
3. Scharrer M, Halton M, Scanlan T (2009) FPGA-based digital pulse width modulator with optimized linearity. In: Applied power electronics conference and exposition (APEC), pp 1220–1225 (2009)
4. Huerta SC, de Castro A, García O, Cobos JA (2008) FPGA-based digital pulse width modulator with time resolution under 2 ns. IEEE Trans Power Electron 23(6):3135–3314
5. Wang K, Rahman N, Lukic Z, Prodic A (2006) All-digital DPWM/DPFM controller for low power dc-dc converters. In: Twenty-first annual IEEE applied power electronics conference and exposition, pp 719–723
6. Sun A, Tan MT, Siek L (2010) Segmented hybrid DPWM and tunable PID controller for digital DC–DC converters. In: IEEE Symposium on next generation electronics, pp 154–157
7. Gao Y, Guo S, Xu Y, Lin SX (2009) FPGA-based DPWM for digitally controlled high-frequency DC–DC SMPS. In: 3rd international conference on power electronics systems and application PESA, pp 1–7 (2009)
8. Rahman N, Wang K, Prodic A (2006) Digital pulse-frequency/pulse-amplitude modulator for improving efficiency of SMPS operating under light load. In: IEEE workshops on computers in power, pp 149–153
9. Syed A, Ahmed E, Maksimovic D (2004) Digital pulse width modulator architectures. In: 35th annual IEEE power electronics specialists conference, pp 4689–4695
10. Chander S, Agarwal P, Gupta I (2013) ASIC and FPGA based DPWM architectures for single-phase and single-output DC–DC converter: a review. Central European J Eng 3: 620–643

11. Gao Y, Guo S, Xu Y, Lin SX, Allard B (2009) FPGA-based DPWM for digitally controlled high frequency DC-DC SMPS. In: 3rd international conference on power electronics systems and applications, pp 01–07
12. de Leon I, Sotta G, Eirea G, Acle JP (2014) Analysis and implementation of low-cost FPGA based digital pulse-width modulators. In: IEEE international instrumentation and measurement technology conference (I2MTC), pp 1523–1528
13. Xilinx Documentation IP Processor Block RAM (BRAM) Block (v1.00a) product specification (2011)
14. le Roux R, van Schoory G, van Vuuren P (2015) Block RAM-based architecture for real-time reconfiguration using Xilinx FPGAs. Research Article-SACJ 56, pp 22–32
15. Nimara S, Boncalo O, Amaricia A, Popa M (2016) FPGA architecture of multi-codeword LDPC decoder with efficient BRAM utilization. In: 19th international symposium on design and diagnostics of electronic circuits and systems (DDECS), pp 1–4

Fractional-Order Controller Design and Analysis of SEPIC Converter

S. Jeyasudha and B. Geethalakshmi

Abstract In this work, the fractional-order PI (FOPI) controller has been proposed for a single-ended primary inductance converter (SEPIC). The state-space model of the converter has been developed using the state equations of the SEPIC under different operating modes. The traditional PI controller has been designed using Ziegler–Nichols method, and the performance analysis is compared with the designed FOPI controller. Both PI and FOPI controller parameters are optimized by the genetic algorithm (GA). Simulation results of FOPI-controlled SEPIC show the better result and improved performance.

Keywords Fractional-order proportional integral controller
Single-ended primary inductance converter · Genetic algorithm
Proportional integral controller · Ziegler–Nichols tuning rule

1 Introduction

Power converter system seems to have a lot of applications such as renewable energy systems, sustainable energy systems, embedded systems, hybrid applications, and uninterruptible power supply. Renewable energy systems such as photovoltaic (PV) systems, small wind turbines, and fuel systems [1, 2] are more attractive to satisfy the energy demand nowadays. Photovoltaic system-based solar panels have more efficiency and less environmental issues. Power converters are one of the essential elements to effectively utilize the renewable energy sources. Among the power converters, DC–DC converters have more advantages which include low cost and reliable output. Different types of DC–DC converters such as Buck, Boost, Buck-boost, Cuk, ZETA, and SEPICs are available for both

S. Jeyasudha (✉) · B. Geethalakshmi
Pondicherry Engineering College, Puducherry, India
e-mail: jeyasudha_s@rediffmail.com

B. Geethalakshmi
e-mail: bgeethalakshmi@pec.edu

M.C. Bhuvaneswari and J. Saxena (eds.), *Intelligent and Efficient Electrical Systems*, Lecture Notes in Electrical Engineering 446,
https://doi.org/10.1007/978-981-10-4852-4_5

low-power and high-power applications. Conventional buck-boost converters have some issues such as inverted output and large ripple at the input current [3]. SEPIC is one of the buck-boost converters, which overcomes the above-said drawbacks, have been considered in the present paper. The mathematical model of the converter is carried out using the state-space analysis. From the model equations, transfer function is derived to design the PI controller parameters K_p and K_i, using Zeigler–Nichols procedure for developing the closed loop. Simulation is carried out using MATLAB/Simulink, for both open-loop and closed-loop operations, and the closed-loop operation is validated by varying supply voltage, reference voltage, and load resistance. The resultant output of PI controller has large disturbance, and it takes more settling time to hunt down the reference voltage. PI controller parameters are not sufficient for good regulation of the converter output and also lack in robustness [4–6]. For perfect regulation, the FOPI controller is proposed, which has three adjustable tuning parameters K_p, K_i, and λ. Fractional-order controller gives a robust performance for a wide range of operating conditions. The PI and FOPI parameters are optimized by using genetic algorithm, a global optimization technique. The genetic algorithm is an example of a search procedure that uses a random choice as a tool to guide a highly exploitative search through coding of a parameter space [7]. The GA-optimized parameters of FOPI are used to the SEPIC and simulated using MATLAB/Simulink. The FOPI controller-based SEPIC tracks the set reference values almost instantaneously.

The rest of the paper is ordered as follows. The working principle of the SEPIC is described in Sect. 2. Section 3 provides the state-space modeling of the SEPIC. Design of PI controller and its performance are shown in the Sect. 4. Section 5 describes the proposed fractional-order PI controller. The performance comparison of FOPI controller with PI controller is done in Sect. 6. Section 7 concludes the paper.

2 Principle of SEPIC

SEPIC is a type of DC–DC converter which allows the output voltage to be more than, less than, or equal to that of its input. The output voltage of the converter is supervised by the duty cycle (D) of the switch. It is similar to a conventional buck-boost converter but has the advantages of non-inverted output, reduced ripple, and non-pulsating input current. Figure 1 shows the circuit diagram of the SEPIC.

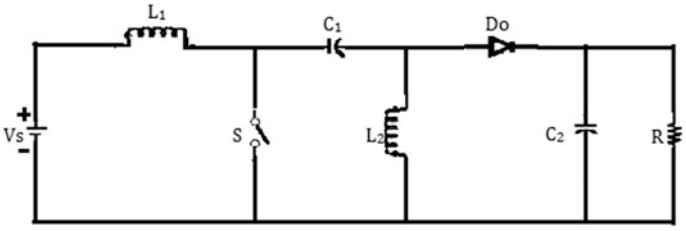

Fig. 1 SEPIC Converter Circuit Diagram

V_s is the input voltage; L_1 and L_2 are the inductors; C_1 and C_2 are the input and output capacitors; D_o represents diode; and R is a load resistance of the circuit. S shows the switch; usually, it is an IGBT or MOSFET. The operation of the SEPIC depicts two types of conduction: one is a continuous conduction and another is a discontinuous conduction. For analysis purpose, we use continuous conduction operation.

2.1 Modes of Operation

A SEPIC is said to be in continuous conduction mode if the current through the inductor L_1 never goes down to zero. Continuous conduction of the converter operates under 2 modes. They are the following:

- Mode I ($0 < t < D$) where D represents duty cycle;
- Mode II ($D < t < (1 - D)$).

2.1.1 Mode I ($0 < t < D$)

When switch S is turned on as shown in Fig. 2, current I_{L1} increases and the current I_{L2} also increases but in the negative direction. The energy stored in the inductor L_1 increases. Therefore, the capacitor C_1 supplies the energy to increase the magnitude of the current in I_{L2} and thus increase the energy stored in inductor L_2. As a result of a short circuit by S, the input inductor current I_{L1} increases and the voltage across the input inductor is same as that of the input voltage V_s.

The KVL and KCL equations corresponding to mode I are as follows:

$$V_s - L_1 \frac{di_{L1}}{dt} = 0 \tag{1}$$

$$C_1 \frac{dv_{c_1}}{dt} + i_{L_2} = 0 \tag{2}$$

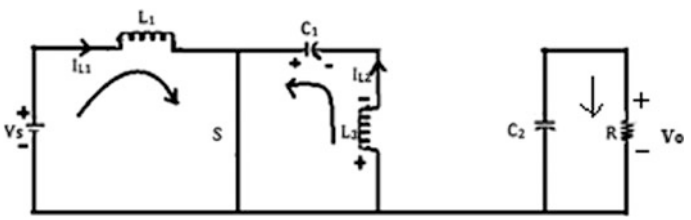

Fig. 2 SEPIC Converter (when the switch is ON)

$$L_2 \frac{\mathrm{d}i_{L2}}{\mathrm{d}t} - v_{c1} = 0 \tag{3}$$

$$\mathrm{C}_2 \frac{\mathrm{d}v_{\mathrm{c}_2}}{\mathrm{d}t} + \frac{v_{\mathrm{c}_2}}{R} = 0 \tag{4}$$

where V_{c1} and V_{c2} are voltage across the capacitors C_1 and C_2, and i_{L1} and i_{L2} are the current flow through the inductors L_1 and L_2, respectively.

2.1.2 Mode II ($D < t < (1 - D)$)

When switch S is turned off as shown in Fig. 3, the input capacitor current is same as that of current I_{L1}, as the inductors will not allow instantaneous changes in current. Current I_{L2} will continue in the negative direction. In fact, it never reverses the direction. The diode D_o conducts.

The KVL and KCL equations corresponding to mode II operations are as follows:

$$V_s = L_1 \frac{\mathrm{d}i_{L1}}{\mathrm{d}t} + v_{c1} + v_{c2} \tag{5}$$

$$L_2 \frac{\mathrm{d}i_{L2}}{\mathrm{d}t} + v_{c2} = 0 \tag{6}$$

$$C_1 \frac{\mathrm{d}v_{c1}}{\mathrm{d}t} - i_{L1} = 0 \tag{7}$$

$$C_2 \frac{\mathrm{d}v_{c2}}{\mathrm{d}t} - i_{L1} - i_{L2} + \frac{v_{c2}}{R} = 0 \tag{8}$$

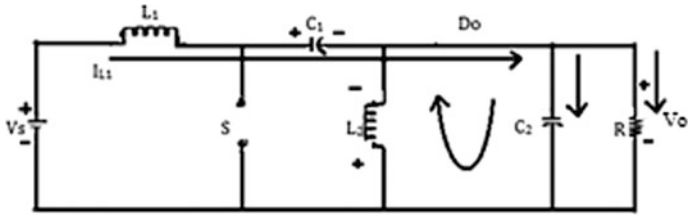

Fig. 3 SEPIC Converter (when the switch is OFF)

3 State-Space Modeling of SEPIC

Different mathematical modeling methods have been established for power converters. Each method is suitable for the converter from a certain point of view. Some models are more suitable for circuit analysis whereas others for control analysis. The state-space model of the converter is used to perform control analysis. The general state equation for the SEPIC operating under mode I is given as

$$\dot{x}(t) = A_1 x(t) + B_1 u(t) \tag{9}$$

$$y(t) = C_1 x(t) \tag{10}$$

Arranging the Eqs. (1)–(4) according to the Eqs. (9)–(10), we get the state matrix as in Eq. (11).

$$\begin{bmatrix} \frac{\mathrm{d}i_{L_1}}{\mathrm{d}t} \\ \frac{\mathrm{d}i_{L_2}}{\mathrm{d}t} \\ \frac{\mathrm{d}v_{C_1}}{\mathrm{d}t} \\ \frac{\mathrm{d}v_{C_2}}{\mathrm{d}t} \end{bmatrix} = \begin{bmatrix} 0 & 0 & 0 & 0 \\ 0 & 0 & \frac{1}{L_2} & 0 \\ 0 & \frac{-1}{C_1} & 0 & 0 \\ 0 & 0 & 0 & \frac{1}{RC_2} \end{bmatrix} \begin{bmatrix} i_{L_1} \\ i_{L_2} \\ v_{C_1} \\ v_{C_2} \end{bmatrix} + \begin{bmatrix} \frac{1}{L_1} \\ 0 \\ 0 \\ 0 \end{bmatrix} V_s \quad y(t) = \begin{bmatrix} 0 & 0 & 0 & 1 \end{bmatrix} \begin{bmatrix} i_{L_1} \\ i_{L_2} \\ v_{C_1} \\ v_{C2} \end{bmatrix} \tag{11}$$

Similarly, the state equation for the SEPIC operating under mode II is given as

$$\dot{x}(t) = A_2 x(t) + B_2 u(t) \tag{12}$$

$$y(t) = C_2 x(t) \tag{13}$$

Rearranging the Eqs. (5)–(8), the state matrix as given in (14) is obtained

$$\begin{bmatrix} \frac{\mathrm{d}i_{L_1}}{\mathrm{d}t} \\ \frac{\mathrm{d}i_{L_2}}{\mathrm{d}t} \\ \frac{\mathrm{d}v_{C_1}}{\mathrm{d}t} \\ \frac{\mathrm{d}v_{C_2}}{\mathrm{d}t} \end{bmatrix} = \begin{bmatrix} 0 & 0 & \frac{-1}{L_1} & \frac{-1}{L_1} \\ 0 & 0 & 0 & \frac{-1}{L_2} \\ \frac{1}{C_1} & 0 & 0 & 0 \\ \frac{1}{C_2} & \frac{1}{C_2} & 0 & \frac{-1}{RC_2} \end{bmatrix} \begin{bmatrix} i_{L_1} \\ i_{L_2} \\ v_{C_1} \\ v_{C_2} \end{bmatrix} + \begin{bmatrix} \frac{1}{L_1} \\ 0 \\ 0 \\ 0 \end{bmatrix} V_s \quad y(t) = \begin{bmatrix} 0 & 0 & 0 & 1 \end{bmatrix} \begin{bmatrix} i_{L_1} \\ i_{L_2} \\ v_{C_1} \\ v_{C_2} \end{bmatrix} \tag{14}$$

Averaging state equations [8] of a SEPIC over a switching cycle is

$$\dot{x}(t) = Ax(t) + Bu(t) \tag{15}$$

$$y(t) = Cx(t) \tag{16}$$

where

$$A = DA_1 + (1 - D)A_2 \tag{17}$$

$$B = DB_1 + (1 - D)B_2 \quad \text{and} \quad C = DC_1 + (1 - D)C_2 \tag{18}$$

A is the system matrix, B is the input matrix, C is the output matrix, and D is the duty ratio of the converter. Considering (17) and (18), the state and input equations are arrived as given in (19) and (20)

$$\begin{bmatrix} \frac{di_{L_1}}{dt} \\ \frac{di_{L_2}}{dt} \\ \frac{dv_{C_1}}{dt} \\ \frac{dv_{C_2}}{dt} \end{bmatrix} = \begin{bmatrix} 0 & 0 & \frac{-(1-D)}{L_1} & \frac{-(1-D)}{L_1} \\ 0 & 0 & \frac{D}{L_2} & \frac{-(1-D)}{L_2} \\ \frac{(1-D)}{C_1} & \frac{-D}{C_1} & 0 & 0 \\ \frac{(1-D)}{C_2} & \frac{(1-D)}{C_2} & 0 & \frac{-1}{RC_2} \end{bmatrix} \begin{bmatrix} i_{L_1} \\ i_{L_2} \\ v_{C_1} \\ v_{C_2} \end{bmatrix} + \begin{bmatrix} \frac{1}{L_1} \\ 0 \\ 0 \\ 0 \end{bmatrix} V_s \tag{19}$$

$$y = \begin{bmatrix} 0 & 0 & 0 & 1 \end{bmatrix} \begin{bmatrix} i_{L_1} \\ i_{L_2} \\ v_{C_1} \\ v_{C_2} \end{bmatrix} \tag{20}$$

For the purpose of analysis, the parameters of SEPICs considered for simulation are tabulated in Table 1.

Substituting the design parameters in Eqs. (19) and (20), the state matrix is given as

$$\begin{bmatrix} \frac{di_{L_1}}{dt} \\ \frac{di_{L_2}}{dt} \\ \frac{dv_{C_1}}{dt} \\ \frac{dv_{C_2}}{dt} \end{bmatrix} = \begin{bmatrix} 0 & 0 & -11.92e3 & -11.92e3 \\ 0 & 0 & 61.66e3 & -11.92e3 \\ 0.162e12 & -0.838e12 & 0 & 0 \\ 8.82e12 & 8.82e12 & 0 & -5.44e8 \end{bmatrix} \begin{bmatrix} i_{L_1} \\ i_{L_2} \\ v_{C_1} \\ v_{C_2} \end{bmatrix} + \begin{bmatrix} 74.07e3 \\ 0 \\ 0 \\ 0 \end{bmatrix} V_s \tag{21}$$

Table 1 Design parameters

S. No.	Parameters	Values
1	V_S	25 V
2	$L_1 = L_2$	0.01358 Mh
3	C_1	1 µF
4	C_2	183.8 µF
5	R	10 Ω
6	D(max)	83.8%

$$y = \begin{bmatrix} 0 & 0 & 0 & 1 \end{bmatrix} \begin{bmatrix} i_{L_1} \\ i_{L_2} \\ v_{C_1} \\ v_{C_2} \end{bmatrix} \tag{22}$$

From the state Eqs. (21) and (22), we get the transfer function which is obtained by using the Eq. (23)

$$G(s) = C(SI - A)^{-1}B \tag{23}$$

The output voltage to input voltage transfer function is shown in the Eq. (24), and the corresponding numerical characteristic equation is shown in the Eq. (25).

$$\frac{V_o(s)}{V_{in}(s)} = G(s) = \frac{\frac{(1-D)^2 s^2}{C_2 L_1} + \frac{D(1-D)^2}{C_2 L_1 C_1 L_2}}{s^4 + \frac{1}{RC_2}s^3 + \frac{D^2 C_2 L_1 + (1-D)^2 (C_2 L_2 + C_2 L_1 + C_1 L_1)}{C_2 L_1 C_1 L_2} s^2 + \frac{D^2}{C_2 L_1 R L_2} s + \frac{(1-D)^2}{C_2 L_1 C_1 L_2}} \tag{24}$$

$$s^4 + 545s^3 + (5.363\text{e}10 + 6.49\text{e}7K_P)s^2 + 2.92\text{e}13s + 7.744\text{e}17 + 4.006\text{e}18K_P = 0 \tag{25}$$

The MATLAB/Simulink simulation response of the open-loop converter with its output current and output voltage for boost and buck mode of operation is represented in Figs. 4 and 5, which reveals that the output current has large oscillations

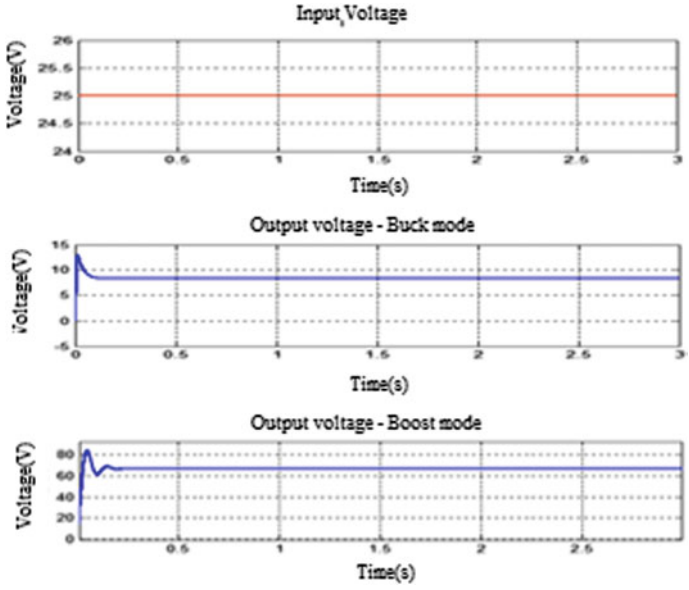

Fig. 4 Input and output voltages of SEPIC

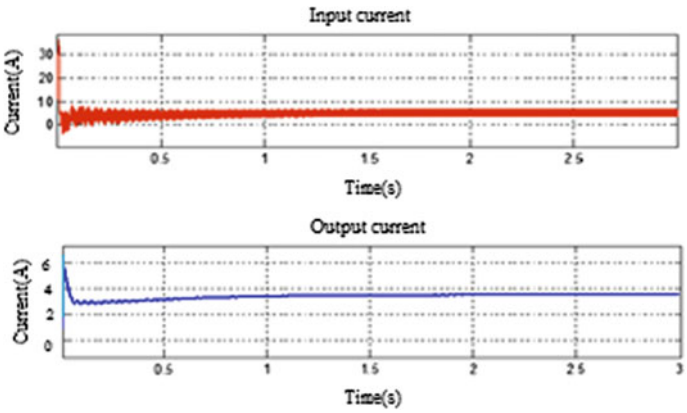

Fig. 5 Input and output current of SEPIC

and the output voltage has high peak overshoot. So to regulate the output voltage in a proper way, the controller has been designed.

(V_s = 25 V and D = 28% the buck o/p voltage V_o = 9.7 V, and if D = 72%, then the boosting o/p voltage V_o = 64.3 V which is shown in Fig. 4).

4 Design of PI Controller

PID controllers are widely used for DC–DC converters. It can be designed easily for converters where the controller parameters are deduced from the approximated small signal model. The PI controller is mainly used to eliminate the steady-state error. Here, we are considering conventional controller as PI (proportional + integral) controller using Ziegler–Nichols tuning rule with critical gain and period [9]. The PI controller transfer function is given by

$$G_c(s) = K_p\left(1 + \frac{1}{T_i s}\right) \tag{26}$$

Then, the closed-loop transfer function of the proposed system is given in the Eq. (27).

$$\frac{V_o(s)}{V_{in}(s)} = G(s) = \frac{K_P(6.49 \times 10^7 s^2 + 4.006 \times 10^{18})}{s^4 + 545s^3 + (5.363 \times 10^{10} + 6.49 \times 10^7 K_P)s^2 + 2.92 \times 10^{13}s + 7.744 \times 10^{17} + 4.006 \times 10^{18} K_P} \tag{27}$$

From the characteristic Eq. (25) and by using Routh–Hurwitz criterion, the controller parameters are determined as K_p = 1.16 and K_i = 16.20. By using the value of PI controller parameters K_p and K_i, the closed-loop operation of the SEPIC has been formed.

4.1 Simulation Results of PI Controller

The aim of closed-loop operation is to get the regulated output voltage for varying load resistance, reference voltage, and input voltage. The proposed converter in a closed loop is operated with a reference voltage of 35 V for input voltage of 25 V and load resistance of 10 Ω. Figure 6 represents the output voltage and current for boosting mode, when the SEPIC is operated with a closed loop of conventional PI controller. This closed-loop converter is tested for 3 conditions (a) by varying the reference voltage, (b) varying the load resistance, and (c) by varying supply voltage.

4.1.1 Reference Voltage Variation

The converter is operated under constant input voltage of 25 V and load resistance of 10 Ω, and the reference voltage is varied from 35 V at 0 s to 25 V at 1.5 s.

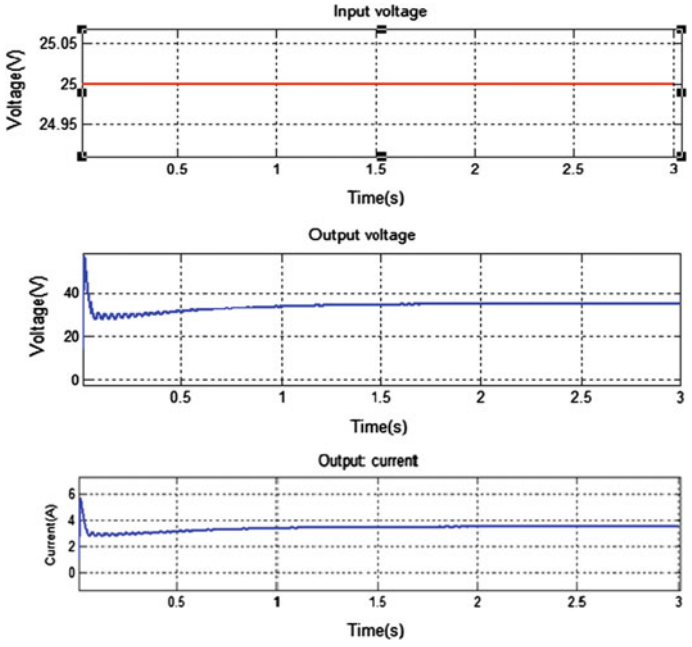

Fig. 6 Closed-loop controller output voltage and current

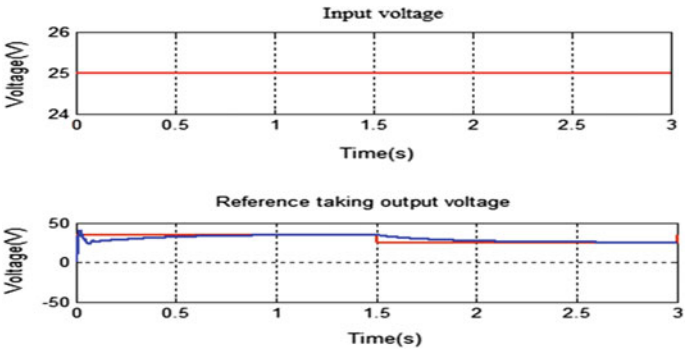

Fig. 7 Reference voltage variation using PI controller

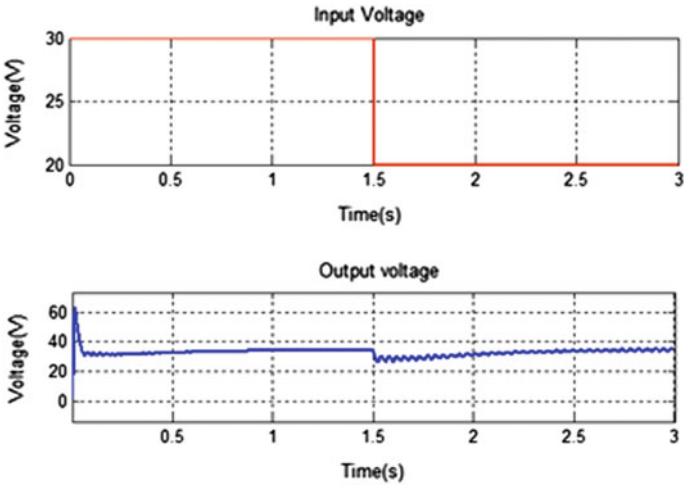

Fig. 8 Variation in supply voltage using PI controller

SEPIC output tracks the reference value given for the above K_p and K_i values. This is shown in Fig. 7.

4.1.2 Supply Voltage Variation

By keeping the load resistance and reference voltage as constant, the supply voltage is varied from 30 to 20 V at 1.5 s. The reference voltage is fixed for 35 V and load resistance is for 10 Ω, and the circuit is simulated. The converter output voltage maintained constant for the given reference value. This operation is shown in Fig. 8.

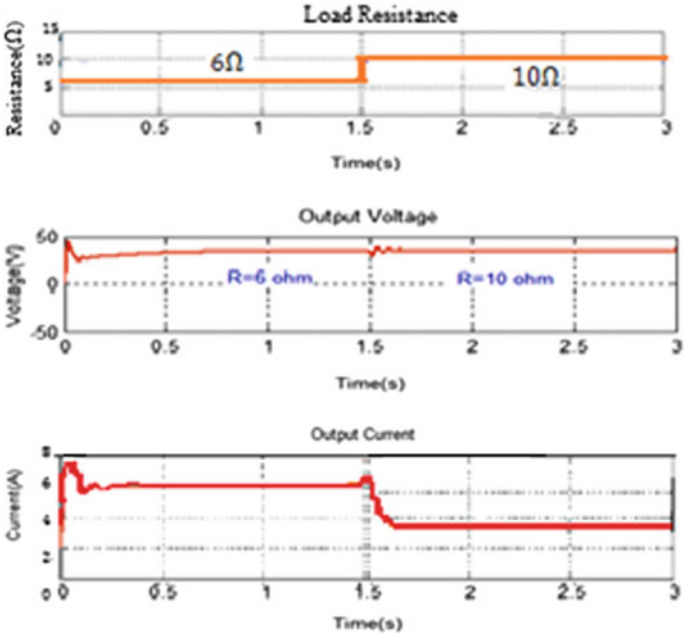

Fig. 9 Load resistance variation using PI controller

4.1.3 Load Resistance Variation

Figure 9 represents the variation of load resistance from 6 to 10 Ω. The input voltage of 25 V and the reference voltage of 35 V are maintained as constant. The output of the converter is varied according to the load value and settled at the reference.

From all the three conditions, it is found that the settling time and the peak overshoot value are very high. To avoid these transients from the conventional PI controller, fractional-order PI controller is designed and the operation of the fractional-order PI controller is explained in the next section.

5 Design of Fractional-Order PI Controller

The fractional-order PI (FOPI) controller, first proposed by Podlubny in 1999 [10], is the expansion of the conventional PI controller based on fractional calculus. The general form of FOPI controller is P, I^{λ} where λ is the order of the integral gain which is a fractional number. The differential equation of a fractional-order PI^{λ} (FOPI) controller can be described by Eq. (28), and its general transfer function is given by Eq. (29)

$$u(t) = K_p e(t) + K_i D^{-\lambda} e(t) \tag{28}$$

$$G_c(s) = \frac{U(s)}{E(s)} = K_p + K_i s^{-\lambda} \tag{29}$$

To ensure good performances especially during transients, the control of this system is realized by a fractional-order PI. In a fractional-order PI controller, the integral action being fractional has wider scope of design. FOPI controller design permits to achieve high performance for the SEPIC, for the purpose of improving the desired characteristics of the step response such as peak overshoot (M_p) and settling time (t_s). The three tuning parameters of the controller are K_p, K_i, and λ. More flexibility is added in accomplishing control objective by this expansion. This FOPI controller parameters K_p, K_i, and λ are optimized using genetic algorithm (GA) to get a stable output.

5.1 GA with FOPI Controller

The genetic algorithm is a global optimization of both constrained and unconstrained problems based on the natural selection. The genetic algorithm modifies a population of individual solutions continuously. Individuals are randomly selected at each step, from the current population, that should be parents of the next generation. Thus, the populations toward an optimal solution over successive generations are evolved. The genetic algorithm starts with a random initial population. The algorithm then produces a series of unique populations. This is done by ranking the current population according to their fitness values and two methods of mutation and crossover for generating a new child population. Mutation is generated by changing the genes of a single parent, and the crossover children formed by combining parents in the present population as the third type of children. Finally, the present population will be replaced with preferred children to structure the next production. The algorithm that stops by stopping criteria, such as the number of generations, time limit, and a fitness limit, is met [11]. The objective function is taken as integral absolute error (IAE), and the fitness function (FF) is the reciprocal of the objective function which is given by FF = 1/IAE.

The algorithm steps are as follows:

Step 1: Create a population of initial solution of parameters, $x = \{K_p, K_i, \lambda\}$.
Step 2: Evaluation of fitness function.

Fitness function (FF) = 1\IAE where IAE represents the objective functions.

Step 3: Generation of offspring.

This involves selection, crossover, and mutation. Roulette wheel selection is employed in this work, and crossover and mutation are carried out using a probabilistic approach.

Step 4: Replace the current population with the new population.
Step 5: Terminate the program if termination reached; else go to step 2.

Algorithmic Parameters

1. Population size: 100,
2. Selection Scheme: roulette wheel selection,
3. Reproduction: probabilistic crossover followed by mutation,
4. Crossover probability: 0.8,
5. Mutation probability: 0.001, and
6. No. of iteration for termination: 200.

The m-file coding [12] is created in MATLAB to implement GA algorithm. The FOPI parameters after optimization through GA are $K_p = 0.004$, $K_i = 3.5$ and $\lambda = 0.9$. The controller parameters so obtained are substituted in Eq. (28) and the FOPI-based SEPIC is simulated. The effectiveness of the proposed controller is varied by performing similar simulation study as that of the conventional PI controller.

5.2 *Simulation Results Using FOPI Controller*

The proposed FOPI controller-based closed loop is operated with a reference voltage of 35 V for input voltage of 25 V and load resistance of 10 Ω. Figure 10 represents the output voltage and current when the SEPIC is operated with FOPI controller.

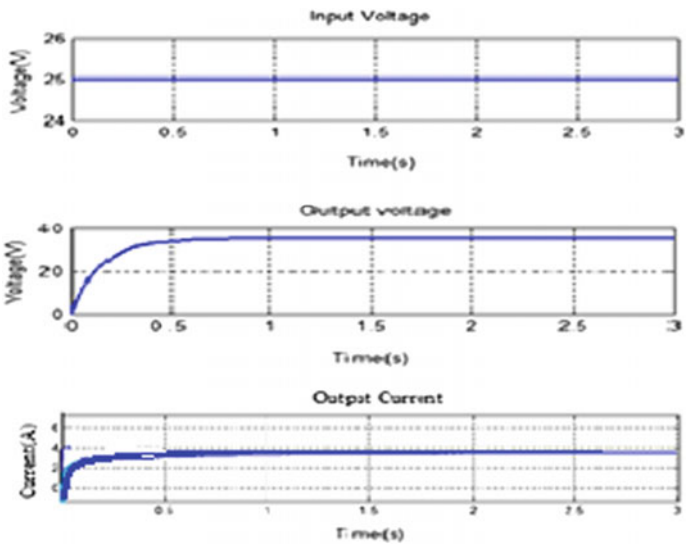

Fig. 10 Closed-loop FOPI controller of SEPIC input voltage, output voltage, and current

5.2.1 Reference Voltage Variation of FOPI Controller

The converter is operated under constant input voltage of 25 V, load resistance of 10 Ω, and the reference voltage is initially maintained as 35 V and varied to 25 V at 1.5 s. SEPIC output tracks the set reference value and maintains the closed-loop operation for the above K_p and K_i values. This is shown in Fig. 11.

5.2.2 Supply Voltage Variation

By keeping the load resistance and reference voltage at constant values, the supply voltage alone is varied from 30 to 20 V at t = 1.5 s. The reference voltage is fixed at 35 V and load resistance is set to 10 Ω, and the circuit is simulated. Due to close-loop operation, the output of the SEPIC is maintained at the set reference value which is depicted in Fig. 12.

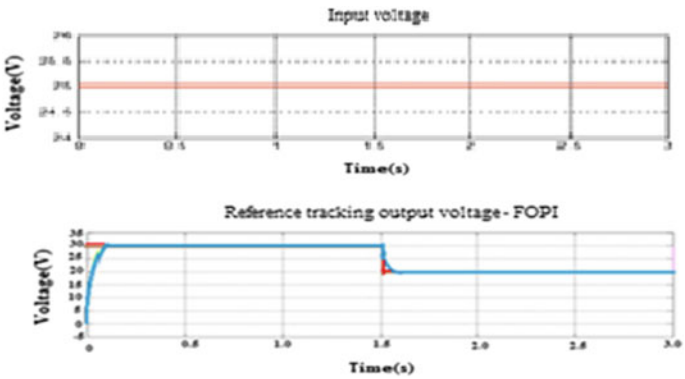

Fig. 11 Reference variation using FOPI controller

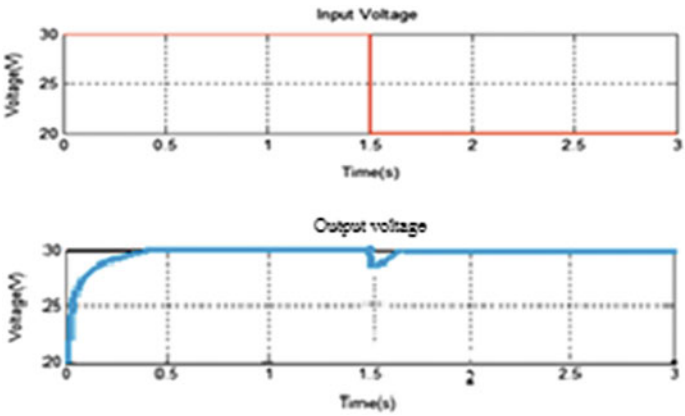

Fig. 12 Variation in supply voltage using FOPI controller

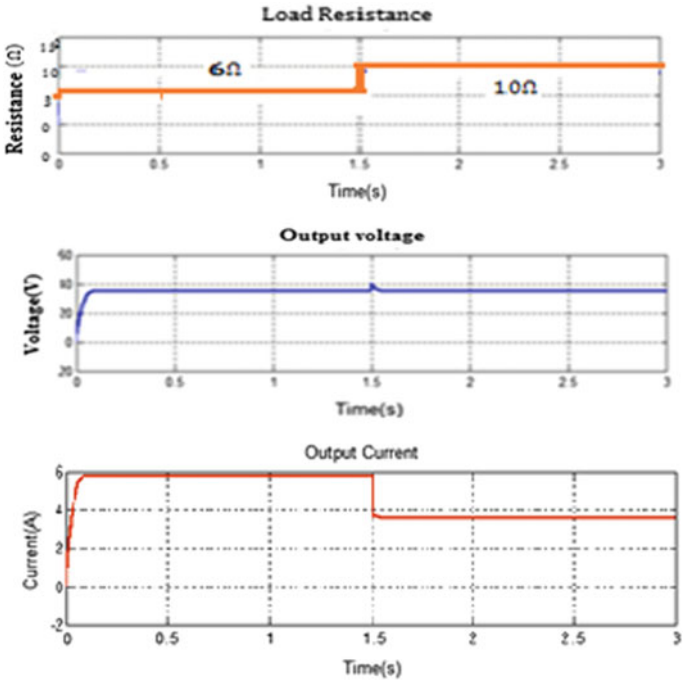

Fig. 13 Load resistance variation using FOPI controller

5.2.3 Load Resistance Variation

Figure 13 represents the variation of load resistance from 6 to 10 Ω. The input voltage of 25 V and the reference voltage of 35 V are maintained as constant. For any load variation, the load current varies correspondingly, but the load voltage is maintained at the desired value as shown in Fig. 13.

From all the above three categories, it is found that the FOPI controller-based SEPIC gives good transient results than the conventional- or integer-order PI controller.

6 Transient Analysis

The transient parameter of the PI and FOPI controllers are measured and tabulated in Table 2. The peak overshoot (M_P), settling time (t_s), and the integral absolute error (IAE) are taken for the comparison. The FOPI-based SEPIC performance shows the upgraded results.

Here, peak over shoot is 100% reduced for all the three conditions of the FOPI controller-based SEPIC and settling time of the FOPI controller is decreased 29, 44,

Table 2 Transient analysis of PI and FOPI

Attributes	PI controller SEPIC			FOPI controller SEPIC		
	M_p (%)	t_s (s)	IAE	M_p (%)	t_s (s)	IAE
Load variation	20	0.7	0.006	0	0.2	0.001
Supply variation	32	0.9	0.04	0	0.4	0.009
Reference variation	15	0.8	0.003	0	0.15	0.0005

and 19% for load variation, supply variation, and reference variation, respectively. According to that, the integral absolute error is also reduced for the above three conditions. From the results, it is proved that the fractional-order PI controller outperforms and exhibits good transient response.

7 Conclusion

The open- and closed-loop performance of the SEPIC is analyzed by using both PI and FOPI controllers. The parameters of the controller are stabilized by the genetic algorithm for parameter stabilization. Transient analysis and simulation are done and compared. The FOPI controller for SEPIC showed the better performance and improved results compared to the conventional PI controller.

References

1. Ajami A, Ardi H, Farakhor A (2014) Design, analysis and implementation of a buck-boost DC/DC converter. IET Power Electron 7(12):2902–2913
2. Adhikari N, Singh B, Vyas AL (2011) Performance evaluation of a low power solar-PV energy system with SEPIC converter. In: IEEE Ninth international conference on power electronics and drive systems, Singapore, pp 763–769
3. El Khateb AH, Rahim NA, Selvaraja J (2013) Fuzzy logic control approach of a maximum power point employing SEPIC converter for standalone photovoltaic System. Procedia Environ Sci 17:529–536
4. Baiyu O, Lei S, Chunlei C (2010) Tuning of fractional PID controllers by using radial basis function neural networks. In: 8th IEEE international conference on control and automation Xiamen, China
5. Maâmar B, Rachid M (2014) IMC-PID-fractional-order-filter controllers design for integer order systems. ISA Trans 53:1620–1628
6. Cao JY, Cao KY (2006) Design of fractional order controllers based on particle swarm optimization. In: 1st IEEE conference on industrial electronics and applications, pp 1–6
7. Samanta S (2014) Genetic algorithm: an approach for optimization. Int J Latest Trends Eng Technol 3(3)
8. Ortiz-Lopez MG, Leyva-Ramos J, Carbajal-Gutierrez EE, Morales-Saldana JA (2008) Modelling and analysis of switch-mode cascade converters with a single active switch. IET Power Electron 1(4):478–487
9. Ogata K (2001) Modern control engineering. New Jersey, Prentice-Hall (4th edn)

10. Podlubny I (1999) Fractional-order systems and $PI^{\lambda}D^{\mu}$ controllers. IEEE Trans Autom Control, 208–214
11. Golderberg DE (1989) Genetic algorithm in search optimization and machine learning, reading. Addison-Wesley, MA
12. Matlab Help Documentation (2010) Global optimization toolbox user's guide. The MathWorks Inc.

Advanced Energy Management of a Micro-grid Using Arduino and Multi-agent System

Leo Raju, Antony Amalraj Morais and R.S. Milton

Abstract The objective of this paper is to develop Arduino-based multi-agent system (MAS) for advanced distributed energy management of a solar-wind micro-grid. High penetration of renewable energy resources needs new coordination and control approaches to meet the stochastic nature of the environment and dynamic loadings. We use multi-agent system for advanced distributed, autonomous energy management of micro-grid to dynamically and flexibly adapt to the changes in the environment as renewable energy resources are intermittent in nature. We consider that a micro-grid which contains two systems each contains solar photo voltaic (PV) system, wind generator system, local consumer, and a battery. We develop a simulation model using Java Agent Development Environment (JADE) in Eclipse IDE for dynamic energy management, which considers the intermittent nature of solar power, randomness of load, dynamic pricing of grid, and variation of critical loads, and choose the best possible action every hour to stabilize and optimize the micro-grid. Furthermore, environment variables are sensed through Arduino Mega micro-controller and given to agents of MAS. The agents take the strategic action, and the resulting actions are reflected in the LED outputs which can be readily deployed in the actual field. MAS increases responsiveness, stability, flexibility, and fault tolerance, thereby increasing operational efficiency and leading to economic and environmental optimization. All the smart grid features are tested using JADE simulations and practically verified through Arduino micro-controller to make micro-grid into smart micro-grid.

L. Raju (✉) · A.A. Morais (✉)
Department of Electrical and Electronics Engineering,
SSN College of Engineering, Chennai 603110, Tamil Nadu, India
e-mail: leor@ssn.edu.in

A.A. Morais
e-mail: antony13012@eee.ssn.edu.in

R.S. Milton (✉)
Department of Computer Science and Engineering,
SSN College of Engineering, Chennai 603110, Tamil Nadu, India
e-mail: miltonrs@ssn.edu.in

M.C. Bhuvaneswari and J. Saxena (eds.), *Intelligent and Efficient Electrical Systems*, Lecture Notes in Electrical Engineering 446,
https://doi.org/10.1007/978-981-10-4852-4_6

Keywords Autonomous agent · Energy management · Multi-agent system
Micro-grid · JADE · Arduino in Eclipse

1 Introduction

Environment consideration is a leading proliferation of renewable resources in electrical industry. We are moving towards a more decentralized, more sustainable, and smarter power system. Centralized approach (SCADA) is used in most of the existing research on micro-grid operation problems. In order to reduce communication overhead and improve robustness, distributed approach is used in energy management problem. One such approach is multi-agent system-based modelling of micro-grid to provide a common communication interface for all agents representing the autonomous physical elements. Furthermore, the distributed nature and potential for modelling autonomous decision-making entities in solving complex problems motivate the use of multi-agent system for the operation of micro-grid. The main operations of a multi-agent system for micro-grid control are discussed in [1]. Optimization of micro-grid using MAS is given in detail in [2]. The design and implementation of multi-agent system in micro-grid energy management is discussed in detail in the paper [3]. Multi-agent-based distributed energy management for intelligent micro-grid is discussed in [4]. The complete review of micro-grids in multi-agent system perspectives is discussed in [5]. Multi-agent-based micro-grid control is discussed in [6]. Only in the very recent paper [7], the integration of micro-grid market operations and distributed energy resources (DERs) is discussed in detail. Although many micro-grid research activities involving MAS have been reported, they did not consider all the options available for optimal energy management of a micro-grid such as grid failure, unavailability of solar power in the night, peak load management, and demand-side management. Also most of the references do MAS simulation in JADE framework. Real-time implementation of MAS is not discussed. So we propose a multi-agent system-based advanced distributed energy optimization of solar micro-grid by comprehensively analysing and simulating all the possible options for the dynamic energy management in Java Agent Development Environment (JADE). Here, the agent autonomously chooses the best option every hour, considering the intermittent nature of solar power, randomness of load, dynamic pricing of grid, and variation of critical loads, to stabilize and optimize the solar micro-grid. Simulation results in this paper are capable of representing the dynamic behaviour of the micro-grid across various possible solar power and load values. All the features of smart grid are implemented, and the agent operations are verified by Arduino micro-controller for various scenarios.

The rest of the paper is organized as follows. A detailed discussion on multi-agent system approach is given in Sect. 2. Problem formulation is given in Sect. 3. Implementation of autonomous energy management in solar micro-grid is given in Sect. 4. Simulation and results are given in Sect. 5. Conclusion is given in Sect. 6.

2 Multi-agent System Approach for Autonomous Energy Management of Micro-grid

2.1 Multi-agent System

Distributed system with many ongoing interactions and continuous communications is almost infeasible. These considerations have motivated the development of approaches to distributed system based on agents, which provide ways for adaptation and ongoing interaction. A multi-agent system (MAS) is a distributed system consisting of multiple software agents, which form 'a loosely coupled network', to work together to solve problems that are beyond their individual capabilities or knowledge of each entity. MAS is emerging subfield of distributed artificial intelligence (DAI). Multi-agents overlay a way to elaborate systems that are decentralized rather than centralized, emergent rather than planned, and concurrent rather than sequential, with many advantages. MAS has inherent benefits such as flexibility, scalability, autonomy, and reduction in problem complexity [8]. In MAS, several autonomous and intelligent entities called agents are working in collaboration to achieve the overall goal of a system. An agent receives information about a state of its environment, takes actions which may alter that state, and expresses preferences among the various possible states. Agents have four behavioural attributes: autonomy, social, proactive, and reactive. Autonomy refers to the principle that agents can operate on their own to meet their goals without the need for human guidance [9]. Agents are proactive, i.e. the ability to take the initiative rather than acting simply in response to their environment. Agent can cooperate with other agents for coordinated action. In order to cooperate, agents need to possess social ability, i.e. the ability to interact with other agents with some communication language like Agent Communication Language (ACL). Agents are reactive to changes in environment. Reasoning, optimizing, controlling, and learning are the inherent characteristics of an agent [10].

Automating electrical distribution systems by implementing a supervisory control and data acquisition (SCADA) system is the present, conventional cost-effective solutions for improving reliability and increasing utilization. SCADA basically refers to a central control system that monitors and controls equipment from a remote location. SCADA systems basically coordinate, communicate, and control among remote substations and control room. Humans have traditionally supervised such problems to reason and resolve issues in SCADA. Also, SCADA is

complicated due to its centralized approach. In the micro-grid, uncertainty in SCADA systems arises when sensor data or inferred knowledge cannot be deemed accurate due to intermittent nature of distributed energy resources (DERs). Applications must deal with inherent noise/error in sensor data or knowledge as well as uncertainty, incompleteness, and inconsistent or conflicting data from multiple, heterogeneous renewable energy resources in micro-grid. A multi-agent energy management system (EMS) can cope with heterogeneity and give better, faster solution than SCADA [11]. MAS can deal with disadvantages of SCADA and increase the operational efficiency of micro-grid due to its inherent characteristics and functionalities taking the automation of micro-grid to the next level.

3 Problem Formulation

The challenges due to penetration of renewable energy resources such as solar and wind have to be dynamically managed in order to maintain stability, reliability, and fault tolerance. Every hour, the cost and the priorities of the resources are considered for optimization. In the micro-grid every hour the solar power, wind power, load, battery level, non-critical loads and dynamic pricing are monitored continuously. The agent considers all possible logical options and chooses the best possible action to maintain stability, reliability, and to increase the responsiveness, fault tolerance and operational efficiency of a smart micro-grid, leading to economic and environmental optimization. The strategic actions of agents are practically verified using Arduino micro-controller.

4 Implementation

4.1 Flow Chart

We consider a grid-connected micro-grid system which consists of two units each has solar and wind resources, a local consumer, and a battery along with grid and diesel. The proposed system has eight agents representing two solar units, two wind units, two battery units, grid and diesel units. Solar power generator agent, load agent, battery agent, grid agent, diesel agent, and control agent. Multi-agent programming is done with JADE platform in Eclipse environment. The overall procedure is the following.

(i) Here, the department load receives power from the department solar. If it is not sufficient, then it gets from the wind unit. If power is still required, it gets from the hostel solar and hostel wind units in the order. If the load requirement is more than the solar and wind power, it gets the available power from the batteries. If power is still required, it goes for non-critical

load (NCL) shedding in department and hostel loads before going to the external power source of grid or diesel. Here, we used preferences for non-critical load shedding such as AC, fridge, and washing machine. Dynamic pricing is followed, and hence, the choice of diesel or grid is made based on the unit price at that point of time. Diesel price is a static one as it is a non-renewable energy source.

(ii) If surplus energy is available in the department solar and wind (S1 and W1), then it checks its battery (B1) to charge, and if excess energy is available, it checks the battery of hostel agent (B2) to charge, and anything further excess available is given back to the grid.

(iii) Similar steps are followed in the hostel unit.

The simple block diagram of energy management of micro-grid is given in Fig. 1. The flow chart is given in Fig. 2.

All the communication is done through Agent Communication Language (ACL). Thus, every hour the solar micro-grid energy management is done dynamically for distributed optimization of solar micro-grid by using multi-agent system in JADE platform [12].

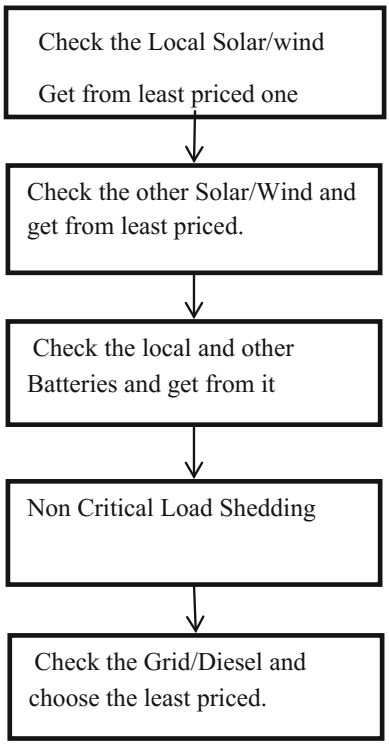

Fig. 1 Block diagram of energy management of micro-grid

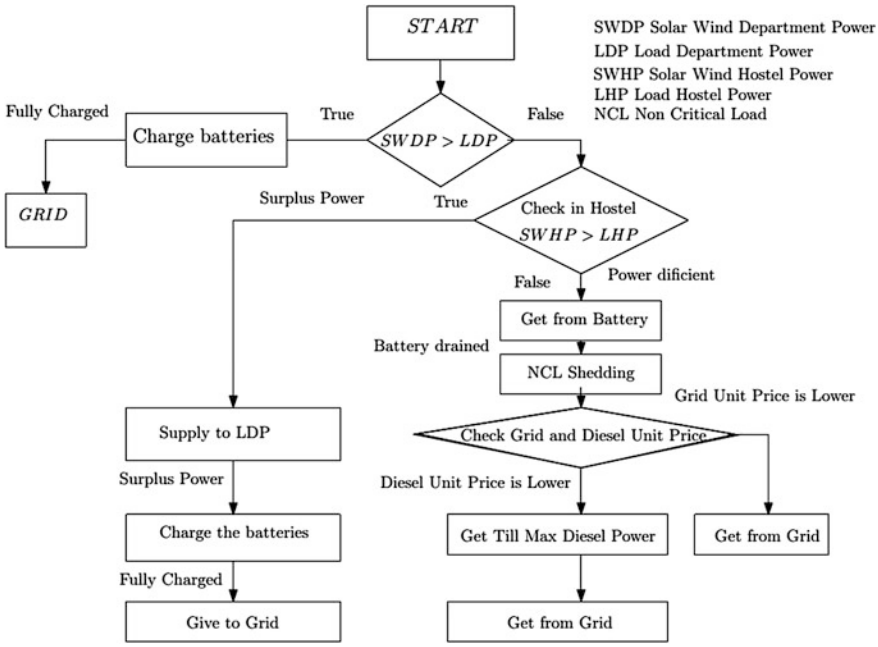

Fig. 2 Flow chart for energy management of micro-grid

4.2 Arduino Serial Communication Using RXTX Library

This is the most suitable method for accessing the Arduino from the Java code. A library called RXTX is used which facilitates serial communication with the Arduino Mega. Messages are sent and received from the Arduino serially. So, even though the communication seems to be serial, it takes place very quickly and can be assumed parallel by which multiple agents can access the micro-controller at a time. In our case, the control agent is responsible for this communication. The Arduino Mega board can, however, sense only a limited number of parameters from the environment due to the lack of analog pins (18). Potentiometers connected to analog pins of the Arduino board are used to input the sensed values of the environment such as load required and solar power available. The LED actions can be given to PLCs for actuating the real elements of the micro-grid in the field. The Arduino IDE itself is written in Embedded C along with Java methods, and it can communicate to the serial port via the RXTX Java library. The required command for turning on the LED is parsed from the message of the communication from Eclipse. The Java application takes the following steps for a successful serial communication:

1. Find the COM serial port connected to the Arduino board;
2. Establish a connection between the Arduino and the PC;
3. Read or write the data available at the connection port through a Java code developed in Eclipse.

Therefore, the potentiometer values can be obtained from the Arduino board through this serial communication. The results of strategic operations of agents can be reflected in the micro-controller which is given to the physical device for actuation. This information is again passed to the Arduino board through serial communication and given to its digital pins to which LEDs are connected. These LEDs indicate the action taken by the agents, and the status of the LEDs triggers the action of the actuators. An Arduino program is written and uploaded for the above-mentioned purpose. The pricing of the grid, solar and wind vary every hour. The predicted value of power that can be produced by solar and wind in a particular geographical location are found with the support of National Renewable Energy Laboratory (NREL). The loads will get power from a source based on priorities mentioned. The first priority is the lowest cost among all other sources, and the second is the nature of source. In this case, renewable sources are preferred. The above two conditions not only gives the consumer an advantage over hectic grid prices but also helps in improving the environment leading to economic and environmental optimization.

During every instance, the Eclipse program will fetch the potentiometer details which in real time correspond to the load required and solar power that can be generated. JADE agents communicate and coordinate for strategic action. The Eclipse communicates with the Arduino Mega at a standard baud rate of 9600 symbols/s. At the end of every instance, Eclipse will send information to Arduino in an asynchronous communication language that contains the pattern of LEDs that has to glow for that instant. This will be parsed by the Arduino to issue the high command to corresponding digital output pins. These LEDs in real time correspond to the command signal issued by agents of MAS to the actuators that allow the power flow between various sources and loads. All these actions take place parallel in Eclipse with the help of inherent concept of MAS for faster actions. During a grid failure, the entire smart grid that consists of different micro-grids will operate under islanding mode. The MAS system senses such faults and initializes non-critical load shedding. Loads such as air conditioner, washing machine, and fridge are shed before going for fatal load shedding to balance the micro-grid.

5 Simulations and Results

All the operations are considers as shown in the flow chart, and for these scenarios, the Java programming is done in JADE and executed in Eclipse Integrated Development Environment. Various scenarios are considered, and sniffer diagrams and the console output representing the interaction of the agents and transaction details are studied. The Arduino Mega board is connected to the breadboard where

all the potentiometer and LEDs are mounted. This Arduino Mega board is connected with computer serial port through Ethernet card. Arduino software is run to upload the program into the board. The potentiometers are fixed with the environment variables of solar and wind power values, load values, battery values, diesel value, grid value, and non-critical load (NCL) value. Eight LEDs are fixed on the breadboard representing two solar units, two wind units, two battery units, and grid and diesel units. The JADE agents are made to run in the Eclipse environment. The intermittent nature of solar power, randomness of load, dynamic pricing of grid, variation of critical loads, grid failure, peak load management, and demand-side management is considered, and the best possible action is chosen every hour to stabilize and optimize the solar micro-grid. The environment variables are sensed through Arduino Mega micro-controller and given to agents of MAS. The resulting strategic actions of agents are reflected in the LED outputs which can be readily deployed in the actual field. The agents receive environment variables from the potentiometer through Arduino micro-controller and take strategic decisions by communicating and coordinating with other agents. The resulting actions in the form of command signals are given to the various micro-grid components represented in the form of LEDs through Arduino. In this case, all the LEDs glow as all the agents are involved in the process. The potentiometers can be varied for various environment values, and the LED actions are verified with environmental dynamics. The console output of hostel, the Arduino output snapshot, and JADE sniffer output are shown in Figs. 3, 4 and 5.

In this case, in the department, the load needs 96 kW. It takes 21 kW from local solar unit and 21 kW from local wind unit. Then, it communicates with hostel solar and wind units, but there is no surplus power in the hostel. Then, it checks with both the batteries and takes the available 19 kW from local battery. But there is no

Fig. 3 Department console output

```
OUTPUT--------------------------------------
                HOSTEL
Solar Power                      : 21kW
Wind Power                       : 21kW
Load                             : 96kW
 WindSource  Price/kWh = Rs.5
Power Tapped from local Wind     : 21kW
 PowerSource Price/kwh = Rs.4
Power Tapped from local Solar    : 21kW
Power Tapped from Other Solar    : 0kW
Power Tapped from Other Wind     : 0kW
Power Tapped from local Battery  : 19kW
Power Tapped from Other Battery  : 0kW
Power Tapped by Local Battery    : 0kW
Power Remaining in Battery       : 0kW
Battery Charge in Percentage     : 0%
Power Remaining in local Solar
Power Needed                     : 35kW
Non Critical Load Shed           : 28kW
Power Needed after Load shedding : 7kW
Diesel Generator(DG)  Price/kWh = Rs.5

Power Tapped from DG                : 7kW
Grid Price/kWh = Rs.6
Power Tapped from Grid               : 0kW
```

```
            DEPARTMENT
Solar Power                       : 30kW
Wind Power                        : 15kW
Load                              : 100kW
 WindSource1  Price/kWh = Rs.8
Power Tapped from local Wind      : 15KW
 PowerSource1 Price/kwh = Rs.7
Power Tapped from local Solar     : 30kW
Power Tapped from Other Solar     : 0kW
Power Tapped from Other Wind      : 0kW
Power Tapped from local Battery   : 10kW
Power Tapped from Other Battery   : 0kW
Power Tapped by Local Battery     : 0kW
Power Remaining in Battery        : 0kW
Battery Charge in Percentage      : 0%
Power Remaining                   : 0kW
Power Needed                      : 45kW
Non Critical Load Shed            : 5kW
Power Needed after Load shedding : 40kW

Preferred non-renewable power Source : Diesel Generator(DG)  Price/kWh = Rs.5
Power Tapped from DG                 : 2kW
Grid Price/kWh = Rs.6
Power Tapped from Grid                : 38kW
```

Fig. 4 Department console output

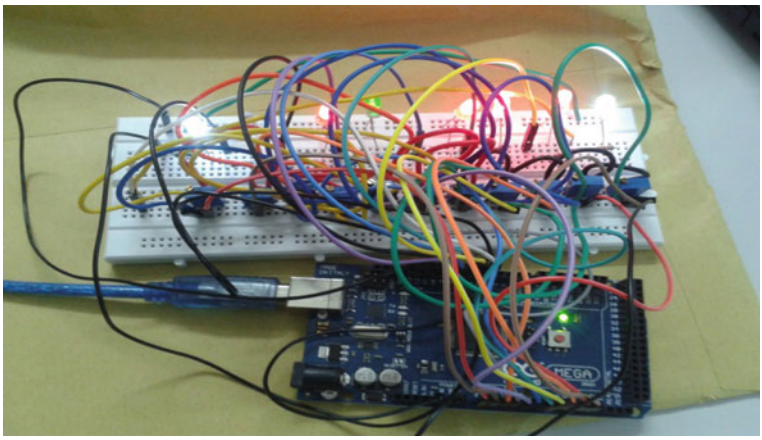

Fig. 5 Arduino output

charge in hostel batteries. It still requires 35 kW. Before going to grid, it sheds the NCL of 28 kW. Since diesel price is less than the grid price, it receives the remaining 7 kW from the diesel unit. In the case of hostel unit, the hostel load requires 100 kW out of which it receives 30 kW from local solar unit, 15 kW from local wind unit, and 10 kW from local battery. It still requires 45 kW. It sheds NCL of 5 kW, and then, it receives 2 kW from the available power in the diesel, and finally, the remaining 38 kW is received from the grid as the diesel unit power is fully exhausted. The environment parameter values are changed, and the agent

operations are verified for various scenarios which reflect all the smart grid features. Whenever the grid experiences a failure, the micro-grid will function in islanding mode. Under this condition, the multi-agent system will do a non-critical load shedding of major power-consuming loads such as AC, refrigerator, and washing machine. So, for every instant, the loads will be shed and the MAS will supply power from its renewable resources. Under such situation (grid failure), the MAS will not use its battery but instead do fatal load shedding after non-critical load shedding. In fatal load shedding, when the load requirement is higher than the solar/wind power generated, the excess load will be cut off. During night-time, when the solar power cannot be generated, MAS will look out for its battery and carry out the same process. In the sniffer output, ACL communication is established between the agents. All the elements of micro-grid are assigned as agents. When any of load agents require power, this load agent will broadcast a message stating the amount of power required. In reply to that, based on the dynamic pricing, an algorithm is formed to ensure that the load agent gets power at the least possible cost at that instant. Also, the renewable source will have more priority over the non-renewable power like diesel generator and grid for environmental consideration. The action taken by the agents to follow the console output according to the algorithm is clearly depicted as a proof of theoretical concept for agents for optimal decision making for advanced energy management of micro-grid. For example, the department load communicates with department solar for receiving the solar power through asynchronous ACL communication.

If there is sufficient solar power. The request is approved by the solar agent, and power is given to the load. The sequence of operation given in the flow chart is followed for both the department and hostel units for optimal, advanced energy management. The agents take reflective actions with its limited knowledge and take

Fig. 6 Sniffer diagram of energy management of solar micro-grid in JADE

deliberate action with the help of the control agent. In the Arduino output shown in Fig. 6, all the LEDs glow as all the agents are in operation to carry out the operations mentioned in the console output of department and hostel. Thus, the agent operations are practically verified through LED operations of Arduino.

6 Conclusion

The optimization of distributed energy management of solar micro-grid is done with a multi-agent system approach. A MAS model was developed for the solar micro-grid by using JADE, and all the options available for the agents in the micro-grid are comprehensively analysed for optimal distributed energy management of advanced, dynamic solar micro-grid to achieve the lowest possible cost of power generation under intermittent nature of solar PV system and randomness of load, leading to economic and environmental optimization. The operations of agents are practically verified by Arduino micro-controller. The proposed framework gives the intelligent consumer the ability to explore all possible logical options, understand the stochastic environment, and select the optimal energy management actions to increase operational efficiency in a distributed environment. Future work will focus on applying to IOT into our system to make it smarter by sensing the values of these potentiometers from a remote location and publishing the Java console output back in a Website which in real time will pave way for using cloud computing for optimization in a larger scale.

References

1. Dimeas A, Hatziargyriou ND (2005) Operation of a multi agent system for micro-grid control. IEEE Trans Power Syst 1447–1455
2. Eddy FYS, Gooi HB (2011) Multi-agent system for optimization of micro-grids. In: Proceedings of 8th international conference on power electronics—ECCE, Asia, Institute of electrical and electronics engineers (IEEE)
3. Pipattanasomporn M, Feroze H, Rahman S (2012) Securing critical loads in a PV-based micro-grid with a multi-agent system. Renew Energy 39(1):166–174
4. Logenthiran T, Srinivasan D, Khambadkone AM, Aung HN (2012) Multi agent system for real-time operation of a micro-grid in real-time digital simulator. IEEE Trans Smart Grid 3(2):925–933
5. Nunna HSVSK, Doolla S (2013) Multi agent-based distributed-energy-resource management for intelligent micro-grids. IEEE Trans Ind Electron 60(4):1678–1687. Available from http://dx.doi.org/10.1109/TIE.2012.2193857
6. Gomez-Sanz J, Garcia–Rodriguez S, Cuartero -Soler N, Hernandez-Callejo L (2014) Reviewing micro-grids from a multi-agent systems perspective. Energies 7(5):3355–3382. Available from http://dx.doi.org/10.3390/en7053355
7. Hatziargyriou ND (2014) Micro-grids architecture and control, IEEE Press, Wiley, New York
8. Eddy YSF, Gooi HB, Chen SX (2015) Multi-agent system for distributed management of micro-grids. IEEE Trans Power Syst 30(1):24–34

9. Merabet GH, Essaaidi M, Talei MR, Khail N, Madkour NM, Benhaddou D (2014) Applications of multi-agent systems in smart grids: a survey. In: Proceedings of 2014 international conference on multimedia computing and systems (ICMCS), IEEE
10. Lagorse J, Paire D, Miraoui A (2013) A multi-agent system for energy management of distributed power sources. Renew Energy 5(1):174–182
11. Calderwood S, Liu W, Hong J, Loughlin M (2013) An architecture of multi agent system for SCADA-dealing with uncertainty, plan and actions. In: Proceedings of ICINCOPP 300–306
12. Java agent development environment (JADE) development toolkit. Available from: http://www.jade.tlab.com

Sustain the Critical Load in Blackout Using Virtual Instrumentation

R. Hariharan, P. Usha Rani and P. Muthu Kannan

Abstract This paper focuses on sustaining the critical load during the blackout with distributed generation using virtual instrumentation. This system designed like whenever blackout occurs, Distributed Generation (DG) source to gives higher priority to provide power to meet critical load demand, So it sustains the critical load at any circumstances. The simulation is done in two areas with different types of loads. It exhibits the outcome in two ways—as to how it reacts with blackout and without blackout, and it is implemented by fuzzy system. The fuzzy result shows the crisp output of each load and input/output relationship for the given input variables.

Keywords Distributed generation (DG) · Blackout
Virtual instrumentation (VI) · Critical load · Fuzzy system

1 Introduction

Blackout is the major issue in the power system, and it takes the maximal time to recover this power system from the blackout [1]. Many strategies are practiced to recover the blacked-out system. Build-up strategy, build-down strategy, and other optimization techniques are also implemented in recovering the system [2]. The major issue in power system restoration is power down in critical load as it affects the other systems too. Power system loads are classified as commercial load, domestic load, industrial load, irrigational load, and traction load. Commercial load

R. Hariharan · P. Muthu Kannan
Saveetha School of Engineering, Saveetha University, Chennai, India
e-mail: harinov22@gmail.com

P. Muthu Kannan
e-mail: pmkannan@gmail.com

P. Usha Rani (✉)
R.M.D. Engineering College, Chennai, India
e-mail: pusharani71@yahoo.com

M.C. Bhuvaneswari and J. Saxena (eds.), *Intelligent and Efficient Electrical Systems*, Lecture Notes in Electrical Engineering 446,
https://doi.org/10.1007/978-981-10-4852-4_7

tends to the shops and restaurants of our daily routine. Load factor of commercial load depends upon the seasonal variations. Domestic load inclines to home appliances. Load factor of domestic load is low as to 10–20%. Industrial load consumes different levels of power with respect to different types of industries as small-scale industries, medium-scale industries, and large-scale industries. Municipal load describes the drainage system, street lights, and water pumps. Municipal load consumes fixed load factor. Irrigation loads are for the agricultural purposes. The emergency loads/very essential loads and hospitals are categorized under critical load.

Distributed generation plays a major role in running this system. They are up for a vital role in the emerging electric power system [3]. Distributed generation is a backup source, comprising both the embedded generations and dispersed generations. They reciprocate diesel or natural gas engines, micro-turbines, combustion gas turbines, fuel cells, photovoltaic, and wind turbines. Methods used in location and integration of the distributed generation are genetic algorithm, ant colony optimization, taboo search, analytical expression, and particle swarm optimization. In India, wind generation holds the fifth rank from all over the world. Wind farms have been installed in more than nine states.

Distributed generation primarily focuses on renewable energy. Its advantages are climate change, global warming, and carbon-free energy [4, 5]. LabVIEW "Laboratory Virtual Instrumentation Engineering Workbench," not only renders simulation outcome, but also connects with the real-time operations and applications. It has two windows, namely front panel and block diagram. Front panel depicts the outer frame of the system wherein it shows the output actions. The block diagram portrays the system circuit connections. They get to be interfaced with the data acquisition device and the actuator device with ease. This was developed by NI instruments.

2 Proposed System

For analysis, consider there are two areas, where each represents the different types of load. This load should actually be consumed by the main grid power and the distribution generation power. In the normal state conditions, all the consumer load components acquire the power from main grid and distributed generation. Only during the blackout state and the restoration state, the critical load consumes the distributed generation. The proposed system consists of two areas which have individual distributed generation plants. If any area experiences mismatch critical power demand and distributed generation, VI model controls to share the DG power from one area to another area.

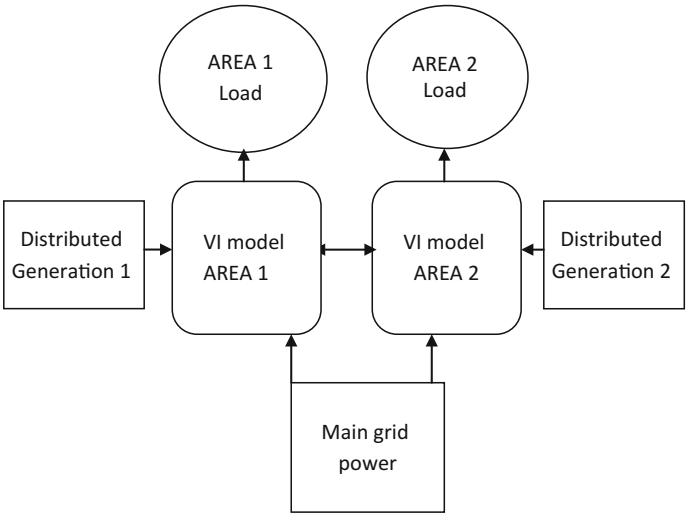

Fig. 1 Block diagram of proposed system

3 Block Diagram

The block diagram represents each VI model that is placed in individual areas. In each area, the load is categorized by priority, and the critical load personifies the higher priority. Every VI model collects the data from the distributed generation, main grid power, and system status to classify it as normal state or restorative state. Depending upon the state classified, it actuates the main power system. In the normal state, it allows the DG power and main grid power to the load centers, whereas in the restoration state, it allows the DG power to the critical load [6]. When demanded for the DG power, it shares the power from one area to another area with the help of a tie line (Fig. 1).

4 LabVIEW Front Panel

The LabVIEW Front panel comprises of two areas—load centers and the indicators. The areas show different types of load with number of loads. It also indicates the total power by control tool and led indicator tool. Distributed generation is represented by the meter indicator tool. Total power load is indicated by the gauge indicator. The restoration state is to be simulated by the Boolean button. Total power generation is indicated by the indicator tool [7, 8]. For simulating the blackout, the Boolean button exhibits the various operations of the system (Fig. 2).

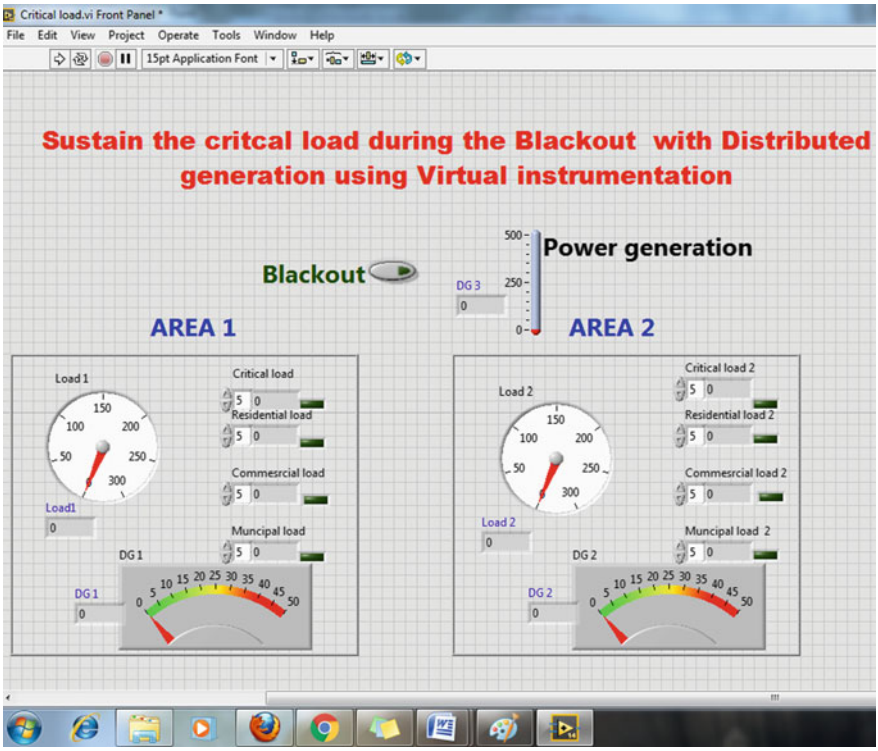

Fig. 2 Front panel of virtual instrumentation

5 LabVIEW Block Diagram Panel

The loads in every area of the system are selected by priorities, and they depend upon the status of the power system. The status of the power system is generally simulated by the Boolean button. At the normal state, in each part, the total load is consumed by distributed generation and main grid power. As a result, during this state, all the loads are loaded with power. At the restoration state, every area decides the load power, and how much the critical load and the total power are being consumed [9, 10]. This power will be extracted from the distributed generation. The load consumption is indicated by the indicator light (Fig. 3).

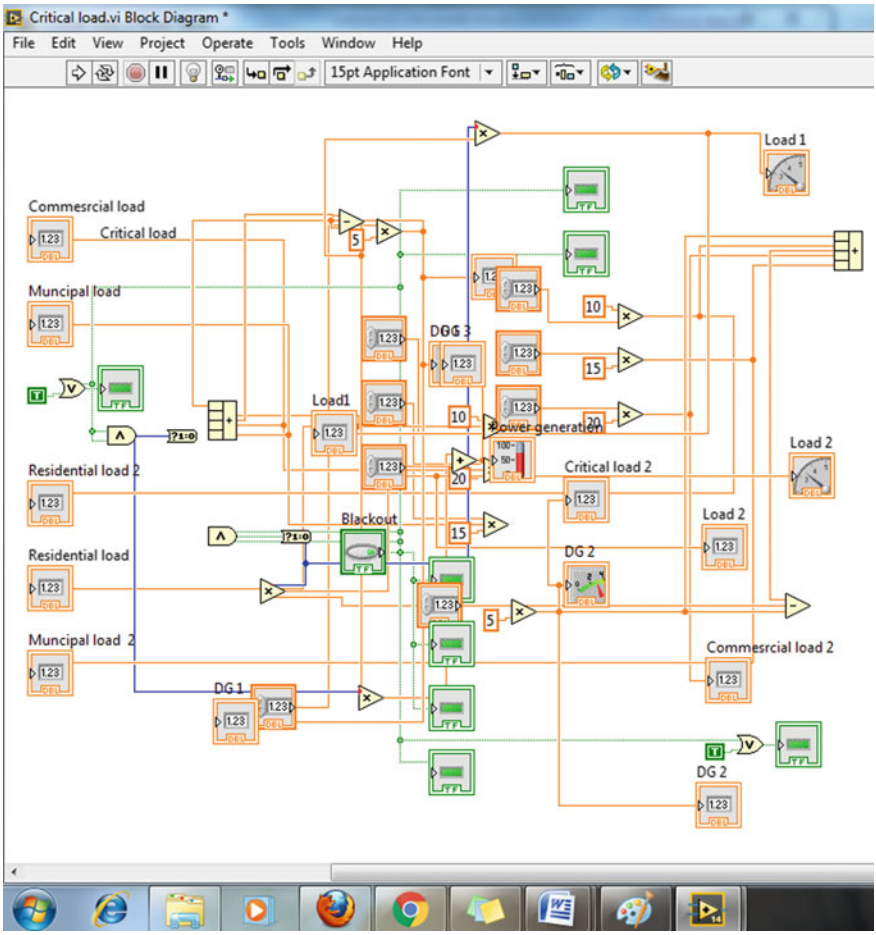

Fig. 3 Block diagram of virtual instrumentation model

6 Simulation Result

6.1 Normal State

At normal state, Area 1 load value is 250 kW and Area 2 load value is 225 kW. In Area 1, if the critical load is 5, then it consumes 25 kW. If the residential load is 5, then it consumes are 50 kW. In the same way, if the commercial load is 5, then it consumes 100 kW and it consumes 75 kW if the municipal load is 5. All the loads consume power from distributed generation and main grid power (shown in Fig. 4 LabVIEW front panel). In area 1, the distributed generation power is found to be 25 kW and main grid power is 250 kW. In area 2, distributed generation power is 25 kW, which is similar to that in DG power, and the main grid power is 225 kW.

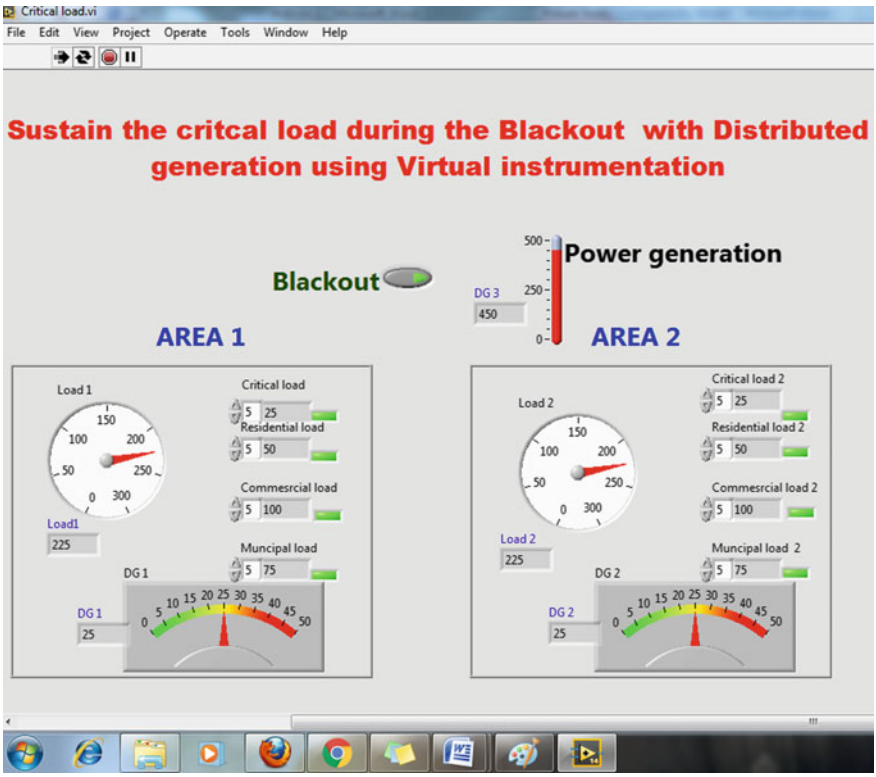

Fig. 4 Simulation result—normal state

6.2 Restoration State

At restoration state, Blackout Boolean button is activated. So, both areas will be isolated from the main grid. The critical load gets power only from the distributed generation, and this is executed by the VI model. Simulation result indicates both the areas—Area 1 and Area 2. Except critical load, all other loads are in OFF condition. In Area 1, distributed generation power of 25 kW is given to critical load, which turns the load to be in active condition and this is indicated by the led indicator (Fig. 5).

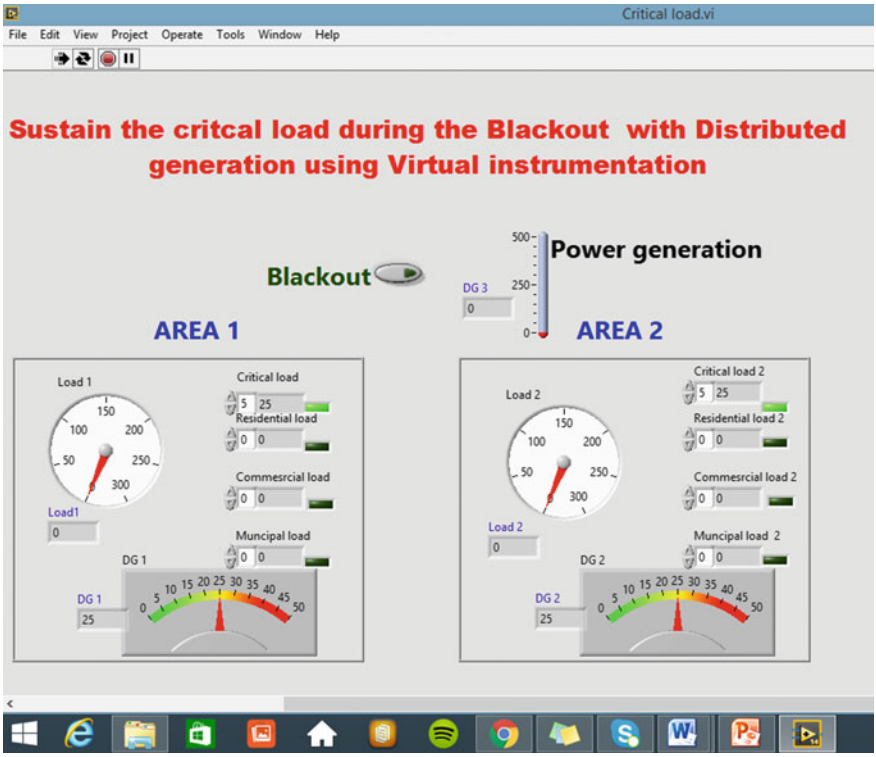

Fig. 5 Simulation result—restoration state

Table 1 Normal state result analysis

State	Normal state	
Load/source	Area 1 (kW)	Area 2 (kW)
Commercial load	75	75
Municipal load	100	100
Critical load	25	25
Residential load	50	50
Distributed generation	25	25
Main grid power	250	225

7 Result Discussion

See Tables 1 and 2.

Table 2 Restoration state result analysis

State	Normal state	
Load/source	Area 1 (kW)	Area 2 (kW)
Commercial load	0	0
Municipal load	0	0
Critical load	25	25
Residential load	0	0
Distributed generation	25	25
Main grid power	0	0

8 Fuzzy Logic Control System for Sustaining the Critical Load in Blackout Restoration

Fuzzy system model is built by LabVIEW for sustaining the critical load during blackout and also for various load demands. Its result gives the crisp solution for all the types of load [11]. In this system, input and output variables are assigned, and these variables are implemented by rule base system, and then it is tested in all the types of loads.

8.1 Fuzzy Input and Output Variables

In this fuzzy system, fuzzy input variables are generating power (P_g) and demand power (P_d). Input variables membership functions are derived by triangular function, and the range is assigned from 0 to 1. Three membership functions are chosen for each input variables (i.e., low, medium, high). Output variables are residential load, commercial load, municipal load, and critical load. Output variables membership function is derived by triangular function, and the range is assigned from 0 to 1. Four memberships are chosen for each output variables (zero, low, medium, high). Input and output variables for fuzzy system are shown in the Fig. 6.

8.2 Fuzzy Rules

In this system, "if-then rules" is used to select the crisp output for each load. Totally 12 rules are framed depending upon the combination of input variables. In this, antecedent connective is AND (Minimum) and consequent implication is minimum. Fuzzy rules window is shown in the Fig. 7.

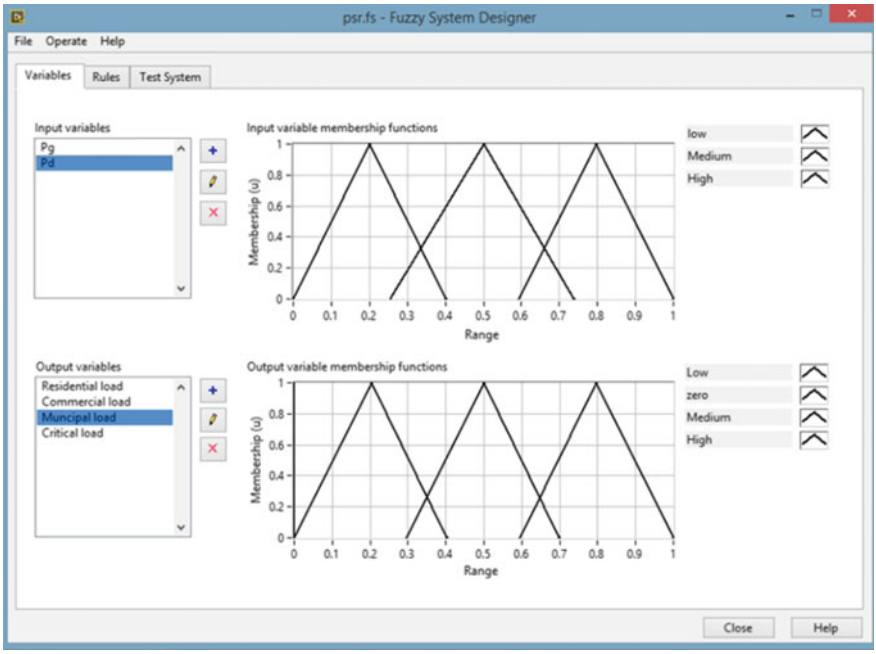

Fig. 6 Input and output variables for fuzzy system

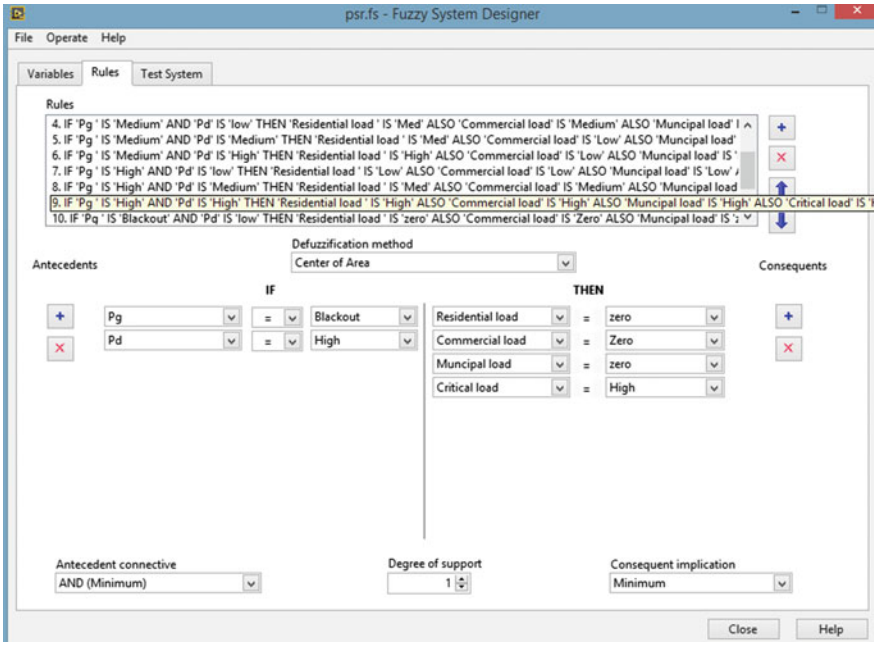

Fig. 7 Fuzzy rules window

8.3 Simulation Result: Test System

The fuzzy system designer shows the different types of load performance by varying input variables. In this, input variables and the value are shown in the window, and the crisp output is produced based on input value and rule-based system. For example, during blackout $P_g = 0$ and $P_d = 0.3479$ unit in this condition, it invokes rule number 10 and 11. Then, output variables are residential load, commercial load, and municipal load and crisp output value is zero. Critical load crisp value is 0.374309, it is shown in the test system screen and input/output relationships for all kind of loads are shown in the Figs. 8, 9 and 10.

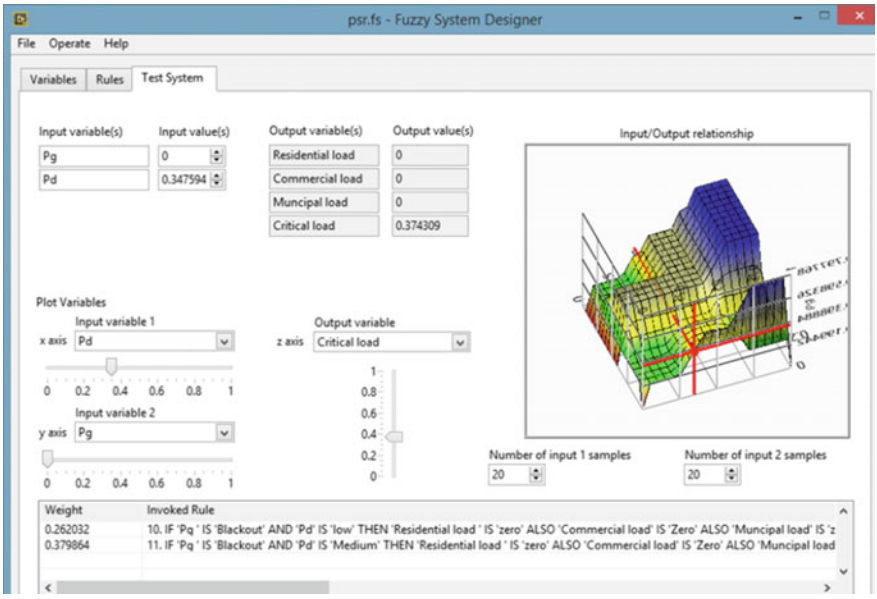

Fig. 8 Test system for critical load—input/output relationship

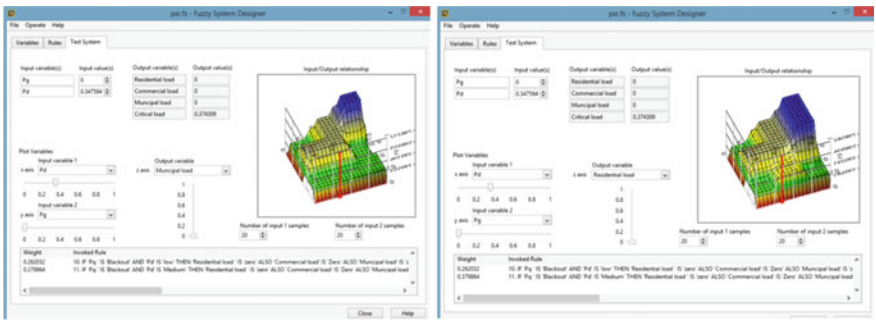

Fig. 9 Test system for municipal load and residential load—input/output relationship

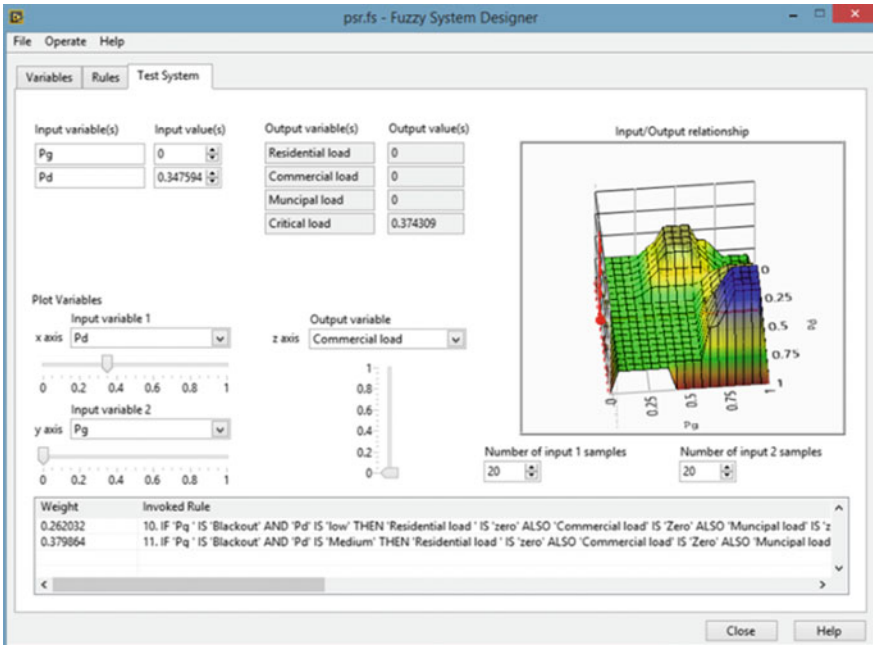

Fig. 10 Test system for commercial load—input/output relationship

9 Conclusion

This paper facilitates for the blackout power system restoration process. Also, this technique motives the distributed generation erection in all the areas so that it can control global warming and improve the renewable energy resources. In blackout, the important issue is to supply power to the critical load and it is overcome by Distributed Generation with Virtual Instrumentation system. Virtual instrumentation is used as the real-time system which easily interfaces with power system for control operations.

References

1. Wang C, Vittal V, Sun K (2011) OBDD-based sectionalizing strategies for parallel power system restoration, student member. IEEE Trans Power Syst 26(3)
2. Hariharan R, Usha Rani P (2016) Optimal allocation distributed generation using artificial bee colony algorithm by Etab. J Chem Pharm Sci. ISSN: 0974-2115
3. Nezamsarmadi SA (2011) A sectionalizing method in power system restoration based on WAMS. IEEE Trans Smart Grid 2(1)
4. Hariharan R, Usha Rani P (2016) A Complete restoration methodology using virtual instrumentation. Int J of Control Theory Appl 9(2):681–686

5. Hariharan R, Usha Rani P (2016) Graph theory based power system restoration using LabVIEW. ARPN J Eng Appl Sci. ISSN 1819-6608
6. Sun W, Liu CC, Zhang L (2011) Optimal generator strart-up strategy for bulk power system restoration. IEEE Trans Power Syst 26(3)
7. Hariharan R (2012) Saveetha school of Engineering, design of controlling the charging station of PHEV system based on virtual instrumentation. In: IET Chennai 3rd International on Sustainable Energy and Intelligent Systems (SEISCON 2012) conference. doi:10.1049/cp.2012.2187.
8. Hariharan R (2013) Saveetha School of Engineering, design of smart meter to equalize the power and demand using virtual instrumentation. In: International Conference on Power, Energy, and Control (ICPEC). doi:10.1109/ICPEC.2013.6527709.
9. Huang A, Audettev L, Harrison S (1995) A systamatic method for power system restoration planning. IEEE Trans Power Syst 10(2)
10. Ancona JJ (1995) A framework for power system restoration following a major power failure. IEEE Trans Power Syst 10(3)
11. Wang C, Niu X, Lei M, Fu L, Qiao L (2011) A combined weighting method for power system restoration decision making. In: seventh international conference on natural computation

Optimal Single and Multiple DG Installations in Radial Distribution Network Using SLPSO Algorithm

R. Arulraj and N. Kumarappan

Abstract This paper investigates optimal location and sizing of single as well as multiple distributed generation (DG) units in radial distribution network using social learning particle swarm optimization (SLPSO) algorithm. The SLPSO is basically developed from particle swarm optimization (PSO) by introducing social learning mechanism concepts into PSO. Moreover, so as to reduce the burden in parameter settings, a parameter control method based on problem dimension is adopted in SLPSO algorithm for solving lower as well as higher dimension problems efficiently. Minimization of total real power loss (P_{loss}) is used as main objective to solve optimal DG location and sizing problem. Results show the efficiency of the proposed algorithm in minimizing total P_{loss}. The supremacy of the proposed algorithm is also illustrated by comparing the results with other optimization approaches.

Keywords Distributed generation (DG) · Power loss reduction
Optimal DG installation · Social learning particle swarm optimization algorithm (SLPSO)

1 Introduction

Earlier, distribution network was treated as passive part of electric power system. But, in recent years, owing to higher integration of DG in distribution system, it has transformed into an active network. Basically distribution network is responsible for quality supply of power to end consumers. However, radial structure, higher R/X ratio, and increasing amount of inductive load in the distribution side cause higher power losses and voltage drop. The integration of DG closer to load in distribution

R. Arulraj (✉) · N. Kumarappan
Department of Electrical Engineering, FEAT, Annamalai University, Annamalai Nagar, Chidambaram, Tamil Nadu, India
e-mail: arulrajcdm88@gmail.com

N. Kumarappan
e-mail: kumarappann@gmail.com

M.C. Bhuvaneswari and J. Saxena (eds.), *Intelligent and Efficient Electrical Systems*, Lecture Notes in Electrical Engineering 446,
https://doi.org/10.1007/978-981-10-4852-4_8

network provides crucial solutions such as reduction in power losses and enhancement in bus voltage magnitudes. A review over various DG terminologies and its potential benefits were presented in [1, 2]. The location and sizing of DG in distribution network should be optimally planned in order to achieve higher technical benefits. For this purpose, several methods were employed for optimal installation of DG in distribution network. In [3, 4], analytical methods were used for optimal DG installation with minimization of P_{loss} objective. In order to avoid complex calculations in analytical methods, artificial intelligent techniques were employed in [5–8] to determine optimal DG installation in distribution network.

Apart from several artificial intelligent techniques mentioned in [5–8], PSO and its variants were also used on account of its higher efficiency and simplicity to identify suitable DG allocation in distribution network. In [9, 10], PSO technique was used for single DG installation and multiple DG installation, respectively. In [11], weight improved particle swarm optimization (WIPSO) algorithm was employed to determine optimal DG installation by minimizing DG generation cost and cost of power loss objective. Basically PSO and its variants employed earlier perform well for problems which have lower dimensions such as single DG installation; however, they perform below average for higher dimension problem that involves multiple DG installations. The premature convergence occurrence due to the heavy influence of *gbest* (global best position) on convergence speed was the core reason behind the aforementioned weakness of PSO and its variants. To overcome this drawback, in this paper, SLPSO algorithm is proposed to identify optimal location and sizing of single DG unit as well as multiple DG units in radial distribution network. In SLPSO algorithm, instead of using historical information such as *gbest* and *pbest* (local best position) for particle update, each particle position in the current swarm is updated by learning from any other better particles called demonstrators. In addition, a parameter control method based on problem dimension is adopted in SLPSO algorithm, in order to perform well for any number of problem dimensions and also to ease the liability in parameter settings. The optimal single and multiple DG installations using the proposed SLPSO algorithm result in greater reduction of P_{loss}, and also the efficiency of the proposed algorithm is shown by comparing the simulation results with other optimization techniques.

2 Problem Formulation

2.1 Objective Function

In any optimal DG installation problem, distribution load flow (DLF) analysis has a crucial role in the solution process. In this study, backward sweep and forward sweep method [12] of DLF is employed in order to perform DLF effectively. For the N_{bus} radial distribution system, the total P_{loss} minimization objective is framed as follow,

$$\text{Min}(P_{\text{loss}}) = \left(P_{\text{SS}} + \sum_{j=1}^{n_{\text{DG}}} P_{\text{DG}(j)} \right) - \sum_{i=1}^{N_{\text{bus}}} P_{\text{load}(i)} \tag{1}$$

where P_{SS} is the total amount of real power delivered at bus 1 from the substation; $P_{\text{DG}(j)}$ is the generated real power of jth DG unit; $P_{\text{load}(i)}$ is the total real power load at bus i; n_{DG} is the total number of installed DG units in the distribution network; N_{bus} is the maximum bus number in the distribution network.

2.2 Technical Constraints

DG Generation Limits.

$$P_{\text{DG}}^{\min} \leq \sum_{j=1}^{n_{\text{DG}}} P_{\text{DG}(j)} \leq P_{\text{DG}}^{\max} \tag{2}$$

$$Q_{\text{DG}}^{\min} \leq \sum_{j=1}^{n_{\text{DG}}} Q_{\text{DG}(j)} \leq Q_{\text{DG}}^{\max} \tag{3}$$

where $P_{\text{DG}}^{\min}$ and $P_{\text{DG}}^{\max}$ are the lower and upper real power limits of DG, respectively; $Q_{\text{DG}}^{\min}$ and $Q_{\text{DG}}^{\max}$ are the lower and upper reactive power limits of DG, respectively; $P_{\text{DG}(j)}$ and $Q_{\text{DG}(j)}$ are the generated real and reactive power of jth DG unit, respectively.

Bus Voltage Limits.

$$V_{\text{bus}}^{\min} \leq V_{\text{bus}(i)} \leq V_{\text{bus}}^{\max} \tag{4}$$

$$i = 1, 2, \ldots, N_{\text{bus}}$$

where $V_{\text{bus}}^{\min}$ and $V_{\text{bus}}^{\max}$ are the lower and upper bus voltage limits, respectively. $V_{\text{bus}(i)}$ is the voltage magnitude of bus i.

3 Implementation of SLPSO Algorithm

The SLPSO is basically emerged from PSO by introducing social learning mechanism concepts [13]. Like the traditional PSO, in SLPSO, a swarm $p(t)$ is initialized that contains n particles. Here, n and t are the swarm size and generation index,

respectively. In $p(t)$, each particle i contains a randomly initialized decision vector $X_i(t)$ that signifies a solution to the total P_{loss} minimization problem formulated in (1). In the swarm $p(t)$, the fitness is evaluated and assigned for each particle using the corresponding decision vector. According to the particle's fitness values, the swarm is then sorted in either increasing order (for maximization problem) or decreasing order (for minimization problem) depending on the problem requirement. Subsequently, in the particle update, apart from the particle that have best fitness, each particle i (an imitator) will learn from its demonstrators (i.e., particles with better fitness) and corrected its behavior accordingly [13]. For any imitator i (where $1 \le i \le n$) in a sorted swarm, its demonstrators can be identified as any particle k which satisfies $i < k \le n$. The expression for particle update based on the imitator learning from different demonstrator's behaviors is formulated as follow:

$$X_{ij}(t+1) = \begin{cases} X_{ij}(t) + \Delta X_{ij}(t+1), & \text{if } p_i(t) \le p_i^L, \\ X_{ij}(t), & \text{otherwise} \end{cases} \tag{5}$$

$$i \in \{1, 2, \ldots, n\} \text{ and } j \in \{1, 2, \ldots, \dim\}$$

In detail $\Delta X_{ij}(t+1)$ is formulated as follows:

$$\Delta X_{ij}(t+1) = \text{rand}_1(t) \cdot \Delta X_{ij}(t) + \text{rand}_2(t) \cdot I_{ij}(t) + \text{rand}_3(t) \cdot \varepsilon \cdot C_{ij}(t), \tag{6}$$

with

$$I_{ij}(t) = X_{kj}(t) - X_{ij}(t); \quad C_{ij}(t) = \overline{X_j}(t) - X_{ij}(t) \tag{7}$$

where

$$\overline{X_j}(t) = \frac{\sum_{i=1}^{n} X_i^j}{n} \tag{8}$$

$$\varepsilon = \beta * (\dim / M) \tag{9}$$

$$p_i^L = \left(1 - \frac{i-1}{n}\right)^{\alpha \cdot \log(\dim / M)} \tag{10}$$

$$n = M + \left(\frac{\dim}{10}\right) \tag{11}$$

where n is the actual size of the swarm; M is the base size of the swarm; dim is the dimension of the problem; $X_{ij}(t)$ is the particle i's jth dimension in generation t; $\Delta X_{ij}(t+1)$ is the behavior correction which contains three components, namely inertia component, imitation component, and social influence component; $\overline{X_j}(t)$ is the mean behavior of entire particles in the current swarm; ε is the social influence factor, and rand_1, rand_2, and rand_3 are the randomly generated numbers between

0and 1; p_i^L is the learning probability of particle i that determines the motivation to learn from its demonstrators; α and β are coefficients with small values. Here, the parameter control method based on problem dimension is achieved by determining the learning probability and the swarm size depending on problem dimension as shown in (10) and (11), respectively. The values of different parameters used in SLPSO algorithm are taken as follow: $M = 100$; $\alpha = 0.5$, and $\beta = 0.01$. For comparison purpose, the results are also acquired using WISPO algorithm, which is already employed in [11] for minimizing generation cost objective. The computational steps involved in determining optimal DG location and sizing using SLPSO algorithm are listed as follow:

Step 1: Input distribution network data (i.e., line and load data), DG limits, and bus voltage limits.
Step 2: Evaluate base case losses and fitness by performing DLF without DG.
Step 3: Set dimension-dependent SLPSO parameters mentioned in (9), (10), and (11). Here, number of optimal DG location and size define the dimension of the algorithm.
Step 4: Randomly initialize behavior vector for each particles and run DLF with DG. Evaluate fitness using (1) for initial behavior vector of each particle. Go to next step if all system constraints are satisfied, else go to step 2 and check for abnormalities in the system.
Step 5: Set iteration count $T = 0$. Perform swarm sorting and update position of each particle using social learning concept expressed in (5), (6), and (7).
Step 6: Run DLF and evaluate fitness using (1) for updated position of each particle. Go to next step if all system constraints are satisfied, else go to step 2 and check for abnormalities in the system.
Step 7: If $T < T_{\max}$, go to step 5 and repeat the process, else print the final optimal solution of DG.

4 Results and Discussion

In this study, the efficiency of the proposed methodology is determined using a standard 33-bus radial distribution system [14]. The values of base kV, P_{load}, and Q_{load} (total reactive power load) for standard 33-bus radial distribution system are 12.66 kV, 3.72 MW, and 2.3 MVAr, respectively. The DLF and the optimization using the proposed SLPSO algorithm are executed in MATLAB environment. Here, DG delivering both real and reactive power (e.g., synchronous machines, fuel cells connected through converter/inverter with suitable control techniques [15]) is taken into account in order to minimize P_{loss} in the system.

The simulation results for single as well as multiple DG installations using proposed SLPSO algorithm are shown in Table 1. From the overall results in Table 1, it is evident that optimal installation of three DG units results in greater reduction of P_{loss} followed by two and one number of installations. In order to illustrate the efficiency of the proposed SLPSO algorithm, the simulations results

Table 1 Optimal DG planning results using proposed SLPSO algorithm

No. of DGs	Method	Optimal DG planning			P_{loss} (kW)	P_{loss} reduction (%)	Q_{loss} (kVAr)	Q_{loss} reduction (%)
		Bus Num	Power (MVA)	Power factor				
Without DG	–	–	–	–	211	–	143.03	–
1 DG	IA [4]	6	3.102	0.85	68.16	67.69	–	–
	PSO [10]	6	3.096	0.83	67.87	67.84	–	–
	WIPSO	6	3.104	0.83	67.72	67.9	55.47	61.22
	SLPSO	6	3.106	0.82	67.26	68.13	54.83	61.67
2 DGs	IA [4]	6, 30	2.1174, 1.0584	0.85, 0.85	44.84	78.77	–	–
	PSO [10]	12, 29	0.9947, 2.0749	0.82, 0.82	39.1	81.49	–	–
	WIPSO	12, 30	1.0487, 1.5115	0.90, 0.72	29.63	85.96	22.05	84.58
	SLPSO	13, 30	0.9349, 1.5579	0.9, 0.73	27.9	86.78	20.41	85.73
3 DGs	IA [4]	6, 14, 30	1.0584, 0.7409, 1.0584	0.85, 0.85, 0.85	23.05	89.09	–	–
	PSO [10]	13, 24, 30	0.9327, 1.2314, 1.2287	0.82, 0.87, 0.83	15	92.89	–	–
	WIPSO	12, 24, 30	1.0137, 1.1956, 1.2516	0.85, 0.89, 0.80	13.86	93.43	11.03	92.29
	SLPSO	13, 24, 30	0.9207, 1.1974, 1.2743	0.88, 0.88, 0.80	11.01	94.78	8.79	93.85

achieved are compared with other promising methods available in literature for multiple DG installations such as improved analytical (IA) [4], PSO [10], and WIPSO. From Table 1, it is observed that, for single DG installation, all techniques provide almost similar P_{loss} minimization result, while SLPSO algorithm achieves slightly better reduction. However, the efficiency of the proposed SLPSO algorithm is evident in higher dimensional multiple DG installations in which SLPSO outperforms all other optimization methods in minimizing P_{loss} as shown in Table 1 with P_{loss} reduction percentage of 86.78 and 94.78% for two and three number of DG installations, respectively. The enhancement in bus voltage magnitude due to optimal DG reactive power generation at optimal bus locations is shown in Fig. 1. The convergence curve of the proposed SLPSO algorithm for three DG installations is shown in Fig. 2, and it is evident that the introduction of social learning

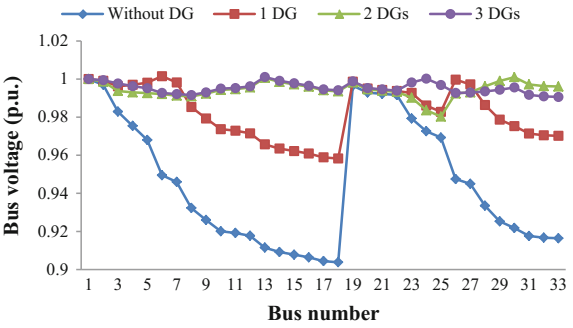

Fig. 1 Bus voltage results for single and multiple DG installations

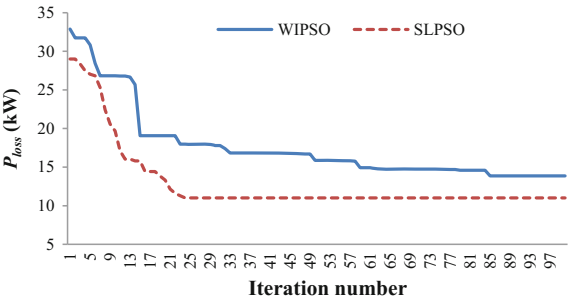

Fig. 2 Convergence curve of proposed SLPSO algorithm for three DG installations

mechanisms avoids premature convergence and provides optimal solution within 20–25 iterations.

5 Conclusion

In this study, SLPSO algorithm is proposed for optimal single and multiple installations of DG in distribution network with minimization of total P_{loss} objective. In SLPSO algorithm, the premature convergence occurrence due to heavy influence of *pbest* and *gbest* in particle update is avoided by introducing social learning mechanism concepts so as to explore the search spare efficiently. Moreover, a parameter control method based on problem dimension is adopted in SLPSO algorithm, so as to reduce the difficulty in parameter settings and also to enhance the performance for different problem dimensions. From the simulation results, when compared with other optimization techniques, it is evident that the proposed SLPSO algorithm achieves greater reduction in P_{loss} for any number of DG installations and also shows greater convergence speed for lower as well as higher problem dimensions. Thus, the proposed SLPSO algorithm is extremely efficient in determining single as well as multiple location and sizing of DG in distribution network.

Acknowledgements The work of Arulraj R was supported by Rajiv Gandhi National Fellowship of University Grants Commission (India) under the grant number RGNF-2014-15-SC-TAM-60538.

References

1. Ackermann T, Andersson G, Soder L (2001) Distributed generation: a definition. Elect Power Syst Res 57(3):195–204
2. Lopes JAP, Hatziargyriou N, Mutale J, Djapic P, Jenkins N (2007) Integrating distributed generation into electric power systems: a review of drivers, challenges and opportunities. Electr Power Syst Res 77:1189–1203
3. Viral R, Khatod DK (2015) An analytical approach for sizing and siting of DGs in balanced radial distribution networks for loss minimization. Int J Electr Power Energy Syst 67:191–201
4. Hung DQ, Mithulananthan N (2013) Multiple distributed generator placement in primary distribution networks for loss reduction. IEEE Trans on Indus Electron 60(4):1700–1708
5. Shukla TN, Singh SP, Srinivasarao V, Naik KB (2010) Optimal sizing of distributed generation placed on radial distribution systems. Electr Power Comp Syst 38(3):260–274
6. Imran MA, Kowsalya M (2014) Optimal size and siting of multiple distributed generators in distribution system using bacterial foraging optimization. Swarm Evolut Comput 15:58–65
7. Moravej Z, Akhlaghi A (2013) A novel approach based on cuckoo search for DG allocation in distribution network. Int J Electr Power Energy Syst 44(1):672–679
8. Mouti FSA, Hawary MEE (2011) Optimal distributed generation allocation and sizing in distribution systems via artificial bee colony algorithm. IEEE Trans on Power Deliv 26 (4):2090–2101
9. Kansal S, Kumar V, Tyagi B (2013) Optimal placement of different type of DG sources in distribution networks. Int J Electr Power Energy Syst 53:752–760
10. Jain N, Singh SN, Srivastava SC (2013) A generalized approach for DG planning and viability analysis under market scenario. IEEE Trans Indus Electron 60(11):5075–5085
11. Arulraj R, Kumarappan N, Vigneysh T (2013) Optimal location and sizing of DG and capacitor in distribution network using weight-improved particle swarm optimization algorithm (WIPSO). In: Proceedings of IEEE international conference on automation, computing, communication, control and compressed sensing. Kerala, India, pp 759–764
12. Shirmohammadi D, Hong HW, Semlyen A, Luo GX (1988) A compensation-based power flow method for weakly meshed distribution and transmission networks. IEEE Trans Power Syst 3(2):753–762
13. Cheng R, Jin Y (2015) A social learning particle swarm optimization algorithm for scalable optimization. Inform Sci 291:43–60
14. Aman MM, Jasmon GB, Bakar AHA, Mokhlis H (2014) A new approach for optimum simultaneous multi-DG distributed generation Units placement and sizing based on maximization of system loadability using HPSO (hybrid particle swarm optimization) algorithm. Energy 66:202–215
15. Vigneysh T, Kumarappan N (2016) Autonomous operation and control of photovoltaic/solid oxide fuel cell/battery energy storage based microgrid using fuzzy logic controller. Int J Hyd Energy 41(3):1877–1891

Dynamic Modeling and Control of Utility-Interactive Microgrid Using Fuzzy Logic Controller

T. Vigneysh and N. Kumarappan

Abstract This paper presents the dynamic modeling and simulation of microgrid consisting of photovoltaic (PV) system and solid oxide fuel cell (SOFC) system. The microgrid system is considered to be operating in grid-connected mode. A bidirectional voltage source converter (VSC) is used to connect the microgrid to the utility grid. The main objective of this work is to smoothly control the power flow between the power sources (PV and SOFC) and utility grid. To achieve this objective, real-reactive power (PQ) control technique based on fuzzy logic controller (FLC) is proposed to control the VSC. The proposed controller provides better response than the traditional proportional-integral (PI) controller by smoothly regulating the active and reactive power flow with reduced overshoot and oscillations. The performance of the proposed FLC is verified through extensive simulation studies carried under MATLAB/Simulink environment.

Keywords Distributed generation · Fuzzy logic control
Microgrid grid-connected mode

1 Introduction

Distributed generation (DG), also known as on-site generation, generates electricity from many small sources such as solar, tidal, natural gas (fuel cells), wind, and small hydro. Due to certain advantages such as environmental friendliness (low or zero emission of pollutant gases), flexibility, and expandability, DGs are considered as the best option to form modern electrical grids by properly locating them. DG technology is decentralized and is gaining increasing attention due to various

T. Vigneysh (✉) · N. Kumarappan
Department of Electrical Engineering, Annamalai University, Annamalai Nagar, Chidambaram 608002, Tamil Nadu, India
e-mail: vigneysh@gmail.com

N. Kumarappan
e-mail: kumarappann@gmail.com

M.C. Bhuvaneswari and J. Saxena (eds.), *Intelligent and Efficient Electrical Systems*, Lecture Notes in Electrical Engineering 446,
https://doi.org/10.1007/978-981-10-4852-4_9

advantages offered by them. The advancement in power electronics technology makes it possible to integrate DG systems to the utility [1]. In this perspective, microgrid is defined as a collection of small generating units, energy storage systems (e.g., battery, super capacitors, and flywheels), and various loads which are interfaced with electrical utility with the help of grid-interactive voltage source converter (VSC).

Combination of different types of DGs along with a good control system leads to improved power quality and reliability to end users, and hence, it attracts many researchers to work on this area. Many combinations of such hybrid power systems have been proposed earlier by various researchers, and various control techniques have been proposed to control the power flow in hybrid power system [2–5]. In this literature, different types of controllers such as proportional-integral (PI) controller, predictive controller, H-infinity controller, and sliding mode controller are used to control the VSC [5–7]. To design these controllers, complete knowledge of the system behavior should be known and the designing task will be more complex. Also, conventional PI controller does not perform well under all scenarios [8]. To overcome this drawback, intelligent controllers such as fuzzy logic controller (FLC), neural network-based controllers, and evolutionary algorithms are generally used to solve various power system problems [9, 10].

In this paper, real-reactive power (PQ) control technique based on fuzzy controller is presented to control the utility-interactive VSC. The proposed FLC is easy to implement and provides better dynamic response than the traditional PI controllers by smoothly regulating power flow between the DG units and the utility grid with reduced overshoot and oscillations. Similarly, to control the VSC's DC-side voltage, another FLC is proposed here. Photovoltaic (PV) and solid oxide fuel cell (SOFC) system are taken as the DG units. The primary objective is to smoothly control the power flow between the DG units, loads, and utility grid. Besides the primary objective, the following objectives are simultaneously achieved: (1) The PV system is operated at MPPT, and SOFC is regulated to generate the power when the load demand is higher than the PV output power, (2) when the PV power output is higher than the load demand, the excessive power is injected to the utility grid (grid-injecting mode), (3) when the load demand is higher than the total output power from the PV and SOFC, the power shortage will be supplied by the utility grid (grid-sharing mode). To validate the performance of the proposed FLC, the microgrid system is simulated under MATLAB/Simulink environment.

2 System Configuration and Modeling

Figure 1 shows the general structure of the microgrid under consideration. It contains a 50 kW PV system and a 50 kW fuel cell system connected to 700 V DC bus. SOFC system is controlled to generate the power during low irradiance period or when there is higher load demand. The DC bus is connected to the utility grid

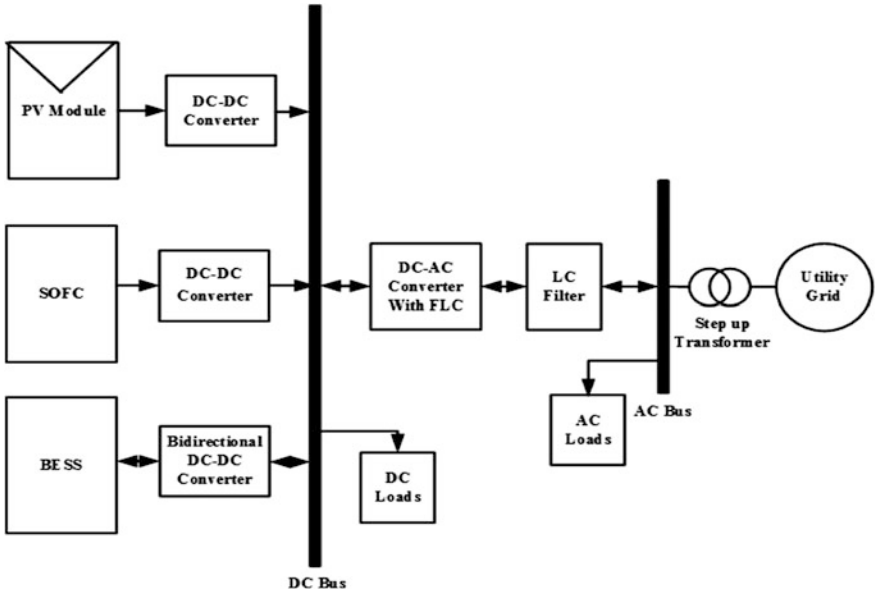

Fig. 1 General structure of grid-connected microgrid

through the bidirectional VSC and a LC filter. Various loads are connected as shown in Fig. 1. As the microgrid system is operating in grid-interactive mode, the role of battery energy storage system is not crucial and so it is considered to be in floating mode.

The modeling equations required to design the PV system and SOFC system are available in literature [11–13], and it is used here to model the DG units.

3 Control of DG Units and Power Converters

3.1 Control of PV System

Figure 2 shows the control diagram of PV power generation system along with perturb and observe (P&O) maximum power point tracking (MPPT) control [14]. The P&O algorithm continuously regulates the duty cycle of the boost converter such that forcing the PV array to function at maximum power point voltage, V_{mpp}. Detailed instruction about controlling PV system can be found in Refs. [11, 12] and implemented here. The converter parameters are given in Table 1.

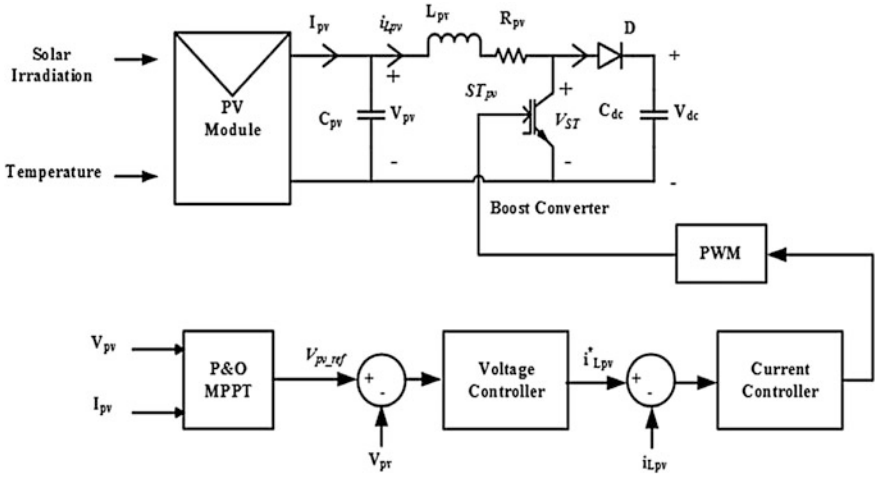

Fig. 2 Control of PV system with MPPT

Table 1 Microgrid parameters

Microgrid parameters	Values
Nominal DC-link voltage	$V_{\text{dcref}} = 700$ V
Filter values	$R_f = 0.01\ \Omega$, $L_f = 3.2$ mH, $C_f = 50\ \mu$F
DC–DC converter parameters	PV converter parameters: $C_{\text{pv}} = 100\ \mu$F, $L_{\text{pv}} = 7.5$ mH $R_{\text{pv}} = 0.005\ \Omega$
	SOFC converter parameters: $C_{fc} = 1$ mF $L_{fc} = 0.5$ mH

3.2 Control of SOFC System

In this work, SOFC is regulated to generate power during power shortages. For the rest of the time, the active power output of the fuel cell system is zero. Power shortages may occur if solar irradiation is low/zero, or during sudden increase in load, that cannot be met by PV system. The control diagram of SOFC system is shown in Fig. 3. The component parameters of the boost converter are given in Table 1.

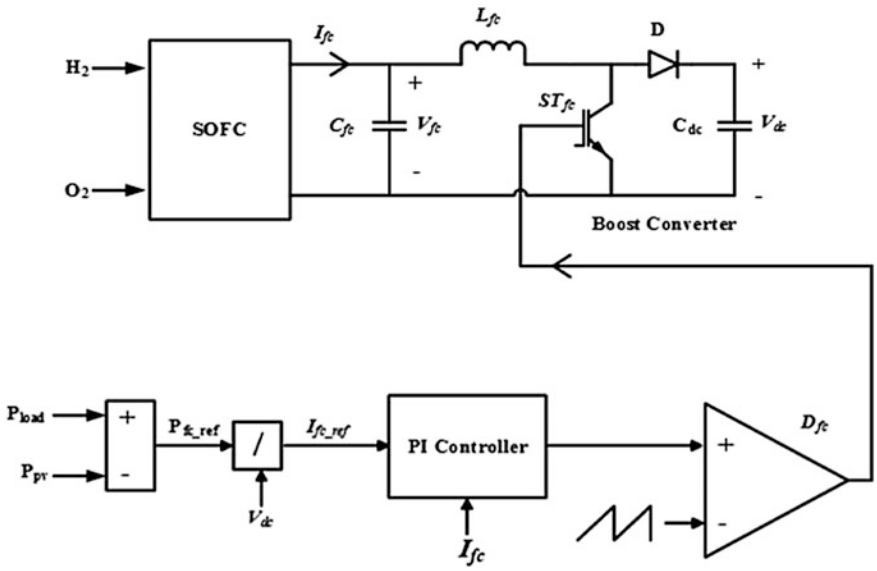

Fig. 3 Control of SOFC system

4 Control of VSC Using FLC

In this work, PQ control technique based on FLC is implemented to smoothly control the required real and reactive power flow between the DG units and the utility grid. The active and reactive power output of the VSC is given by (1)–(2) [5, 15],

$$P = \frac{3}{2}(v_d i_d + v_q i_q) \tag{1}$$

$$Q = \frac{3}{2}(v_q i_d - v_d i_q) \tag{2}$$

where v_d, v_q are the *dq-axis* components of the VSC output voltage, and i_d, i_q are the *dq-axis* components of the VSC output current. For grid synchronization purpose, v_d is synchronized with the grid voltage (v_{sd}) with the help of phase-locked loop and v_q is set as zero. On setting $v_q = 0$ in the above equations, it can be said that real power can be controlled by regulating *d-axis* component of the output current, $i_{d,}$ and reactive power can be controlled by controlling the q-axis component of the output current, i_q respectively. The reference *d-axis* current i_d^* is generated by controlling DC-link voltage. The reference q-axis current i_q^* is generated directly from Eq. (2).

To achieve the above said objective, PQ control technique based on FLC is used here to control the grid-interactive VSC as shown in Fig. 4. For this purpose, the current control loop and DC-link voltage control loop is designed using FLC. The FLC for *d-axis* and *q-axis* current controller is shown in Fig. 4. The *d-axis*

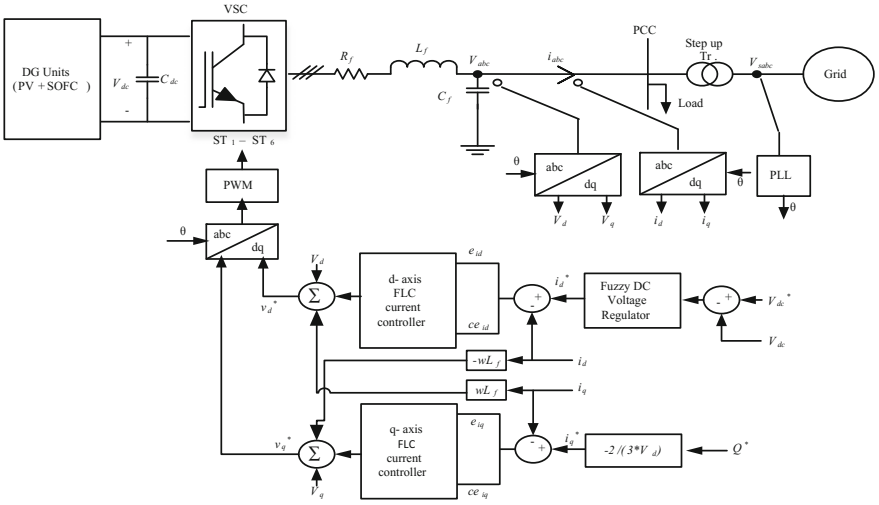

Fig. 4 PQ control of VSC using FLC

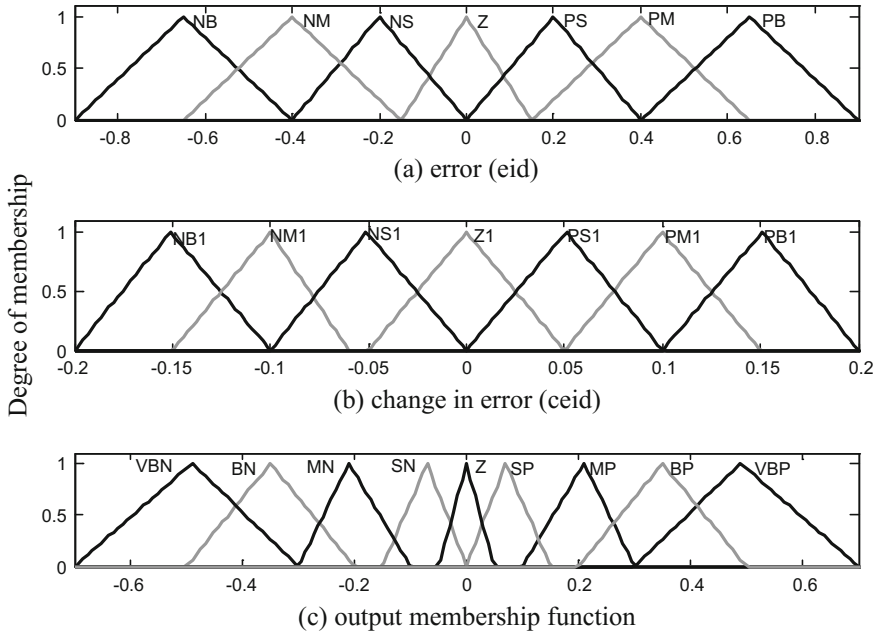

Fig. 5 Membership function of d-axis FLC

current error (ei_d) and its derivative (cei_d) are given as input. Similarly, the *q-axis* error current (ei_q) between i_q and iq^* and its derivative (cei_q) are fed as input to the *q-axis* FLC. Here, set of triangular membership functions are used to represent the input and output variables. Figure 5 shows the membership functions of the fuzzy *d-axis* current controller, and the developed rule base is shown in the Table 2.

Table 2 Rule table for d-axis and q-axis current controller

Error (ei_d)	Change in error (cei_d)						
	NB1	NM1	NS1	Z1	PS1	PM1	PB1
NB	VBN	VBN	BN	MN	SN	SN	Z
NM	VBN	BN	MN	SN	SN	Z	SP
NS	BN	MN	SN	SN	Z	SP	MP
Z	MN	SN	SN	Z	SP	MP	MP
PS	SN	SN	Z	SP	SP	MP	BP
PM	SN	Z	SP	SP	MP	BP	VBP
PB	Z	SP	SP	MP	BP	VBP	VBP

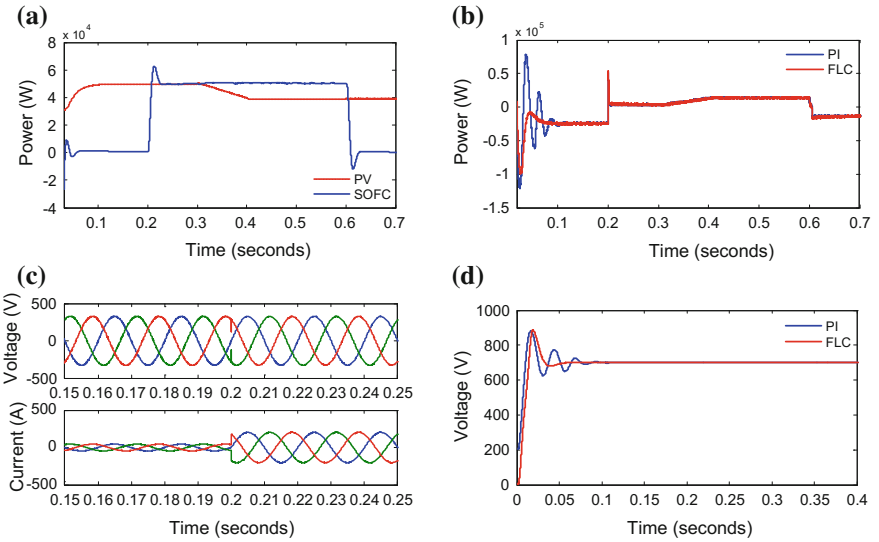

Fig. 6 **a** DG power output, **b** grid active power output, **c** VSC output voltage and current, and **d** VSC DC-side voltage

5 Results and Discussions

5.1 Case 1: Sudden Increase in Resistive Load

For this case, the irradiance is considered to be varying. Initially, a resistive load with active power consumption of 20 kW is connected to the system. At time $t = 0.2$ s, the active power consumption is increased to 90 kW, and at time $t = 0.6$ s, the active power is decreased to 20 kW. Figure 6a shows the power generated by the DG units. It can be noted that the output of SOFC is zero until $t = 0.2$ s. Until $t = 0.2$ s, the additionally available power from the PV system is exported to the grid (grid-injecting mode) as shown in Fig. 6b. During $t = 0.2$ to

0.6 s, as the load increases, SOFC is controlled to generate the deficit power as shown in Fig. 6a. During this time interval, until $t = 0.3$ s, the power exchange between the grid and DG is zero as shown in Fig. 6b. Between $t = 0.3$ and 0.6 s, the SOFC is generating its rated power and the PV output power starts decreasing, and hence, the power shortage is supplied by the grid (grid-sharing mode).

The system response is shown in Fig. 6c. Figure 6d shows the comparison between DC-link voltages obtained using PI and FLC.

5.2 *Case 2: During Sudden Change in Irradiance*

For this case, the irradiance level is considered as shown in Fig. 7a. Initially, a 20 kW resistive load is used, and at $t = 0.2$ s, the active power consumption of load is raised to 90 kW and inductive load of 20 kVAr is connected to the system. Various system responses for this case are shown in Fig. 7b–d. It is seen that as irradiance goes to zero at $t = 0.4$ s, the output power of PV unit decreased to zero as shown in Fig. 7b. SOFC is regulated to produce the deficit power. The real and reactive power exchanged between the DG units and grid using the PI and FLC is shown in Fig. 7c. It can be noted that the proposed controller provides good performance than the conventional PI controller. The DC-link voltage comparison is shown in Fig. 7d. It shows that the response offered by the proposed controller is better than the PI controller during varying irradiance. To validate the performance of the proposed controller, the results are compared with present literature. It is shown in Table 3.

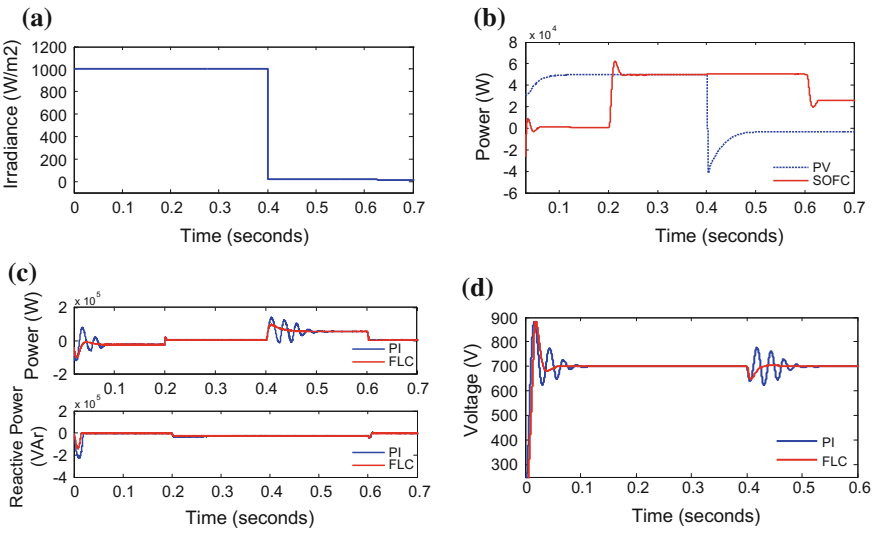

Fig. 7 **a** Irradiance level, **b** DG output power, **c** real and reactive power output of grid, and **d** DC-link voltage of VSC

Table 3 Performance comparison of the proposed controller

Irradiance step change	Controller type	DC voltage	
		Overshoot (in %)	Settling time (s)
500 > 250 W/m^2	Proposed	1.19	0.04
	PS0-PI [15]	0.83	0.198

6 Conclusion

The operation and control of utility-interactive microgrid consisting of PV and SOFC system were simulated using MATLAB/Simulink. To smoothly regulate the power flow, an effective current controller was designed using FLC. Besides the simplicity in designing the FLC, it exhibits good control performance in regulating the active and reactive power flow between DG units and grid. Thus, it can be concluded that the proposed FLC effectively regulates the power flow than the conventional PI controller with reduced oscillations and overshoot. Further, to achieve power balance on ac and DC side of VSC, DC-link voltage control loop was implemented using FLC. From the results, it was observed that the FLC effectively controls the DC-link voltage.

References

1. Akorede MF, Hizam H, Pouresmaeil E (2010) Distributed energy resources and benefits to the environment. Renew Sustain Energy Rev 14(2):724–734
2. Ahmed NA, Al-Othman AK, AlRashidi MR (2011) Development of an efficient utility interactive combined wind/photovoltaic/fuel cell power system with MPPT and DC bus voltage regulation. Electr Power Syst Res 81(5):1096–1106
3. Ye L, Sun HB, Song XR (2012) Cheng Li.: dynamic modeling of a hybrid wind/solar/hydro microgrid in EMTP/ATP. Renew Energy 39(1):96–106
4. Vigneysh T, Kumarappan N, Arulraj R (2013) Operation and control of wind/fuel cell based hybrid microgrid in grid connected mode. In: Proceedings of international multi-conference in automation, computing, communication, control and compressed sensing (iMac4s), pp 754–758
5. Eid A (2014) Utility integration of PV-wind-fuel cell hybrid distributed generation systems under variable load demands. Int J Elect Power Energy Syst 62:689–699
6. Chen Z, Luo A, Wang H, Chen Y, Li M, Huang Y (2015) Adaptive sliding-mode voltage control for inverter operating in islanded mode in microgrid. Int J Elect Power Energy Syst 66:133–143
7. Hornik T, Zhong QC (2011) A current-control strategy for voltage-source inverters in microgrids based on h-infinity and repetitive control. IEEE Trans Power Electron 26(3): 943–952
8. Ahmad S, Albatsh FM, Mekhilef S, Mokhlis H (2014) Fuzzy based controller for dynamic unified power flow controller to enhance power transfer capability. Energy Convers Manage 79:652–665

9. Arulraj R, Kumarappan N, Vigneysh T (2013) Optimal location and sizing of DG and capacitor in distribution network using weight-improved particle swarm optimization algorithm (WIPSO). In: Proceedings of international multi-conference in automation, computing, communication, control and compressed sensing (iMac4s), pp 759–764
10. Bose BK (2007) Neural network applications in power electronics and motor drives—an introduction and perspective. IEEE Trans Ind Electron 54(1):14–33
11. Reisi AR, Moradi MH, Jamasb S (2013) Classification and comparison of maximum power point tracking techniques for photovoltaic system: a review. Renew Sustain Energy Rev 19:433–443
12. Vigneysh T, Kumarappan N (2016) Autonomous operation and control of photovoltaic/solid oxide fuel cell/battery energy storage based microgrid using fuzzy logic controller. Int J Hydrogen Energy 41(3):1877–1891
13. Zhu Y, Tomsovic K (2002) Development of models for analyzing the load-following performance of microturbines and fuel cells. Electr Power Syst Res 62(1):1–11
14. Mahmood H, Michaelson D, Jiang J (2012) Control strategy for a standalone PV/battery hybrid system. In: Proceedings of 38th annual conference on IEEE Industrial Electronics Society, pp 3412–3418
15. Arzani A, Arunagirinathan P, Venayagamoorthy GK (2015) Development of optimal PI controllers for a grid-tied photovoltaic inverter. In: Proceedings of IEEE symposium series on computational intelligence, pp 1272–1279

A Novel Method of Power Quality Improvement in BLDC Motor Using Cascaded H-Bridge MLI Topology

S. Arunkumar and J. Pearly Catherine

Abstract In this paper, a conventional two-level inverter used in BLDC motor drive is replaced with cascaded H-bridge multilevel inverter, in order to improve the performance features of motor drive. The rotor position of BLDC motor sensed as Hall signals is converted into sinusoidal back EMF and used as sinusoidal pulse width modulated carrier wave for electronic commutation. The nonlinearity normally existing in inverter switching is taken into account in this proposed method, which is an added advantage. The modeling is done using MATLAB/Simulink software and simulated for parameters such as speed, stator current, back EMF, and torque. It is found that the proposed single inverter topology helps both in torque ripple minimization and in harmonic reduction, thereby leading to power quality enhancement than existing method.

Keywords BLDC · Torque ripple · Cascaded H-bridge MLI · Back EMF Power quality

1 Introduction

The continuous technological advancements in power semiconductors and microprocessors/logic ICs have resulted in the combination of permanent-magnet brushless electric motor production and adjustable speed driver (ASD) control schemes to enable reliable and cost-effective solution for a wide range of adjustable speed applications. The majority of such electronically controlled motor system applications will be of the BLDC type because of their high efficiency, silent operation, compact form, reliability, and low maintenance.

S. Arunkumar (✉)
Kumaraguru College of Technology, Coimbatore, India
e-mail: akumar5989@gmail.com

J. Pearly Catherine
J.K.K. Nattraja College of Engineering and Technology, Kumarapalayam, India
e-mail: pearlykpm@gmail.com

M.C. Bhuvaneswari and J. Saxena (eds.), *Intelligent and Efficient Electrical Systems*, Lecture Notes in Electrical Engineering 446,
https://doi.org/10.1007/978-981-10-4852-4_10

The BLDC motors are commonly powered by a two-level voltage source inverter (VSI) along with rotor position sensors. The signals sensed by the sensors result in nonlinear way of commutating the inverter switches, which causes ripples in electromagnetic torque. With this arrangement, the harmonic content also increased failing to meet the IEEE standards and results in poor quality at ac mains.

Undesirable torque pulsation in the BLDC motor drive causes speed oscillations and excitation of resonances in mechanical portions of the drive leading to acoustic noise and visible vibration patterns in high-precision machines. Therefore, minimization or elimination of noise and vibration is a major issue in BLDC motor drive [1]. The method proposed in [2] states that the BLDC motor will be free from acoustics and torque ripple, if operated with ideal sinusoidal or rectangular waveform.

In [3], the reason for commutation torque ripple in BLDC motor is found to be the loss of exact phase current control during phase current commutation. It presents a method of using DC current sensor, to regulate the motor phase current with the help of proper duty ratio control. The various PWM techniques used for torque ripple minimization are compared in [4], and it has been concluded that H-PWM-L-ON pattern will be better in performance owing to upper commutation.

The work in [5] proposes setting up of a buck converter in front of VSI to reduce the torque ripple during commutation period. In this topology, the pulses for buck converter are derived using PWM ON pattern, to regulate the phase current. Since this method does not consider the bandwidth of the pulse waveform, its application is limited to low-speed operation only. Similar approach has been carried out for buck-boost and Cuk converter-fed BLDC motor drives, the features of which are discussed in [6–8].

2 Methodology

In the existing methods of BLDC motor control, the commutation of inverter switches is improperly done, owing to non-consideration of back EMF non-ideality. Though some of the new algorithms take this property into account, they fail to regard the freewheeling current available in inactive phase. Further, these algorithms are time-consuming and require fast controllers and high-resolution decoders. Hence, modifying the inverter output voltage will be the best way to reduce the ripples in the load torque.

In the proposed method, the two-level inverter is replaced by a cascaded H-bridge multilevel inverter and the generation of control pulses is modified to depend on the back EMF generation. As shown in Fig. 1, the trapezoidal shape back EMF is converted into a sinusoidal shape with the help of second-order low-pass filter and used as carrier signal for pulse generation. Hence, all the non-ideality existing in back EMF is considered in pulse generation, and the inverter switches are accordingly commutated. This automatically reduces the ripples in back EMF. Figure 1 also shows that the stator winding of the motor is

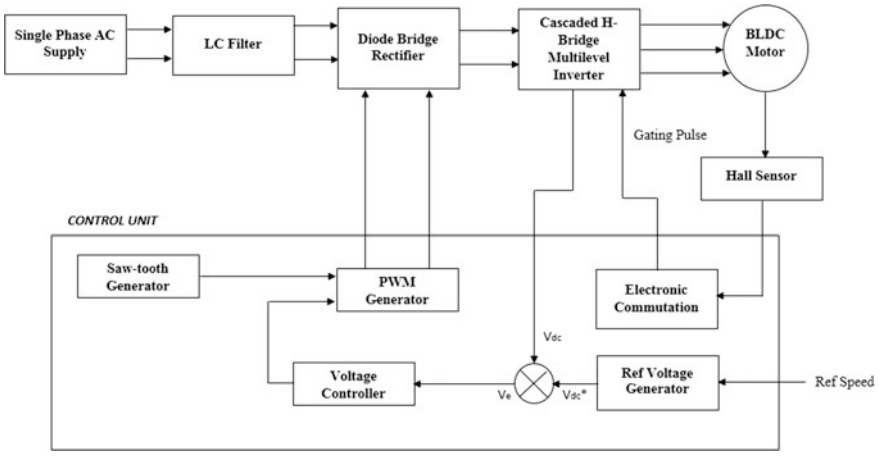

Fig. 1 Proposed block diagram

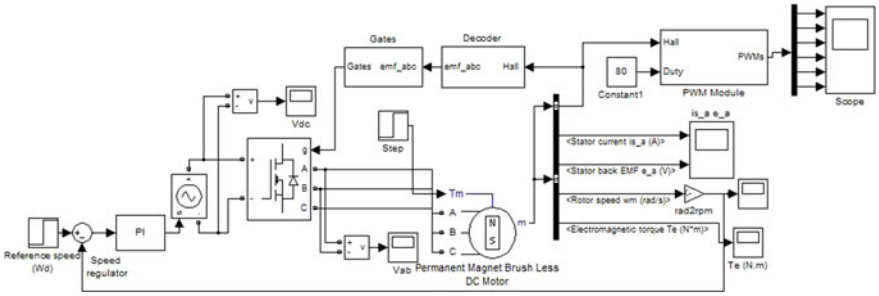

Fig. 2 MATLAB/Simulink model of two-level inverter-fed BLDC motor drive

energized by sinusoidal current waveform obtained from the cascaded H-bridge multilevel inverter. By increasing the output voltage level of the inverter, the stator current can be made more sinusoidal, thereby reducing the harmonic content and increasing the supply-side power factor. The better quality of stator current, load torque overweighs the disadvantage of having more components in the circuit.

3 Modeling and Simulation

The simulation model for existing two-level inverter-fed BLDC motor is developed using the MATLAB/Simulink software, as shown in Fig. 2. The gates are fired corresponding to the rotor position. From Table 1, it is understood that at any instant, one switch from upper arm and one switch from lower arm will alone conduct. The switches are not commutated, if the Hall signals are either high or low.

Table 1 Switching states for two-level inverter-fed BLDC motor

S. No.	Hall signal			Back EMF			Switches commutated
	H_A	H_B	H_C	E_A	E_B	E_C	
1.	0	0	0	0	0	0	–
2.	0	0	1	0	−1	+1	Q_4, Q_5
3.	0	1	0	−1	+1	0	Q_2, Q_3
4.	0	1	1	−1	0	+1	Q_2, Q_5
5.	1	0	0	+1	0	−1	Q_1, Q_6
6.	1	0	1	+1	−1	0	Q_1, Q_4
7.	1	1	0	0	+1	−1	Q_3, Q_6
8.	1	1	1	0	0	0	–

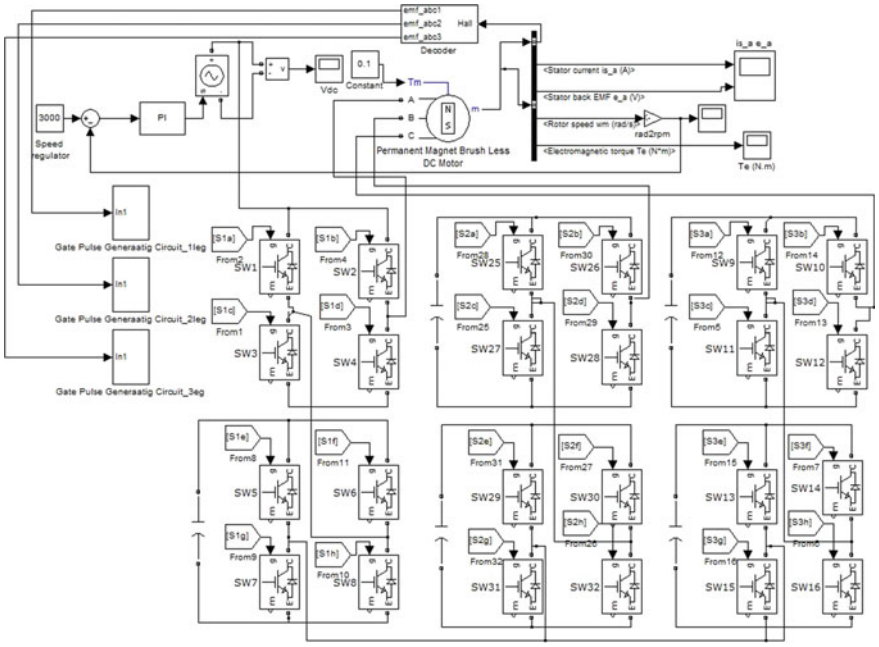

Fig. 3 Five-level cascaded H-bridge multilevel inverter-fed BLDC motor drive

Figure 3 shows the Simulink model of the proposed cascaded H-bridge multilevel inverter-fed BLDC motor drive. The switches in this inverter are commutated using sinusoidal pulse width modulation, where the sinusoidally converted back EMF will be the carrier wave. The corresponding switching state combinations are given in Table 2.

Table 2 Switching states for five-level CHB inverter-fed BLDC motor

Switches turn on	Voltage level
S1, S2	$+V_{dc}$
S1, S2, S5, S6	$+2\ V_{dc}$
S4, D2, S8, D6	0
S3, S4	$-V_{dc}$
S3, S4, S7, S8	$-2\ V_{dc}$

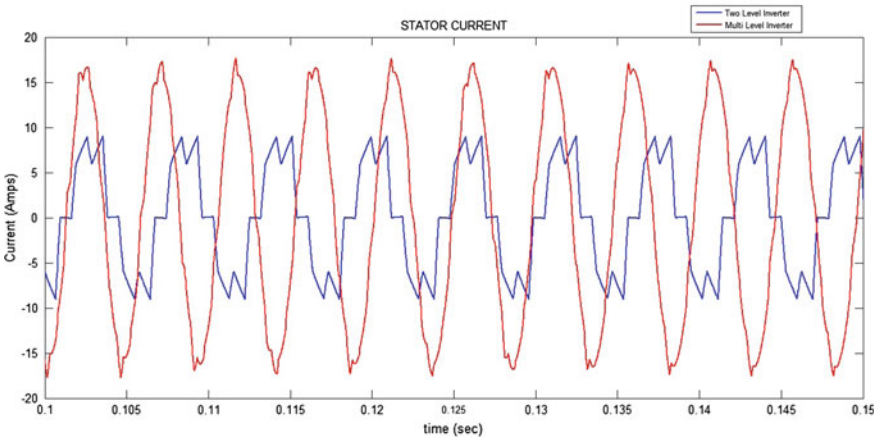

Fig. 4 Stator current waveform

4 Results and Discussion

The electrical parameters taken for analysis are stator current, back EMF, and mechanical parameters such as motor speed and electromagnetic torque. The simulation results of each factor are compared between existing and proposed methodologies.

In Fig. 4, it is seen that stator current waveform in a two-level inverter-fed motor drive is distorted from its ideal shape owing to harmonics in the supply current. With the cascaded H-bridge multilevel inverter, the harmonic content is much reduced with increased level of inverter output voltage. Hence, the stator current appears nearly sinusoidal, leading to improved electromagnetic torque and speed.

The stator back EMF waveform for both the topologies is compared in Fig. 5. In case of two-level inverter, the nonlinearity in the back EMF is more pronounced due to the harmonic effects. In case of multilevel inverter, as the nonlinearity is taken into account in pulse generation, the back EMF waveforms look exactly in trapezoidal shape.

As the nonlinearity in back EMF is not considered in the existing method, the phase winding energized by two-level inverter may produce ripples in electromagnetic torque. But in the proposed method, the back EMF is considered as carrier

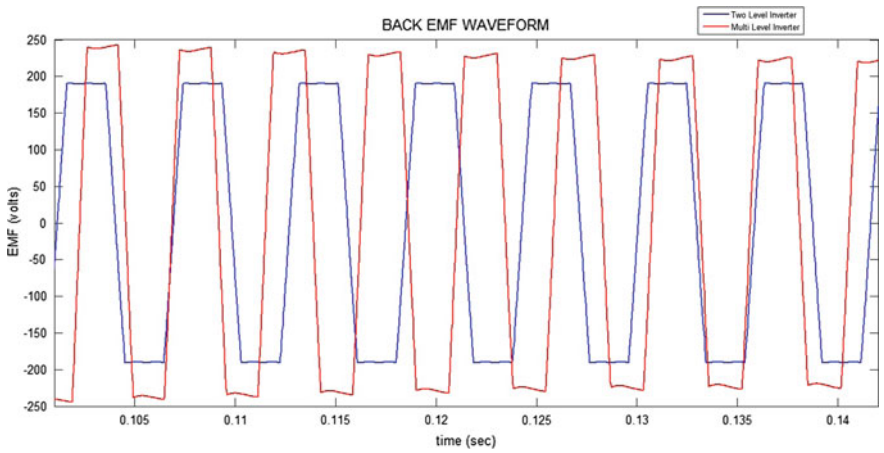

Fig. 5 Back EMF waveform

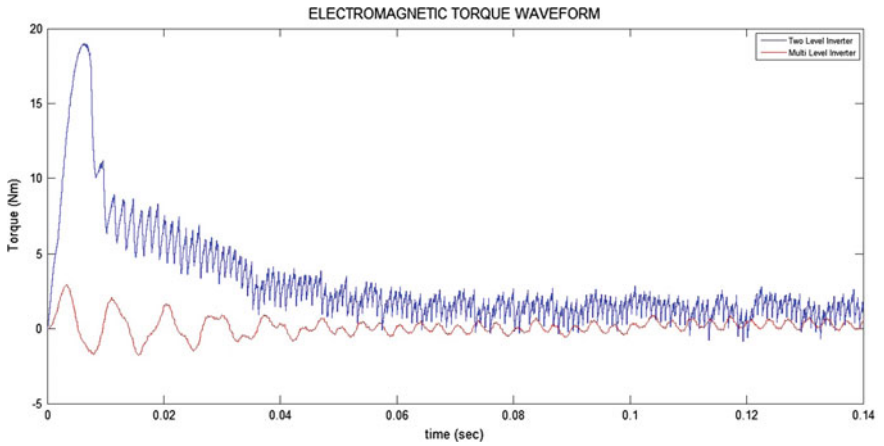

Fig. 6 Electromagnetic torque waveform

signal for pulse generation, and the ripples are comparatively reduced much as shown in Fig. 6. This also leads to improved motor efficiency.

The speed response of the BLDC motor with reference speed of 3000 rpm for two-level and multilevel inverter-fed BLDC motor drive is shown in Fig. 7. For two-level inverter, initially the speed is very high and oscillatory and settles to the reference speed at about 0.13 ms only. But in multilevel inverter-fed drive, the speed is linearly increased up to 0.06 ms and it reaches the reference value faster. The latter method thus allows smooth variation of speed.

Figure 8 displays the increased level of multilevel inverter output voltage. With higher output level, the harmonics in the output waveform get reduced, which

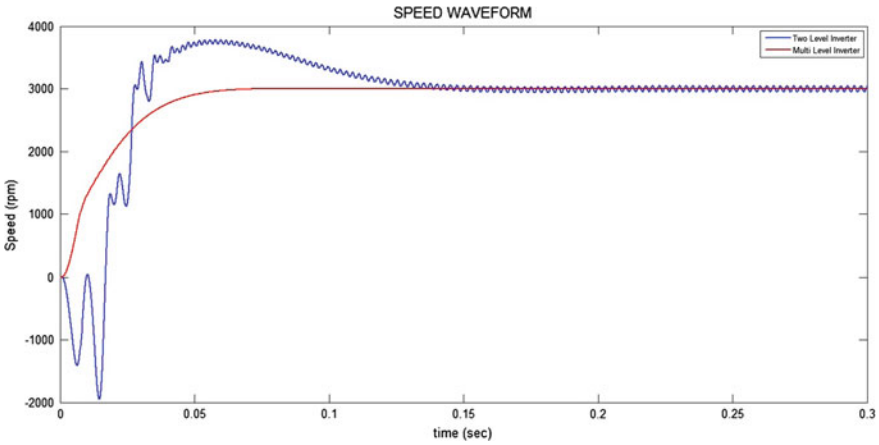

Fig. 7 Motor speed waveform

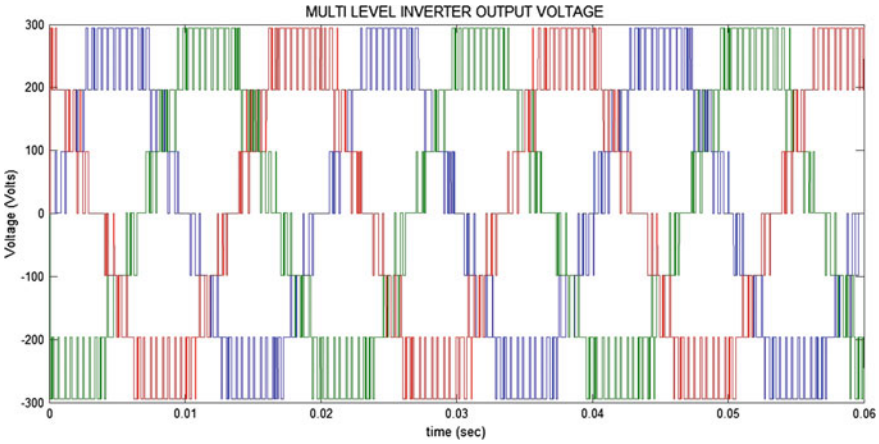

Fig. 8 Multilevel inverter output voltage waveform

minimizes the THD content. In the proposed topology, five-level inverter is employed and the FFT analysis performed in both the cases is shown in Figs. 9 and 10. It is found that the total harmonic distortion in multilevel inverter-fed BLDC motor drive is 10.34%, which is better when compared with that of two-level inverter, where the THD is 26.87%.

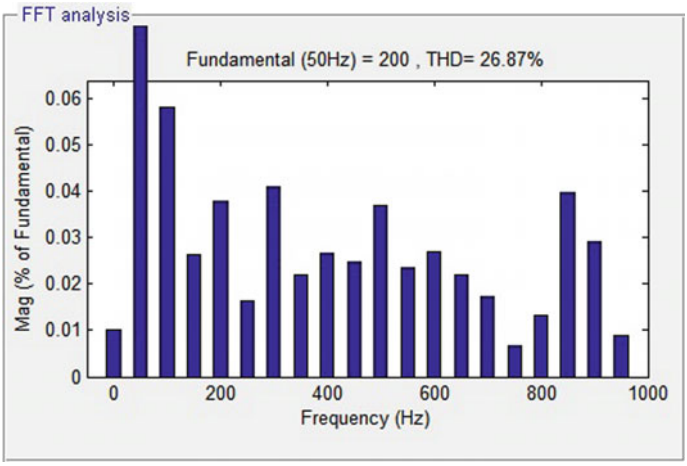

Fig. 9 FFT analysis of two-level inverter

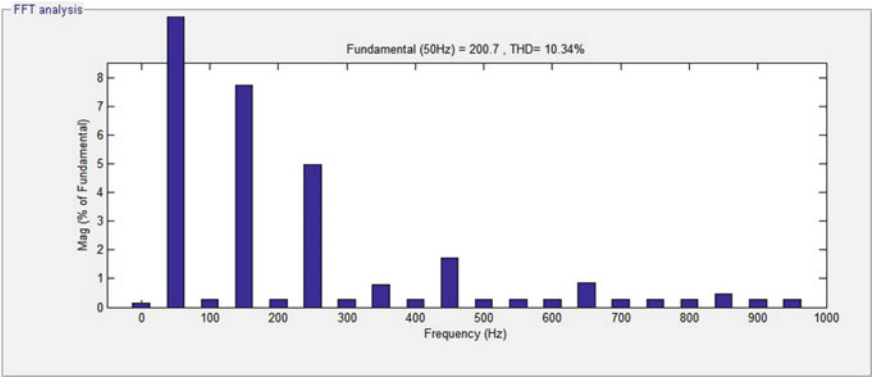

Fig. 10 FFT analysis of multilevel inverter

5 Conclusion

The BLDC motor drive is commonly used in conjunction with VSI, in order to derive the features of a general DC motor. The pulses used for triggering the inverter do not take into account the nonlinearity existing in the back EMF. This leads to degradation of motor performance in way of high torque ripple, harmonic content in stator current. Hence, a new method of replacing the VSI with cascaded H-bridge MLI is proposed in this work, to make the motor more reliable and efficient. The inverter switching states are decided based on the nonlinearity present in the back EMF, by converting it to sinusoidal form. Further, higher level of output

voltage causes the stator current to be more sinusoidal. The simulation of the proposed model is done using MATLAB/Simulink, and the comparative results clearly reveal the improved performance of motor drive in terms of smooth speed variation, minimum torque ripple, and stator harmonics. This, in turn, enhances the power factor at ac mains as well the power quality.

References

1. Ghule AB, Sankeshwari SS (2015) Sliding mode observer for torque control in sensorless BLDC motor. IOSR J Electr Electron Eng 10(5):16–20
2. Hanselman D (1994) Minimum torque, ripple maximum efficiency excitation of brushless permanent magnet motors. IEEE Trans Ind Electron 41(3):292–300
3. Song J-H, Choy I (2004) Commutation torque ripple reduction in brushless DC motor drives using a single DC current sensor. IEEE Trans Power Electron 19(2):312–319
4. Chuang HS, Ke YL (2009) Analysis of commutation torque ripple using different PWM modes in BLDC motors. IEEE Trans Ind Electron 22(3):2213–2229
5. Zhang XF, Lu ZY (2006) A new BLDC motor drives method based on BUCK converter for torque ripple reduction. IEEE Trans Power Electron 16(4):1880–1895
6. Singh B, Bist V (2013) Improved power quality bridgeless Cuk converter fed brushless DC motor drive for air conditioning system. IET Power Electron 6(5):902–913
7. Bist V, Singh B (2014) An adjustable-speed PFC bridgeless buck-boost converter-fed BLDC motor drive. IEEE Trans Ind Electron 61(6):2665–2677
8. Arunkumar S, Thangavel S (2015) A review paper on torque ripple reduction in brushless DC motor drives with different multilevel inverter topology. Indonesian J Electr Eng 13(1):65–75

Tuning of Fractional Order Proportional Integral Derivative Controller for Speed Control of Sensorless BLDC Motor using Artificial Bee Colony Optimization Technique

K. Vanchinathan and K.R. Valluvan

Abstract This paper introduces a novel method based on the artificial bee colony (ABC) presented for optimal tuning fractional-order proportional–integral–derivative (FOPID) controller for speed control of sensorless brushless direct current (BLDC) motor which can guarantee the desired speed control and the robustness of the closed-loop system. ABC algorithm is a recently proposed global search optimization technique which simulates the behavior of natural bees for determining the optimal parameter values. The proposed method minimizes the steady-state and transient response, i.e., steady-state error, peak overshoot time, rise time, peak time, and settling time with the help of ABC optimal tuning five-degree parameters K_p, K_i, K_d, λ, and μ. In addition, the comparative study has been made to analyze the step response characteristics of BLDC motor drive using ABC over come conventional genetic algorithm (GA) for speed regulation of the motor. MATLAB simulation and extensive analysis of results obtained show the effectiveness of the proposed approach.

Keywords Fractional-order PID controller · Sensorless BLDC motor drive
Artificial bee colony optimization technique

1 Introduction

Nowadays rapid development of modern industries and domestic appliances using permanent magnet BLDC motor. The BLDC motor is the biggest contribution to robotics, aerospace, and medical equipment and is automotive to attain desired objectives. The BLDC motor is highly reliable, more efficient, and produces less noise. In addition, in this motor, same power is distributed with the help of

K. Vanchinathan (✉) · K.R. Valluvan
Velalar College of Engineering and Technology, Erode 638012, Tamil Nadu, India
e-mail: vanchinathan@velalarengg.ac.in

M.C. Bhuvaneswari and J. Saxena (eds.), *Intelligent and Efficient Electrical Systems*, Lecture Notes in Electrical Engineering 446,
https://doi.org/10.1007/978-981-10-4852-4_11

electronics commutator compared to conventional DC motor. The conventional DC motor produces sparking and more noise so it is never used for lifelong usage. Generally, a BLDC motor drive uses one or more Hall effect sensors giving permanent magnet rotor positional information for synchronization of stator and rotor winding. Such implementation results in a higher drive cost due to sensors' electrical wiring and implementation in the motor. Also, Hall effect sensors cannot be used in some applications where the rotor is in closed housing, and the number of electrical entries must be reduced. Therefore, for cost and technical reasons, the sensorless BLDC motor drive is essential for speed control application [1].

The fractional-order PID controller concept was proposed by Podlubny in 1997. He also demonstrated the better transient and steady-state response of this type of controller, in comparison with the classical integer-order PID controller, when used for the control of fractional-order PID controller systems. A frequency- and time-domain approach by using FOPID controllers is also studied [2]. In meta-heuristics, optimization method is presented where the parameters of the FOPID controller are fine-tuned such that the predefined design specifications are satisfied. Ziegler–Nichols tuning rules for FOPID are reported. The transient and steady-state time responses have utmost importance for the design and analysis of closed-loop control systems because these are essentially time-domain systems where time is the independent variables. During the speed control analysis of response, the variation of output with respect to time can be studied. The satisfactory performance of the systems and the output behavior of systems with respect to time must be within the specified limits from time response analysis. The response of systems is a function of time. There are two parts of response of any systems: transient response, i.e., rise time, peak time, and settling time; steady-state response which are called as steady-state error [3].

The rest of this chapter is organized as follows: In Sect. 2, sensorless BLDC Motor drives is presented. Section 3 Includes the design of Fractional Order PID Controler for sensorless BLDC Motor drives. Section 4 describes the artificial bee colony optimization techniques. Section 5 Results and Discussion. Section 6 finaly some relevant concluding remains are presented.

2 Speed Control of Sensorless BLDC Motor Drives

The principle of speed control for BLDC motor is developed from the basic electromagnetic force (EMF) equation, torque, flux, current, and induced back EMF of the motor. The sensorless drive is operated based on the finding of the trapezoidal shape back electromagnetic force induced by the movement of a permanent magnet rotor winding in front of the stator winding which opposes the main voltage supplied to the stator windings in accordance with Lenz's law [4].

2.1 Mathematical Model of BLDC Motor

Three-phase star-connected brushless DC motor can be described by the following equation:

$$V_{ab} = R(i_a - i_b) + L\frac{\mathrm{d}}{\mathrm{d}t}(i_a - i_b) + e_a - e_b \tag{1}$$

$$V_{bc} = R(i_b - i_c) + L\frac{\mathrm{d}}{\mathrm{d}t}(i_b - i_c) + e_b - e_c \tag{2}$$

$$V_{ca} = R(i_c - i_a) + L\frac{\mathrm{d}}{\mathrm{d}t}(i_c - i_a) + e_c - e_a \tag{3}$$

The electromagnetic torque is given by:

$$T_e = [e_a i_a + e_b i_b + e_c i_c]\frac{1}{\omega m}(N - m) \tag{4}$$

Therefore

$$\omega_m = \frac{\mathrm{d}}{\mathrm{d}t}\varphi_m \tag{5}$$

The back emf is a function of rotor position φ and amplitude $E = Ke * \omega$ (Ke is a back EMF constant). The instantaneously induced back emf in BLDC motor is written as follows:

$$E_a = f_a\varphi * K_a\omega_m \tag{6}$$

$$E_b = f_b\varphi * K_b\omega_m \tag{7}$$

$$E_c = f_c\varphi * K_c\omega_m \tag{8}$$

The modeling equation is based on the assumption that the induced currents in the rotor due to stator harmonics fields are neglected and that iron and stray losses are also neglected. Damper winding is not usually a part of the BLDC motor. Damping provides inverter control. The motor is considered to have three phases. Figure 1 shows the equivalent circuit of BLDC motor [5].

2.2 Sensorless BLDC Motor

The sensorless BLDC motor drive has high potential application, incurs less maintenance, and lasts lifelong. It is less noisy, easy to access, weighs less, and

more compact in construction. Generally, the BLDC motor drives used two types of sensorless control technique, which can be found in the literature survey [6]. The first one is the position sensing using back EMF of the BLDC, motor and the second one is the position estimation using motor parameters, i.e., torque, speed, flux, terminal voltages, and currents. The position estimation frequently needs intelligent control algorithms to estimate motor parameters and also to do the uncomplicated computation process. Figure 2 shows the basic block of sensorless BLDC motor drive.

The sensorless brushless DC motor's basic control strategy is that the error between measured and calculated current from the machine model gives the different between the assumed rotor speed and actual speed of the motor drive. Three-phase currents constitute the input to the speed estimator. The error between the reference speed and estimated rotor speed is amplified and limited to provide the torque-producing component of the stator current. Consider that the machines are running at a speed ω_r, whereas model starts with an assumed rotor speed ω_{rm} related to the actual and assumed or model speed as follows [7]:

$$\theta_r = \int \omega r \, \mathrm{d}t$$

$$\theta_{rm} = \int \omega_{rm} \, \mathrm{d}t \tag{9}$$

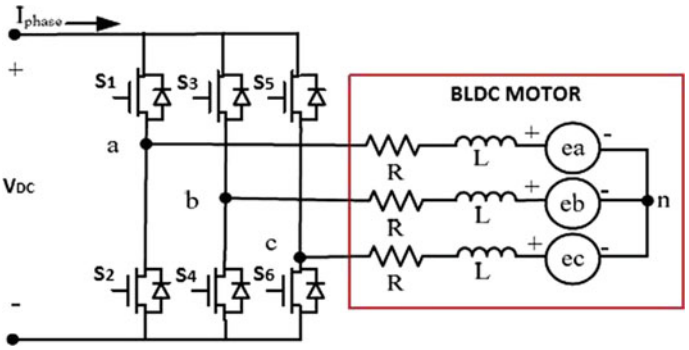

Fig. 1 Equivalent circuit of BLDC motor

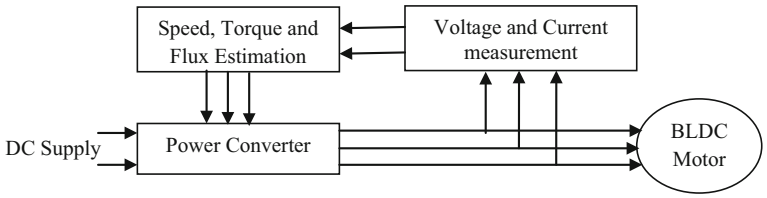

Fig. 2 Basic block of sensorless BLDC motor drive

$$\delta\theta = \delta_r - \theta_{rm} = \int (\omega_r - \omega_{rm})\mathrm{d}t \tag{10}$$

The machine model is utilized to compute the stator current and note that it is carried out in a reference frame at an assumed rotor speed. The machines equation in the assumed rotor speed reference frames is as follows:

$$\begin{bmatrix} pi\alpha_m \\ pi\beta_m \end{bmatrix} = \begin{bmatrix} \frac{-R_s}{L_q} & -\omega_{rm}\frac{L_d}{L_q} \\ \omega_{rm}\frac{L_q}{L_d} & -\frac{R_s}{L_q} \end{bmatrix} \begin{bmatrix} i\alpha_m \\ i\beta_m \end{bmatrix} + \begin{bmatrix} \frac{-\omega_{rm}\lambda_{af}}{L_q} \\ 0 \end{bmatrix} + \begin{bmatrix} \frac{V_\alpha}{L_q} \\ \frac{V_\beta}{L_d} \end{bmatrix} \tag{11}$$

The variables without the second subscript indicate the actual machines variables, the machines model, or estimated variables end with subscript *m*. The actual machines equation is derived from the understanding that $\alpha - \beta$ axes are the considered reference axes. The error current results are as follows:

$$\delta i\alpha(kT) = \frac{-\lambda_{af}}{L_q} T(-\omega_{rm} + \omega_r) \tag{12}$$

$$\delta i\beta(kT) = \omega_r \frac{\lambda_{af}}{L_d} \delta\varphi \tag{13}$$

The actual rotor speed is obtained as follows:

$$\omega_r = \frac{-L_q}{\lambda_{af}} \frac{1}{T} \delta i\alpha\ (kT) + \omega_{rm}. \tag{14}$$

3 Optimum Tuning of Fractional-Order PID Controller

3.1 Fractional-Order PID Controller

The FOPID controller is a control loop feedback mechanism (controller) commonly used in industrial control systems. A FOPID controller continuously calculates an error value as the difference between a measured process variable and a desired set point [8]. The fractional-order PID controller has five degree of freedom, that is, five parameters—K_p, K_i, K_d, μ, and λ, for tuning to achieve a desired set point [9]. The FOPID provides adaptable time and frequency step responses of the closed-loop control system for efficient as well as robust speed control performance. It shows that the FOPID controller will always provide improved step response characteristics than integer-order PID controller if it is accurately tuned whatever may be the type of system. Therefore, FOPID controller is designed for minimizing step response time-domain specification, i.e., transient and steady-state behavior [10].

3.2 Optimal Tuning of FOPID Controller

In order to find the FOPID controller optimal parameter tuning values for speed control of sensorless BLDC motor which minimization the time-domain specification, i.e., rise time, peak time, settling time, and steady-state error by artificial bee colony optimization techniques. Figure 3 shows the schematic diagram of optimal tuning of FOPID controller [11].

The transfer function of FOPID is given as follows:

$$G_c(s) = \frac{U(s)}{E(s)} = K_P + K_I S^{-\lambda} + K_D S^{\mu}, \quad (\lambda, \mu > 0) \tag{15}$$

The equation for the FOPID controller in the time domain is as follows:

$$U(t) = K_P e(t) + K_I D^{-\lambda} e(t) + K_D D^{\mu} e(t) \tag{16}$$

Unit step responses of closed-loop speed control system with FOPID controller is given by:

$$\begin{aligned} &\sum_{k=0}^{n} a_k D^{\beta k} y(t) + K_P y(t) + K_I D^{-\lambda} y(t) + K_D D^{\mu} y(t) \\ &\quad = K_P w(t) + K_I D^{-\lambda} w(t) + D^{\mu} w(t) \end{aligned} \tag{17}$$

From Eq. (17), the following expression for the transfer function of the considered closed-loop system is obtained as follows:

$$G_{\text{Closed}}(s) = \frac{K_P S^{\lambda} + K_I + K_D S^{\mu+\lambda}}{\sum_{k=0}^{n} a_k S^{\beta_{k+\lambda}} + K_P S^{\lambda} + K_I + K_D S^{\mu+\lambda}} \tag{18}$$

The unit step response $G_{\text{closed}}(t)$ is then obtained by the Laplace inversion of Eq. (18).

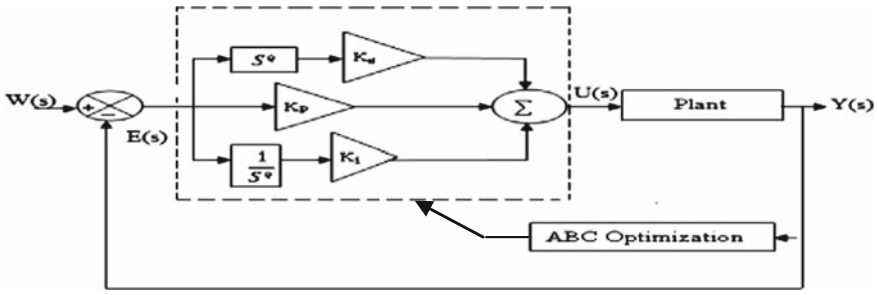

Fig. 3 Schematic diagram of optimal tuning of FOPID controller

4 Proposed ABC-Based FOPID Controller

The ABC have three groups of bees: employed bee, onlooker bee, and scout bee. The first half of the colony is employed bees, and the other half of the colony is onlooker bee for attaining their objectives. The number of employed bees is equal to that of food source which is available in the natural world. In particular, each food source which is available in the nature world is exploited by one employed bee. The employed bee whose food source has been exhausted becomes a scout bee. In ABC algorithm [12], the position of a food source represents a possible solution to be optimized. The profitability of the food source coincides with the value (fitness) of the optimized solution.

The main steps of the algorithm are described as follows:

Step 1 Initialize the food source positions − population size, 10; length of bee, 3; no. of iteration, 10 − k_d, k_p, k_i, λ, μ (bee = abs(10 * (rand(pop_size, L) − 0.5))).

Step 2 Each employed bee produces a new food source in her food source site and exploits in the better food source—fitness call function (Em = [bee(ind (1),:) Fit(ind(1))]).

Step 3 Each onlooker bee selects a food source depending on the value of her solution, produces a new food source in preferred food source site, and exploits the better food source: Q_i = 0.5 (Onlooker = [bee(ind(1),:) Fit(ind (1))]).

Step 4 Determine the source to be deserted and assign its employed bee as scout for searching new food sources (best_out = abs(10 * (rand(2, length (pi_ann_in)) − 0.5))).

Step 5 Memorize the best food source found so far (Best_Weight = Best (1:end −1)).

Step 6 Repeat ABC algorithm steps 2–5 until the stopping optimal parameter values K_p, K_i, K_d, and λ, μ are met.

In the first step of the algorithm i = (1–10), solutions are randomly produced in range of optimal parameters where K_p, K_i, K_d, λ, and μ are the number of the food sources. In the second step of the ABC algorithm for each employed bee, whose total number of bee equals to the half of the number of food sources, a new food source is produced by $v_{ij} = x_{ij} + \varphi_{ij}\,(x_{ij} - x_{kj})$ where φ_{ij} is a uniformly distributed real random number within the range of speed [1000, 1500], k is the index of the optimal solution select randomly from the bee colony k = int(rand $*$ optimal five degree of freedom parameter + 1), and D is the dimension of problem for optimization of FOPID controller parameters K_p, K_i, K_d, λ, and μ, where D = 5. After producing v_{i}, this new solution is compared to x_{i} solution, and the employed bee exploits the better source. In the third step of ABC algorithm, an onlooker bee selects a food source with the probability $pi = \mathrm{fit}_i / \sum_{n=1}^{\mathrm{SN}} \mathrm{fit}_n$ where fit_i is the fitness value of the solution x_i after all onlookers are distributed to the sources. Sources are checked whether they are to be abandoned. SN is the number of food sources which

is equal to the number of employed bees (BN). The employed bee associated with the exhausted source becomes a scout and makes a random search in problem domain by $x_{ij} = x_{ij}$ min + rand $*$ x_i max $-$ x_j min. The above method is used for speed control of sensorless BLDC motor with fractional-order PID controller based on local search artificial bee colony optimization algorithm. Finally, the optimal parameter values are as follows: $K_p = 2.72$, $K_i = 2.20$, $K_d = 2.20$, $\lambda = 0.72$, $\mu = 0.172$.

5 Results and Discussion

The Simulink model with FOPID controller for speed control of sensorless BLDC motor is developed in MATLAB using ABC optimization techniques module to set the parameter (K_p, K_d, K_i, λ, and μ) which give the desired speed control of sensorless BLDC motor. Figure 4 shows the stator current of sensorless BLDC motor.

Figure 5 shows the performance of the conventional FOPID-GA controller and proposed FOPID-ABC controller of stator back EMF of sensorless BLDC motor on reference speed 1500 rpm with no load condition of speed and torque. The performance of electromagnetic torque of sensorless BLDC motor with FOPID-GA and proposed FOPID-ABC controller is shown in Fig. 6. To evaluate the step response of the system, a series of measurements have been accomplished. The time-domain transient and steady-state step response comparison between FOPID-GA and FOPID-ABC of sensorless BLDC motor is shown in Table 1.

The results show that the settling time of conventional controller FOPID-GA and proposed FOPID-ABC controller is 0.840 and 0.631 s, respectively. Figure 7 shows the step response characteristics of BLDC motor.

A FOPID controller comparative study has been made to analyze the unit step response characteristics using ABC over come conventional GA for speed regulation of the motor. Initially, the machine runs at a constant speed, i.e., reference

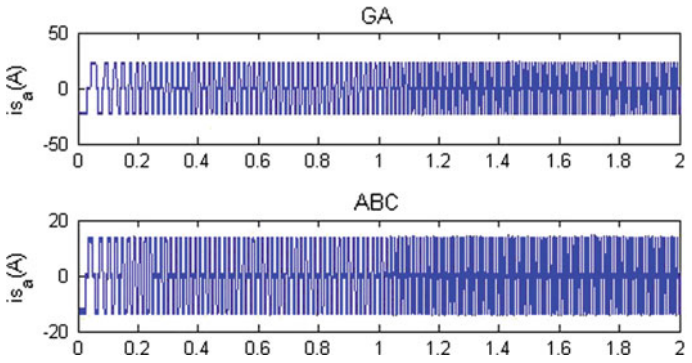

Fig. 4 Stator current of sensorless BLDC motor with GA and ABC

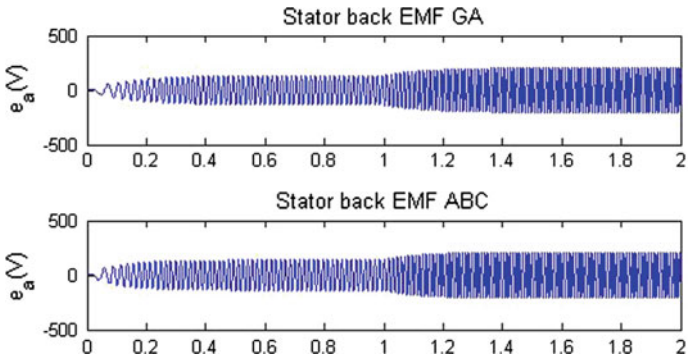

Fig. 5 Stator back EMF of sensorless BLDC motor with GA and ABC

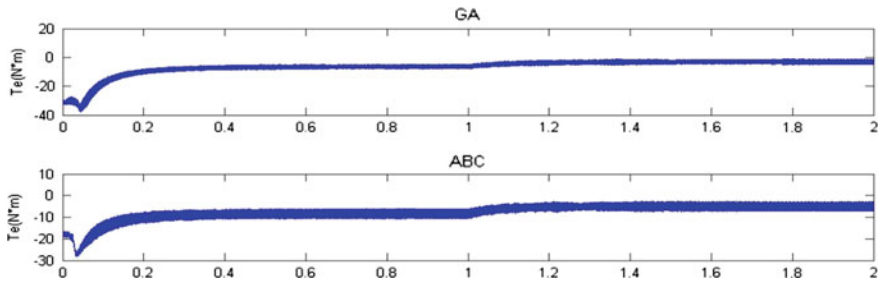

Fig. 6 Electromagnetic torques of sensorless BLDC motor with GA and ABC

Table 1 Time-domain specification of FOPID controller with GA and ABC

Techniques	Time responses						
	Settling time (s)	Rise time (s)	Peak time (s)	Steady-state error Ess (%)	Settling		Peak values
					Minimum	Maximum	
Genetic algorithm	0.840	0.351	0.641	2.04	1323	1470	1470
Artificial bee colony	0.631	0.270	0.420	0.67	1460	1490	1490

speed of 1000 rpm. The reference speed is changed from 1000 to 1500 rpm due to user requirements. Suddenly, the machine speed will reach 1500 rpm and the unit step response time-domain specifications such as rise time, peak time, settling time, and steady-state error are measured. Table 1 shows that the rise time, settling time, and steady-state error are reduced (improved) in the case of a FOPID-ABC controller than in the case of a FOPID-GA controller. Here, the overshoot is almost negligible when FOPID-ABC controller is applied. It can also be observed that

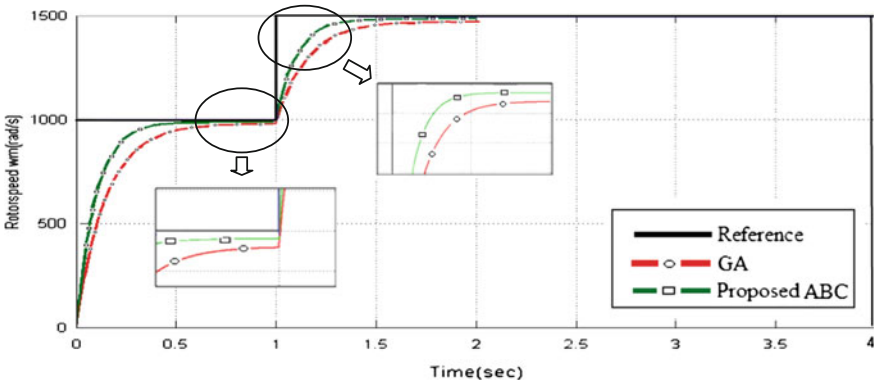

Fig. 7 Step response characteristics of sensorless BLDC motor with GA and ABC

Table 2 Specification of BLDC motor

BLDC motor parameter	Values
Rated voltage and current	36 V and 5 A
Number of poles and phases	4 pole and 3 phase
Rated speed and torque	1500 rpm and 0.42 N m
Torque constant and mass	0.082 N m/A and 25 kg
Inertia	$23e^{-06}$ kg m^2
Resistance and inductance per phase	0.57 Ω and 1.5 mH

percentage reduction in step response characteristics is more than in case of FOPID-GA. It is clear that FOPID controller with ABC optimization reduces the time-domain specifications, i.e., settling time, rise time, and steady-state error. Table 2 shows the specification of BLDC motor for experimental setup.

6 Conclusion

In this work, a comparison study of using GA and ABC methods for the tuning of FOPID controller for speed control of a sensorless BLDC motor is carried out. Obtained through simulation of speed control of sensorless BLDC motor, the simulation results show that the proposed FOPID-ABC controller can perform an efficient search for the optimal parameters K_p, K_i, K_d, λ, and μ. By comparing GA method to ABC optimization technique, it shows that ABC optimization technique can improve the transient and steady-state performance of the system in a better way.

References

1. Ozturk SB, Toliyat HA (2011) Direct torque and indirect flux control of brushless DC motor. IEEE/ASME Trans Mechatron 16(2):351–360
2. Monje CA et al (2008) Tuning and auto-tuning of fractional order controllers for industry applications. Control Eng Pract 16(7):798–812
3. Ibrahim H, Hassan F, Shomer AO (2014) Optimal PID control of a brushless DC motor using PSO and BF techniques. Ain Shams Eng J 5(2):391–398
4. Vanchinathan K, Valluvan KR (2015) Improvement of time response for sensorless control of BLDC motor drive using ant colony optimization technique. Int J A ppl Eng Res 10(55):6
5. Krishnan R (2001) Electric motor drives: modeling, analysis, and control. Prentice Hall, New Jersey
6. Vanchinathan K, Valluvan K (2016) A study of sensorless BLDC motor drives and future trends. Asian J Res Soc Sci Humanit 6(9):1863–1887
7. Gamazo-Real JC, Vázquez-Sánchez E, Gómez-Gil J (2010) Position and speed control of brushless DC motors using sensorless techniques and application trends. Sensors 10(7):6901–6947
8. Pan I, Das S (2012) Intelligent fractional order systems and control: an introduction, vol 438. Springer, Berlin
9. Padula F, Visioli A (2011) Tuning rules for optimal PID and fractional-order PID controllers. J Process Control 21(1):69–81
10. Kesarkar AA, Selvaganesan N (2015) Tuning of optimal fractional-order PID controller using an artificial bee colony algorithm. Syst Sci Control Eng 3(1):99–105
11. Rajasekhar A, Chaitanya V, Das S (2011) Fractional-order $PI^{\lambda}D^{\mu}$ controller design using a modified artificial bee colony algorithm. In: Swarm, evolutionary, and memetic computing, 2011. Springer, Berlin, pp 670–678
12. Rajasekhar A, Das S, Abraham A (2013) Fractional order PID controller design for speed control of chopper fed DC motor drive using artificial bee colony algorithm. In: World Congress on nature and biologically inspired computing (NaBIC), 2013, IEEE

Torque Ripple Minimization of a FOC-Fed PMSM with MRAS Using Popov's Hyper-Stability Criterion

N. Krishna Kumari and D. Ravi Kumar

Abstract This paper focuses on Field-Oriented Control (FOC) of a Permanent Magnet Synchronous Motor (PMSM). Model Reference Adaptive Control System (MRAS) is selected to estimate the speed of a drive. Electrical torque distortion of the machine under dynamic performance is relatively high, and if proper measures are taken, it can be significantly decreased. The first anticipated solution here is to combine FOC with the Sinusoidal Pulse Width Modulation (SPWM) technique. The intention of the sensorless control is to get better speed control performance with reduced torque ripples under load variations in MATLAB/Simulink/Simpower environment.

Keywords Permanent magnet synchronous motor (PMSM)
Field-oriented control (FOC) · Model reference adaptive system (MRAS)
Sensorless control · Sinusoidal pulse width modulation (SPWM)

1 Introduction

Due to the availability of rare earth permanent magnet materials, PMSMs are used in applications where it requires fast torque response with better dynamic operation [1]. As rotor cage is absent in PMSM, it gives quick response with applied load torque [2]. And the outstanding features of PMSM are high torque to inertia, high power density, reliability, and high efficiency; it is used in high-performance applications such as electric vehicles, servo, robotics, machine tools, and traction applications [3–7]. In general, the high-performance operation can be obtained with surface-mounted magnets fixing on a rotor, and this gives minimum armature effect with large air gap [8].

N. Krishna Kumari (✉) · D. Ravi Kumar
EEE Department, VNR VJIET, Hyderabad, Telangana, India
e-mail: nkkpsg@gmail.com; krishnakumari_n@vnrvjiet.in

D. Ravi Kumar
e-mail: ravikumar_d@vnrvjiet.in; ravi44d@gmail.com

M.C. Bhuvaneswari and J. Saxena (eds.), *Intelligent and Efficient Electrical Systems*, Lecture Notes in Electrical Engineering 446,
https://doi.org/10.1007/978-981-10-4852-4_12

The most renowned control techniques for PMSM are field-oriented control (FOC) and direct torque control (DTC) [9, 10]. The objective of both the control techniques is to control the flux and torque effectively. In spite of variations in parameters of the motor and external disturbances, the motor forces to follow command trajectory [11]. To achieve the requirement of high-performance characteristics obtained by DC drives, variable speed AC drives employing PMSM with FOC have been expanded in recent years [12].

In FOC, the torque- and flux-generating components are made orthogonal so that independent control of torque and flux is possible as in separately excited DC motor [4]. That means flux control is obtained through d-axis stator current and torque control through q-axis stator current [13].

To design an advanced control system with better performance and accuracy, an adaptive control method is one of the extensively employed control methods. Model Reference Adaptive System (MRAS) is a powerful adaptive controller with adaptive mechanism and adjustable controller parameters [14]. MRAS method is adopted with AC drives to estimate the speed of the rotor for PMSM drive, and has advantages such as easy execution and simple formation. Also, it ensures the system stability through adaptive adjustable model and reference plant model [15]. The main disadvantages of AC drives are its torque pulsations, especially at low speeds. These pulsations result in periodic speed oscillations of the drive. This leads to poor performance of the drive, particularly in high-precision applications. In addition, the torque pulsation leads to acoustic noise along with mechanical vibrations [7].

This paper adopts the MRAS scheme with PI controller, which uses the PMSM itself as the reference model to estimate the speed of the motor. To minimize the torque ripples, MRAS is applied for FOC of PMSM using PI controller [16].

The organization of the paper is given as follows: Sect. 2 discusses the modeling of FOC of PMSM. Section 3 explains the FOC of PMSM drive with sensorless control and MRAS based on Popov's Hyper-Stability Criterion. Section 4 discusses the dynamic behavior of PMSM. Finally, the concluding remarks are given in Sect. 5.

2 Field-Oriented Control of Permanent Magnet Synchronous Motor

The aim of FOC is to perform real-time control of torque and the flux components separately to control the rotor mechanical speed and also to regulate phase currents in order to avoid current spikes during transient phases.

The principle idea of FOC is to introduce decoupling between field- and torque-producing components. This makes PMSM behave like a separately excited DC motor. If the magnets are placed inside the rotor, then $L_q > L_d$; otherwise, if the magnets are placed on the surface of a rotor, then $L_q = L_d$. The block diagram of FOC for PMSM is shown in Fig. 1.

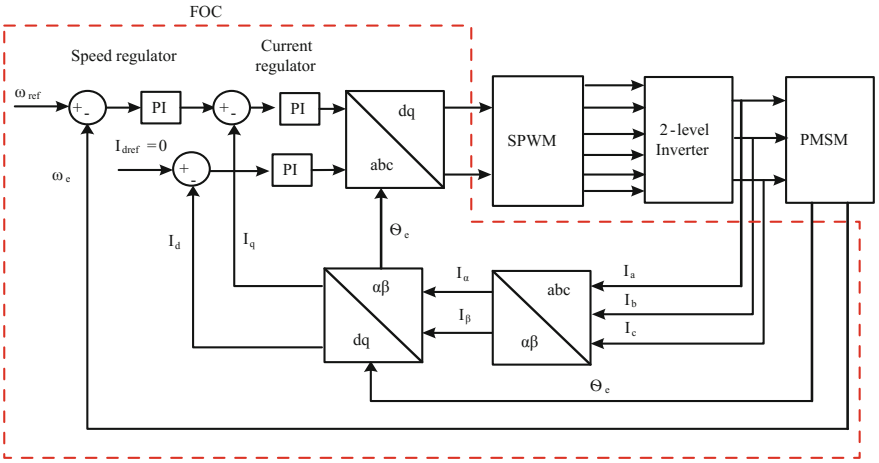

Fig. 1 Block diagram of field-oriented control for PMSM

The modeling of PMSM with rotor reference frame is considered in this work. Modeling equations for PMSM are given in Eqs. (1)–(13). With rotor reference frame, the stator *a*, *b*, *c* voltages are converted into *d*, *q* voltages using Park's transformation. Now, let *S* represent any of the variables (current, voltage, and flux linkage) to be transformed from the *abc* frame to *d-q* frame. The Park's transformation in matrix form is given by:

$$\begin{bmatrix} s_d \\ s_q \\ s_0 \end{bmatrix} = (2/3) \begin{bmatrix} \cos\theta & \cos(\theta-120) & \cos(\theta+120) \\ \sin\theta & \sin(\theta-120) & \sin(\theta+120) \\ 0.5 & 0.5 & 0.5 \end{bmatrix} \begin{bmatrix} V_a \\ V_b \\ V_c \end{bmatrix} \tag{1}$$

From Eq. (1), the following equations are obtained:

$$v_q = -\frac{2}{3}\left[v_a \sin\theta + v_b \sin\left(\theta - \frac{2\pi}{3}\right) + v_c \sin\left(\theta - \frac{4\pi}{3}\right)\right] \tag{2}$$

$$v_d = \frac{2}{3}\left[v_a \cos\theta + v_b \cos\left(\theta - \frac{2\pi}{3}\right) + v_c \cos\left(\theta - \frac{4\pi}{3}\right)\right] \tag{3}$$

Here, S_0 component is called the zero sequence component, and under balanced three-phase system, this component is always zero. Since it is a linear transformation, its inverse transformation exists and is as follows:

$$\begin{bmatrix} s_a \\ s_b \\ s_c \end{bmatrix} = (2/3) \begin{bmatrix} \cos\theta & \sin\theta & 1 \\ \cos(\theta-120) & \sin(\theta-120) & 1 \\ \cos(\theta+120) & \sin(\theta+120) & 1 \end{bmatrix} \begin{bmatrix} V_q \\ V_d \\ V_0 \end{bmatrix} \tag{4}$$

From Eq. (4), the following equations are obtained:

$$i_a = i_d \cos\theta - i_q \sin\theta \tag{5}$$

$$i_b = i_d \cos\left(\theta - \frac{2\pi}{3}\right) - i_q \sin\left(\theta - \frac{2\pi}{3}\right) \tag{6}$$

$$i_c = i_d \cos\left(\theta - \frac{4\pi}{3}\right) - i_q \sin\left(\theta - \frac{4\pi}{3}\right) \tag{7}$$

Now, by applying the transformation of Eqs. (5), (6), and (7) to voltages, flux linkages, and currents, Eqs. (8) and (9) are obtained as follows:

$$V_{qs} = R_s i_{qs} + p\lambda_{qs} + \omega_r \lambda_{ds} \tag{8}$$

$$V_{ds} = R_s i_{ds} + p\lambda_{ds} + \omega_r \lambda_{qs} \tag{9}$$

where

$$\lambda_{ds} = L_{ds} i_{ds} + \lambda_f \tag{10}$$

$$\lambda_{qs} = L_{qs} i_{qs} \tag{11}$$

The produced torque T_e by electrical currents can be represented as follows:

$$T_e = \frac{3}{2}\frac{P}{2}\left[\left(L_{ds} - L_{qs}\right) i_{ds} i_{qs} + \lambda_f i_{qs}\right] \tag{12}$$

The produced torque T_e, which is power divided by mechanical speed, can be represented as follows:

$$J\frac{\mathrm{d}\omega_m}{\mathrm{d}t} + B\omega_m + T_L = T_e \tag{13}$$

3 Implementation of FOC for PMSM Drive with MRAS

The concept of MRAS is that it employs a reference model to generate a reference input. In this work, the adaptive laws are derived from Popov's Hyper-Stability Criterion. FOC of PMSM with MRAS is given in Fig. 2. The sensorless speed control of MRAS-based FOC of PMSM is executed in this paper. Here, speed estimation is obtained from MRAS.

This work proposes a sensorless speed control based on MRAS, which is based on the comparison between outputs of two estimators. This estimated error is used

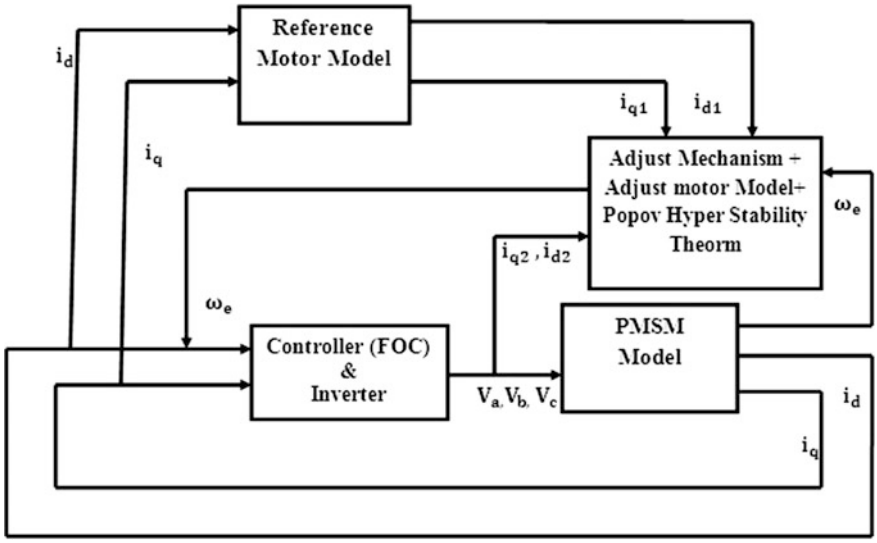

Fig. 2 Block diagram of FOC of PMSM with MRAS

to drive PMSM with a suitable adaptive mechanism to estimate the error speed. In this work, MRAS is based on i_d, i_q of a PMSM since FOC is used as a speed controller. As the control variables in this controller method (FOC) are i_d and i_q, there is a need to represent these variables as state variables. Hence, i_d, i_q is selected as a state variables, and the equations are given by:

$$p\begin{bmatrix} i_d \\ i_q \end{bmatrix} = \begin{bmatrix} -\frac{R_s}{L_d} & \omega_e \frac{L_q}{L_d} \\ -\omega_e \frac{L_d}{L_q} & -\frac{R_s}{L_q} \end{bmatrix} \begin{bmatrix} i_d \\ i_q \end{bmatrix} + \begin{bmatrix} \frac{v_d}{L_d} \\ \frac{v_q}{L_q} - \omega_e \frac{\lambda_f}{L_q} \end{bmatrix} \tag{14}$$

Define i_d^* i_q^* v_d^* v_q^* for FOC of a PMSM are as follows:

$$i_d^* = i_d + \frac{\lambda_f}{L_d}, \quad i_q^* = i_q, \quad v_d^* = v_d + \frac{R_s}{L_d}\lambda_f, \quad v_q^* = v_q \tag{15}$$

So Eq. (14) can be converted into Eq. (16):

$$p\begin{bmatrix} i_d^* \\ i_q^* \end{bmatrix} = \begin{bmatrix} -\frac{R_s}{L_d} & \omega_e \frac{L_q}{L_d} \\ -\omega_e \frac{L_d}{L_q} & -\frac{R_s}{L_q} \end{bmatrix} \begin{bmatrix} i_d^* \\ i_q^* \end{bmatrix} + \begin{bmatrix} \frac{1}{L_d} v_d^* \\ \frac{1}{L_q} v_q^* \end{bmatrix} \tag{16}$$

According to Eq. (16), the state equation of adjustable model of PMSM with speed angle as the adjustable parameter is obtained and it is given in Eq. (17)

$$p\begin{bmatrix}\widehat{i_d^*}\\ \widehat{i_q^*}\end{bmatrix}=\begin{bmatrix}-\frac{R_s}{L_s} & \widehat{\omega_e}\\ -\widehat{\omega_e} & -\frac{R_s}{L_s}\end{bmatrix}\begin{bmatrix}\widehat{i_d^*}\\ \widehat{i_q^*}\end{bmatrix}+\frac{1}{L_s}\begin{bmatrix}\widehat{v_d^*}\\ \widehat{v_q^*}\end{bmatrix} \tag{17}$$

In SPM, $L_d = L_q = L_s$, so the adaptive mechanism can be simplified as follows:

$$\widehat{\omega_e}=\left(K_P+\frac{K_i}{p}\right)\left[i_d\widehat{i_q}-i_q\widehat{i_d}-\frac{\lambda_f}{L_s}(i_q-\widehat{i_q})\right]+\widehat{\omega_e}(0) \tag{18}$$

4 Results and Discussion

The motor is operated with constant torque up to its rated speed and flux weakening mode of operation is adopted beyond its rated speed. The motor model is tested for three different cases:

(i) Dynamic modeling of motor under balanced supply,
(ii) FOC, and
(iii) MRAS along with FOC.

4.1 Analysis of Speed Response

At first, the motor starts on no-load, and after reaching to a rated speed of 1500 rpm, the load of 2 Nm is applied at 0.1 s on motor. In the first case, the dynamic modeling of motor under balanced phase supply is modeled in MATLAB/Simulink and the result of speed is shown in Fig. 3.

In this case there are many transients in reaching steady state at no load. And also there are many transients when load 2 Nm is applied at t = 0.1 s.

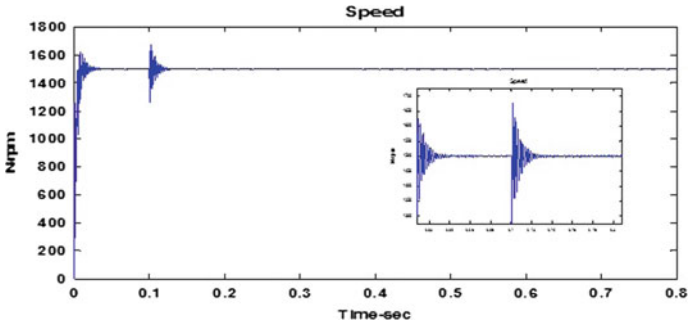

Fig. 3 Speed response with balanced supply

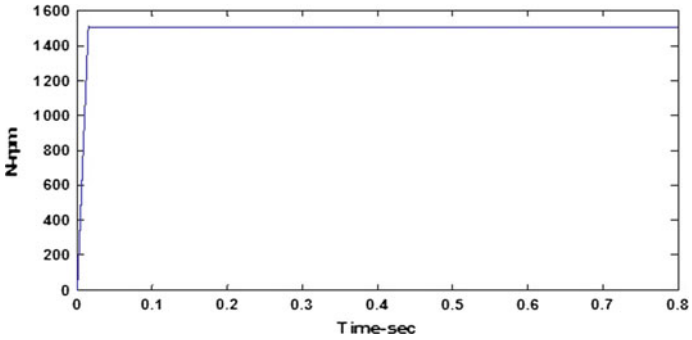

Fig. 4 Speed response with FOC

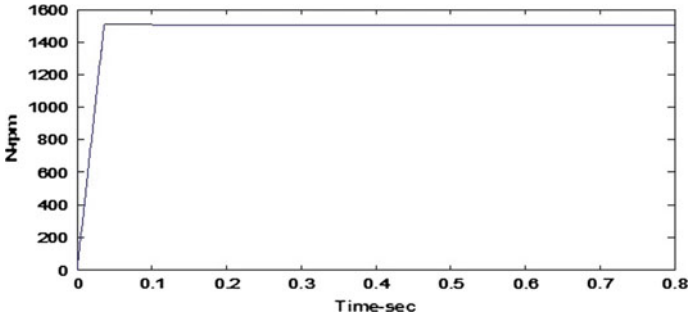

Fig. 5 Speed response with FOC and MRAS

In the second case the motor is tested for the same load conditions with FOC. Here the speed response has no disturbances and it is shown in Fig. 4.

In the third case, there are two sub-models that differ in adaptive mechanism. In adaptive block of sensorless control, two types of controllers are used to minimize the error and to regulate the speed at different rotor positions. At first, the traditional PI controller is used in sensorless control to estimate the speed as feedback. The speed response is plotted in Fig. 5 and it is noticed that the speed response is very smooth as compared to the previous two cases.

4.2 Analysis of Torque Response

In the first case, the load torque of 2 Nm is applied to the motor. The results are shown in Fig. 6. The results show that there are many ripples, harmonics, and disturbances in reaching the steady state.

In the second case, the FOC is modeled and a load torque is applied at 0.1 s. The result is shown in Fig. 7. The average torque ripple is 0.2986. The ripple of this model is less compared to the above case. The electromagnetic torque follows the command torque with less ripples.

In the third case, sensorless control with the adaptive block minimizes the error between actual one and reference one. In this, at first, traditional PI controller is used to minimize the error. The torque result is shown in Fig. 8. The average torque ripple is reduced compared to FOC. The average torque ripple is 0.04522.

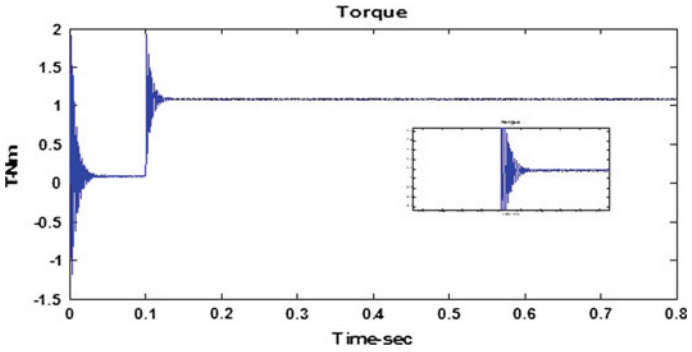

Fig. 6 Torque response with balanced supply

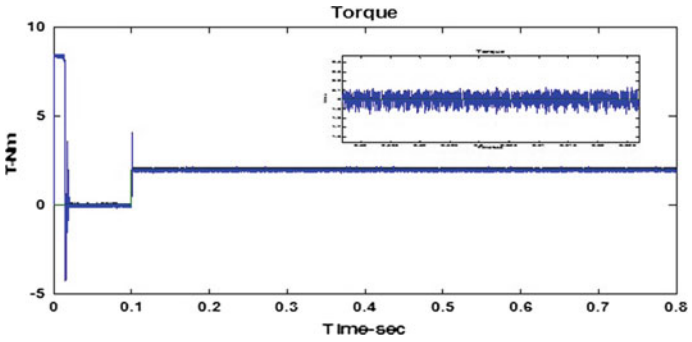

Fig. 7 Torque response with FOC

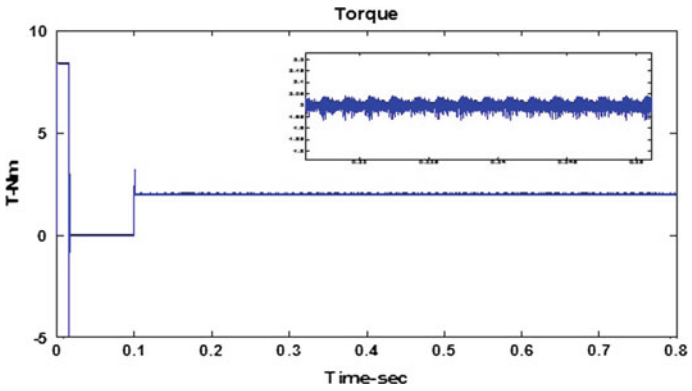

Fig. 8 Torque response with FOC and MRAS

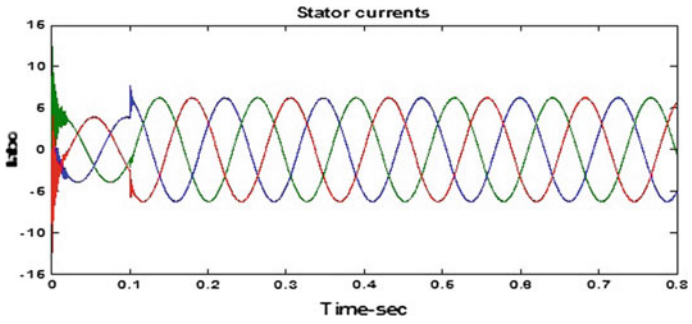

Fig. 9 Stator current response with balanced supply

4.3 Analysis of Three-Phase Stator Currents

The currents are obtained using Park's reverse transformation. It is clear that the current is non-sinusoidal at the starting and becomes sinusoidal when the motor reaches the controller command speed at steady state, as shown in Fig. 9. The steady-state error is reduced in FOC compared to stator currents under balanced supply as shown in Fig. 10.

The stator current error is more reduced with MRAS sensorless control. The MRAS based on stator currents of PMSM is used to estimate the speed at different load conditions. The results are shown in Fig. 11. In MRAS, current ripples are highly reduced and steady-state error is almost reduced to small value.

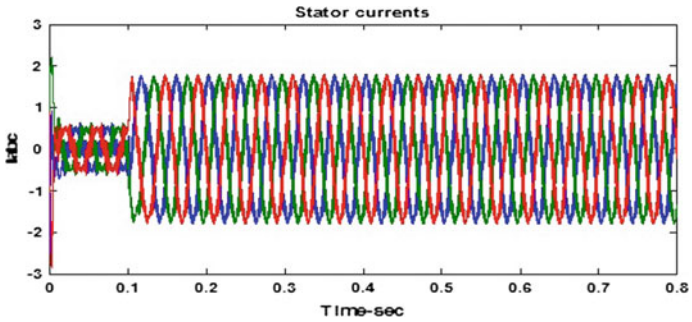

Fig. 10 Stator current response with FOC

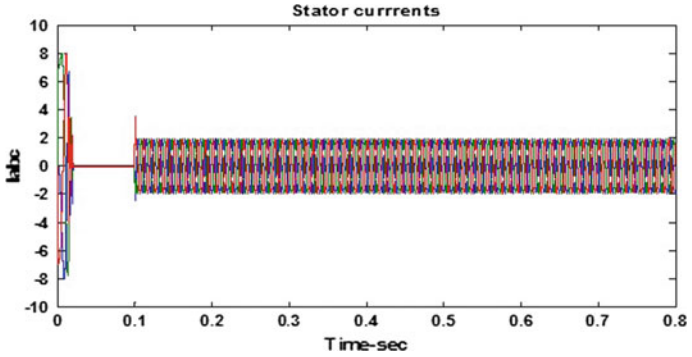

Fig. 11 Stator current response with FOC and MRAS

4.4 Analysis of Stator Flux Response

The total stator flux in three cases is shown in Figs. 12, 13 and 14. The rotor flux is $\lambda = 0.1750$, and the flux is increased with balanced supply but the flux ripples are more in FOC. Whereas in sensorless, the ripples are reduced to small magnitude due to correct estimate of speed and reduction torque harmonics.

4.5 Dynamic Performance of PMSM

The dynamic performances of PMSM with MRAS and without MRAS are shown in Figs. 15, 16, 17 and 18 for two cases:

(i) Dynamic response with constant speed and variable loads applied at different instants;

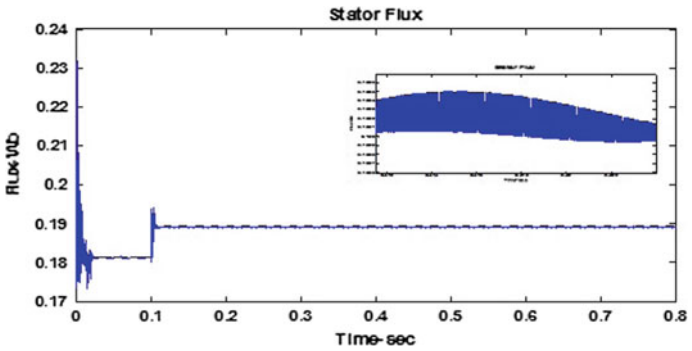

Fig. 12 Flux response with balanced supply

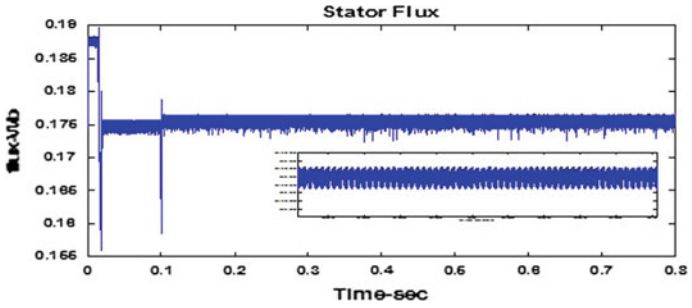

Fig. 13 Flux response with FOC

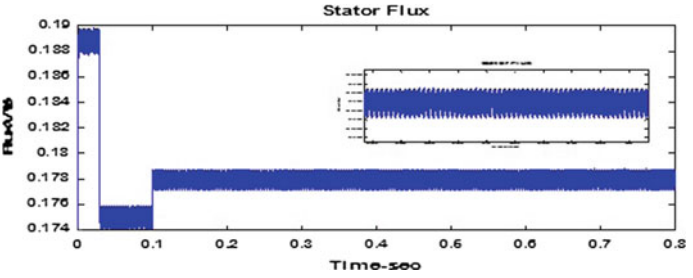

Fig. 14 Flux response with FOC and MRAS

(ii) Dynamic response with constant load and variable speeds applied at different instants.

The speed response is smooth with FOC, whereas torque response, flux response, and quadrature current responses are smooth with MRAS using FOC even though distortion is present; i.e., the magnitude of flux and torque ripples are less with MRAS than without MRAS (Figs. 7, 8, 13 and 14).

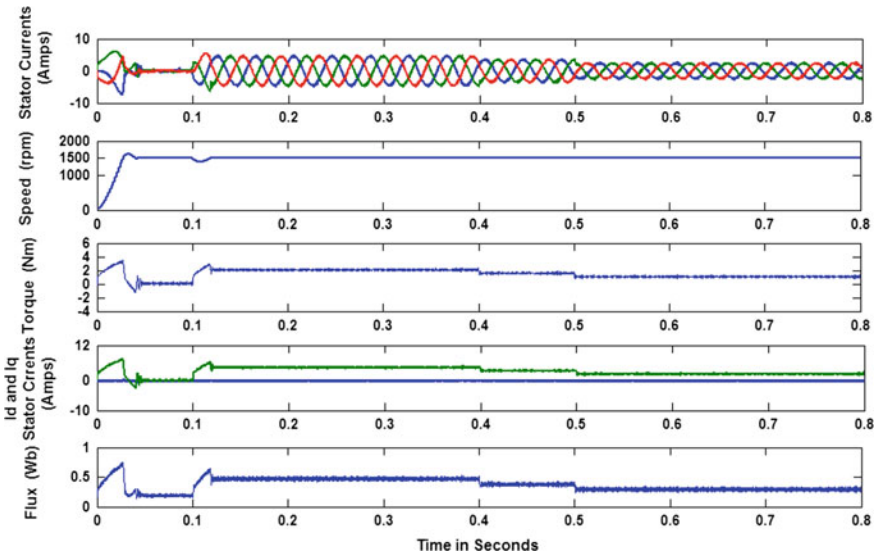

Fig. 15 Dynamic response of stator currents, speed, torque, direct current, quadrature current, and flux with FOC for constant speed

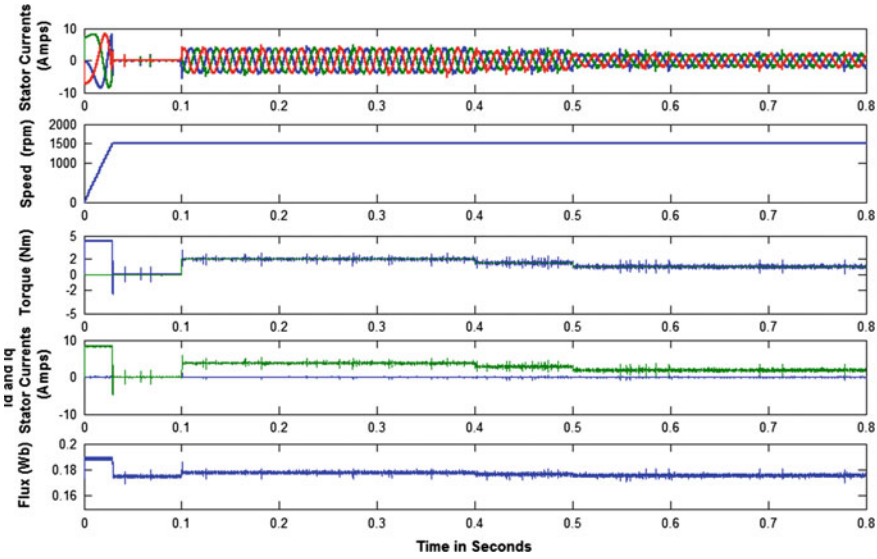

Fig. 16 Dynamic response of stator currents, speed, torque, direct current, quadrature current, and flux with FOC and MRAS for constant speed

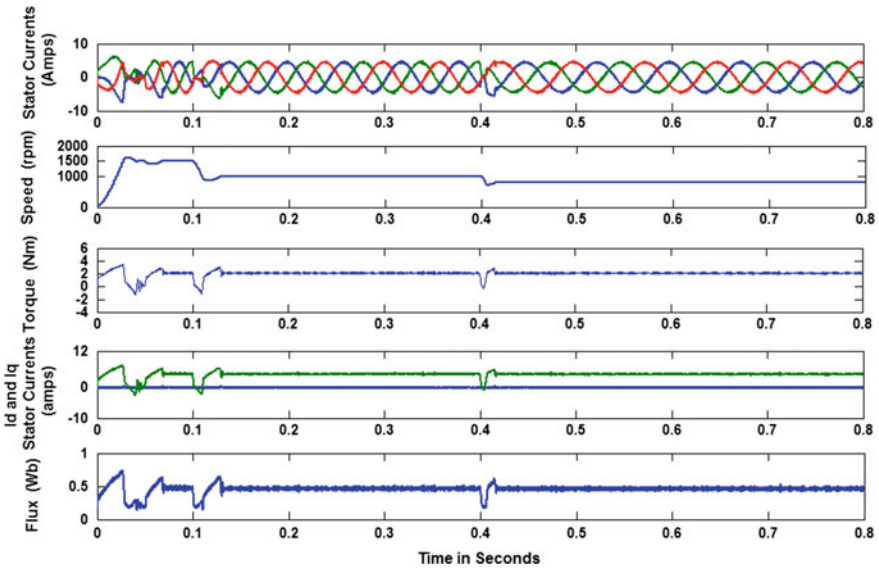

Fig. 17 Dynamic response of stator currents, speed, torque, direct current, quadrature current, and flux with FOC for constant torque

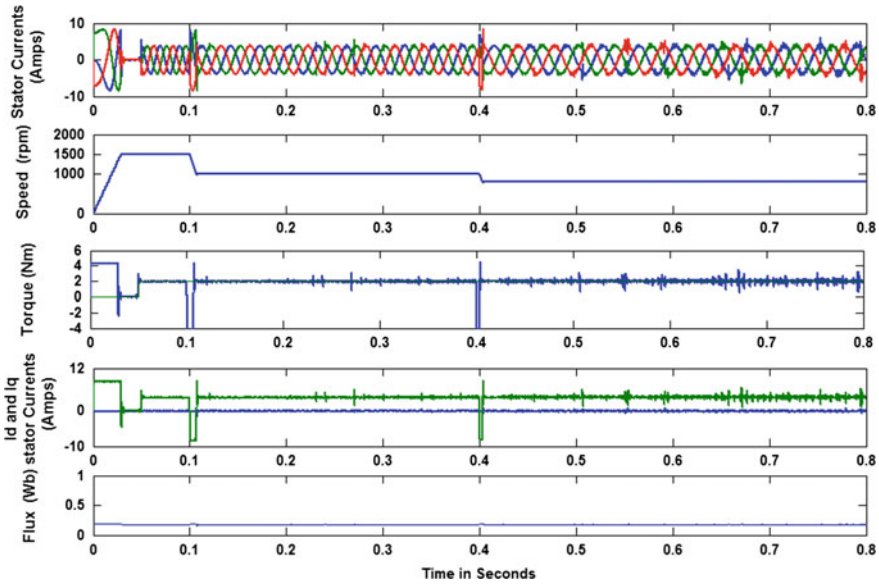

Fig. 18 Dynamic response of stator currents, speed, torque, direct current, quadrature current, and flux with FOC and MRAS for constant torque

5 Conclusion

The output of the adaptation mechanism is the estimated quantity ($\omega_{r,\text{est}}$), which is used for tuning the adjustable model and also for feedback. The stability of such closed-loop estimator is achieved through Popov's hyper-stability criterion. The method is simple and requires less computation. The drive is tested for three cases and also for dynamic conditions. It is found that with MRAS with PI controller, the drive performance is smooth, and torque and flux ripples are less. Further, this work can be extended with fuzzy logic controller along multilevel inverter topology.

References

1. Zhong L, Rahman MF (1997) Analysis of direct torque control in permanent magnet synchronous motor drives. IEEE Trans Power Electron 12(3):528–536
2. Pillay P, Krishnan R (1991) Application characteristics of permanent magnet synchronous and brushless dc motors for servo drives. IEEE Trans Ind Appl 27(5):986–996
3. Gulez K, Adam AA (2007) Adaptive neural network based controller for direct torque control of PMSM with minimum torque ripples. In: SICE Annual Conference, Kagawa University, Japan (2007)
4. Li S (2009) Adaptive speed control for permanent-magnet synchronous motor system with variations of load inertia. IEEE Trans Ind Electron 56(8):3050–3059
5. Swierczynski D, Wojcik P (2008) Direct torque controlled PWM inverter fed PMSM drive for public transport. IEEE 978-1-4244-1703-2/08, pp 716–720
6. Romeral L, Fabrega A (2008) Torque ripple reduction in a PMSM driven by direct torque control. IEEE 978-1-4244-1668-4/08, pp 4745–4751
7. Qian W, Sanjib K (2004) Torque ripple minimization in pm synchronous motors using iterative learning control. IEEE Trans Power Electron 19(2):272–279
8. French C, Acarnley P (1996) Direct torque control of permanent magnet drives. IEEE Trans Ind Appl 32(5):1080–1088
9. Boby K, Kottalil AM, Ananthamoorthy NP (2013) Simulation of PMSM vector control system with fuzzy self-adjusting PID controller using MATLAB. Int J Sci Res Publ 3(3), 1–3 (2013)
10. Zidani F, Said RN (2005) Direct torque control of induction motor with fuzzy minimization torque ripple. J Electr Eng 56(7–8):183–188 FEI STU
11. Merzoug MS, Naceri F (2008) Comparison of field-oriented control and direct torque control for permanent magnet synchronous motor (PMSM). Int J Electr Comput Energ Electron Commun Eng 2(9):1797–1802
12. Boharia AA, Utomoa WM, Harona ZA, Zina NM, Sima SY, Ariffa RM (2013) Speed tracking of indirect field oriented control induction using neural network. ICEEI Procedia Technol 11:141–146
13. Vaez-Zadeh S (2001) Variable flux control of permanent magnet synchronous motor drives for constant torque operation. IEEE Trans Power Electron 16(4):527–534
14. Jain P, Nigam MJ (2013) Design of a model reference adaptive controller using modified mit rule for a second order system. Adv Electr Electr Eng 3(4):477–484
15. Luo YC, Ke ZS, Kuo YP (2014) Sensorless rotor-field oriented controlled induction motor drive with particle swarm optimization algorithm speed controller design strategy, vol 2014, Article ID 861462, . Hindawi Publishing Corporation Mathematical Problems in Engineering, 13 p
16. Yongdong L, Hao, Z (2008) Sensorless control of permanent magnet synchronous motor—a survey. In: IEEE Vehicle Power and Propulsion Conference (VPPC), Harbin, China (2008)

Effectual Particle Swarm Optimization Algorithm for the Solution of Non-convex Economic Load Dispatch Problem

M. Vanitha and Smrithi Radhakrishnan

Abstract The economic load dispatch (ELD) problem is a significant problem in the operation of thermal generating station. It is considered as an optimization problem and is defined for minimized total generation cost, subject to various constraints such as linear constraints and nonlinear constraints in order to meet the power demand. To solve the ELD problem, a new effectual particle swarm optimization (EPSO) algorithm is developed. In this algorithm, the PSO is initialized and the diversity of the PSO is improved by applying the mutation operation of Differential evolution (DE). Enrichment of the population is done by applying the migration operation of Biogeography-based optimization (BBO). Hence, the EPSO algorithm is applied to a non-convex ELD problem to get a better optimal solution. As a result, the total generation cost is much reduced with minimum transmission loss compared to other methods. In order to prove its ability, the EPSO algorithm is applied to a six-unit system.

Keywords Economic dispatch · Particle swam optimization
Biogeography-based optimization · Differential evolution

1 Introduction

In any part of world, the electrical power has indispensable role to make human in comfort. In order to carry on this human comfort more electrical power is to be generated with least cost. The electrical power generated must meet the power

M. Vanitha
Department of Electrical Power, Al Musanna College of Technology, Muscat, Oman

Smrithi Radhakrishnan (✉)
Department of Electrical and Electronics Engineering, Karpagam College of Engineering, Coimbatore, India
e-mail: simi5690@gmail.com

M.C. Bhuvaneswari and J. Saxena (eds.), *Intelligent and Efficient Electrical Systems*, Lecture Notes in Electrical Engineering 446,
https://doi.org/10.1007/978-981-10-4852-4_13

demanded by the society. So, the problem of scheduling of generators arises in order to dispatch the load economically in generating stations having a number of generators. The economic load dispatch (ELD) problem is the most important optimization problem in scheduling the generation among thermal generating units in power system. The ELD problem is classified in two different ways, as convex ELD problem and non-convex ELD problem. The convex ELD problem is modeled by considering the objective function as minimizing the generator cost functions with linear constraints. The non-convex ELD problem considers the nonlinear constraints in addition to the linear constraints while minimizing the cost function. The linear constraints, that is, the generation capacity and power balance, lead the ELD problem as approximate, simplified problem, and the characteristics curve is assumed to be piecewise linear. A more precise and accurate problem is modeled by having the nonlinear constraints such as ramp rate limits, valve point loadings, and prohibited operating zones. In traditional optimization techniques, the ELD problem is considered as convex ELD problem. Hence, to solve non-convex ELD problem, many non-traditional algorithms have been developed; however, they have its own disadvantages [1–5]. Thus, a new hybrid optimization algorithm, effectual particle swarm optimization (EPSO) algorithm, is developed. It hybridizes the mutation operation of differential evolution (DE) and migration operation of biogeography-based optimization (BBO) with particle swarm optimization (PSO) in order to improve its searching ability [6, 7]. To demonstrate the capability of EPSO, it is tested on a six-unit system. As a result, it gives best feasible solution compared with other non-traditional algorithms.

2 Problem

2.1 Objective Function

The ELD problem is having an objective function so as to minimize the total generation cost F_T, while fulfilling the various constraints, when supplying the required load demand of a power system. The total generation cost is the arithmetic sum of the individual generator cost function [8].

The objective function is:

$$\min F_T = \min\left(\sum_{i=1}^{n} F_i(P_{Gi})\right) \tag{1}$$

where P_{Gi} is the output power generated by the ith generator; $F_i(P_{Gi})$ is the generation cost function of ith generator; and n is the number of generators.

To simplify the optimization problem, generators are normally modeled by smooth quadratic function as follows:

$$F_T = \sum_{i=1}^{n} A_i P_{\mathrm{G}i}^2 + B_i P_{\mathrm{G}i} + C_i \tag{2}$$

where A_i, B_i, and C_i are the cost coefficients of the ith generator.

2.2 Linear Constraints

The incremental fuel cost curves of the generating units are approximated and assumed to be piecewise linear, as well as increasing monotonically by having linear constraints with the objective function [8, 9].

2.2.1 Generation Capacity Constraint

This is an inequality constraint for each generator. For normal system operations, real power output of each generator is within its lower and upper limits as follows:

$$P_{\mathrm{G}i}^{\min} \leq P_{\mathrm{G}i} \leq P_{\mathrm{G}i}^{\max} \tag{3}$$

where $P_{\mathrm{G}i}^{\min}$ and $P_{\mathrm{G}i}^{\max}$ are the lower and upper limit of the power generated by ith generator.

2.2.2 Power Balance Constraint

This constraint is an equality constraint, in which the equilibrium is met when the total power generation equals the total demand, P_{D}, and the real power loss in transmission lines, P_{L}. This relation can be expressed as follows:

$$\sum_{i=1}^{n} P_{\mathrm{G}i} = P_{\mathrm{D}} + P_{\mathrm{L}} \tag{4}$$

Over long distances, the transmission loss is taken into account as a function of generator output power through Kron's loss coefficients.

The Kron's loss formula can be expressed as follows:

$$P_{\mathrm{L}} = \sum_{i=1}^{n} \sum_{j=1}^{n} P_{\mathrm{G}i} B_{ij} P_{\mathrm{G}j} + \sum_{i=1}^{n} B_{oi} P_{\mathrm{G}i} + B_{oo} \tag{5}$$

where B_{ij}, B_{oi}, and B_{oo} are the transmission network power loss B-coefficients, which are assumed to be constant.

2.3 Nonlinear Constraints

The actual characteristics of generators are drawn by considering the nonlinear constraints. These characteristics exhibit higher-order nonlinearity and discontinuities. Thus, the ELD problem becomes a complex non-convex optimization problem [9, 10].

2.3.1 Generator Ramp Rate Limits

The online generators operating range is always restricted by their ramp rate limits, and the inequality constraints due to ramp rate limits can be written as follows:

As generation increases,

$$P_{\mathrm{G}i} - P_{\mathrm{G}i0} \leq \mathrm{UR}_i \tag{6}$$

As generation decreases,

$$P_{\mathrm{G}i0} - P_{\mathrm{G}i} \leq \mathrm{DR}_i \tag{7}$$

$$\max(P_{\mathrm{G}i}^{\min}, P_{\mathrm{G}i0} - \mathrm{DR}_i) \leq P_{\mathrm{G}i} \leq \min(P_{\mathrm{G}i}^{\max}, P_{\mathrm{G}i0} + \mathrm{UR}_i) \tag{8}$$

where UR_i is the up-ramp limit of the generator; DR_i is the down-ramp limit of the generator; $P_{\mathrm{G}i}$ is the present generation value at time t; $P_{\mathrm{G}i0}$ is the previous generation value at time $t - 1$.

2.3.2 Prohibited Operating Zones

The prohibited operating zones are present in the cost curve due to steam valve operations or vibration in the shaft bearings. The prohibited zones create a gap on the cost curves and cause discontinuity on the cost curve. It is very difficult to determine the exact shape of the cost curve in the prohibited zone by actual testing or from operating records. Normally, operation is avoided in such regions, and this concept can be considered in the ELD problem in the form of constraints as given:

$$P_{\mathrm{G}i} \in \begin{cases} P_{\mathrm{G}i}^{\min} \leq P_{\mathrm{G}i} \leq P_{\mathrm{G}i,1}^{l} \\ P_{\mathrm{G}i,j-1}^{u} \leq P_{\mathrm{G}i} \leq P_{\mathrm{G}i,j}^{l}; \quad j = 2, 3, \ldots, n_i \\ P_{\mathrm{G}i,n_i}^{u} \leq P_{\mathrm{G}i} \leq P_{\mathrm{G}i}^{\max}; \quad i = 1,\ 2, \ldots, n_{\mathrm{pz}} \end{cases} \tag{9}$$

where j represents the prohibited operating zone of unit i. $P_{\mathrm{G}i,j-1}^{u}$ is the upper limit of $(j-1)$th prohibited operating zone of unit i, and $P_{\mathrm{G}i,j}^{l}$ is the lower limit of jth prohibited operating zone of unit i. The total number of prohibited operating zone of unit i is n_i, the number of units which have prohibited operating zones, n_{pz}.

3 Proposed Method

One of the most popular optimization algorithms is particle swarm optimization algorithm. The convergence is very fast in PSO system, but it does not guarantee the convergence to local minima and it always depends on initial point and parameters [11, 12]. To overcome this drawback, a new hybrid PSO known as effectual particle swarm optimization (EPSO) algorithm is developed. In this algorithm, the PSO is initialized and the diversity of the PSO is improved by applying the mutation operation of DE. Enrichment of the population is done by applying the migration operation of BBO.

3.1 Effectual Particle Swarm Optimization (EPSO) Algorithm

The EPSO proceeds with PSO by initializing the individuals or particles randomly in a population pool. The velocity and the position of each particle are also initialized randomly. The velocity must be in its maximum and minimum range of 0.5 to −0.5. The fitness function of each particle in a population is calculated. Every particle keeps track of its best value achieved so far and memorizes the best solution with its position called as *Pbest*, the personal best. The obtained *Pbests* of all particles are compared, and the best among *Pbests* are said to be *Gbest*, the global best. Using *Pbests* and *Gbest*, the velocity is updated by Eq. (10). The constants c_1, c_2, r_1, r_2, $\omega_{\min}$, and $\omega_{\max}$ are chosen by the user within the limits specified for them while executing the program. Thus, the updated velocity is to be within the boundary that is between zero and one. The mutation operation of DE is otherwise activated to calculate the new velocity in order to improve the diversity of the population. Khamsawang [13] suggests the activation of mutation operation in PSO. The new velocity of the particles $V_i^{(t+1)}$ is calculated with the help of Eq. (13).

This new velocity should be less than the crossover factor (CR) value chosen by the user. If the condition is not satisfied, the migration operation of BBO is then proceeded to modify the population with the help of immigration rate (λ) and emigration rate (μ) calculated for each individual X_i. The positions of the particles are updated by means of Eq. (12). For these updated positions, the fitness function is once again calculated and the *Pbests* and *Gbest* are then obtained. If the constant value of *Gbest* is attained, that value is the optimum solution.

$$V_i^{(t+1)} = \omega \times V_i^{(t)} + c_1 \times r_1 \times (Pbest_i - X_i^{(t)}) + c_2 \times r_2 \times (Gbest - X_i^{(t)}) \quad (10)$$

where

$V_i^{(t)}$	velocity of the ith particle at iteration t,
t	pointer of iterations (generations),
ω	inertia weight factor that is used to control the impact of the previous velocity over the new velocity,
c_1, c_2	acceleration coefficients, where c_1 and c_2 are positive constants called as coefficient of self-recognition component and coefficient of social component,
r_1, r_2	random numbers equally spread within the range (0, 2),
$X_i^{(t)}$	position of the particle i at iteration t,
$Pbest_i$	best position of particle i until iteration t,
$Gbest$	best position of the group until iteration t,

The predefined values of the acceleration coefficient c_1, c_2 and inertia weight ω are substituted in Eq. (10), and random numbers r_1, r_2 are uniformly generated within the limit (0, 2) in order to calculate the new velocity.

The inertia weight ω is calculated by Eq. (11):

$$\omega = \omega_{\max} - \frac{\omega_{\max} - \omega_{\min}}{\text{Iter}_{\max}} \times \text{Iter} \tag{11}$$

where

$\omega_{\max}$	initial weight
$\omega_{\min}$	final weight
$\text{Iter}_{\max}$	maximum iteration number
Iter	current iteration number

Hence, a new velocity which is used to perform a shift in the current searching point in the direction of *Pbest* and *Gbest* is calculated. Each particle tries to move from the current position to the new one by using the modified velocity, which is given by Eq. (12):

$$X_i^{(t+1)} = X_i^{(t)} + V_i^{(t+1)} \tag{12}$$

$$V_i^{(t+1)} = F \times \left(\left(x_k^{(t)} - x_i^{(t)} \right) - \left(x_q^{(t)} - x_i^{(t)} \right) \right) \tag{13}$$

where F is known as scaling factor or mutation factor within the range (0, 1). Random vectors selected from the population are $x_k^{(t)}$ and $x_q^{(t)}$ at iteration t and $k \neq q \neq i$. New position of the particle i at iteration t is $x_i^{(t)}$.

3.2 EPSO Algorithm Applied to ELD Problem

Step 1: The individuals of the population are randomly initialized with its position. The velocities of the different particles are also randomly generated keeping the velocity within the maximum and minimum values [0.5 to −0.5]. These initial individuals must be feasible candidate solutions that satisfy the practical operation constraints (both the linear and nonlinear constraints) of the given problem. Choose the required parameters, maximum number of iteration n and $t = 1$.

Step 2: The fitness function, that is, cost function of each individual, is calculated in the population using the evaluation function F_T by considering both the nonlinear and linear constraints. The present value is set as the *Pbest* value.

Step 3: Each *Pbest* value is compared with the other *Pbest* values in the population. The best evaluation value among *Pbests* is denoted as *Gbest*.

Step 4: The member velocity V of each individual in the population is updated according to the velocity update equation.

Step 5: The member velocity, V, of each individual in the population is checked. If the calculated velocity is out of boundary (rand(0, 1)), a mutation operation of DE is activated and the velocity of this particle is to be recalculated by using the mutation operation equation.
Else, go to step 8, without activating DE mutation operation.

Step 6: If the calculated velocity using the mutation operation of DE is less than CR value, then the immigration rate λ and the emigration rate μ for each individual X_i are to be calculated.
Else, go to step 8.

Step 7: The population is to be modified with migration operation and proceed step 2.

Step 8: The position of each individual is modified according to the position update equation.
New position = Old position + Updated velocity

Step 9: Recalculate the cost function F_T for this new position. Choose *Pbest* of each individual achieved so far. The best evaluation value among *Pbests* is denoted as *Gbest*.

Step 10: If either the constant value of *Gbest*, that is, optimum solution, is achieved or the maximum number of iteration is reached, that is, $t = n$, then go to step 11.
Else, increment $t = t + 1$, go to step 4.

Step 11: Terminate the process.

4 Result

The proposed approach is tested for its competence to solve the ELD problem. This section presents the simulation results of the proposed approach. For the test case, the maximum number of iteration is considered as 1000, population size as 60, CR as 1, step size of integration as 1, immigration and emigration rates as 1, and mutation probability as 1.

A six-unit system is taken with transmission loss, ramp rate limits, and prohibited operating zones. A load demand of 1263 MW is considered here. Table 1 shows the individual units generation, total power output, total generation cost, and transmission loss obtained by EPSO method. Table 2 shows the comparison of generation cost among different methods after 50 trial runs. Figure 1 shows the characteristic graph between the iteration and total cost of generation.

The parameters to attain the best solution while doing the simulation are as follows: c_1 and c_2 are assumed as 1.3 and 1.5; ω_{max} and ω_{min} are 0.4 and 0.1, respectively; the value of F is 0.8; habitat modification probability is 0.05.

Table 1 Best power dispatch obtained by proposed EPSO method for a six-unit system

Unit output	EPSO	Lambda iteration [14]
P1 (MW)	447.3991	447.122
P2 (MW)	173.4998	173.22
P3 (MW)	263.1557	263.962
P4 (MW)	139.7969	139.093
P5 (MW)	165.2179	165.617
P6 (MW)	86.3289	86.6583
Total power output (MW)	1275.3988	
Total generation cost ($/h)	15442.6720	15446.1
Power loss (MW)	12.3988	12.4204

Table 2 Comparison of generation cost obtained after 50 trials for a six-unit system

Methods	Generation cost ($/h)		
	Maximum	Minimum	Average
EPSO	15443.8765	15442.6720	15442.9935

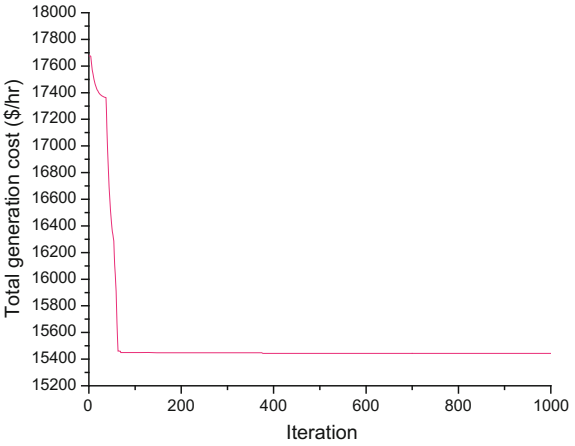

Fig. 1 Convergence characteristic of proposed EPSO method for a six-unit system

5 Conclusion

A promising optimization technique EPSO is proposed in this paper to solve the non-convex ELD problems. The proposed method shows the potentiality to find the optimum solution so as to minimize the generation cost and transmission loss. The PSO is used here with the mutation operation of DE to improve the diversity of the population and the migration operation of BBO to get a better population. This method is applied to 6 units test case to assess its performance over other optimization techniques and is found to be the best one. To conclude, the EPSO is the prominent approach in order to produce minimum generation cost and minimum transmission loss compared with the other techniques.

References

1. Balamurugan R, Subramanian S (2008) Differential evolution-based dynamic economic dispatch of generating units with valve-point effects. Electr Power Compon Syst 36(8):828–843
2. Bhattacharya A, Chattopadhyay PK (2010) Biogeography-based optimization for different economic load dispatch problems. IEEE Trans Power Syst 25(2):1064–1077
3. Deb K (2000) Optimization for engineering design: algorithms and examples. Prentice Hall, India Fourth Printing
4. Selvakumar AI, Thanushkodi K (2007) A new particle swarm optimization solution to nonconvex economic dispatch problems. IEEE Trans Power Syst 22(1):42–51
5. Simon D (2008) Biogeography-based optimization. IEEE Trans Evol Comput 12(6):702–713
6. Bhattacharya A, Chattopadhyay PK (2010) Hybrid differential evolution with biogeography based optimization for solution of economic load dispatch. IEEE Trans Power Syst 25 (4):1955–1964

7. Das S, Abraham A, Konar A (2008) Particle swarm optimization and differential evolution algorithms: technical analysis, applications and hybridization perspectives. J Comput Inf Sci 38:1–38
8. Wood AJ, Wollenberg BF (2007) Power generation, operation and control, 2nd edn. Wiley, New York
9. Neto AP, Unsihuay C, Saavedra OR (2005) Efficient evolutionary strategy optimization procedure to solve the nonconvex economic dispatch problem with generator constraints. IEE Proc Gener Transm Distrib 152(5):653–660
10. Park JB, Jeong YW, Kim HH, Shin JR (2006) An improved particle swarm optimization for economic dispatch with valve-point effect. Int J Innov Energy Syst Power 1(1):1–7
11. Kennedy J, Eberhart RC (1995) Particle swarm optimization. In: Proceedings of IEEE international conference on neural networks, vol 4, pp 1942–1948 (1995)
12. Gaing ZL (2003) Particle swarm optimization to solving the economic dispatch considering the generator constraints. IEEE Trans Power Syst 18(3):1187–1195
13. Khamsawang S, Jiriwibhakorn S (2009) Solving the economic dispatch problem using novel particle swarm optimization. Int J Electr Electron Eng 3(1):41–46
14. Dewangan SK, Jain A, Huddar AP (2015) A traditional approach to solve economic load dispatch problem considering the generator constraints. IOSR J Electr Electron Eng (IOSR-JEEE) 10(2) Ver. III, 27–32

Differential Evolution with Parameter Adaptation Strategy to Economic Dispatch Incorporating Wind

G.R. Venkatakrishnan, J. Mahadevan and R. Rengaraj

Abstract In this paper, a simple DE algorithm with parameter adaptation strategy (DE-PAS) for the control parameters is proposed to solve the economic dispatch problem incorporating wind power. In a normal differential evolution (DE) algorithm, three control parameters, i.e., population size N, scaling factor or mutation rate F and crossover rate CR are kept fixed throughout the algorithm. However, it is a difficult task to properly set these control parameters in DE for the chosen problem. Therefore, a suitable adapting scheme for these parameters is selected and incorporated in the proposed DE-PAS algorithm. To validate the effectiveness of the proposed DE-PAS algorithm, standard and well-known algorithms are implemented for the chosen economic dispatch problem and compared. The simulation results prove that the proposed algorithm outperforms the other well-known algorithms in terms of accuracy, computational time and robustness of the solution.

Keywords Differential evolution with parameter adaptation strategy (DE-PAS) Control parameters · Self-adapting scheme · Economic dispatch Wind power

1 Introduction

The fundamental objective of classical economic dispatch (ED) problem is to determine the optimal active power output of available generating units by minimizing the total operating cost by satisfying all the operational constraints of the

G.R. Venkatakrishnan (✉) · R. Rengaraj
Department of Electrical and Electronics Engineering, SSN College of Engineering, Chennai, India
e-mail: venkatakrishnangr@ssn.edu.in

R. Rengaraj
e-mail: rengarajr@ssn.edu.in

J. Mahadevan
Department of Electrical and Electronics Engineering, Dhanalakshmi Srinivasan College of Engineering and Technology, Chennai, India

M.C. Bhuvaneswari and J. Saxena (eds.), *Intelligent and Efficient Electrical Systems*, Lecture Notes in Electrical Engineering 446,
https://doi.org/10.1007/978-981-10-4852-4_14

power system. Prior to the widespread use of renewable energy sources, the ED problem involves only conventional thermal energy depletable resources such as fossil fuels. Hence, a need for alternatives to thermal energy power generation becomes apparent [1].

Penetration of renewable power generation has increased in existing power systems with the increase in energy crisis and intemperate increment of power consumption. Also, exploitation of renewable energy is one of the most important proposals in promoting the smart grid program as these sources are viewed as green and clean as they are non-depletable and non-polluting sources. In addition, these sources are considered to be environmentally friendlier as it creates minimal environmental and health impacts when compared to conventional sources [2, 3].

In this paper, the wind-powered generators are incorporated into the classical ED problem. But this problem faces many complications due to the stochastic availability of the wind power. These nonlinearities and discontinuities represent the ED problems as a non-smooth or non-convex optimization problem which makes difficult for the traditional methods to obtain the global optimum [4]. Therefore, in power system research, development of fast, reliable and efficient algorithm is a much needed one. More than considerable amount of work has been done by researchers in developing an efficient algorithm in solve the ED problem with these nonlinearities [5].

Differential evolution (DE) algorithm which is one of the most powerful, reliable, stochastic, versatile population-based heuristic real parameter optimization techniques is first proposed by Storn and Price [6]. The performance of DE algorithm depends on the parameters population size N, mutation rate or scale factor F and crossover rate or constant CR like other evolutionary algorithms to both empirical studies and theoretical analyses. However, there is no suitable method or technique for setting these parameters for a particular problem [7]. In this paper, a new differential evolution with parameter adaptation strategy (DE-PAS) is proposed to solve the ED problem with nonlinearities. As perceived from the literatures over the past decade, many claims and counterclaims have been reported regarding the choice of suitable values of the parameters or regarding the tuning and adaption strategies of these parameters. Proper choice of value or tuning strategy of the parameters is necessary as the objective function of a system is sensitive to them [8]. In [9–15] different techniques in determining the optimal set of control parameters automatically is described. In recent trends, the self-adaptive strategies as described in [9, 10, 16] are used in the optimization algorithm to tune their parameters. The successful mutation rate and crossover rate adaptation strategy along with the optimal population size are implemented in the proposed DE-PAS algorithm. A comparative study of the proposed DE-PAS algorithm with the other well-known algorithms is made in this paper.

The rest of the paper is organized as follows: Sect. 2 describes the formulation of ED problem with wind. The proposed DE-PAS algorithm is described in Sect. 3. Section 4 describes the implementation of DE-PAS algorithm to the chosen problem. Simulation results obtained for various known algorithms are discussed in Sect. 5, and conclusion is drawn in Sect. 6.

2 Economic Dispatch Incorporating Wind

2.1 Objective Function

The constrained optimization ED problem with wind power is formulated as

$$\text{Minimize} \quad F_{\mathrm{T}} = \sum_{i=1}^{N} F_i(P_i) + \sum_{j=1}^{M} F_j\left(P_{\mathrm{W}j}\right) \tag{1}$$

where F_{T} is the total cost function of all the generators present in the system ($/h), and N and M are the total number of thermal and wind generator present in the system, respectively, $F_i(P_i)$ and $F_i\left(P_{\mathrm{W}j}\right)$ are the cost function in $/h of the ith thermal generator and jth wind generator, respectively, and P_i and P_j are the power generated in MW by the ith thermal generator and jth wind generator, respectively.

In general, the smooth cost function of ith generator $F_i(P_i)$ is expressed in a quadratic polynomial as

$$F_i(P_i) = a_i P_i^2 + b_i P_i + c_i + \left|e_i \times \sin\left(f_i \times \left(P_{i,\min} - P_i\right)\right)\right| \tag{2}$$

where a_i, b_i, c_i, e_i and f_i are the cost coefficients of ith generator.

A linear cost function for the jth wind-generated power $F\left(P_{\mathrm{W}j}\right)$ is given by

$$F\left(P_{\mathrm{W}j}\right) = d_j P_{\mathrm{W}j} \tag{3}$$

where d_j is the direct cost coefficient of the jth wind-powered generator.

The different practical implications to which the above minimization problem is subjected are power balance or demand constraint and generator output limits which are discussed below.

2.2 Real Power Balance or Demand Constraint

The sum of individual power generated from each unit existing in the system must be equal to the sum of total power demand and transmission loss of the system which is represented as:

$$\sum_{i=1}^{N} P_i + \sum_{j=1}^{M} P_{\mathrm{W}j} = P_{\mathrm{D}} \tag{4}$$

where P_{D} is the total power demand of the system in MW, P_i is the power generated from the ith thermal generator in MW, and $P_{\mathrm{W}j}$ is the power generated from the jth wind-powered generator in MW.

2.3 Real Power Generating Limits

The power generated from each thermal generator unit P_i should be within its permissible limits which is represented as

$$P_{i,\min} \leq P_i \leq P_{i,\max} \tag{5}$$

where $P_{i,\min}$ and $P_{i,\max}$ are the minimum and maximum limits of the thermal generator i in MW.

The power generated from each wind generator unit P_{Wj} should be within its permissible limits which is represented as

$$P_{Wj,\min} \leq P_{Wj} \leq P_{Wj,\max} \tag{6}$$

where $P_{Wj,\min}$ and $P_{Wj,\max}$ are the minimum and maximum limits of the wind-powered generator j in MW.

3 Proposed DE-PAS Algorithm

The differential evolution (DE) algorithm which has been widely used in solving optimization problems in various engineering fields was first proposed by Storn and Price in 1995. The success of DE algorithm over a decade is due to its ability to handle nonlinear and multimodal real-time problems. Similar to the operations in DE, the proposed DE-PAS algorithm has four main phases of operations which are described as follows [6, 17–19].

3.1 Initialization of Parameter Vectors

The initial population vector in DE-PAS algorithm is represented as $X_{i,G} = \left(x^1_{i,G}, x^2_{i,G}, \ldots, x^D_{i,G}\right)$, where $i = 1, 2, \ldots, N$ and G represents the current generation is initialized using

$$x^j_{i,G} = x^j_{\min} + \text{rand}\left(x^j_{\max} - x^j_{\min}\right), \quad j = 1, 2, \ldots, D, \;\; i = 1, 2, \ldots, N, \tag{7}$$

where rand is a uniformly distributed random number lying between 0 and 1, D is the number of decision variable, $x^j_{\min}$ and $x^j_{\max}$ are the minimum and maximum value of the decision variable j, N is the population size, G represents the current generation and $x^j_{i,G}$ is the value of jth decision variable in population i.

3.2 Mutation

The different mutation strategies discussed in this paper are [17]

$$\text{DE/best/1: } V_{i,\mathrm{G}} = X_{\text{best,G}} + F\left(X_{r_1,\mathrm{G}} - X_{r_2,\mathrm{G}}\right) \tag{8}$$

$$\text{DE/rand/1: } V_{i,\mathrm{G}} = X_{r_1,\mathrm{G}} + F\left(X_{r_2,\mathrm{G}} - X_{r_3,\mathrm{G}}\right) \tag{9}$$

where $r_{1,\mathrm{G}}, r_{2,\mathrm{G}}$ and $r_{3,\mathrm{G}}$ are mutually exclusive integers which are randomly generated within [1, N] which also differs from index i such that $r_{1,\mathrm{G}} \neq r_{2,\mathrm{G}} \neq r_{3,\mathrm{G}} \neq i$. The scaling factor or mutation factor F is a positive control parameter for scaling the difference vector is in the range $0 < F \leq 1.2$. $X_{\text{best,G}}$ is the best individual target vector with the best fitness in the population of the current generation G and the mutant vector $V_{i,\mathrm{G}} = \left(v^1_{i,\mathrm{G}}, v^2_{i,\mathrm{G}}, \ldots, v^{\mathrm{D}}_{i,\mathrm{G}}\right)$ where $v^j_{i,\mathrm{G}}$ is the mutant vector of decision variable j in vector i.

3.3 Crossover

In DE, the trial vector $U_{i,\mathrm{G}}$ where $U_{i,\mathrm{G}} = \left[u^1_{i,\mathrm{G}}, u^2_{i,\mathrm{G}}, \ldots, u^{\mathrm{D}}_{i,\mathrm{G}}\right]$, $u^j_{i,\mathrm{G}}$ is the trial vector of decision variable j in the vector i is produced from mutant vector and parameter vector using the following scheme [19]:

$$u^j_{i,\mathrm{G}} = \begin{cases} v^j_{i,\mathrm{G}} & \text{if} \quad \text{rand}^j_i \leq \mathrm{CR} \ \text{ or } \ j = j_{\text{rand}} \\ x^j_{i,\mathrm{G}} & \text{otherwise} \end{cases} \tag{10}$$

where $i = 1, 2, \ldots, N$, $j = 1, 2, \ldots, D$, CR is the crossover rate which is a user-specified constant within the range of 0–1 which controls the fraction of variables to be copied from the mutant vector, rand^j_i is the randomly generated number between 0 and 1, and j_{rand} is the randomly chosen integer in the range $[1, D]$ which ensures that trial vector $U_{i,\mathrm{G}}$ differs from its target or parameter vector.

3.4 Selection

The one-to-one greedy selection scheme which is applied in DE algorithm is given by Storn and Price [18]

$$X_{i,G+1} = \begin{cases} U_{i,G} & \text{if } f(U_{i,G}) \leq f(X_{i,G}) \\ X_{i,G} & \text{otherwise} \end{cases} \tag{11}$$

where $f(U_{i,G})$ and $f(X_{i,G})$ are the fitness values of $U_{i,G}$ and $X_{i,G}$.

3.5 Terminating Condition

The terminating condition which is used in this paper for a DE-PAS algorithm is fixing a certain number of generations G_{max} as 100. It is to be noted that all the vectors, parameter, mutant and trial vector, must satisfy the constraints.

The proposed DE-PAS algorithm includes the adaptation techniques for mutation rate F and crossover rate CR. Self-adaptation technique for these parameters is necessary since the former regulates the step size taken during mutation and latter regulates the search variables inherited by offspring from parent during recombination process. The trial-and-error method of choosing F and CR leads to huge computational cost and larger computational time [17, 20]. Two modifications were introduced in DE algorithm to overcome these limitations to enhance the searching capability and to increase the convergence speed of the algorithm. The details of the two modification introduced in the proposed DE-PAS algorithm to enhance the searching capability and to increase the convergence speed of the algorithm are given below.

3.6 Adaption Techniques for Mutation Rate, F

Choosing a small value of F leads to premature convergence, and large value of F slows down the search [21]. Therefore, interest in SA techniques increases and the techniques to tune its value are listed in [17]. The fitness-based adaptation technique proposed by Ali and Törn [14] is used in the proposed DE-PAS algorithm and is given by

$$F_{G+1} = \begin{cases} \max\left\{l_{min}, 1 - \left|\frac{f_{max}}{f_{min}}\right|\right\} & \text{if } \left|\frac{f_{max}}{f_{min}}\right| < 1, \\ \max\left\{l_{min}, 1 - \left|\frac{f_{min}}{f_{max}}\right|\right\} & \text{otherwise,} \end{cases} \tag{12}$$

where $l_{min} = 0.4$ is the lower bound of F, f_{min} and f_{max} are the minimum and maximum objective function values in the particular generations. Using this scheme, the search gets diversified at early stages and gets intensified at latter

stages. The reasons for using this strategy in proposed DE-PAS algorithm for the chosen problem are as follows: (i) it considers both the extremity fitness values (i.e., maximum fitness value and minimum fitness value) of the objective function, (ii) it does not include any random values in the scheme and (iii) it limits the range of F between 0.4 and 1.

3.7 Adaptation Technique for Crossover Rate, CR

Similar to the choice of mutation rate, the crossover rate has a significant impact on the success of the proposed DE-PAS algorithm. As a matter of fact, if CR value is small, it increases the stagnation problem and slows the search process and on the other hand, if CR value is assigned a higher value, it increases the population diversity. Different CR adaptation strategy was suggested by various researchers to avoid these problems. The SA scheme suggested in [10] is used in the proposed DE-PAS algorithm and is given by:

$$\mathrm{CR}_{i,\mathrm{G}+1} = \begin{cases} \mathrm{rand}_1 & \mathrm{rand}_2 \leq \tau_2 \\ C_{i,\mathrm{G}} & \text{otherwise} \end{cases} \tag{13}$$

where $\mathrm{CR}_{i,\mathrm{G}+1}$ is the crossover rate for the next generation, $\mathrm{CR}_{i,\mathrm{G}}$ is the crossover rate of the current generation. In this paper, it is assumed that $\tau_2 = 0.1$.

4 Implementation of Proposed DE-PAS Algorithm to the Chosen Problem

The implementation of proposed DE-PAS algorithm for the chosen ED problem with wind power is given below:

Step 1: For the chosen ED problem with wind power, read the input data to compute the total cost of the system to meet the demand.

Step 2: Initialization of DE-PAS, i.e., population size N, $l_{\min} = 0.4$, $\mathrm{CR}_{i,\mathrm{G}} = 0.5$ and select the stopping criteria.

Step 3: Select the number of design variables, D and initialize the design variables, i.e., the number of renewable energy sources in the chosen system. In accordance to the population size, the design variable is generated randomly within the limits using Eq. (14).

$$P_{ij} = P_{i,\min} + \mathrm{rand}(1) \times \left(P_{i,\max} - P_{i,\min}\right) \tag{14}$$

where $j = 1, 2, \ldots, N$, $i = 1, 2, \ldots, D$

Therefore, the matrix of $D \times N$ is initialized using Eq. (14).

Step 4: The fitness of each population, F_T is calculated using Eq. (1).
Step 5: Apply the DE-PAS operators to the system, i.e., DE/rand/1 mutation method, binomial crossover and one-to-one greedy selection method.
Step 6: Use fitness-based adaptation strategy and SA-based adaptation strategy to update the value of F and CR for the next generation.
Step 7: Select the termination criterion

Step 4 to Step 7 will be repeated till the termination criteria are reached by the algorithm.

5 Results and Discussion

The proposed DE-PAS algorithm is tested on wind thermal power systems from literature with four thermal generators and two wind generator. The load demand for the system for each hour of the day is shown in Fig. 2a. The maximum and minimum generation limits and cost coefficients for each unit of the system are given in [22]. Simulation tests are carried out in MATLAB 2013a on Intel (R) Core (TM) i7-3517U CPU 2.40 GHz with 8G-RAM. The proposed DE-PAS algorithm is found to be efficient as it has more adaptive parameters which smoothly balances the exploration and exploitation. The performance of proposed DE-PAS algorithm is validated with the results obtained from other well-known algorithms. A population size of 50 was used in this paper with 100 as maximum number of generations. The probability of mutation and crossover for the algorithms was fixed to 0.1 and 0.8 respectively.

The total optimal cost obtained for the system for a day using the proposed DE-PAS algorithm is 53611.69$, and the individual power generated from each thermal generator and wind generator for each hour is shown in Fig. 1a, b. The cost of the system for each hour in a day is shown in Fig. 2a, and the convergence characteristics of different algorithms are shown in Fig. 2b. The adaptive strategies for F and CR incorporated in the proposed DE-PAS algorithm, eliminate the randomness nature, explore the promising regions of the solution space and determine the optimal solution quickly when compared to other known algorithms.

In order to have a significant comparison, same values are assigned to the parameters in different algorithms, i.e., population size is fixed as 50, crossover and mutation probability as 0.8 and 0.1, respectively. To study the robustness and effectiveness of the proposed DE-PAS algorithm for the chosen ED problem, the algorithm is allowed to run 100 different test runs and the results are obtained. The statistical results obtained for the chosen problem using different algorithms for 100 test runs is shown in Fig. 3a. The search agents in the proposed DE-PAS algorithm explore the promising regions of the solution space and determine the optimal solution quickly. As the proposed DE-PAS algorithm is a variant of DE algorithm

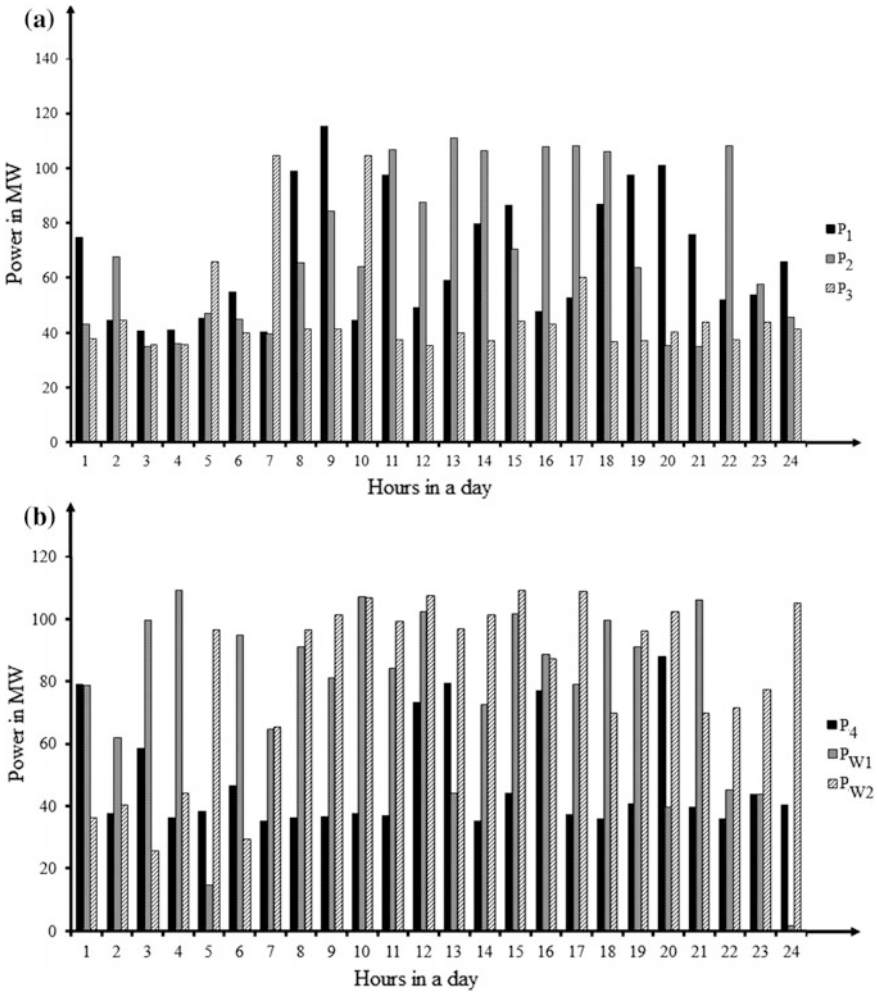

Fig. 1 Power generated from different source

which has good computational and search mechanism, the proposed DE-PAS algorithm attains the optimal solution within 100 iterations. In this paper, a self-adaptation technique has been implemented for F to eliminate disadvantaged in the trial-and-error method. Figure 3b shows that as the program progress, the value of F gets settled to 0.4 which eliminates the problem for the user in selecting an initial optimal value of F.

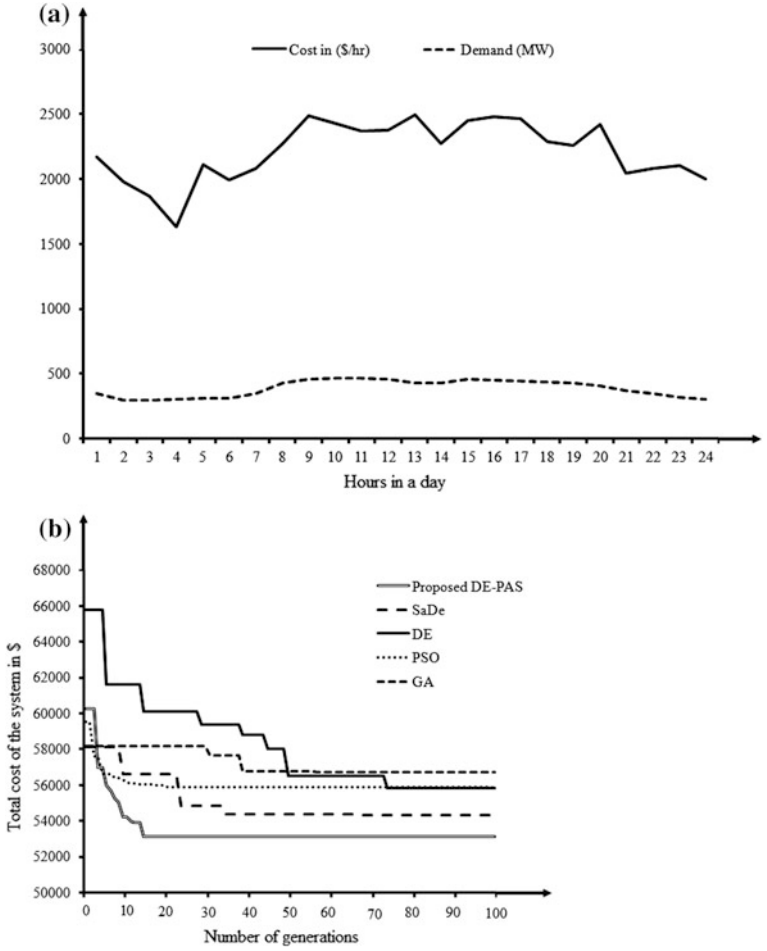

Fig. 2 **a** Demand and cost of the system per hour. **b** Convergence characteristics of different algorithms

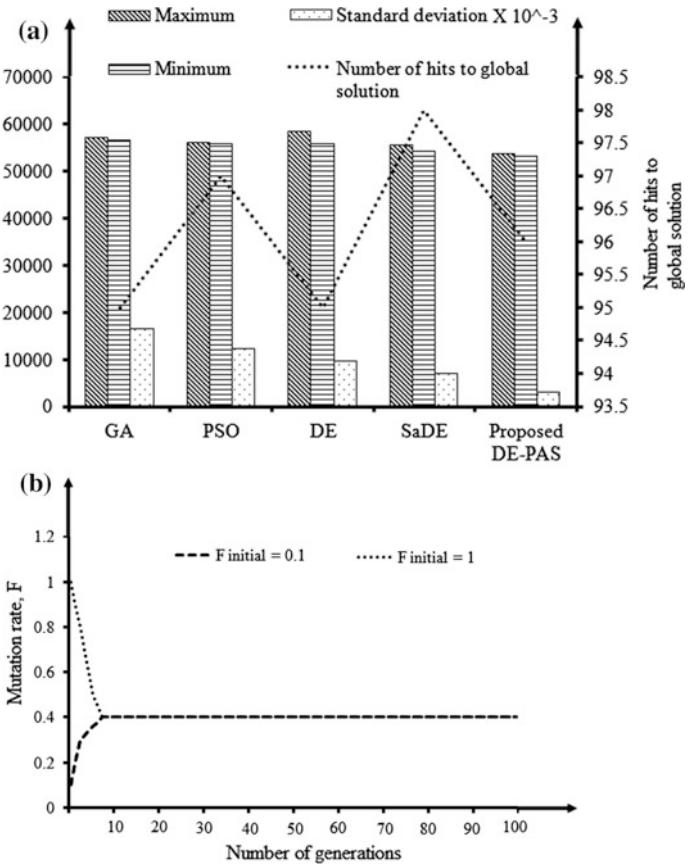

Fig. 3 **a** Statistical analysis of different algorithms and **b** self-adaptation of F

6 Conclusion

The proposed DE-PAS algorithm is a simple, efficient, reliable and powerful population-based real parameter optimization algorithm which can be widely used in different engineering fields. The performance and success of DE-PAS algorithm depend on its most important control parameters: crossover rate CR and mutation rate F. However, there is no separate technique or method to choose these parameters as their best settings varies for different problems and also during the different phase of the algorithm. The fitness-based adaptation technique for F and the SA technique for CR which eliminate the disadvantages of trial-error technique of assigning values to these parameters have been studied for the selected ED problem with wind. The proposed DE-PAS algorithm incorporates these adaptation strategies with an optimal population size to enhance significant superiority of the selected adaptation techniques. The result obtained by implementing the proposed

DE-PAS algorithm for the chosen ED problem with wind shows that the proposed algorithm outperforms the best known variants of DE algorithm and other state-of-the-art algorithms for the given problem.

References

1. Hetzer J, Yu DC, Bhattarai K (2008) An economic dispatch model incorporating wind power. IEEE Trans Energy Convers 23:603–611
2. Velamuri S, Sreejith S (2016) Reserve constrained economic dispatch incorporating solar farm using particle swarm optimization. J Renew Energy Res 6
3. Changa K-H, Linb G (2015) Optimal design of hybrid renewable energy systems using simulation optimization. Simul Model Pract Theory 52:40–51
4. Park J-B, Lee K-S, Shin J-R, Lee KY (2005) A modified particle swarm optimization for economic dispatch with non-smooth cost functions. IEEE Trans Power Syst 20:34–42 (2005)
5. Mandala B, Roy PK, Mandal S (2014) Economic load dispatch using krill herd algorithm. J Eletrc Power Energy Syst 57:1–10
6. Storn R, Price K (1997) Differential evolution—a simple and efficient heuristic for global optimization over continuous spaces. J Global Optim 11:341–359
7. Zhao S, Wang X, Chen L, Zhu W (2014) A Novel self-adaptive differential evolution algorithm with population size adjustment scheme. Arab J Sci Eng 39:6149–6174
8. Ghosh A, Das S, Chowdhury A, Giri R (2011) An improved differential evolution algorithm with fitness-based adaptation of the control parameters. Inf Sci 181:3749–3765
9. Qin AK, Huang VL, Suganthan PN (2008) Differential evolution algorithm with strategy adaptation for global numerical optimization. IEEE Trans Evol Comput 13:398–417
10. Brest J, Greiner S, Boškovic B, Mernik M, Z˘umer VZ (2006) Self-adapting control parameters in differential evolution: a comparative study on numerical benchmark problems. IEEE Trans Evol Comput 10:646–657
11. Liu J, Lampinen J (2005) A fuzzy adaptive differential evolution algorithm, soft computing—a fusion of foundations. Method Appl 9:448–462
12. Liu J, Lampinen J (2002) Adaptive parameter control of differential evolution. In: 8th international conference on soft computing, pp 19–26 (2002)
13. Rönkkönen J, Lampinen J (2003) On using normally distributed mutation step length for the differential evolution algorithm. In: 9th international conference on soft computing (MENDEL 2003), Brno, Czech Republic, pp 11–18 (2003)
14. Ali MM, Törn A (2004) Population set based global optimization algorithms: some modifications and numerical studies. Comput Oper Res 31:1703–1725
15. Mallipeddi R, Suganthan PN (2008) Empirical study on the effect of population size on Differential evolution algorithm. In: Proceedings of IEEE Congress on Evolutionary Computation, pp 3663–3670 (2008)
16. Subbaraj P, Rengaraj R, Salivahanan S (2011) Enhancement of self-adaptive real-coded genetic algorithm using taguchi method for economic dispatch problem. Appl Soft Comput 11:83–92
17. Das S, Suganthan PN (2011) Differential evolution: a survey of the state-of-the-art. IEEE Trans Evol Comput 15:4–31 (2011)
18. Storn R, Price K (1997) Differential evolution—a simple and efficient heuristic for global optimization over continuous spaces. J Global Optim 11:341–359
19. Mallipeddi R, Suganthan PN, Pan QK, Tasgetiren MF (2011) Differential evolution algorithm with ensemble of parameters and mutation strategies. Appl Soft Comput 11:1679–1696
20. Pan Q-K, Suganathan PN, Wang L, Gao L, Mallipeddi R (2011) A differential evolution algorithm with self-adapting strategy and control parameters. Comput Oper Res 38:394–408

21. Mohamed AW, Sabry HZ, Khorshid M (2012) An alternative differential evolution algorithm for global optimization. J Adv Res 3:149–165
22. Dubey HM, Pandit M, Panigrahi BK (2015) Hybrid flower pollination algorithm with time-varying fuzzy selection mechanism for wind integrated multi-objective dynamic economic dispatch. Renew Energy 83:188–202

Application of Cuckoo Search Algorithm in Deregulated Economic Load Dispatch

John Valder and A.J. Pinto Pius

Abstract The deregulated power systems are importantly needed to reduce the bidding cost. The economic dispatch concept yields minimum cost. The economic dispatch problem can be solved with many methods. Each method has its own advantage and disadvantages. In this paper, economic dispatch problem with deregulated power system is implemented. The meta-heuristic method changes the results in each run. Here the comparisons of cuckoo search with other methods for its success rate are analyzed and demonstrated. The system is applied for 3-seller system, and results are tabulated.

Keywords Deregulated power system · Economic load dispatch (ELD) Cuckoo search algorithm (CSA) · 3-seller power system

1 Introduction

The economic dispatch problems can be solved in many methods. The meta-heuristic or stochastic search methods are used in many literatures like genetic algorithms (GA), particle swarm optimization (PSO), simulated annealing (SA), evolutionary programming (EP), shuffled frog leap algorithm (SFLA), bacterial foraging algorithm (BFA), artificial bee colony algorithm (ABC), harmony search algorithm (HSA), firefly algorithm (FA), cuckoo search algorithm (CSA) and even more. But the results of each algorithm move to the optimal solution.

In 1993, Walters [1] has proposed that genetic algorithm is used to solve the economic dispatch problem with valve point effect and compared it with the dynamic programming. In 2003, Sinha [2] has presented economic load dispatch

J. Valder (✉)
PA College of Engineering, Mangalore 574153, Karnataka, India
e-mail: johnvd@rediffmail.com

A.J. Pinto Pius
NMAMIT, Nitte, Karkala Taluk, Udupi District 574110, Karnataka, India
e-mail: loypinto@yahoo.com

M.C. Bhuvaneswari and J. Saxena (eds.), *Intelligent and Efficient Electrical Systems*, Lecture Notes in Electrical Engineering 446,
https://doi.org/10.1007/978-981-10-4852-4_15

problem solution with evolutionary programming (EP). The results of EP are still enhanced by including some factors, which are newly derived. In 2004, Aruldoss Albert Victoire [3] has presented a hybrid particle swarm optimization with sequential quadratic programming and proved for better solution in economic load dispatch problem. In 2006, dos Santos Coelho [4] has discussed about the hybrid differential evolution with sequential quadratic programming for better results. Ji-Pyng Chiou in 2007 [5] has presented variable scale differential evolution methods for improving the solutions. And for the first time, auction-based economic dispatch is solved by differential algorithm by Swain RK.

In 2013, cuckoo [6] search algorithm is compared with six of the new algorithm and proved it gives best results without any complex hybridization. Cuckoo search is invented in 2011 by Xin She Yang. While on multiple run, the algorithms that are not giving exact 100% result are identified and solved using cuckoo. In this paper, auction-based economic dispatch is evaluated using cuckoo search algorithm for the first time and compared for 10 runs with PSO, GA and DE. The CSA always converges nearer to solution in 10 run while not other algorithm performs it. The test is made with the 3-seller system, and results are tabulated and graphed.

2 Problem Definition

The seller cost is assumed as thermal power system, and the incremental cost function is taken as the bidding cost. So the bidding cost function can be represented as below [7],

$$F_i\left(P_{gi}\right) = a_i + b_i P_{gi} + c_i P_{gi}^2 \tag{1}$$

Incremental cost is defined of the bidden cost function,

$$\mathrm{IC}_i\left(P_{gi}\right) = b_i + 2c_i P_{gi} \tag{2}$$

The economic dispatch problem for deregulated environment can be defined as follows,

$$\text{Minimize} : \sum_{i=1}^{n} F_i\left(P_{gi}\right) \tag{3}$$

$$\text{subjected to} : \sum_{P_{gi}}^{N_g} P_{gi} = P_d \tag{4}$$

$$P_{gi_{\min}} < P_{gi} < P_{gi_{\max}}, \quad i \in \left[1, N_g\right] \tag{5}$$

When $\sum_{i=1}^{N_g} P_{gi_{min}} > P_d$ or $\sum_{i=1}^{N_g} P_{gi_{max}} = P_d$, there is no acceptable solution.

When $\sum_{i=1}^{N_g} P_{gi_{min}} = P_d$, each seller's contracted amount is at its capacity lower limit.

When $\sum_{i=1}^{N_g} P_{gi_{min}} < P_d$ and $\sum_{i=1}^{N_g} P_{gi_{max}} > P_d$ is a non-trivial case.

Here,

$F_i(P_{gi})$	Cost of generator i
P_{gi}	Power in MW of ith generator
a_i, b_i, c_i	Constant coordinate
$P_{gi_{min}}, P_{gi_{max}}$	Minimum and maximum limits of ith generator
P_d	Power demand in MW
n, N_g	Number of generators

With all the above constraints, deregulated power system problem is formulated [7].

3 Solution Methods Used

(1) Particle Swarm Optimization (PSO)

The particle swarm optimization [8] is a simple stochastic search method inspired from the nature behavior. The algorithm is done with the behavior of insects on its food searching behavior. Steps of the algorithm are given below.

(i) The size of the swarm (control variable 'X' (generated power P_g)) is initialized as N.

(ii) Initial population of X is given as within the power limit. And initial velocity of the particle (V_j) is taken as zero.

(iii) Calculate the fitness (Cost of the fuel (F)) for each population; and find the new velocities; then increment the iteration count.

(iv) The fitness values for each population are assigned to the personal best (P_{best}) of its own X value. Then, the X value which is responsible for the lower cost value is taken as global best (G_{best}). Then velocity function is calculated using the following equation,

$$V_j(i) = V_j(i-1) + c_1 r_1 \left[P_{best\,j} - X_j(i-1)\right] + c_2 r_2 \left[G_{best} - X_j(i-1)\right] \quad (6)$$

where $j = 1, 2, \ldots, N$.

Here,

c_1, c_2 are cognitive and social learning rates taken 2

r_1, r_2 are uniform y distributed random sin range 0 and 1

(v) Then the X value is updated with the following equation

$$X_j(i) = X_j(i-1) + V_j(i) \tag{7}$$

(vi) Then go to step three and do it until the stop criteria. Here total number of iteration is stopping criteria. The final G_{best} value is the final result.

(2) **Genetic Algorithm (GA)**

Genetic algorithm is inspired by the genetic behavior in the human. This is also population-based search method like particle swarm optimization. The solution steps are given below [9].

(i) Total number of population is fixed (N). And the initial population for X (control variable) is initialized with the limits given.
(ii) Each population string is evaluated with its fitness value (bidding cost).
(iii) The X value is passed through three cycles.
Reproduction: It is used to select the good strings from the matting pool. It copies the characteristic of good string and multiplies the copies in the mating pool using probabilistic proportion to its fitness. The formula used is

$$p_i = \frac{F_i}{\sum_{j=1}^{n} F_j}; \quad \text{where } i = 1, 2, \ldots, n. \tag{8}$$

(iv) **Crossover**: This operation creates the new strings based on the data available on the mating pool.
(v) **Mutation**: It alters the strings locally to get best of it.
(vi) Evaluate the fitness values.
(vii) Test for convergence. Here it is taken as the final iteration count.
(viii) Increment the iteration count and go to step three.

(3) **Deferential Evolution algorithm (DE)**

The DE algorithm has much similarity with the genetic algorithm. It is also a stochastic search method for solving complex problems [7].

(i) The number of population is initialized and control variable (X) also.
(ii) Evaluate the fitness value.
(iii) Then mutation operator creates mutant vectors with X variables.
(iv) Crossover vector generates trial vector by mixing the parameters of the mutant vector with selected probability distribution.
(v) The selection is made with the trial vectors and their predecessors.
(vi) Go to Step (ii). This is done till the stopping criteria reached.

(4) **Cuckoo Search Algorithm (CSA)**

The cuckoo search algorithm [10] is based on the cuckoo bird on behavior of its breeding. The cuckoo bird cannot build the nest. It depends on the host bird nest for laying eggs and hatching it. But host bird nest not allows to do so. It may abandon the nest or it may damage the cuckoo birds' eggs. But cuckoo lays eggs similar to

the host bird and if it hatches, the cuckoo chicks mimic the sound of the host bird. So finding the best nest to survive the cuckoo birds makes a search that is represented as the mathematical equation steps are following.

(i) Generate the initial population with X variable of n host nests.
(ii) The cuckoo is selected randomly by levy flights equation, and then evaluates the fitness.
(iii) Choose the nest among n randomly and compare with the fitness initially calculated. If the new solution fits then replace with the old one.
(iv) Remaining fraction of (pa) nests is abandoned and best nest are kept.
(v) Rank the current solution and find the best X value.
(vi) Increment the iteration count and go to Step (ii).
(vii) Do it till the last iteration count reached.

4 Results and Discussion

The three-seller system along with the system data as given in Table 1 is taken as test system in the case study using these solution algorithms. PSO, GA, DE and CSA are chosen for getting the optimal cost value. Figure 1 shows the results of 10 runs with respect to fitness value with PSO. The deviation can be seen in the figure clearly. It deviates from $8340 to 8190. Figure 2 shows the same results of GA;

Table 1 3-seller test system data

Unit	$P_{gi_{\min}}$ (MW)	$P_{gi_{\max}}$ (MW)	a	b	c
1	100	600	561	7.92	0.001562
2	100	400	310	7.85	0.00194
3	50	200	78	7.7	0.00482

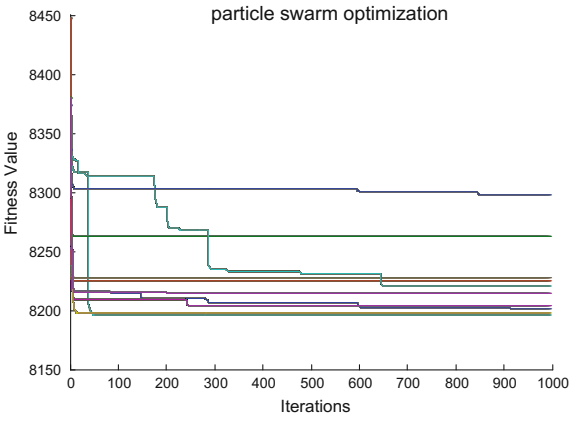

Fig. 1 PSO algorithm results for 10 runs with 3-seller system

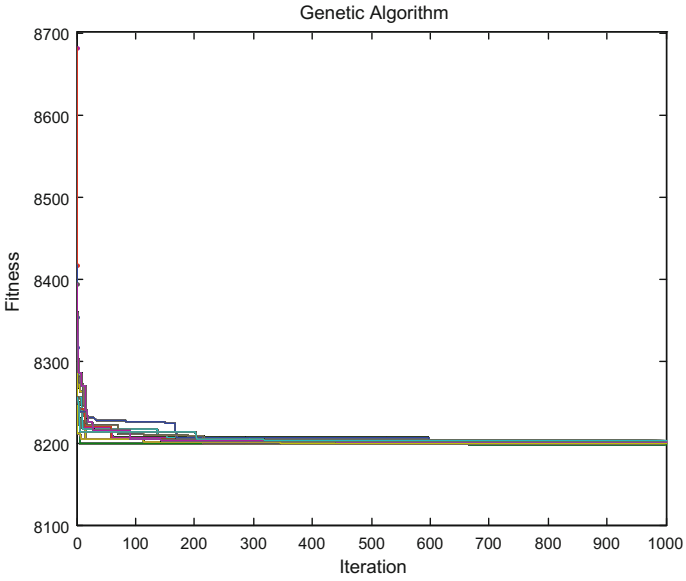

Fig. 2 GA algorithm for 10 runs with 3-seller system

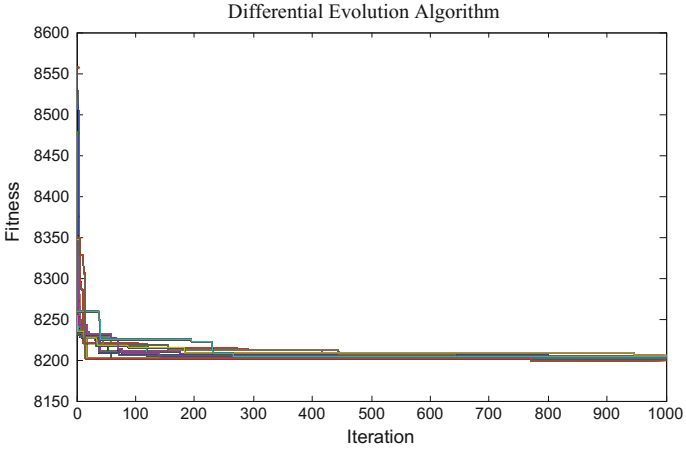

Fig. 3 DE algorithm for 10 runs with 3-seller system

there are lesser deviations compared to PSO algorithm. Figure 3 shows the results of DE. Here its deviation is more compared to GA and lesser compared to PSO. Figure 4 shows the results of CSA. Here, in all the 10 runs, it comparatively gives lesser deviation with other algorithms. Table 2 shows the final cost value of each algorithm in all the 10 runs.

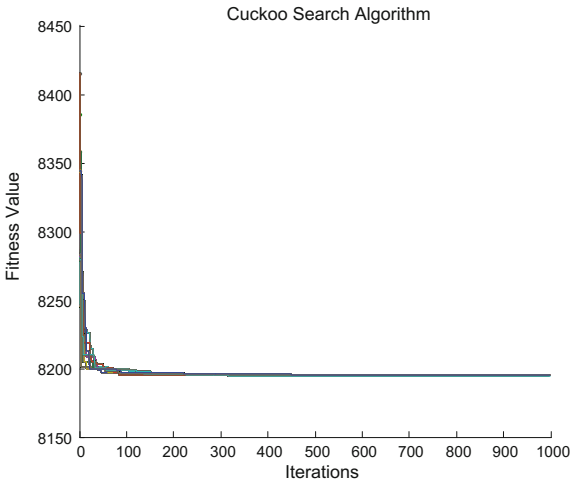

Fig. 4 CSA algorithm for 10 runs with 3-seller system

Table 2 3-seller system comparisons for 10 runs

3-seller system best cost values in $				
Run	PSO	GA	DE	CUCKOO
1	8196.2	8201.2	8202	8195
2	8200.9	8201.7	8201.6	8195.2
3	8203.6	8200.2	8201.3	8194.8
4	8262.8	8199.6	8202.9	8195
5	8198	8197	8199	8194.9
6	8224.9	8201.7	8202.1	8194.9
7	8227.6	8199.4	8200.3	8194.8
8	8220.3	8198.3	8203.2	8194.7
9	8298	8200.4	8200.7	8195.3
10	8214.6	8202.5	8196	8194.4

(1) **PSO Algorithm**
See Fig. 1.
(2) **GA Algorithm**
See Fig. 2.
(3) **DE Algorithm**
See Fig. 3.
(4) **CS algorithm**
See Fig. 4.

5 Conclusion

The economic load dispatch with deregulated power system is solved for four different algorithms to identify the best algorithm. For this, 3-seller test system is taken. The 3-seller system has three-control variable. Here many meta-heuristic algorithms like PSO, GA, DE and CSA are used, and for different run, the final solution varied by some percent. It can be seen that CSA algorithm gives always same results while running 10 times. But other algorithms give deviation in each run.

References

1. Walters DC, Sheble GB (1993) Genetic algorithm solution of economic dispatch with valve point loading. IEEE Trans Power Syst 8(3):1325–1332
2. Sinha N, Chakrabarti R, Chattopadhyay PK (2003) Evolutionary programming techniques for economic load dispatch. IEEE Trans Evol Comput 7(1):83–94
3. Victoire TAA, Jeyakumar AE (2004) Hybrid PSO–SQP for economic dispatch with valve-point effect. Int J Elect Power Energy Syst 71(1):51–59
4. Coelho LDS, Mariani VC (2006) Combining of chaotic differential evolution and quadratic programming for economic dispatch optimization with valve-point effect. IEEE Trans Power Syst 21(2):989–996
5. Chiou J-P (2007) Variable scaling hybrid differential evolution for large-scale economic dispatch problems. Elect Power Syst Res 77
6. Serapião ABS (2013) Cuckoo search for solving economic dispatch load problem. Intell Control Autom 4:385–390
7. Swain RK, Hota PK, Chakrabarty R (2008) An auction based dispatch algorithm for deregulated power systems using differential evolution technique. In: Fifteenth national power systems conference (NPSC), IIT Bombay
8. Singiresu SR (2009) Engineering optimization: theory and practice. Willey, New Jersey
9. Allen JW, Bruce FW (1996) Power generation, operation and control. Willey, New Delhi
10. Xin-She Y (2009) Cuckoo search and levy flights. In: Nature & biological inspired computing

An Investigation of Small-Signal Stability of IEEE 14 Bus System with AVR, PSS and Performance Comparison with FACTS Devices

N. Mohana Sundaram, C. Udhayashankar and Rani Thottungal

Abstract This paper is about the improvement of system stability, reliability and power transfer of a power system using FACTS devices like SVC and UPFC. In this work, small-signal stability analysis is done on an IEEE 14 Bus System by considering it as single-machine infinite-bus (SMIB) system. The improvement of system stability using AVR, PSS and FACTS devices like SVC and UPFC are analytically verified using synchronizing torque and damping torque coefficients. The examination of each category is done with the help of MATLAB simulation software. From the results, it is proved that addition of FACTS devices helps in improving the stability of the power system than other compensators. It is also found that, among the FACTS controllers, the UPFC outplays other controllers in terms of increased rotor angle stability, power transfer and damping of oscillations.

Keywords Power system stability · FACTS · SVC · UPFC · Torque component Phillips–Heffron model

1 Introduction

Extensive growth of electric power systems and the development of high-voltage long-distance transmission systems, separating generation from load, have accentuated the importance of increasing the dynamic and transient stability limits of synchronous machines. Over long distance of transmission, the system will experience instability due to insufficient synchronizing torque where it gives rise to low

N. Mohana Sundaram (✉) · C. Udhayashankar · Rani Thottungal
Kumaraguru College of Technology, Coimbatore, India
e-mail: mohanasundaram.nms@gmail.com

C. Udhayashankar
e-mail: haiudhaya@rediffmail.com

Rani Thottungal
e-mail: ranithottungal@yahoo.com

M.C. Bhuvaneswari and J. Saxena (eds.), *Intelligent and Efficient Electrical Systems*, Lecture Notes in Electrical Engineering 446,
https://doi.org/10.1007/978-981-10-4852-4_16

frequency oscillations. These oscillations may grow in magnitude if not properly damped until loss of synchronism [1–4].

The electrical characteristics of the synchronous machine most pertinent to stability calculations are the synchronizing torque coefficient K_s and damping torque coefficient K_d [5, 6]. Different methods for improving the machine oscillation using stabilization of synchronous machines through output feedback control have been developed [4].

Flexible alternating current transmission systems (FACTS) devices, namely static VAR compensators (SVC), STATic synchronous COMpensator (STATCOM), static synchronous series compensator (SSSC) and unified power flow controller (UPFC), are used to control the power flow through an electrical transmission line connecting various generators and loads at its sending and receiving ends [7, 8]. Among these FACTS devices, SVC and UPFC are taken for analysis in this work.

The stability limits between areas of a power system interconnected by long-distance transmission circuits can be increased by the use of static VAR compensators which are composed of thyristor-controlled reactors (TCR), and fixed capacitors (FC) or thyristor-switched capacitors (TSC). The almost instantaneous action of the SVC allows its application in order to increase steady-state and transient synchronizing torques provided that a properly rated compensator is specified [9, 10]. Unified power flow controller (UPFC) is another alternative, which can be used for power flow control, loop flow control, load sharing among parallel corridors, enhancement of transient stability, mitigation of system oscillations and voltage (reactive power) regulation [11, 12]. The performance of UPFC is found to be superior to SVC in terms of stability improvement.

2 Methodology

For the small-signal stability analysis, an IEEE 14 Bus Test system is modeled as a single-machine infinite-bus (SMIB) system, with Generator Bus 1 alone, as shown in Fig. 1. Based on the load flow results, the Phillips–Heffron model is constructed and six *K*-constants are evaluated (Tables 1 and 2).

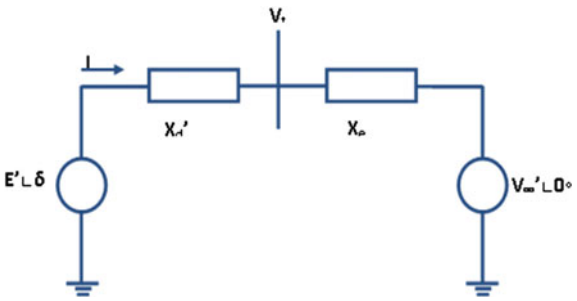

Fig. 1 SMIB system

Table 1 SMIB voltage and current values

Stator current, I	2.3234−0.1679j
Infinite bus voltage, V_{inf}	1.1095
Voltage behind transient reactance, E'	1.2599

Table 2 Values of K-constants

K_1	1.3792
K_2	1.7608
K_3	0.4739
K_4	1.0537
K_5	−0.0904
K_6	1.1104

2.1 Modeling and Analysis of SMIB System Connected with AVR

The state space equation of the SMIB system including field dynamics and AVR is given by,

$$\begin{bmatrix} \Delta\dot{E}'_q \\ \Delta\dot{\delta} \\ \Delta\dot{V} \\ \Delta\dot{E}_{\text{fd}} \end{bmatrix} = \begin{bmatrix} \frac{-1}{K_3 T'_{\text{do}}} & \frac{-K_4}{T'_{\text{do}}} & 0 & \frac{1}{T'_{\text{do}}} \\ 0 & 0 & \omega_{\text{s}} & 0 \\ \frac{-K_2}{2H} & \frac{-K_1}{2H} & \frac{-D\omega_{\text{s}}}{2H} & 0 \\ \frac{-K_{\text{A}}K_6}{T_{\text{A}}} & \frac{-K_{\text{A}}K_5}{T_{\text{A}}} & 0 & \frac{-1}{T_{\text{A}}} \end{bmatrix} \begin{bmatrix} \Delta E'_q \\ \Delta\delta \\ \Delta V \\ \Delta E_{\text{fd}} \end{bmatrix} + \begin{bmatrix} 0 \\ 0 \\ 0 \\ \frac{K_{\text{A}}}{T_{\text{A}}} \end{bmatrix} \Delta V \tag{1}$$

The K_{s} and K_{d} values for various values of exciter gain, K_{A} are calculated using below equations.

$$x = \frac{1}{K_3} + K_{\text{A}}K_6 - \omega^2 T'_{\text{do}} T_{\text{A}} \tag{2}$$

$$y = \omega\left(\frac{T_{\text{A}}}{K_3} + T'_{\text{do}}\right) \tag{3}$$

Synchronising Torque Coefficient,

$$K_{\text{S}} = K_1 - \frac{K_2 K_{\text{A}} K_5 x}{x^2 + y^2} \tag{4}$$

Damping Torque Coefficient,

$$K_{\text{D}} = \frac{K_2 K_{\text{A}} K_5 y}{x^2 + y^2} \tag{5}$$

Table 3 Comparison of K_S and K_D values of system for various exciter gains

K_A	Re[$H(jw)$]	K_s	K_D	Response time
0	0	1.3792	0	Slow response
10	−0.0005	1.3787	−0.0124	
15	0.0017	1.3809	−0.032	
25	0.0104	1.3896	−0.0514	
50	0.0462	1.4254	−0.0803	
100	0.1029	1.4821	−0.0779	Fast response
200	0.135	1.5142	−0.048	
400	0.1433	1.5225	−0.0247	
1000	0.1443	1.5235	−0.0098	
5000	0.1437	1.5229	−0.0019	
10,000	0.1435	1.5227	−0.001	

Table 4 PSS controller data

Gain, K_{PSS}	T_1	T_2
7.4	0.8	0.05

It can be inferred from Table 3 that for the range of $0 < K_A < 50$, though the synchronizing torque coefficient, K_s increases, the damping torque coefficient K_D, increases negatively, which may cause the response to be slow. For the range of $100 < K_A < 10{,}000$, the K_s value increases and the K_D value decreases negatively. The response for this range will be better due to the improvement in K_D. For the same range, it is found that the K_s value starts decreasing when $K_A > 1000$. Hence, the optimal value of K_A for the system with AVR is found to be 1000.

For the SMIB system connected with AVR alone, the K_D value is found to be negative for any values of exciter gain. This is the disadvantage of having AVR. But it is required to maintain the terminal voltage of the bus. Hence, in order to overcome this, the power system stabilizer (PSS) can be added to system in addition to AVR, which provides additional damping torque (Table 4).

2.2 *Modeling and Analysis of SMIB System Connected with AVR and PSS*

The modified system matrix and K_s, K_D equations are

$$A = \begin{bmatrix} \frac{-1}{K_3 T'_{do}} & \frac{-K_4}{T'_{do}} & 0 & \frac{1}{T'_{do}} & 0 \\ 0 & 0 & \omega_s & 0 & 0 \\ \frac{-K_2}{2H} & \frac{-K_1}{2H} & 0 & 0 & 0 \\ \frac{-K_A K_6}{T_A} & \frac{-K_A K_5}{T_A} & 0 & \frac{-1}{T_A} & \frac{K_A}{T_A} \\ \frac{-K_2 T_1 K_{PSS}}{2HT_2} & \frac{-K_1 T_1 K_{PSS}}{2HT_2} & \frac{K_{PSS}}{T_2} & 0 & \frac{-1}{T_2} \end{bmatrix} \tag{6}$$

Table 5 Comparison of K_S and K_D values of system with and without PSS

K_A	K_s without PSS	K_s with PSS	K_D without PSS	K_D with PSS
0	1.3792	1.3792	0	0
10	1.3787	1.5729	−0.0124	0.2783
15	1.3809	1.64	−0.032	0.4374
25	1.3896	1.7044	−0.0514	0.7698
50	1.4254	1.5221	−0.0803	1.4677
100	1.4821	0.8087	−0.0779	1.9342
200	1.5142	0.1542	−0.048	1.8217
400	1.5225	−0.1521	−0.0247	1.5878
1000	1.5235	−0.2962	−0.0098	1.3998
5000	1.5229	−0.3569	−0.0019	1.29
10,000	1.5227	−0.3637	−0.001	1.276

$$\frac{\Delta T_{\mathrm{PSS}}(s)}{\Delta V(s)} = \frac{K_{\mathrm{PSS}} K_2 K_{\mathrm{A}} (1 + sT_1)}{\left\{ \left(\frac{1}{K_3} + K_{\mathrm{A}} K_6 \right) + S \left(\frac{T_{\mathrm{A}}}{K_3} + T'_{\mathrm{do}} \right) + s^2 T'_{\mathrm{do}} T_{\mathrm{A}} \right\} (1 + sT_2)} \tag{7}$$

$$\Delta T_{\mathrm{PSS}}(s) = K_{\mathrm{syn}} \Delta\delta + K_{\mathrm{damp}} \Delta\omega \tag{8}$$

Table 5 clearly highlights the effect of adding power system stabilizer (PSS) to the system in addition with automatic voltage regulator (AVR). The system with PSS provides good improvement both in K_s and K_D values, thereby contributing to the system stability.

Also, it is observed that the K_s value (with PSS) is found to increase till $K_A = 25$, after which it falls. The high values of K_D lie in the range $0 < K_A < 100$. Comparing both, the optimal value is found to be $K_A = 25$, where both K_s and K_D are remarkably high. In this case, the system stability is increased to a good margin. For the exciter gain, $K_A > 400$, the K_s values for system (with PSS) become negative. This implies that above this particular gain, the system moves toward the verge of instability.

As seen in Table 5, though the power system stabilizers used in conjunction with AVR damp out oscillations, at some point of time, they may not provide adequate damping. In that case, it is wise to have an alternative controller either by replacing them or adding along with them. One such option is by adding a FACTS controller. In the forthcoming discussion, the effect of adding static VAR compensator (SVC) and unified power flow controller (UPFC) is described with analytical and simulation results.

2.3 Modeling and Analysis of SMIB System Connected with SVC

In this analysis, the SVC is connected to the middle of the transmission line as in Fig. 2. The susceptance value of SVC, B_{svs} taken is 0.7.

$$X_E = (X_1 + X_2) - X_1 X_2 B_{SVS} \tag{9}$$

$$K_S = \frac{E'V_\infty}{X_E}\cos\delta + \frac{X_1 X_2}{X_E}\left(\frac{E'V_\infty}{X_E V_O}\sin\delta\right)^2 \tag{10}$$

As shown in Table 6, the K_s value for the system connected with SVC is found to be increased significantly compared with the other types of system. Also, it is to be noted that, addition of SVC has no effect on damping torque coefficient, K_D.

The time response of the system with respect to changes in rotor angle ($\Delta\delta$) is plotted with an initial change in rotor angle of 5°. When the system is added with PSS and SVC, it is found that the settling time of the rotor oscillations is reduced considerably. Figures 3 and 4 show the response for various gain settings. Even though the system is connected with PSS and SVC, the settling time and the frequency of oscillations are more pronounced for this gain setting, indicating the state of system instability.

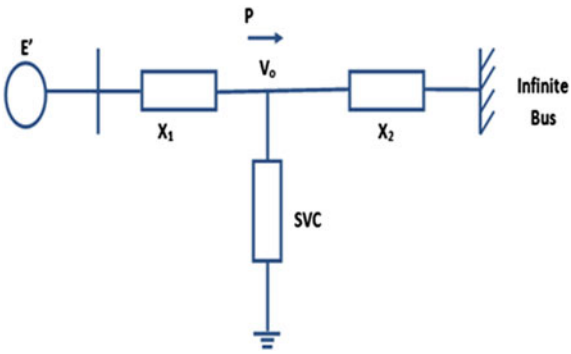

Fig. 2 SMIB system connected with SVC at the middle of the transmission line

Table 6 Comparison of K_S and K_D values of various system modes

Exciter gain, K_A	Synchronizing torque coefficient, K_s			Damping torque coefficient, K_D		
	AVR	PSS	SVC	AVR	PSS	SVC
0	1.3792	1.3792	1.8251	0	0	0
50	1.4254	1.5221	1.8251	−0.0803	1.4677	1.4677
100	1.4821	0.8087	1.8251	−0.0779	1.9342	1.9342
200	1.5142	0.1542	1.8251	−0.0480	1.8217	1.8217
500	1.5232	−0.2042	1.8251	−0.0198	1.5283	1.5283

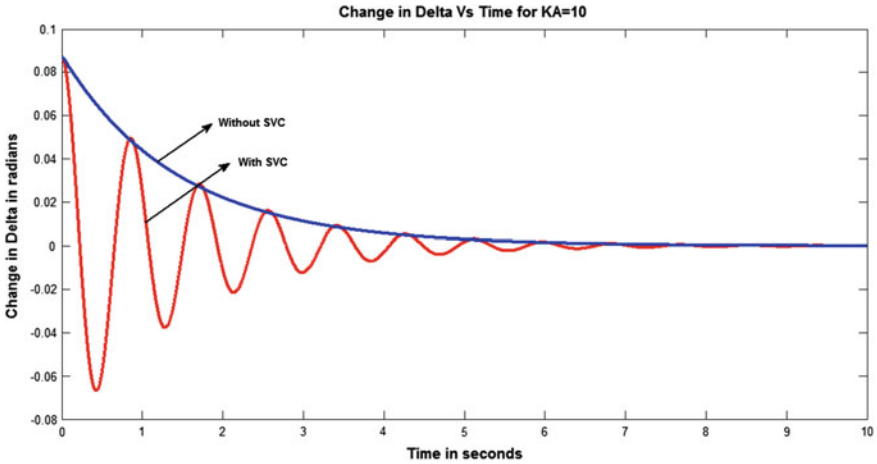

Fig. 3 Change in delta versus time connected with and without SVC (for $K_A = 10$)

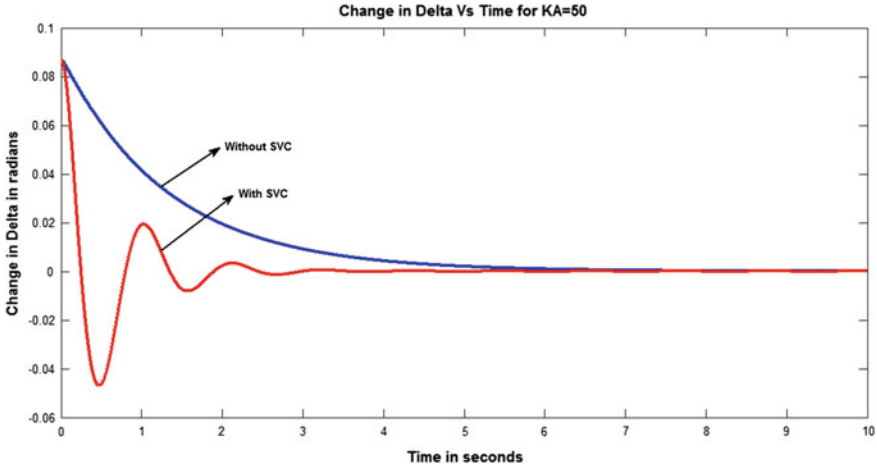

Fig. 4 Change in delta versus time connected with and without SVC (for $K_A = 50$)

It is revealed from Fig. 5 that for the system with SVC, the maximum power transfer limit is increased which provides improved efficiency. Also, the rotor angle is also found to be reduced for the same mechanical input. This provides a greater stability margin.

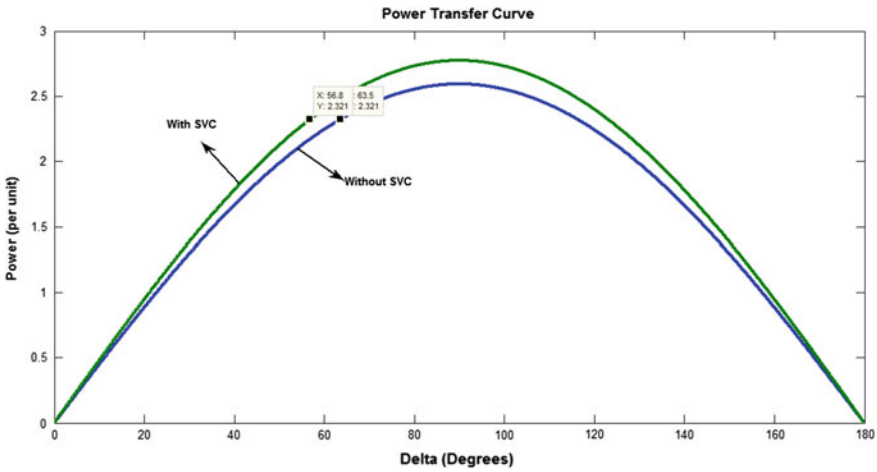

Fig. 5 Power transfer comparison of the SMIB with and without SVC

Table 7 Rotor angle, δ and K-constants obtained for different values of UPFC controllable range

Parameters	System without UPFC	System with UPFC having $VV_{pq\max}/X$				
		0.1	0.2	0.3	0.4	0.5
δ	63.64°	59.2°	55.4°	51.9°	48.8°	45.9°
K_1	1.3792	1.3738	1.4246	1.4659	1.4978	1.5238
K_2	1.7608	1.7608	1.7608	1.7608	1.7608	1.7608
K_3	0.4739	0.4739	0.4739	0.4739	0.479	0.4739
K_4	1.0537	1.0578	1.0137	0.9691	0.9266	0.8844
K_5	−0.0904	−0.0950	−0.0478	−0.0042	0.0345	0.0706
K_6	1.1104	1.1104	1.1104	1.1104	1.1104	1.1104

2.4 *Modeling and Analysis of SMIB System Connected with UPFC*

The real power equation of system connected with UPFC is given by,

$$P(\delta,\rho) = P_o(\delta) + P_{pq}(\rho) = \frac{V^2}{X}\sin\delta + \frac{VV_{pq}}{X}\sin\left(\frac{\delta}{2}+\rho\right). \tag{11}$$

Since angle ρ is freely variable between 0 and 2π at any given transmission angle δ ($0 \le \delta \le \pi$), $P_{pq}(\rho)$ is controllable between $-VV_{pq}/X$ and $+VV_{pq}/X$ independent of angle δ. The maximum allowable value for $VV_{pq\max}/X$ is 0.5 p.u. Table 7 lists out the newly calculated K-constants for various values of $VV_{pq\max}/X$ (0.1–0.5).

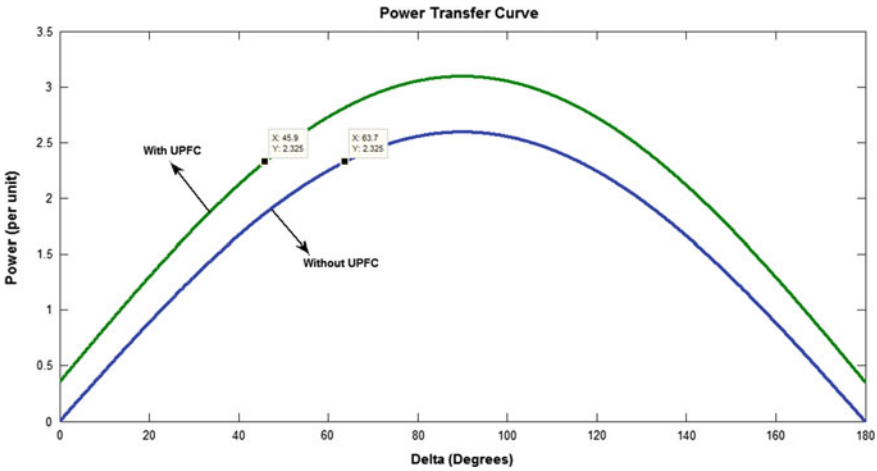

Fig. 6 Power transfer comparison of the SMIB with and without UPFC

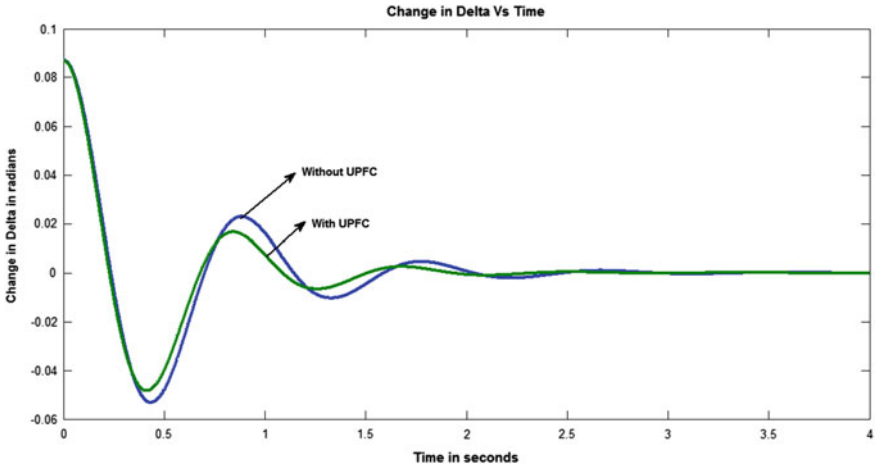

Fig. 7 Change in delta versus time of the system connected with and without UPFC

Table 7 shows that, when the UPFC is connected to the system, K_5 constant improves gradually with increase in controllable range. In this case, for $VV_{pq\max}/X > 0.3$, K_5 increases positively, which helps in reducing the magnitude of the rotor oscillations.

The power transfer curve for the system connected with and without UPFC is shown in Fig. 6 for the value $VV_{pq\max}/X = 0.5$. It can be seen that the rotor angle has reduced greatly by 18° approximately.

With the new *K*-constants, the system response obtained is compared with the standard response. It can be observed from Fig. 7 that with UPFC, the rotor oscillations are damped significantly.

3 Conclusion

The stability analysis of an IEEE 14 Bus Test System is done on the Generator Bus No. 1. The Generator Bus under consideration is constructed as a single-machine infinite-bus (SMIB) system using Phillips–Heffron model. The effect of variable excitation and power system stabilizer (PSS) on the system is discussed for different exciter gains. The analysis of the system is further extended by connecting FACTS controllers like static VAR compensator (SVC) and unified power flow controller (UPFC) to them. Analytically, it is shown that the addition of SVC increases the power transfer and also the synchronizing torque component. And, the UPFC is found to be superior by providing high transient stability margin, increased power transfer, real and reactive power compensation and good power oscillation damping.

References

1. Kundur P (1994) Power system stability and control. McGraw-Hill
2. Rogers G (2000) Power system oscillations. Kluwer Academic Publishers
3. Pai MA, Sen Gupta DP, Padiyar KR (2004) Small signal analysis of power systems. Narosa Publishing House, New Delhi
4. Sambariya DK, Prasad R (2013) Design of PSS for SMIB system using robust fast output sampling feedback technique. In: 2013 7th international conference on intelligent systems and control (ISCO), 4–5 Jan 2013. doi:10.1109/ISCO.2013.6481142
5. Jiang N, Chiang H-D (2013) Numerical investigation on the damping property in power system transient behavior. IEEE Trans Power Syst 28(3). doi:10.1109/TPWRS.2012.2230030
6. Bakhtvar M, Vittal E, Zheng K, Keane A (2017) Synchronizing torque impacts on rotor speed in power systems. IEEE Trans Power Syst (99). doi:10.1109/TPWRS.2016.2600478
7. Sen KK, Stacey EJ (1998) UPFC—unified power flow controller: theory, modeling, and applications. IEEE Trans Power Deliv 13:1454–1460
8. Okeke TU, Zaher RG (2013) Flexible AC transmission systems (FACTS). In: 2013 international conference on new concepts in smart cities: fostering public and private alliances (SmartMILE), 11–13 Dec 2013. doi:10.1109/SmartMILE.2013.6708208
9. Khan S, Meena R, Bhowmick S (2015) Small signal stability improvement of a single machine infinite bus system using SVC. In: India conference (INDICON), 2015 annual IEEE, 17–20 Dec 2015. doi:10.1109/INDICON.2015.7443269
10. Mahdavian M, Shahgholian G, Shafaghi P, Azadeh M, Farazpey S, Janghorbani M (2016) Power system oscillations improvement by using static VAR compensator. In: 2016 13th international conference on electrical engineering/electronics, computer, telecommunications and information technology (ECTI-CON), 28 June–1 July 2016. doi:10.1109/ECTICon.2016.7560905

11. Ahmad S, Albatsh FM, Mekhilef S, Mokhlis H (2014) An approach to improve active power flow capability by using dynamic unified power flow controller. In: Innovative smart grid technologies—Asia (ISGT Asia), 2014 IEEE, 20–23 May 2014. doi:10.1109/ISGT-Asia.2014.6873798
12. Arizadayana Z, Irwanto M, Fazliana F, Syafawati AN (2014) Improvement of dynamic power system stability by installing UPFC based on fuzzy logic power system stabilizer (FLPSS). In: 2014 IEEE 8th international power engineering and optimization conference (PEOCO2014), Langkawi, The Jewel of Kedah, Malaysia, 24–25 Mar 2014

Investigation on the Properties of Natural Esters Blended with Mineral Oil and Pyrolysis Oil as Liquid Insulation for High Voltage Transformers

M. Bakrutheen, M. Willjuice Iruthayarajan and S. Senthil Kumar

Abstract For the several decades, petroleum-derived mineral oil has been used as liquid insulation due to its better operating properties, low cost and availability. Many research works have been performed over the years to find the potential replacement of traditional mineral oil to overcome its disadvantages such as poor biodegradability, environmental issues and scarcity of availability in future. In these aspects, various vegetable oil-based natural esters are investigated by the researchers throughout the world. With the objective of developing functional efficient liquid insulation for high-voltage transformers, investigation is carried out with natural esters (sunflower oil, rice bran oil, corn oil and olive oil), blended with traditional mineral oil and biomass-based pyrolysis oil. In this work, for ensuring the characteristics of investigating liquid insulation, properties such as breakdown voltage, flash point and viscosity are measured according to international standards. From the investigations, it is found that the natural esters and blended oil samples have the properties as nearer to standard values for liquid insulations used in high-voltage transformers and have the ability to replace traditional mineral oil as alternate liquid insulation.

Keywords Liquid insulation · Mineral oil · Transformer · Pyrolysis oil Natural esters

M. Bakrutheen (✉) · M. Willjuice Iruthayarajan · S. Senthil Kumar
Department of Electrical and Electronics Engineering, National Engineering College, Kovilpatti, Tamil Nadu, India
e-mail: bakrutheenme@gmail.com

M. Willjuice Iruthayarajan
e-mail: m.willjuice@gmail.com

S. Senthil Kumar
e-mail: senthilkumarneceee@gmail.com

M.C. Bhuvaneswari and J. Saxena (eds.), *Intelligent and Efficient Electrical Systems*, Lecture Notes in Electrical Engineering 446,
https://doi.org/10.1007/978-981-10-4852-4_17

1 Introduction

In electrical power system network, oil-filled high-voltage transformers are the important electrical component [1]. The liquid insulation used in transformers has played a major role in determining the functional efficiency and lifetime of high-voltage transformers [2]. They act as both electrical insulation and cooling medium inside the transformers [3]. For several decades, petroleum-derived mineral oil has been used as liquid insulation for many high-voltage applications, particularly in high-voltage transformers [4, 5]. Even though mineral oil is used in the transformers due to its operating properties, low cost and availability, it has some environmental effects such as contaminations on soil and water when it spills on that area. It has some other drawbacks such as non-biodegradable nature and reduction in available resources [6]. These aspects lead towards the development of biodegradable, environmentally friendly liquid insulation as suitable substitute for traditional mineral oil [7].

Vegetable oil-based insulating liquids have been investigated in various research works for finding the ability to replace the mineral oil. It has some merits over mineral oil such as good biodegradable nature, less environmental hazards, larger availability, higher dielectric properties and thermal properties [6–13]. Edible based commercial oil products developed by Cooper Power Systems and ABB are used in the distribution transforms [14, 15]. The main constitutes of natural esters are triglycerides such as saturated fatty acids, monounsaturated fatty acids and polyunsaturated fatty acids. These fatty acids are crucial in physical and chemical properties of natural esters [8–10]. Higher percentage of unsaturated content leads to lower viscosity and higher susceptibility to oxidation of vegetable oils. Higher saturated content in vegetable oil indicates the higher viscosity and higher pour points which makes the complexity in using those oils as liquid insulation [16]. One of the drawbacks in the vegetable oil-based insulation is its high viscosity which should be low for providing the better cooling performance inside the transformers [12, 13].

Vegetable oils are investigated with the inclusion of enhancing additives (nanoparticles, antioxidants, etc.), modification of its ester content by transesterifications, ageing analysis without and with solid insulations for ensuring the development of potential replacement of mineral oil for future applications in transformers, apart from analysing the individual vegetable oil [17–22]. One of the methods to alter the properties of liquid insulation is blending of different oils with various concentrations to develop new liquid insulation. The properties are changed with respect to miscibility of those blended oils. For example, the viscosity of higher viscous medium is reduced by the blending with low viscous medium [23–25].

In recent years, biomass-based pyrolysis oil (bio oil) has gained attention and they are used in other engineering application fields such as heat and power generations, liquid fuels, raw chemical products, antioxidants and surfactants [26]. They have the low value of viscosity compared with the natural esters [27].

In this work, investigation is carried out with analysing the natural esters blended with mineral oil and biomass-based pyrolysis oil to develop low viscous liquid insulation from natural esters. The characteristics of blended oil samples such as breakdown voltage, flash point and viscosity are measured as per the guidelines provided by IEC and ASTM standards.

2 Samples Descriptions

Natural esters are vegetable oils which are derived from seeds and plants. They are processed and refined through various chemical and physical processes for converting it into refined oil from its crude stage [20]. Refined form of vegetable oil is taken for this investigation. The selected vegetable oil (natural esters) samples are tabulated in Table 1 with their fatty acids composition.

Bio oil is the liquid form of biomass developed by the process of pyrolysis. It is a dark brown coloured free flowing liquid. It is also been termed as pyrolysis oil, liquid pyrolysis and pyroligneous. Pyrolysis is the degradation of biomass by thermal process in the absence of oxygen. The bio oil is derived by the processes of thermal degradation, cooling and condensation of biomass. In this work, wood-based bio pyrolysis oil (PO) is used in the investigation to analyse the reduction of viscosity in natural ester-based oil samples after blending process [26–29].

With the aim of developing functional efficient low viscous natural esters, the selected vegetable oils are blended with mineral oil and pyrolysis oil in the ranges of 25, 50 and 75%. The oil samples prepared by blending with their blending combinations are given in Table 2.

Table 1 Vegetable oil samples and their fatty acid composition

Oil samples	Fatty acid content (%)		
	Saturated	Unsaturated	
		Mono	Poly
Sunflower oil (SO)	11	20	69
Rice bran oil (RBO)	20	45	35
Corn oil (CO)	13	25	62
Olive oil (OO)	14	60	26

Table 2 Blended oil samples and their combinations

Samples	Combinations	Samples	Combinations
A1	25% MO + 75% SO	E1	25% PO + 75% SO
A2	50% MO + 50% SO	E2	50% PO + 50% SO
A3	75% MO + 25% SO	E3	75% PO + 25% SO
B1	25% MO + 75% RBO	F1	25% PO + 75% RBO
B2	50% MO + 50% RBO	F2	50% PO + 50% RBO
B3	75% MO + 25% RBO	F3	75% PO + 25% RBO
C1	25% MO + 75% CO	G1	25% PO + 75% CO
C2	50% MO + 50% CO	G2	50% PO + 50% CO
C3	75% MO + 25% CO	G3	75% PO + 25% CO
D1	25% MO + 75% OO	H1	25% PO + 75% OO
D2	50% MO + 50% OO	H2	50% PO + 50% OO
D3	75% MO + 25% OO	H3	75% PO + 25% OO

Fig. 1 Breakdown voltage measurement test cell with electrodes

3 Experimental Details

For analysing the influence and effect of blending, the properties such as breakdown voltage, flash point and viscosity are measured for the blended combinations of oil samples as per international standards of IEC and ASTM. All the measurements are carried out at room temperature and pressure.

The electrical withstand capacity for high electrical stress of any liquid insulation is measured with the breakdown voltage. Breakdown voltage is also the indication of quality of insulating liquids. The breakdown voltage of oil affects with the presence of moisture, solid dusts and air bubbles [30]. The breakdown voltage measurements are conducted as per guidelines provided by IEC 60156 [31]. A test cell with 2.5-mm special spherical electrodes (Fig. 1) and breakdown voltage test kit with variac (Fig. 2) are used to measure the breakdown voltage. The rate of rise of test voltage should be in the range of 2 kV/s. The breakdown voltage of liquid insulation is calculated from the mean of five readings taken with the same oil samples.

Flash point temperature is the limit of safest temperature of oil inside the transformers [30]. The flash point temperature is measured as per the standard of ASTM D93 [32]. Pensky Martin flash point apparatus (Fig. 3) with 60 ml capacity test cell

Fig. 2 Breakdown voltage measurement test kit with variac

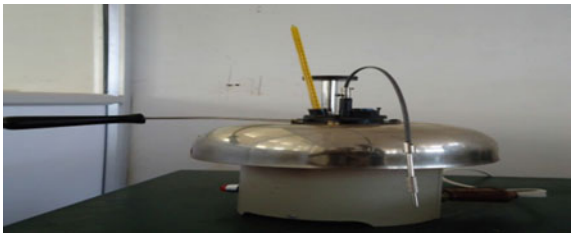

Fig. 3 Pensky Martin flash point apparatus

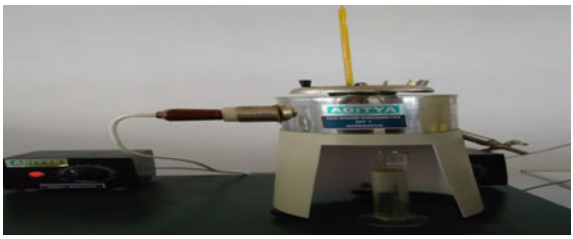

Fig. 4 Redwood viscometer

and heater arrangement is used in measurement of flash point. By increasing the oil temperature with heater set-up, the flash point is indicated with temporary flame on the surface of oil sample when a test flame is introduced in the test orifice.

Resistance offered by the oil to flow is measured by the viscosity property as per standard of ASTM D445 [33]. Viscosity is indirectly indicating the oil cooling ability inside the transformer [30]. Time taken for 50 ml of oil flow through test orifice in Redwood viscometer (Fig. 4) is measured, and from that, time viscosity of oil is calculated by time-viscosity chart.

4 Results and Discussion

The properties of mineral oil, pyrolysis oil and natural esters such as breakdown voltage, flash point and viscosity are measured as per the international standards. The values of proprieties of individual oil samples are tabulated in Table 3. The

Table 3 Properties of individual oil samples

Oil samples	Breakdown voltage (kV)	Flash point (°C)	Viscosity (cSt)
Mineral oil (MO)	31.2	158	19.54
Pyrolysis oil (PO)	29.8	60	22.33
Sunflower oil (SO)	34.6	265	97.68
Rice bran oil (RBO)	36.2	240	124.33
Corn oil (CO)	30.4	290	80.09
Olive oil (OO)	33.8	280	115.58

Table 4 Properties of sunflower oil-based blended samples

Samples	Breakdown voltage (kV)	Flash point (°C)	Viscosity (cSt)
A1	34.2	235	61.81
A2	33.4	205	40.52
A3	31.8	185	27.63
E1	33.8	180	64.61
E2	32.4	125	43.94
E3	31.2	85	30.87

Table 5 Properties of rice bran oil-based blended samples

Samples	Breakdown voltage (kV)	Flash point (°C)	Viscosity (cSt)
B1	34.8	215	72.34
B2	33.6	195	44.53
B3	32.2	175	28.84
F1	34.4	165	75.76
F2	32.8	115	48.38
F3	31.8	80	32.26

Table 6 Properties of corn oil-based blended samples

Samples	Breakdown voltage (kV)	Flash point (°C)	Viscosity (cSt)
C1	30.8	250	53.65
C2	30.2	215	37.18
C3	29.8	185	26.57
G1	29.8	190	56.01
G2	29.4	130	40.25
G3	28.6	85	29.65

properties of blended oil samples are given in Tables 4, 5, 6 and 7 for sunflower oil-based blended samples, rice bran oil-based blended samples, corn oil-based blended samples and olive oil-based blended samples, respectively.

Table 7 Properties of olive oil-based blended samples

Samples	Breakdown voltage (kV)	Flash point (°C)	Viscosity (cSt)
D1	33.2	245	69.25
D2	32.4	210	43.39
D3	31.8	185	28.51
H1	32.8	190	72.49
H2	32.1	125	47.81
H3	30.8	85	31.87

4.1 Breakdown Voltage

From the measurement of breakdown voltage of various oil samples in this investigation, the following inferences are made.

- Breakdown voltage of pyrolysis oil is near equal to that of mineral oil. At the same condition, the natural esters have higher breakdown voltage than the mineral oil except corn oil.
- Among the investigated vegetable-based oils, rice bran oil has the higher breakdown voltage and corn has the lowest breakdown voltage.
- In the mineral oil blended natural ester samples, samples A1–A3, B1–B3 and D1–D3 have higher breakdown voltage than the mineral oil and lower breakdown voltage than base natural ester. Samples C1 has the breakdown voltage which is higher than base natural ester (corn oil) and lower than the mineral oil. Samples C2 and C3 have lower breakdown voltage than the mineral oil and corn oil.
- The breakdown voltage is higher than the pyrolysis oil and lower than the base natural ester for the samples prepared with pyrolysis blended natural esters (E1–E3, F1–F3 and H1–H3). Sample G1 has the same breakdown voltage value as pyrolysis oil, and other two samples in the group G2 and G3 have the lower breakdown voltage than both pyrolysis oil and corn oil.
- In overall, as the concentration of mineral oil/pyrolysis oil increases, the breakdown voltage has shown reduction trends for blended oil samples. The blended oil samples have reduced breakdown voltage for lower percentage concentration of natural esters in it.
- The breakdown voltage of blended oil samples is majorly influenced by the natural esters than the mineral oil/pyrolysis oil.

4.2 Flash Point

From the measurement of flash point of investigating oil samples, the following implications are made.

- Flash point temperatures of natural esters are very much higher than the mineral oil and pyrolysis oil. Pyrolysis oil has very low flash point temperature of 60 °C. This shows the poor thermal characteristics of pyrolysis oil.
- After blending with mineral oil, the flash point temperature of blended oil has shown decrement nature as the concentration of mineral oil increases. All mineral oil-based blended samples have the higher flash point values than mineral oil and lower values than the natural esters. In the pyrolysis oil-based blended samples, the flash point values have decreased as the pyrolysis oil content increases in the blended combinations. The flash point values of blended oils are reduced very much than those of natural esters.
- The flash point temperature of blended samples is majorly dependent on the concentration of mineral oil/pyrolysis oil.

4.3 Viscosity

From the viscosity measurement on oil samples, the following observations are made.

- The viscosities of natural ester have higher values than the mineral oil and pyrolysis oil. Pyrolysis oil and mineral oil have similar values of viscosity.
- Oils with the high polyunsaturated fatty acid content have the lower viscosity among the natural esters. The higher viscosities are observed for the oils with high monounsaturated fatty acid content.
- Reduced values for viscosity have obtained as blending the low viscous mineral oil/pyrolysis oil and high viscous natural esters. All the blended samples have the lower viscosities values than the natural esters.
- As the composition of mineral oil/pyrolysis oil increases in the blended samples, the viscosity value of natural esters has reduced after blending.
- The reduction in the viscosity of natural esters after blending is mainly due to the mineral oil/pyrolysis oil.

5 Conclusion

In this work, four natural esters (sunflower oil, rice bran oil, corn oil and olive oil), mineral oil and biomass-based pyrolysis oil are investigated to develop and analyse the properties for the applications in high-voltage transformers as alternate liquid insulation. Natural esters have good dielectric and thermal characteristics. Its viscosity is very much higher than the required low value for the application in transformer. Even though the pyrolysis oil has higher breakdown voltage and low viscosity, its flash point is too low. So pyrolysis oil has to be improved as liquid insulation. In our work, the pyrolysis oil is used to reduce viscosity of natural esters by blending process. From the experimental results, it is found that the blended oil samples have changed the properties based on the blended oil percentages and original properties of base samples. All the samples have the same kind of changes in their properties after blending. All the blended samples except the samples prepared with 75% of pyrolysis oil have the properties nearer to the range of values required for the application in high-voltage transformers. This work may be extended to improve the properties of natural esters by various physical and chemical processes.

References

1. IEEE, Guide: Loading Mineral oil-immersed Transformers, Annex I: Transformer Insulation Life. IEEE Standard C57.91 (1995)
2. Young W (1998) Transformer life management-condition monitoring. In: IEEE Coloquim, (Digest) IEE Stevane, England, pp 1–4
3. Bakrutheen M, Raymon A, Samuel Pakianathan P, Rajamani MPE, Karthik R (2014) Enhancement of critical characteristics of aged transformer oil using regenerative additives. Aust J Electr Electron Eng 11(1):77–86
4. Rouse TO (1998) Mineral oil in transformers. IEEE Electr Insul Mag 14(3):6–16
5. Vishal B, Saurabh M, Vikas T, Prashant K (2011) Transformer's history and its insulating oil. In: 5th national conference, INDIACom, computing for nation development
6. Oommen TV (2002) Vegetable oils for liquid filled transformers. IEEE Electr Insul Mag 18 (1):6–11
7. Karthik M, Willjuice Iruthayarajan M, Bakrutheen M (2015) Suitability analysis of natural esters based liquid insulating medium for high voltage transformers. Int J Appl Eng Res 10 (20):15331–15335
8. McShane P (2002) Vegetable oil based dielectric coolants. IEEE Ind Appl Mag 8(3):34–41
9. McShane P, Oommen TV, Tanger WC (2003) Report—ester transformer fluids. In: IEEE/PES transformer committee, Charles Tanger, Cargill, USA
10. Bertrand Y, Hoang LC (2004) Vegetable oils as substitute for mineral insulating oils in medium-voltage equipments. In: CIGRE
11. Senthil Kumar S, Willjuice Iruthayarajan M, Bakrutheen M (2014) Analysis of vegetable liquid insulating medium for applications in high voltage transformers. In: IEEE international conference on science, engineering and management research, Chennai, pp 1–5
12. Syed Mohammed Mazood L, Bakrutheen M, Willjuice Iruthayarajan M, Karthik M (2015) Studies on critical properties of vegetable oil based insulating fluids. In: IEEE INDICON, New Delhi, pp 1–4

13. Radha R, Willjuice Iruthayarajan M, Bakrutheen M (2016) Performance of natural high oleic ester based blended oil insulation for transformer. In: international conference on intelligent systems and control, Comibatore
14. Xiang C, Zhou Q, Li J, Huang Q, Song H, Zhang Z (2016) Comparison of dissolved gases in mineral and vegetable insulating oils under typical electrical and thermal faults. J Energ 9:1–22
15. Mehta DM, Kundu P, Chowdhury A, Lakhiani VK, Jhala AS (2016) A review on critical evaluation of natural ester vis-a-vis mineral oil insulating liquid for use in transformers: Part 1. IEEE Trans Dielectr Electr Insul 23(2):873–880
16. Hosier L, Guushaa A, Westenbrink EW, Rogers C, Vaughan AS, Swingler SG (2011) Aging of biodegradable oils and assessment of their suitability for high voltage applications. IEEE Trans Dielectr Electr Insul 18(3):728–738
17. Bakrutheen M, Karthik R, Madavan R (2013) Investigation of critical parameters of insulating mineral oil using semiconductive nanoparticles. In: IEEE international conference on circuits, power and computing technologies, Nagercoil, pp 294–299
18. Raymon A, Karthik R (2013) Enhancement of critical parameters of used transformer oil with naturally activated bentonite and investigation of vegetable oil performance with antioxidants. In: IEEE international conference on circuit, power and computing technologies, Nagercoil, pp 625–629
19. Samuel Pakianathan P, Rajamani MPE (2013) Enhancement of critical characteristics of vegetable oil and used mineral oil of power transformer. In: IEEE international conference on circuit, power and computing technologies, Nagercoil, pp 648–652
20. Sindhuja K, Srinivasan M (2015) Enhancement of critical characteristics of natural ester based insulating fluids using nanoparticles for transformer applications. Int J Appl Eng Res 10(20)
21. Srinivasan M, Ragupathy US, Sindhuja K, Raymon A (2016) Investigation and performance analysis of nanoparticles and antioxidants based natural ester. Int J Adv Eng Technol 7 (2):1000–1007
22. Karthik M, Willjuice Iruthayarajan M, Bakrutheen M (2015) Investigation of vegetable oil blended with antioxidant. In: IEEE international conference on electrical, computer and communication technologies, Coimbatore, pp 1–7
23. Fofana I, Wasserberg V, Borsi H, Gockenbach E (2002) Challenge of mixed insulating liquids for use in high voltage transformers—Part 2: investigations of mixed liquid impregnated paper insulation. IEEE Electr Insul Mag 18(4):5–16
24. Perrier C, Beroual A, Bessede JL (2006) Improvement of power transformer by using mixtures of mineral oil with synthetic esters. IEEE Trans Dielectr Electr Insul 13(3):556–564
25. Karthik R, Raja TSR, Shanmugam SS, Sudhakar T (2012) Performance evaluation of ester oil and mixed insulating fluids. J Inst Eng India Ser B 93(3):173–178
26. Murray T, Resende F, Luo G (2014) Bio-oil: an introduction to fast pyrolysis and its applications. In: Washington state university extension fact sheet, USA, pp 1–8
27. Kan T, Strezov V, Evans TJ (2016) Lingocellulosic biomass pyrolysis: a review of product properties and effects of pyrolysis parameters. J Renew Sustain Energy Rev 57:1126–1140
28. Mohan D, Pittman CU, Steele PH (2006) Pyrolysis of wood/biomass for bio-oil: a critical review. J Energy Fuels 20:848–889
29. Bridgewater AV (2012) Upgrading biomass fast pyrolysis liquids. J Environ Prog Sustain Energy 32(2):262–268
30. Karthik R, Sree Renga Raja T (2012) Investigations of transformer oil characteristics. IEEJ Trans Electr Electron Eng 7:369–374
31. IEC 60156: Insulating liquids—Determination of the breakdown voltage at power frequency —Test method. Third Edition, 11 (2003)
32. ASTM D 93: Standard Test Methods for Flash Point by Pensky-Martens Closed Cup Tester (2012)
33. ASTM D 445: Standard Test Method for Kinematic Viscosity of Transparent and Opaque Liquids and Calculation of Dynamic viscosity (2011)

A Novel Approach to Using Energy-Efficient LED-Based Visible Light Communication in Hospitals

B. Anitha Vijayalakshmi and M. Nesa Sudha

Abstract Promising developments in the light-emitting diode (LED) technology have urged the interest to adapt LEDs for both illumination and data transmission. LED is expected to be the main lighting source in the future due to its energy-efficient characteristics as compared to the conventional incandescent and fluorescent lighting. Visible light communication (VLC) provides flexibility and convenience for patients and avoids the risk of disturbance from electromagnetic waves. VLC has no associated health concerns, and it is suitable for use in hospitals and also provides high data rates. This paper proposes a novel approach in the transmission of healthcare information using the up-and-coming wireless visible light communication technology.

Keywords Visible light communication · LED · Hospitals · Li-Fi · Wireless

1 Introduction

Optical wireless communication using light-emitting diodes (LEDs) is a talented harmonizing technology for the existing commercial radio frequency (RF) transmission scheme. The contemporary RF spectrum having dexterous frequency and spatial reprocess is not able to meet present spectrum needs with increasing traffic demand. Visible light communication supports the broadband transmission technology to transfer data and compensates the network traffic taking place in indoor environments and at fixed locations [1]. Visible light communication

B. Anitha Vijayalakshmi (✉)
Kings Engineering College, Chennai, Tamil Nadu, India
e-mail: anithaneil@yahoo.co.in

M. Nesa Sudha
Karunya University, Coimbatore, Tamil Nadu, India
e-mail: nesasudha@karunya.edu

M.C. Bhuvaneswari and J. Saxena (eds.), *Intelligent and Efficient Electrical Systems*, Lecture Notes in Electrical Engineering 446,
https://doi.org/10.1007/978-981-10-4852-4_18

systems provide secure method of transferring information between a transmitter and a receiver, since it does not allow high mobility through obstacles. And too the VLC offers very less interference when compared with RF waves and provides a reasonably reliable and precise data transfer.

2 Li-Fi to Revolutionize Our Future

LED, a lightbulb, is not only a light spending unit but also acts as wireless transceiver or as an access point that does not rely on base station for connectivity like radio-based wireless connectivity. As LED consumes less energy it will be more competent in future. Li-Fi signals cannot pass through walls as like radio waves. Data streams will be more secured from external hacking since it will be contained in a room. Li-Fi is faster, and it can convey data at a speed of 1 gigabit per second, which is 100 times faster than the existing Wi-Fi. Li-Fi is safe as it does not interfere with other radio signals as like Wi-Fi so it can be used in places like hospitals.

3 Network Capacity Evolution

In the order of the day with the speedy development of mobile digital devices, the need of high-speed wireless transmission is going up exponentially. The predicted, almost exponential increase in the demand of mobile communications services over the next years, and the corresponding network capacity evolution [2] is shown in Fig. 1. Overall, mobile data traffic is expected to grow to 30.6 exabytes per month by 2020; there will be an eightfold increase over 2015. Mobile data traffic will grow at a CAGR of 53% from 2015 to 2020 [3] as shown in Fig. 2.

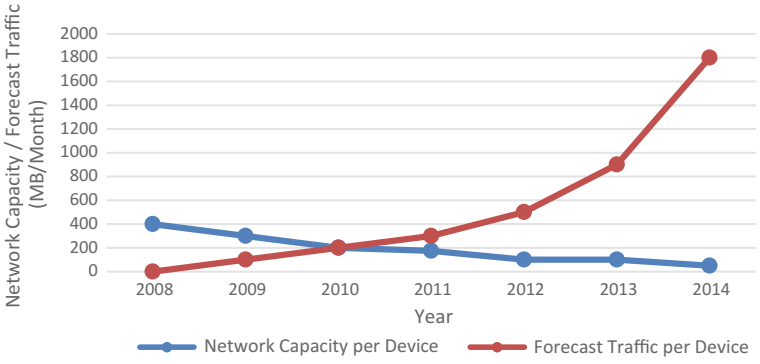

Fig. 1 Increase in demand of mobile communication services over the coming years (*Source* GBI research, Technical report 2011)

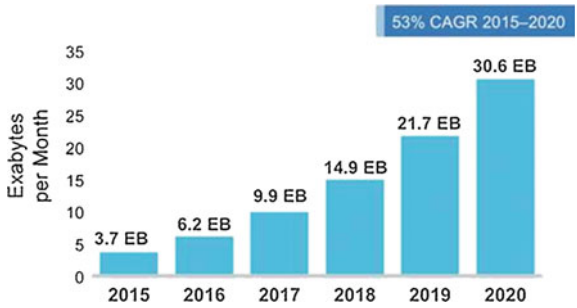

Fig. 2 Cisco forecasts 30.6 exabytes per month of mobile data traffic by 2020 (*Source* Cisco VNI Mobile, 2016)

Table 1 Performance of the conventional and LED lighting technology

	Watts	Lumens	Operating lifetime (h)
Incandescent	60	900	1000
Compact florescent lamp	15	900	8500
LED	5.8	800	40,000

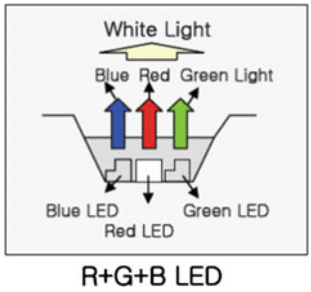

Fig. 3 Three separate LEDs, when lit at the same time, emit a light that is perceived to be white

4 Lighting Sources

The prime sources of artificial lighting are incandescent and fluorescent lamps, as incandescent units are being phased out worldwide to avoid energy wastage, and the energy-efficient alternative is LEDs, which is the main catalyst behind VLC.

LEDs are uni-directional light sources; They avoid brightness and heat in all directions. The performance comparison of the conventional and LED lighting technology [4] is mentioned in the Table 1. LED lighting saves energy in more efficient way in many applications. LEDs react faster to ones and zeros. The on and off by LEDs are undetectable to the human eye due its fast switching times. RGBs (red, green, and blue lights), as shown in Fig. 3, have three separate LEDs that emit white light when seen with the naked eye. The data rates in RGBs can reach up to 100 Mb/s.

5 Why VLC in Hospitals?

A wavelength range of approximately 400–700 nm is the visible white light region as shown in Fig. 4. Within that range, visible light communications through lighting can also be implemented in the hospital and it removes conceivable fear about interference due to RF in the hospital environment.

The care of patients unavoidably involves sharing of patient information as shown in Fig. 5. As a result, there is need of advanced communication technology to support information transfer along with health concerns. Wi-Fi communication can be replaced via Li-Fi [5, 6], which is sheltered to patient's body from attack of many types of disease as confrontation power of patient is very low.

The need of wireless technology in hospital includes various applications such as updating information wirelessly, maintaining patient records, collecting real-time handheld patient observation data, and even observing medical images via ultrasound. VLC is intrinsically safe, has no health concerns, and avoids interference caused by electromagnetic field. This makes VLC a highly credible technology for wireless access networks in hospitals. Moreover, as light is restricted to an area bounded by obscure boundaries, the coverage region of a VLC system has superior security. A comparison performance analysis between VLC and RF is shown in Table 2.

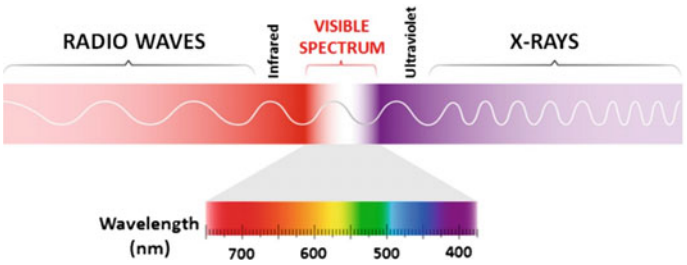

Fig. 4 Spectrum of visible region

Fig. 5 Patient's data sharing

Table 2 Comparison of performance between VLC and RF

	VLC	RF
Bandwidth	Unlimited, 400–700 nm	BW limited
Line of sight	Yes	No
Hazard	No	Yes
Security	Yes	No
Power consumption	Relatively low	Medium
distance	Short	Medium
Mobility	Limited	Yes
Coverage	Narrow	Wide
EMI	No	High

Many concerns follow with the use of wireless technology in hospitals as accuracy of information via wireless communication is essential in a hospital atmosphere. For real-time applications, the devices must be reliable and must have a delay of less than 300 ms. Security is also needed in order to maintain confidentiality about patient records and to ensure that only authorized person can access to the data being transferred wirelessly. This attracts the growth of visible light communications in hospitals.

6 Proposed Architecture of VLCs in Hospital Applications

6.1 LED Lighting in MRI

Lighting is very vital for an MRI facility. In incandescent bulbs, despite the fact that the tungsten filament is of nonferrous in nature, even microscopic impurities are exaggerated by the high-intensity magnetic field. Fluorescent light generates noise artifacts in scans. MRI facilities are benefited by light-emitting diode-based lighting devices since they are free from magnetic fields and excellent in light quality. LEDs provide basic illumination levels for operating the instruments, and backlight displays help in dipping patient stress.

6.2 LEDs in Operating Room/Examination Room

LED bulbs can be installed in various locations, which results in slighter shadows and creates a comfort zone to physicians while examining the patients. And the patients can be under vigilance for 24 h to avoid the unexpected happenings in critical situations. The recorded information about patients can be transferred to physician's portable devices (Fig. 6).

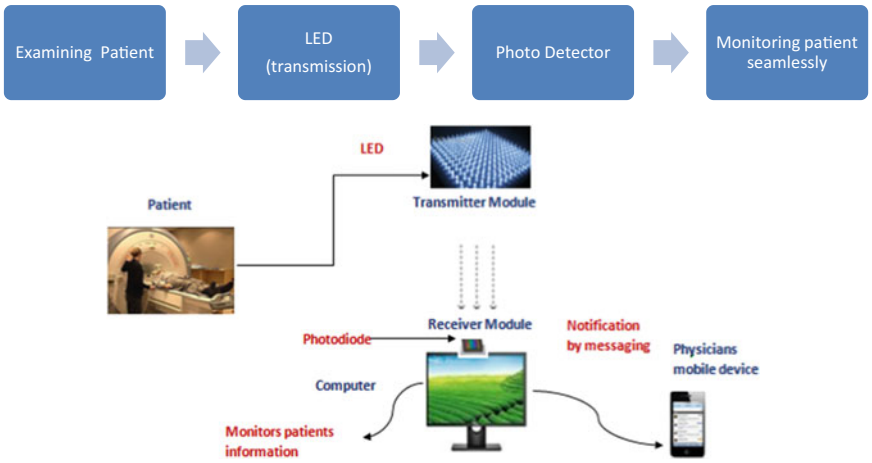

Fig. 6 The proposed system architecture for health monitoring of patients using VLC transmission and reception. Adapted from Bio-Medical Materials and Engineering (2014)

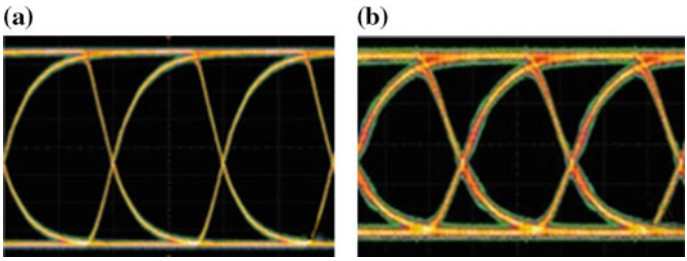

Fig. 7 Eye diagram waveforms at speeds of 1 and 2 Mbps

7 VLC Transmitter (Intensity Modulation)

The data can be transmitted by choosing two different levels of light intensity. On–off keying modulation can be used to modulate the data. An LED luminaire consists of one or more LEDs and includes a driver circuit to control the current flowing through the LEDs in turn its brightness also.

8 VLC Receiver (Direct Detection)

Photodetector receives the signal transmitted by an LED luminaire, and it converts the received light into current. The existing commercial photodetectors can easily sample the received visible light at rates of tens of Mhz. Figures 7 and 8 show the

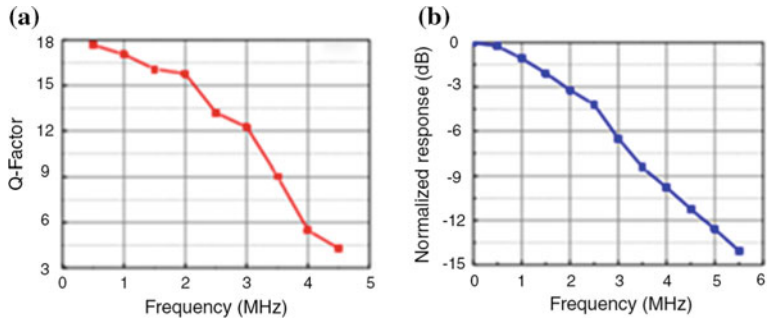

Fig. 8 Eye diagram **a** Q-factor curve and **b** normalized response curve

error-free performance at speeds of 1 and 2 Mbps after optical signal conversion into current by its eye diagram. BER is estimated from Q-factor, and all BERs are below 10^{-6} when data rate goes up to 4.5 Mbit/s [7].

9 Future Prospects

In hospitals, three leading objectives are to be taken for lighting. The urgent need now is to find a light source that doesn't cause health risks like fluorscent lights. Lights should retain longer and must require less service. Finally, the energy is saved by means of dimming; this absolutely keeps patients comfortable.

10 Conclusion

Hospitals can invest light-emitting diode which saves energy and is on the edge to benefit communication technology. This is of great importance in hospital as it ensures patient safety and also equipment safety from power fluctuations in urgent situation. Bearing in mind about the benefits of the LED, there is no surprise of adopting in hospitals.

References

1. IEEE 802.15 WPAN™ Task Group 7 (TG7). Visible light communication. http://ieee802.org/15/pub/TG7.html
2. Visible light communication (VLC)—a potential solution to the global wireless spectrum shortage. GBI Research, Technical Report 2011. http://www.gbiresearch.com
3. Cisco visual networking index: global mobile data traffic forecast update, 2015–2020. White Paper

4. Bio-medical materials and engineering 24 (2014) 3529–3538. doi:10.3233/BME-141179, IOS Press
5. Technopits.blogspot.comtechnology.cgap.org (Viewed 19 Jan 2014, verified 21 Jan 2014)
6. Li-Fi—Internet at the speed of light, by Ian Lim, the gangster (Viewed 28 Jan 2014, verified 29 Jan 2014)
7. Optics and Photonics J 3:148–152. doi:10.4236/opj.2013.32B036. Published Online June 2013. http://www.scirp.org/journal/opj

Implementation of Mesh Network Using Bluetooth Low Energy Devices

P. Gomathinayagam and S. Jayanthy

Abstract This paper aims in design and implementation of a mesh network topology for Bluetooth Low Energy (BLE) devices. BLE has become a recent topic of research in both the Internet and the wireless industry. This paper introduces BLEmesh, a wireless mesh network protocol which utilizes the broadcasting capability of wireless transmissions. The available data payload using BLE's Generic Access Profile (GAP) is used for data transfer. The data from different number of nodes and packets are send in batches. The nRF51822 device is used to implement the mesh network with the use of the soft device application provided by the developers to configure the node to switch between a peripheral and central node for data transfer. Three different sensors, namely heart beat sensor, temperature sensor, and touch sensor, are interfaced with the nRF51822 to show the mesh network working, and also the values are tabulated. The results indicate that the latency and power consumption of the proposed BLEmesh network is less than previous implementations.

Keywords Bluetooth low energy · Wireless mesh network protocol
Soft devices · Data transfer · Connection interval · Latency

1 Introduction

Bluetooth Low Energy (BLE) is an emerging wireless technology developed by the Bluetooth Special Interest Group (SIG) for short-range communication [1]. In contrast with previous Bluetooth flavors, BLE has been designed as a low-power solution for control and monitoring applications. BLE is the distinctive feature of the Bluetooth 4.0 specification [2]. Hence in this paper, the BLEmesh is

P. Gomathinayagam (✉) · S. Jayanthy
Sri Ramakrishna Engineering College, Coimbatore, Tamil Nadu, India
e-mail: gomathinayagam71192@gmail.com

S. Jayanthy
e-mail: jayanthy.s@srec.ac.in

M.C. Bhuvaneswari and J. Saxena (eds.), *Intelligent and Efficient Electrical Systems*, Lecture Notes in Electrical Engineering 446,
https://doi.org/10.1007/978-981-10-4852-4_19

implemented to use the multihop application in various domain applications. A wireless mesh network is a network topology in which each smart device (e.g., Smartphone, tablet, wearable, and laptop) transfers the data for the network. All devices in the network cooperate for sharing the data in the network. Mesh networks use flooding and routing techniques for relaying the data [3–5].

In this work, the proposed model for a BLEMesh Network (BMN) for mobile (non-static) devices is suitable for forming instant groups among smart devices. The proposed system is implemented by using the nRF51822-based BLE devices [6]. The devices are considered to be non-static, so that they can be in a dynamic movement while collecting the data and also there is no change in the protocol stack of the Nordic Semiconductors. The implementation is done by using the soft devices which will help us to configure the BLE devices as the peripheral and central device which will use the respected services to implement data transfer over the mesh network. The results show that the BMN consumes low power, data loss, and delay.

2 Prior Work

In [7], the authors have discussed the simple and efficient protocols for forming and maintaining a Bluetooth network. The protocols are designed for mobile situations with frequent topology changes and for routing of translated messages between Bluetooth network members. The proposed protocol in their paper enables re-configuration of the network after communication failure and test in simulation. The simulation is limited to testing the rules for the initial situations and node movements requiring restructuring. Problem is Bluetooth discovery itself takes up 10 s.

The authors in [8] have discussed an important issue of research in wireless networks is to dynamically organize the nodes into a wireless network and route the data from the source to the destination. In this paper, they present a mesh network for mobile devices using Bluetooth Low Energy (BLE) on android-based phones. But the principle uses the service where all the devices connected in the service can access the information, and data was not protected.

In [9], they have discussed the BLEmesh, an opportunistic routing-based wireless mesh network protocol for BLE is discussed. They have identified the available data payload using BLE Generic Access Profile (GAP), Non-connectable Advertisement Data, for different nodes participating in BLEmesh and the number of packets to send in a batch. One major characteristics of BLE, the authors have not taken account for the three advertisement channels used in BLE. The drawback of the project is that the simulations were done under the assumption of one advertising channel in existence. Furthermore, the support for multiple simultaneous flows in opportunistic routing could also enrich BLEmesh.

In [10], author has discussed the tools and techniques to monitor and inject packets in Bluetooth Low Energy devices found in recent high-end smart phones, sports

devices, sensors, and many medical devices. The author demonstrates that it can effectively render useless the encryption of any Bluetooth Low Energy link. But the problem is that all the BLE links are not safe and encrypted. These links can easily be monitored or can be attacked since it does not support encryption algorithm.

3 System Design

The existing works majorly used simulation as the basic tool to perform routing [11] and configure the device to utilize the data transfer. In this system, the BLEmesh network has been implemented by using the nRF51822 controller. The device has an inbuilt BLE stack which helps to reduce the work load of the processor to a minimum level. Using a configured stack will reduce the error in the program and also provide a stable memory. The final destination node system was implemented by using the BLE present in the device like android phones.

3.1 Block Diagram of Implementation

Figure 1 shows the block diagram of the data transfer between the nodes. The data is routed from BLE1 to the android phone though BLE2. The system implementation has 3 nodes where the source has the sensor connected to it. The data and acknowledgment signals are shown for data transfer.

3.2 Schematic Diagram

The source BLE schematic diagram is shown Fig. 2, multiple sensors have been connected to collect data and hop the data over the network. The different sensors are heart beat sensor, analog temperature sensor, and touch sensor.

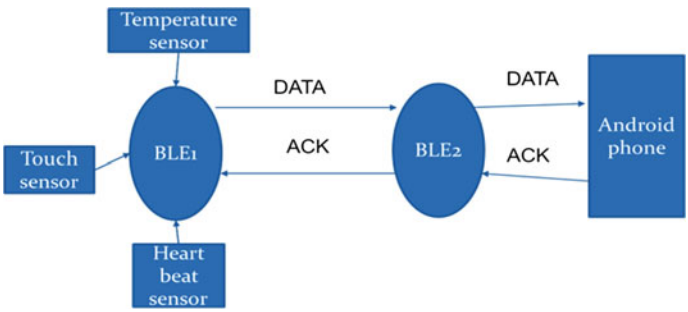

Fig. 1 Block diagram of the implementation

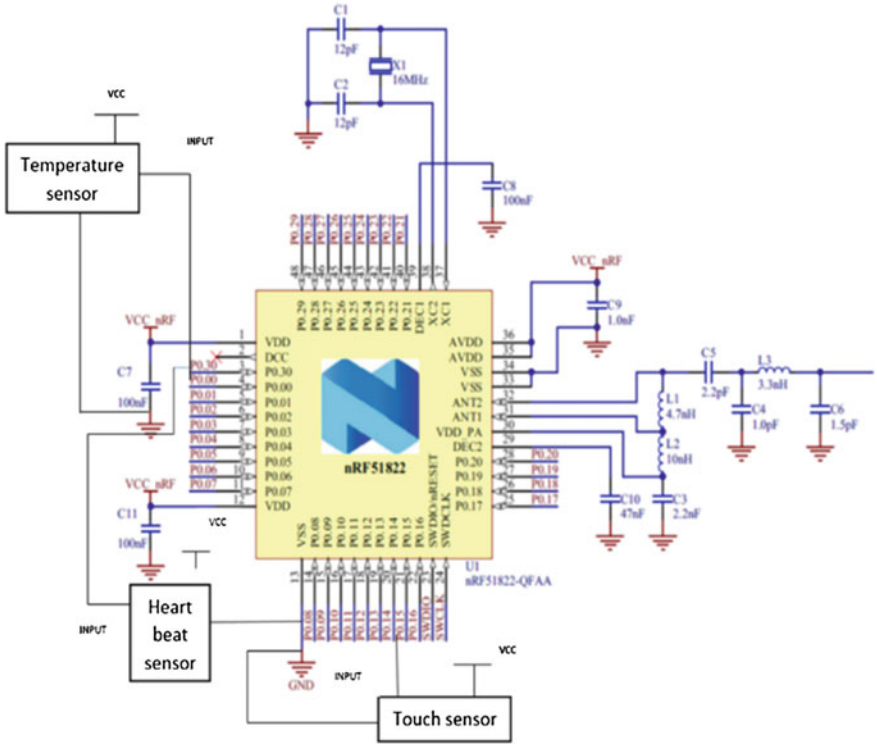

Fig. 2 Schematic diagram

The heart beat sensor has three pins where the two pins are connected to the VCC and Ground pins. The third pin is the Source pin which is connected to the Pin P0.0 of the nRf51822 chip, then heart beat sensor has to be attached to the finger of the user. The temperature sensor has four pins where the two pins are connected to the VCC and Ground pins. The third pin is the Analog Out pin which is connected to the Pin P0.1 of the nRf51822 chip, the sensor can be used to measure both the room temperature and the temperature of the person in contact.

The metal touch sensor has four pins where the two pins are connected to the VCC and Ground pins. The third pin is the Source pin which is connected to the Pin P0.15 of the nRf51822 chip, the sensor when comes in contact with a conductor element, it starts sensing.

3.3 Software Algorithm

The algorithms describe the free node connection flow and the master–slave connectivity flow.

Algorithm 1: Free node connectivity
The algorithm is for a Free node connectivity rules

Seek;
if(invited) Connect, become *SLAVE* IF(discovered any) Try to connect;
if(not connected) Go back to Seek;
else if(connected to master) become *SLAVE* ELSE IF(connected to bridge with visible master)
try to connect(to its master);
if(connected) Drop the bridge, become *SLAVE*; ELSE become *MASTER*;

Algorithm 2: Master node connectivity
The algorithm is for a Master node connectivity rules

if(time to seek and slaves less than 5) seek;
if(invited by a free node) accept it as a slave;
if(found unreachable node) try to connect; if(time for slaves to seek) let slaves seek;
if(still unreachable master found) connect
BRIDGE;

Algorithm 3: Slave node connectivity
The algorithm is for Slave node connectivity rules

if(master order to seek) Seek; IF(invited) accept, become a *BRIDGE* IF(found unreachable)
Try to connect;
IF(connected) become *BRIDGE*

```
ERASE BONDS OF PREVIOUS
CONNECTION;
DECLARE VARIABLES (uint8_t strBuff[50];double alpha = 0.75;int period =20;double change = 0.0
CONFIGURE ADC
INITIALIZE (led, stack, gap_parametrs, services,advertising, connection_parameter)
START ADVERTISING
WHILE(TRUE)
{
INTERRUPT (GIVES adc_sample)
      int value = alpha * oldValue + (1 - alpha) * adc_sample
UART_TX(value)
      if (err_code !=NRF_ERROR_INVALID_STATE)
      {
      APP_ERROR_CHECK(err_code);
      }
      CHECK POWER
```

Fig. 3 Pseudocode of main program

3.4 Pseudocode

The pseudocode for the main program calculation is given below Fig. 3 shows the pseudocode of the main algorithm for the initialization and calculation of the sensor values.

4 Experimental Results

The entire system was designed and the experiments were conducted using the BLE devices to evaluate the effectiveness of the proposed BMN. The proposed BMN was implemented on the nrf51822 SoC connected with a heartbeat sensor. The data from the BLE has to hop from the peripheral (source) to the destination (android phone) through various BLE nodes. Here, the android phone acts as the end of the network which is the destination. The node with the sensor connected to it is assigned as the source node. The maximum packet size was 20 bytes. The nodes were separated by 10 m.

The parameters taken for consideration of the BLE include the connection interval time, RSSI, and the latency.

Figure 4 shows the heart beat sensor in connection with the nRF51822 starting node. The sensor is connected as input to the pin P0.1 in the BLE kit; the other pins are connected to ground and VCC, respectively.

4.1 Performance Metrics

4.1.1 Connection Interval

The hopping can be achieved in the BLE by the switching of modes in the device [5]. So each time a hop happens, the BLE has to switch from the central to peripheral mode. The connection interval is the total time taken for the connection to be established for data transfer. It is shown in Table 1.

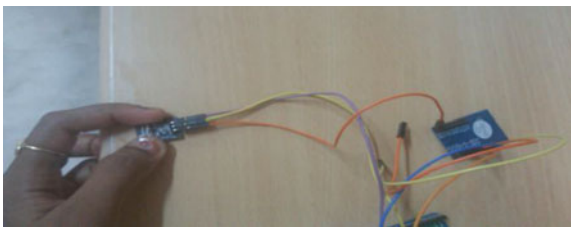

Fig. 4 Sensor in connection with nRF51822

4.1.2 RSSI

In telecommunications, received signal strength indicator (RSSI) is a measurement of the power present in a received radio signal. RSSI is usually invisible to a user of a receiving device. However, because signal strength can vary greatly and affect functionality in wireless networking, IEEE 802.11 devices often make the measurement available to users. It can also be sampled by an internal ADC and the resulting codes available directly or via peripheral or internal processor bus. The RSSI value changes if there is any obstacle present in the path between the source and receiver. The RSSI value can be used to locate the transmitter. The RSSI value helps to decide the use of device for various applications (such as data, video, and audio). The lower the RSSI value, the greater will be its power consumption.

Table 1 shows the analysis of the connection interval timing and the RRSI value for the heart beat sensor. The experimental values were taken in different instances of time and the values were tabulated.

4.1.3 Latency

The latency is measured as half the round trip time of a message in milliseconds. The time taken for data to transfer after establishment of the connection is termed as the latency. The deviation in the latency value may be because of the obstacle in path and delay in data acquisition and connection interval.

Table 2 is the comparison for the latency time calculated from the proposed system and the system proposed by Sirur et al. (2015). The experiments values are taken in random by changing the distance between the devices and also at different time intervals.

The proposed system has very less latency than the previous implementation. The major advantage of the implemented system is that it is dedicated only for the data collection and routing of data as referred in the system proposed by Sirur et al. (2015). Their paper was implemented in smart phones so the latency was due to another functional interrupt. Thus, by using a dedicated system for BLE devices, the hop interval and latency have been reduced.

In [12], a Wireless Sensor Network using Bluetooth Low energy has been designed for 3 nodes, each node using different SoC chips. The power consumption of their system was higher. The proposed system was also implemented using three nodes and consumes much reduced power, because of the higher control of the

Table 1 Connection interval with RSSI value

Experiment	Connection lnterval (ms)	RSSI (dBm)
1	10	−68
2	26	−71
3	18	−75
4	30	−78
5	21	−73

Table 2 Latency comparison

Experiment	Latency (ms)			
	Proposed system	Sirur et al. (2015)	Proposed system	Sirur et al. (2015)
	1-hop		2-hop	
1	521	665	1004	1150
2	666	1320	1208	1610
3	651	1570	1372	2115
4	852	1555	1452	2115
5	1333	3205	2345	3440

sleep states, and power consumption of the implemented SoC chip used is also less. RSSI values are also higher compared to the previous work for the same transmission power of −8 dB. For a distance of 10 m, the RSSI value was on an average −70 dB in the proposed system, whereas the RSSI values in their implementation was −70 dB for 0.5 m and it decreases to −90 dB for 3 m.

5 Conclusion and Future Work

The paper aims in developing BLEmesh network for the wireless environment to implement the data transfer in the BLE devices. The device is configured to send data over the network in multihop process. The use of the UUID characteristic will differentiate the devices in the network, and the data can only be transferred and read using only the respective UUID value. An interesting observation from this result is that the network latency is almost same in all experiments for a given value of hop counts. It indicates the stability of the proposed BMN.

The future work will include the use of programming a BLE stack based on the application. The BLE stack can only be designed by the permission from the Bluetooth SIG.

References

1. Bluetooth Special Interest Group (2014) Bluetooth internet protocol support profile specification Version 1.0.0, Dec 2014
2. http://www.bluetooth.com/Pages/Press-Releases-Detail.aspx?ItemID=224
3. Kim SH, Chong PK, Kim D (2014) A location-free semi-directional flooding technique for on-demand routing in low-rate wireless mesh networks. IEEE Trans Parallel Distrib Syst 25 (12):3066–3075
4. Zhao X, Guo J, Chao CT, Misra A, Jha SK (2013) High-throughput reliable multicast in multi-hop wireless mesh networks. IEEE Trans Mob Comput 14(4):728–741

5. Guo Z (2015) An on-demand scatternet formation and multi-hop routing protocol for BLE-based wireless sensor networks. In: IEEE Wireless Communications and Networking Conference (WCNC), pp 1590–1595
6. https://www.nordicsemi.com/eng/Products/Bluetooth-low-energy/nRF51822
7. Hyn˘cica O, Zezulka F, Fiedle P (2005) Bluetooth mesh network protocol. In: ACMOS'05 proceedings of the 7th WSEAS international conference on automatic control, modeling and simulation, pp 96–101
8. Sirur S, Juturu P, Gupta HP, Serikar PR, Reddy YK, Barak S, Kim B (2015) A mesh network for mobile devices using bluetooth low energy, SENSORS, IEEE, pp 1–4
9. Kim HS, Lee J, Jang JW (2015) BLEmesh: a wireless mesh network protocol for bluetooth low energy devices. In: 3rd international conference on future internet of things and cloud, pp 558–563
10. Ryan M (2013) Bluetooth: with low energy comes low security. In: Proceedings WOOT'13 proceedings of the 7th USENIX conference on offensive technologies, pp 4–4
11. Kum DW, Le AN, Cho YZ, Toh CK, Lee IS (2010) An efficient on-demand routing approach with directional flooding for wireless mesh networks. J Commun Netw 12(1):67–73
12. Hughes J, Yan J, Soga K (2015) Development of wireless sensor network using bluetooth low energy (BLE) for construction noise monitoring. Int J Smart Sens Intell Syst 8(2):1379–1405

Online Static Security Assessment Module Using Radial Basis Neural Network Trained with Particle Swarm Optimization

M. Lekshmi and M.S. Nagaraj

Abstract Secure operation of power system is a big concern in recent power industries. Contingency selection and ranking method used is very important for the security assessment. The multilayer feed-forward artificial neural network and radial basis neural network for implementation of online static assessment take less time to assess the contingency. Composite security index is used for contingency selection and ranking. Generation power, load power, and voltages are used as input to the artificial neural network (ANN) and composite security index is decided by the trained data of ANN. In this paper, radial basis neural network is trained with particle swarm optimization (PSO) to reduce the training time and improve the accuracy. MATAB 2013a is used for building algorithms and testing. IEEE 30 bus system is used as the test system. Single line removal is taken as contingency conditions.

Keywords Security systems · Contingency analysis · Neural network
Particle swarm optimization · Power systems

1 Introduction

The security of the power system is one of the main concerns. The security analysis should give the reliability of the power system i.e., till what extend it can be safe to operate. Major power system security analysis involved with bus voltage, currents, power flows, and status of circuit breaker to identify normal and abnormal conditions. Contingency analysis is important to evaluate the outages [1, 2]. The preventive actions should be taken if any insecurity happens. Static security assessment checks the degree of security for all static constraints of post contingency steady

M. Lekshmi (✉)
Jain University, Bangalore, India
e-mail: lekshmim@hotmail.com

M.S. Nagaraj
Department of EEE, Acharya Institute of Technology, Bangalore, India
e-mail: msndvg@gmail.com

M.C. Bhuvaneswari and J. Saxena (eds.), *Intelligent and Efficient Electrical Systems*, Lecture Notes in Electrical Engineering 446,
https://doi.org/10.1007/978-981-10-4852-4_20

states is needed to solve a large set of nonlinear equations for N and $N - 1$ contingency. In online security assessment, solving a large equation may take larger computational time. So there is a need for more accurate and powerful tool for security assessment [3–6]. There is a need for improving the accuracy in the online security assessment for accurate decision making for the controllers. The accuracy in identifying the critical contingencies in contingency screening method is also needed. The ranking and selection of contingency is done by performance index (PI) derived from DC or fast-decoupled load flow for each contingency [7]. There are some problems in the above-mentioned method due to the quadratic nature of the equations [8, 9]. The performance indices are calculated separately for line flows and bus voltages, and the over all performance index defined as the sum or weighted-sum of the scalar performance indices for bus voltages and the line flows cannot provide accurate results [1, 10].

The security assessment was done with many artificial neural networks techniques for classification of security. So that the accuracy and computation improved by using ANN. Generally, ANN is done with feed-forward and error back propagation methods. The multilayer perceptron, radial basis neural network gives better results [11, 12] comparatively. The composite security index gives accurate feature extraction. The neural network trained with PSO gives accurate results recently [13–15]. This paper mainly deals with the training of the radial basis neural network with PSO algorithm for getting accurate screening.

2 Composite Security Index [1]

For N-bus, M-line system, there are $(N + M)$ dimensional normalized limit violation vectors of both bus voltages and line flows; the PI_C from [1] is defined as

$$PI_C = \left[\sum_i \left(\frac{d^u_{v,i}}{g^u_{v,i}} \right)^{2n} + \sum_i \left(\frac{d^l_{v,i}}{g^l_{v,i}} \right)^{2n} + \sum_i \left(\frac{d_{p,i}}{g^l_{p,i}} \right)^{2n} \right] \tag{1}$$

n—exponent used in the hyper ellipse equation (n is chosen as 2) [10]
d, g—normalization factors [1]

- Secure state if $PI_C = 0$
- Alarm state if $0 < PI_C < 1$
- Insecure state if $PI_C > 1$

The contingencies can be ranked in the descending order of severity-based PI_C.

3 Online Static Security Assessment Module Using PSO-Trained ANN

The online static security assessment module is modeled with artificial neural network trained with PSO algorithm. ANN gives the better results in formulation of minimum computation time comparatively. ANN trained with PSO gives better results compared to back propagation. So the implementation of online static assessment module (OSSA) is made with PSO-trained ANN method. Figure 1 shows the structure of PSO-trained ANN for OSSA implementation.

The generator buses (P_G—realpower, Q_G—Reactive Power), real and reactive power loads at all load buses (P_D, Q_D), voltage magnitudes (V), and phase angle (δ) for all buses are used for describing the system operating point and are chosen as the input for the OSSA module. The outputs are set as secure or insecure, critical contingency screening and contingency ranking. The OSSA takes loading condition and contingency as input and composite security index as output. The contingencies are represented as binary '0' (no outage) and '1' (outage).

3.1 Radial Basis Neural Network Trained with PSO

The radial basis neural network with R input is shown in Fig. 2. Radial basis neural network is different from other neural network. Here, the net input to the radial

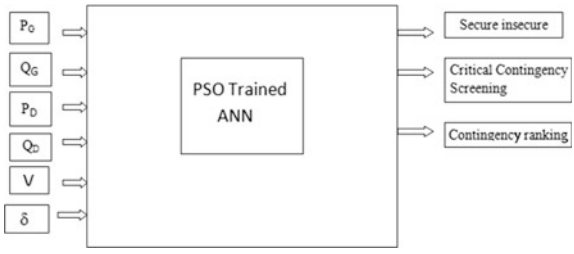

Fig. 1 Structure of online static security assessment (OSSA) module with PSO-trained ANN

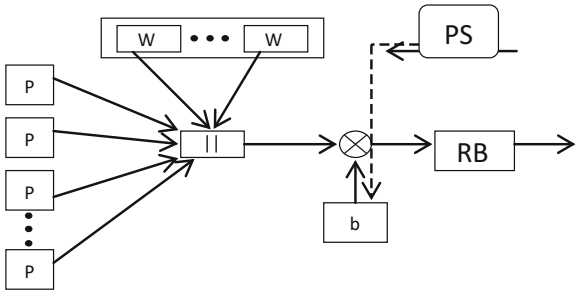

Fig. 2 Radial basis neural network trained with PSO

transfer function is vector distance between its weight vector 'w' and input vector 'p', multiplied by bias 'b'. Dist block multiples the weight value with the input p.

The transfer function for a radial basis neuron is

$$\text{radbias}(n) = e^{-n^2} \tag{2}$$

The radial basis function has a maximum of 1 when its input is 0. As the distance between w and p decreases, the output increases. The bias b allows the sensitivity of the radbias neuron to be adjusted. So while training, the neural network weights and bias are made as random population, which has to be identified by minimizing the mean square error. The procedure of PSO and its flow chart is explained in Fig. 1.

Particle swarm optimization in RBFNN training

The fitness function for minimization of mean square error (MSE) is used as below

$$\text{Minimize } F(w, b) = \sum \text{MSE} \tag{3}$$

Constrained to

$$w_{\min} \leq w \leq w_{\max} \tag{4}$$

$$0 \leq b \leq 1 \tag{5}$$

In particle swarm optimization, there are two equations: one is for updating the velocity and other one is for updating the new variable, which is to be found.

Velocity equation is given as below,

$$V_{k+1} = V_k + c_1 r_1 (\text{P}_{\text{best}} - x_k) + c_2 r_2 (\text{G}_{\text{best}} - x_k) \tag{6}$$

New weight and bias value can be found using below equation

$$x_{k+1} = x_k + V_{k+1} \tag{7}$$

where

k	iteration number
V	velocity
c_1, c_2	learning factors
r_1, r_2	random values between 0 and 1
P_{best}	personal best
G_{best}	global best
x	weight and bias vector

The flow chart below shows the PSO algorithm for minimization of a Mean Square Error (MSE) function. The initial particles are taken as the weights (w) and bias (b). For each population, fitness values of MSE are calculated. Assign all the

values as P_{best} means particle best. Then, if current P_{best} is better than the older, update the new P_{best}. Find the global best value (G_{best}—Single best values from entire population). Then, calculate velocity using velocity equation. Update the new w and b values. Continue the above process till the total number epochs. After this identify the best value of w and b for each training epochs of neural network. This is continued till the end of training epochs. Now, the entire module is trained (Fig. 3).

4 Results and Discussion

IEEE 30 bus system is taken as test system for contingency analysis. The procedure of online assessment is given below.

Step (1) The IEEE 30 data has 41 number of lines. Each line is removed and Newton–Raphson Load flow method is used to evaluate the values of $P_{G,}$ $Q_{G,}$ V, δ, and composite security index.

Step (2) For calculating the severity, Newton–Raphson Load flow has to be run each time.

Step (3) For Multilayer perceptron and radial basis neural network, training is sufficient. But by using PSO-based radial basis neural network, each epochs has to be trained with PSO algorithm shown as above.

Step (4) Here, the generator buses (P_G—real power, Q_G—Reactive Power), real and reactive power loads at all load buses (P_D, Q_D), voltage magnitudes (V), and phase angle (δ) are used as input and output is taken for composite security index. Here, for each removal $P_{G,}$ $Q_{G,}$ V, δ, and composite security are calculated for one time with Newton–Raphson method. $P_{G,}$ $Q_{G,}$ V and δ are taken as input and composite security index is taken as target.

Base load (100% of P_D and Q_D), light load (80% of P_D and Q_D), and heavy load (120% P_D and Q_D) conditions are considered in this analysis. Newton–Raphson method (NR), multilayer perceptron (MLP), radial basis function (RBF), particle swarm optimization-trained radial basis function (PSORBF) are the methods used here.

IEEE 30 bus data is depicted in Table 2. Figure 4 shows the time elapsed for NR, MLPNN, RBF, and PSORBF. It shows that PSORBF method takes the lesser time. Figures 5a, b and 6 show the contingency versus composite security index with base load condition, light load condition, and heavy load conditions, respectively. Figure 4 shows the bar chart of time elapsed. Figures 5 and 6 show the composite security index for each contingency test conditions. Time elapsed for assessment of security index is listed in Table 1 For base load, light load and heavy load time elapsed is approximately same. PSORBF gives better performance compared to other methods. And it gives over all better performances with conventional NR, MLPPNN, and RBF (Table 3).

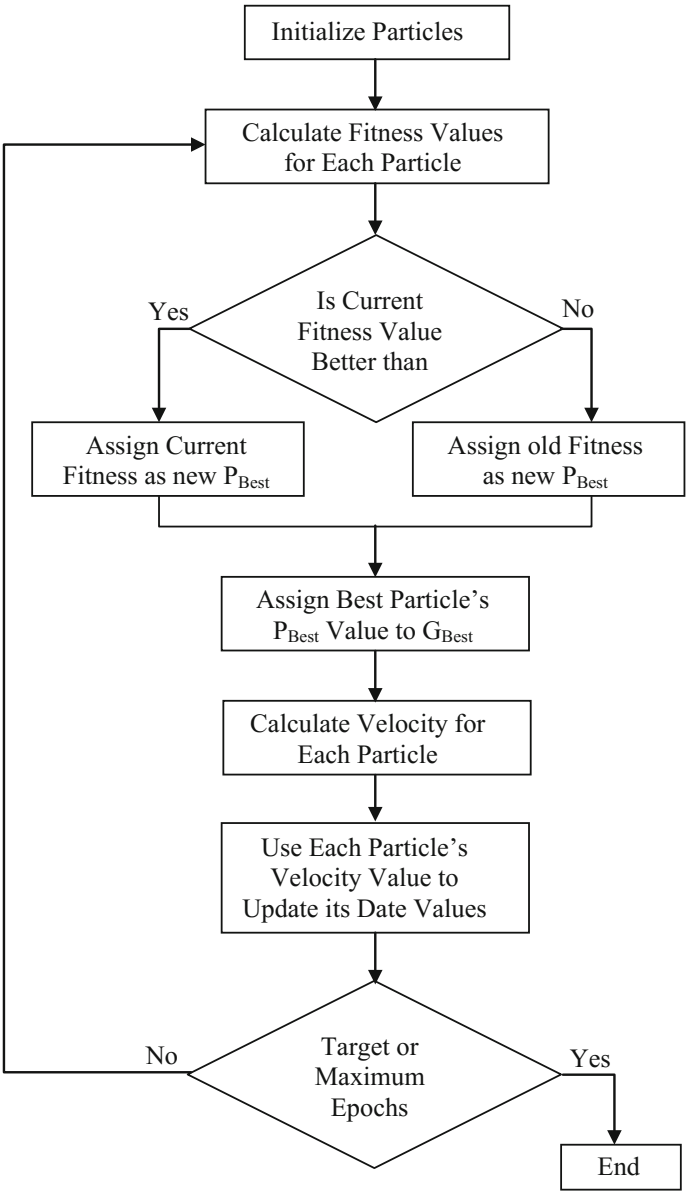

Fig. 3 Flow chart of PSO algorithm

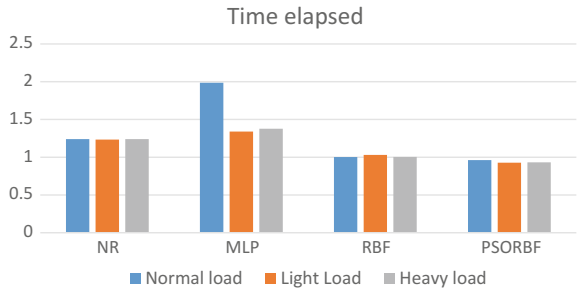

Fig. 4 Time elapsed for NR, MLP, RBF and PSORBF methods

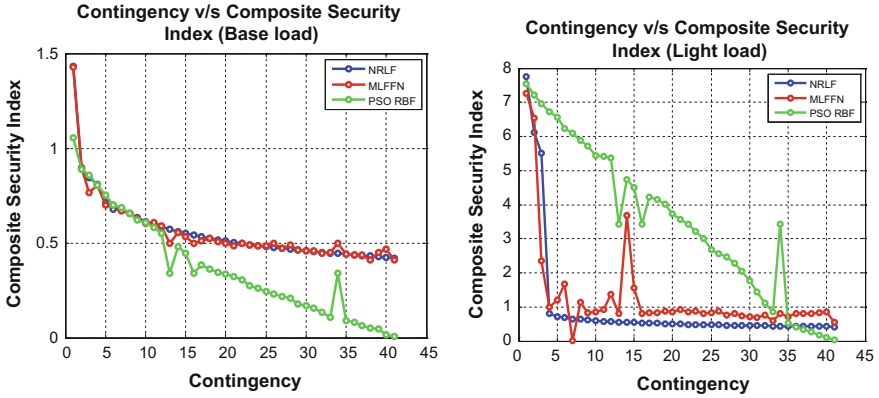

(a) Base Load (b) Light Load

Fig. 5 Contingency versus composite security index

Fig. 6 Contingency versus composite security index heavy load

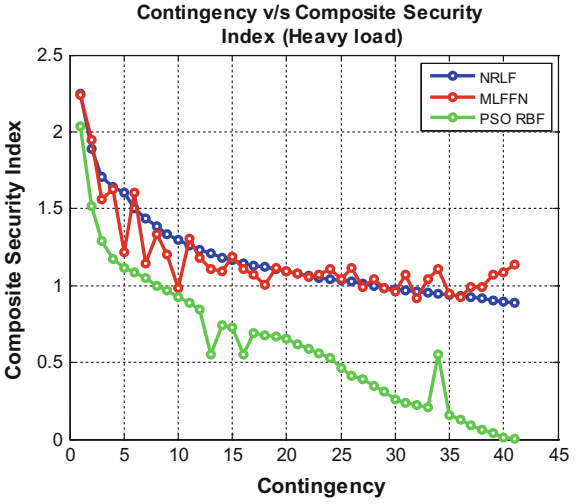

Table 1 Time elapsed for NR, MLP, RBF and PSORBF

Time in (s)	Normal load	Light load	Heavy load
NR	1.240455	1.233661	1.239358
MLP	1.986412	1.339329	1.377307
RBF	1.002822	1.030061	1.004061
PSORBF	0.962242	0.927906	0.932515

Table 2 IEEE 30 bus real power data

Bus	Load (MW)	Bus	Load (MW)
1	0.0	16	3.5
2	21.7	17	9.0
3	2.4	18	3.2
4	67.6	19	9.5
5	34.2	20	2.2
6	0.0	21	17.5
7	22.8	22	0.0
8	30.0	23	3.2
9	0.0	24	8.7
10	5.8	25	0.0
11	0.0	26	3.5
12	11.2	27	0.0
13	0.0	28	0.0
14	6.2	29	2.4
15	8.2	30	10.6

Table 3 IEEE 30 bus line data

Line	From bus	To bus	*R* (p.u.)	*X* (p.u.)	Tap ratio	Rating (p.u.)
1	1	2	0.0192	0.0575		0.300
2	1	3	0.0452	0.1852	0.9610	0.300
3	2	4	0.0570	0.1737	0.9560	0.300
4	3	4	0.0132	0.0379		0.300
5	2	5	0.0472	0.1983		0.300
6	2	6	0.0581	0.1763		0.300
7	4	6	0.0119	0.0414		0.300
8	5	7	0.0460	0.1160		0.300
9	6	7	0.0267	0.0820		0.300
10	6	8	0.0120	0.0420		0.300
11	6	9	0.0000	0.2080		0.300
12	6	10	0.0000	0.5560		0.300
13	9	11	0.0000	0.2080		0.300
14	9	10	0.0000	0.1100	0.9700	0.300

(continued)

Table 3 (continued)

Line	From bus	To bus	*R* (p.u.)	*X* (p.u.)	Tap ratio	Rating (p.u.)
15	4	12	0.0000	0.2560	0.9650	0.650
16	12	13	0.0000	0.1400	0.9635	0.650
17	12	14	0.1231	0.2559		0.320
18	12	15	0.0662	0.1304		0.320
19	12	16	0.0945	0.1987		0.320
20	14	15	0.2210	0.1997		0.160
21	16	17	0.0824	0.1932		0.160
22	15	18	0.1070	0.2185		0.160
23	18	19	0.0639	0.1292	0.9590	0.160
24	19	20	0.0340	0.0680		0.320
25	10	20	0.0936	0.2090		0.320
26	10	17	0.0324	0.0845	0.9850	0.320
27	10	21	0.0348	0.0749		0.300
28	10	22	0.0727	0.1499		0.300
29	21	22	0.0116	0.0236		0.300
30	15	23	0.1000	0.2020		0.160
31	22	24	0.1150	0.1790		0.300
32	23	24	0.1320	0.2700	0.9655	0.160
33	24	25	0.1885	0.3292		0.300
34	25	26	0.2544	0.3800		0.300
35	25	27	0.1093	0.2087		0.300
36	28	27	0.0000	0.3960		0.300
37	27	29	0.2198	0.4153	0.9810	0.300
38	27	30	0.3202	0.6027		0.300
39	29	30	0.2399	0.4533		0.300
40	8	28	0.0636	0.2000	0.9530	0.300
41	6	28	0.0169	0.0599		0.300

5 Conclusion

The online static security analysis module is modeled with neural network. IEEE-30 bus system is used for making the contingency analysis for light, heavy, and normal load conditions. Multilayer perceptron, radial basis functions, and particle swarm optimization-trained radial basis functions neural network are implemented and compared the performance. Time elapsed for training the neural network is less in PSORBF. RBF is nearing the solutions of PSORBF. NR and MLPNN are taking more time comparatively. So the PSORBF performs better in this application, which can be used for real time implementation.

References

1. Sunitha R, et al (2013) Online static security assessment module using artificial neural networks. IEEE Trans Power Syst 28(4):4328–4335
2. Morison K, Wang L, Kundur P (2004) Power system security assessment. IEEE Power Energy Mag 2(5), 30–39
3. Morison K (2000) Power system security in the new market environment: future directions. In: Proceeding IEEE PES winter meeting, pp 78–83
4. Alves AB, Monticelli A (1998) Static security analysis using pipeline decomposition. Proc Inst Elect Eng Gen Transm Distrib 145(2):105–110
5. Schainker R, Miller P, Dubbelday W, Hirsch P, Zhang G (2006) Real—time dynamic security assessment: Fast simulation and modeling applied to emergency outage security of electric grid. IEEE Power Energy Mag 4(2):51–58
6. Zhang P, Li F, Bhatt N (2010) Next generation monitoring, analysis and control for the future smart control centre. IEEE Trans. Smart Grid 1(2):186–192
7. Jensen CA, El-Sharkawi MA, Marks RJ (2001) Powersystem security assessment using neural networks: feature selection using fisher discrimination. IEEE Trans Power Syst 16(4): 757–763
8. Mikolinnas TA, Wollenberg BF (1981) An advanced contingency selection algorithm. IEEE Trans Power Appl Syst 100(2):608–617
9. Song H, Kezunovic M (2006) Static analysis of vulnerability and security margin of the power system. In: Proceeding of PES IEEE transmission and distribution conference exposition T&D, pp 147–152 May 2006
10. Halpin TF, Fischl R, Fink R (1984) Analysis of automatic contingency selection algorithms. IEEE Trans Power Appl Syst 103(5):938–945
11. Sunitha R, Sreerama RK, Mathew AT (2011) A composite security index for on-line static security evaluation. Elect Power Compon Syst 39(1):1–14
12. Vankayala VS, Rao ND (1993) Artificial neural network and their application to power system—a bibliographical survey. Elect Power Syst Res 28:67–69
13. Saeh IS, Khairuddin A (2008) Static security assessment using artificial neural network. In: Proceeding of IEEE international conference power and energy, pp 1172–1177, Dec 2008
14. Liu X (2010) Radial basis function neural network based on pso with mutation operation to solve function approximation problem. Adv Swarm Intell 6146:92–99
15. Tuba Kurban and ErkanBeşdok (2009) A Comparison of RBF neural network training algorithms for inertial sensor based terrain classification. Sensors 9:6312–6329

Ocular Artifact Suppression in Single Trial EEG Using DWT-Combined ANC

P. Prema, T. Kesavamurthy and K. Ramadoss

Abstract Artifacts are variations in the desired signal due to other external phenomenon. Major contributors of EEG artifacts are eye movement-related artifacts. As this signal propagates over the scalp, it appears in the recorded electroencephalogram (EEG) as noise that presents serious problems in EEG interpretation and analysis. Hence, preprocessing is required before any further analysis. This paper reports on effective ocular artifact suppression using discrete wavelet transform (DWT)-combined recursive least square (RLS) adaptive noise canceller (ANC) by comparing the mean square error (MSE) and artifact-to-signal ratio (ASR) metrics for the signal obtained in the fronto-polar region where the ocular artifact is dominant.

Keywords EEG · EOG · DWT · Mother wavelet · Adaptive filter

1 Introduction

Electroencephalogram (EEG) is the record of electrical activity, produced by the firing of neurons within the brain [1], and has a wide range of use in clinical diagnosis, and in past few decades, it has its extensive application in the field of brain–computer interface and neuroscience. Noninvasive BCIs use brain signals

P. Prema (✉)
Department of Biomedical Engineering, PSG College of Technology, Coimbatore, India
e-mail: ppr@bme.psgtech.ac.in

T. Kesavamurthy
Department of Electronics and Communication Engineering, PSG College of Technology, Coimbatore, India
e-mail: tkm@ece.psgtech.ac.in

K. Ramadoss
Department of Neurology, PSG Institute of Medical Sciences and Research, Coimbatore, India
e-mail: ramneuro@yahoo.com

M.C. Bhuvaneswari and J. Saxena (eds.), *Intelligent and Efficient Electrical Systems*, Lecture Notes in Electrical Engineering 446,
https://doi.org/10.1007/978-981-10-4852-4_21

recorded with sensors outside the body boundaries [2]. Such EEG records have major source of artifact that degrades the clinical analysis of signals.

2 Methodology

2.1 Experimental Setup

The EEG signal was obtained from the open-source ERP-BCI database of PhysioNet [3]. In the experimental setup, each participant was asked to spell a total of 20 characters using a traditional matrix speller. The dataset is annotated and contains the signals and triggers corresponding to a single trial for each record. Each row and column of the standard 6 × 6 matrix of characters was randomly highlighted with a stimulus onset asynchrony (SOA) of 150 ms. Target characters were randomly selected before the beginning of the run. During a run, each row and column flashed approximately 20 times and subjects were asked to focus on the target character and to mentally count the number of times it was highlighted. The electrode placements are according to 10–20 electrode system [4] (Fig. 1).

2.2 Denoising Process

Wavelet transform is one of the superior techniques in analyzing nonstationary signals like EEG [5]. It transforms time-domain signal into time-frequency

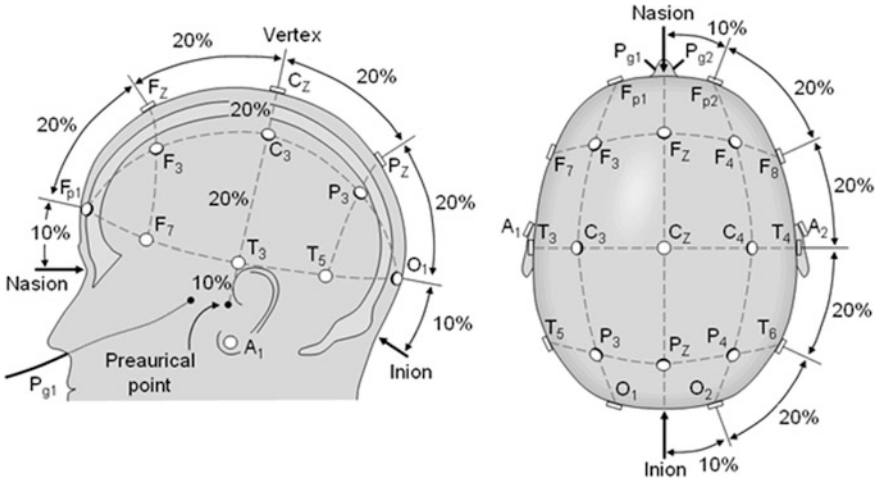

Fig. 1 10–20 electrode system (*Source* American-electroencephalographic-society guidelines in electroencephalography, evoked-potentials, and polysomnography)

localization, which helps to understand more the behavior of a signal. The mother wavelet (db4) was chosen since; it has the morphology similar to that of ocular artifact [6]. Its translation and scaling parameter acts as high- and low-pass filters. The detrending of EEG is achieved by decomposition of original signal into 5 levels by thresholding the detail coefficients at all levels as shown in Fig. 2. The reconstructed A5 coefficients are used as reference input to the adaptive filter as shown in Fig. 3. The noise component in the primary input is highly correlated to the reference input obtained by wavelet thresholding. To achieve the desired output, i.e., the denoised EEG, the adaptive filter weights are updated using exponentially weighted RLS algorithm which has good performance in nonstationary environments and is able to track slowly varying parameter [6]. The denoised EEG is shown in Fig. 4. The performance of DWT combined with adaptive filter is quantitatively evaluated and compared using the metrics mean square error (MSE) and artifact-to-signal ratio (ASR). The results were tabulated as shown in Table 1.

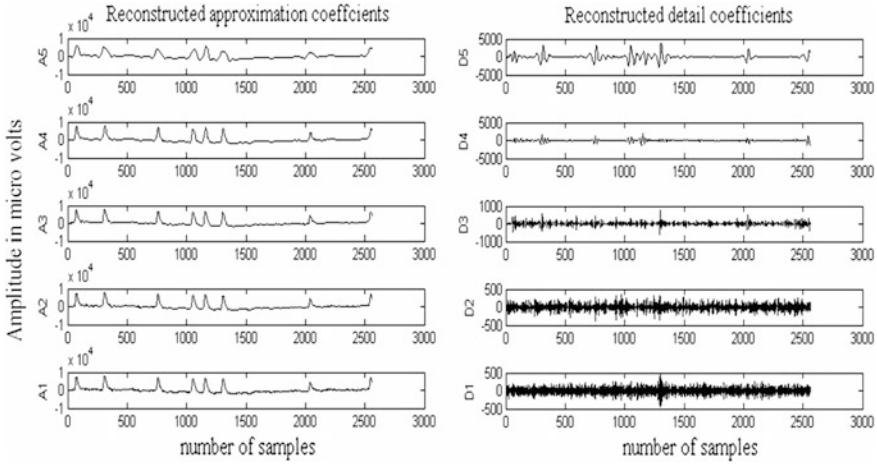

Fig. 2 Five-level decomposition of EEG

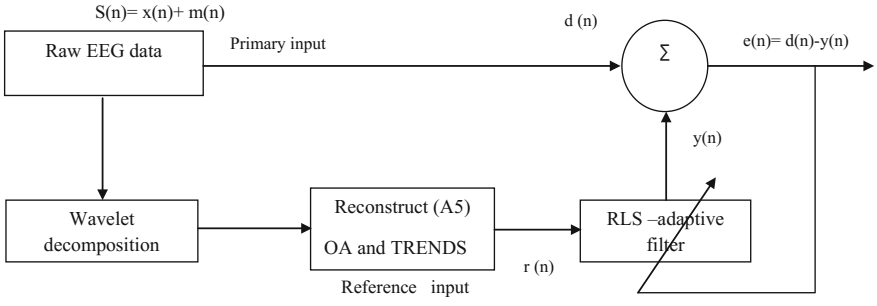

Fig. 3 Block diagram of adaptive noise canceller

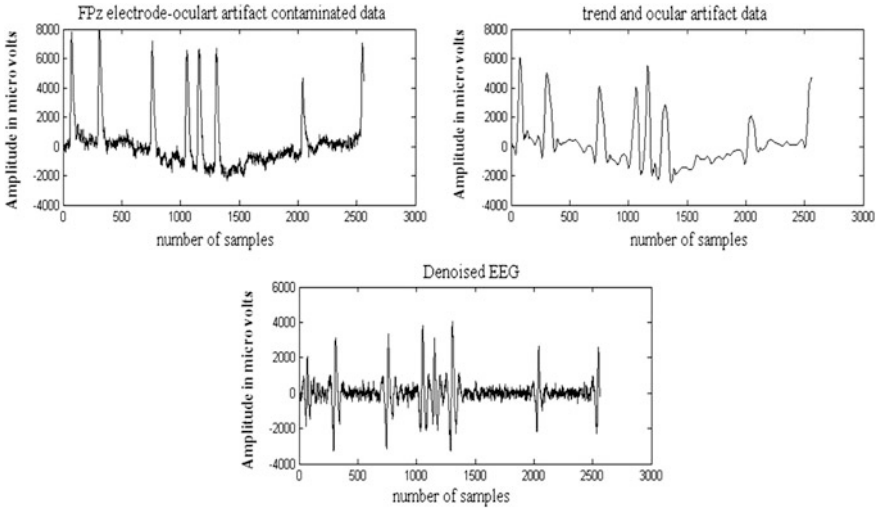

Fig. 4 Output of adaptive noise cancellation process

Table 1 Performance analysis DWT-combined RLS adaptive filter

Methods (Db4 basis function)	Mean square error (MSE)	Artifact-to-signal ratio (ASR)
DWT	1.0914e+004	1.6635
DWT + ANC (M = 1)	2.1065	3.3553
SWT	1.0554e+004	3.5986

Mean Square Error (**MSE**): For RLS adaptive filters, the MSE [7] is given by

$$\text{MSE} = \frac{\sum_{i=p}^{N} \lambda^{n-i} e^2(i)}{N - P + 1} \tag{1}$$

where N is the length of the window or number of samples, P is the length of FIR filters, λ is forgetting factor, and $e(n)$ is the error signal. Least the value of MSE, best is the performance.

For DWT and SWT, MSE is given by [8]

$$\text{MSE} = \sum_{n=1}^{N} [e(n) - x(n)]^2 / N \tag{2}$$

where $x(n)$ is the true EEG.

R^2 Value or Artifact-to-Signal Ratio (ASR): For real signals, the artifact-to-signal ratio is the metric to measure the performance, since the artifact-free EEG signal is unknown. As given by [9], ASR is calculated as

$$R^2 = \frac{\sum_{n=1}^{N} (d(n) - e(n))^2}{\sum_{n=1}^{N} e(n)^2} \tag{3}$$

where $d(n)$ is the primary or measured EEG signal, $e(n)$ is the error signal or estimated EEG signal, and N is the number of samples. The R^2 is the ratio of the power of the artifact removed from the primary signal to the estimated EEG [10]. Minimum MSE and high ASR describes better performance.

2.3 Cancellation of Power-Line Interference

The ocular artifact-suppressed EEG is found to have 50 Hz power-line interference, which was eliminated by using an eighth-order Butterworth band-pass filter [11], and the results were shown in Fig. 5.

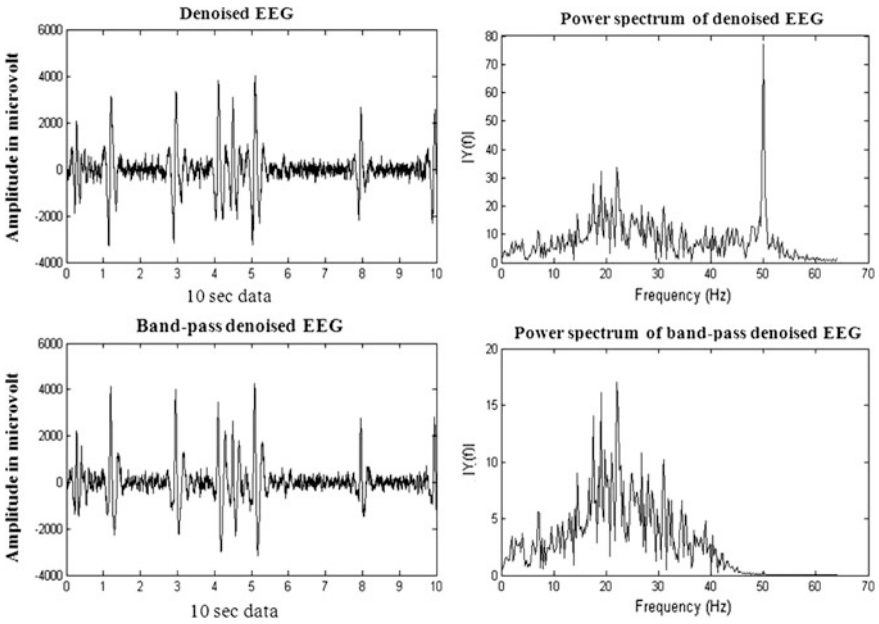

Fig. 5 Removal of power-line interference

3 Discussion

DWT-combined RLS adaptive filter (order $M = 1$) performance was compared with discrete wavelet transform and stationary wavelet transform (SWT) methods using MSE and ASR performance metrics. The minimum mean square error and high ASR are chosen to be the best performance. Table 1 shows DWT with Db4 basis-combined ANC has best performance of minimum MSE out of all the 3 methods and high ASR when compared to DWT and almost closer value as that of SWT. This work is preliminary, and further, it has to be analyzed for performance with BCI-based experiments evaluating its efficacy with other existing denoising algorithms.

References

1. Niedermeyer E, da Silva FHL (1998) Electroencephalography: basic principles, clinical applications and related fields
2. Birbaumer N (2006) Breaking the silence: brain–computer interfaces (BCI) for communication and motor control. Psychophysiology 43(6):517–532
3. Goldberger AL, Amaral LA, Glass L, Hausdorff JM, Ivanov PC, Mark RG, Mietus JE, Moody GB, Peng CK, Stanley HE (2000) Physiobank, physiotoolkit, and physionet components of a new research resource for complex physiologic signals. Circulation 101(23): e215–e220
4. Gilmore RL (1994) American-electroencephalographic-society guidelines in electroencephalography, evoked-potentials, and polysomnography. J Clin Neurophysiol 11(1):1–142
5. Mallat SA (1999) Wavelet tour of signal processing. Academic press, New York
6. Peng H, Hu B, Shi Q, Ratcliffe M, Zhao Q, Qi Y, Gao G (2013) Removal of ocular artifacts in EEG—an improved approach combining dwt and anc for portable applications. IEEE J Biomed Health Inform 17(3):600–607
7. He P, Wilson G, Russell C (2004) Removal of ocular artifacts from electro-encephalogram by adaptive filtering. Med Biol Eng Comput 42(3):407–412
8. He P, Wilson G, Russell C, Gerschutz M (2007) Removal of ocular artifacts from the EEG: a comparison between time-domain regression method and adaptive filtering method using simulated data. Med Biol Eng Compu 45(5):495–503
9. Puthusserypady S, Ratnarajah T (2006) Robust adaptive techniques for minimization of EOG artefacts from EEG signals. Sig Process 86(9):2351–2363
10. Jervis BW, Thomlinson M, Mair C, Lopez JML, Garcia MIB (1999) Residual ocular artefact subsequent to ocular artefact removal from the electroencephalogram. IEE Proc Sci, Meas Technol (IET) 146(6):293–298
11. Rangayyan RM (2015) Biomedical signal analysis, vol 33, Wiley, New York

Egomotion Estimation Using Background Feature Point Matching in OpenCV Environment

Sharmila Bakthavachalam and Nedumaran Damodaran

Abstract Autonomous systems are generally equipped with multiple sensor (such as radar, ultrasonic, IMU (Inertial Measurement Units), cameras, and GPS) assembly. Under complex scenarios, control of unmanned systems in GPS denied environment that depends on a quick estimate of their current position in space using cameras. Cameras provide information similar to human vision with an advantage of small construction space at low cost. Thus, estimating a camera's egomotion from an image sequence helps to overcome these practical difficulties of autonomous camera control. The main disadvantage of using cameras under dynamic environments includes unwanted movement and jittering in the captured data, which causes a consequence in embedded vision applications. In this paper, we described an algorithm of feature-based high frame rate egomotion estimation with gradient projection and Gabor wavelet transform, which is capable of computing real-time computer vision applications. Here, the reliable singularity points were extracted through gradient projection for reducing the processing time, and egomotion was derived by applying RANSAC. The simulation was carried out in OpenCV environment, and the results demonstrate the efficiency of the proposed technique.

Keywords Egomotion · Gabor wavelet transform · Gradient projection RANSAC · OpenCV

1 Introduction

Sophisticated human-machine interface or virtual reality relies on the basic foundation of computer vision tasks. Recently, camera-based approaches play a vital role in many automotive applications. The integration of an embedded system with smart cameras [1] performs computer vision tasks that find its way in robotics and

Sharmila Bakthavachalam · N. Damodaran (✉)
Central Instrumentation and Service Laboratory, University of Madras, Chennai, India
e-mail: dnmaran@gmail.com

M.C. Bhuvaneswari and J. Saxena (eds.), *Intelligent and Efficient Electrical Systems*, Lecture Notes in Electrical Engineering 446,
https://doi.org/10.1007/978-981-10-4852-4_22

advanced driver assistance systems. In general, robot localization involves the process of tracking the robot movement with respect to its environment [2]. The disadvantage of using cameras in these applications depends on the stability of the camera. The self-motion of the camera at the time of recording the sequence is known as egomotion or visual odometry. Usually, in urban environments, ground terrains are not flat; this leads to pitchy motions that severely affect the accuracy in motion control of the autonomous systems. Once the egomotion is estimated, the results are used to either stabilize the input video or to control autonomous vehicles in real-time. Figure 1 describes a video sequence recorded by a hand-held camera. Due to the movement and jittering, the very next frame of the video shows a drastic change in the appearance of the object (elephant).

Present work focuses on the estimation of egomotion of a camera using feature-based estimation that consists of two stages of interpretation. In the first stage, the key singular points in the current frame of input video sequence robust to small variations in illumination and textures are extracted using gradient projection method [3] and Gabor Wavelet Transform (GWT) [4]. By applying random sample consensus (RANSAC), [5] the outliers, independently moving objects inside the frame, are eliminated, and inliers such as rotational and translational movements are calculated. The inverse of the so obtained motion of the inliers results in egomotion of the camera/observer. The proposed algorithm results in good prediction and less computation time than the commonly used optical-flow [6] based motion estimation algorithms [7–12].

According to Fraundorfer and Scaramuzza [13], visual odometry yields a very small position errors ranging from 0.1 to 2% of the observer's actual position. In traditional computer vision systems, the egomotion estimation has drawbacks of complex processing and high cost. In 2004, Nister and Bergen [14] recorded stereo image pairs and derived egomotion of a camera in the absence of other external sensors and studied the problems due to mechanical issues. Combinational method of different sensor assembly, both active and passive sensors, presented a new hybrid system of low cost at the application end. Having a flying insect as a model, egomotion was estimated using combinational inputs of optical flow fields from image sensors and inertial measurement units (IMU) known as opto-aeronautic algorithm [8], which lagged in accuracy as different sensors resulted in various errors and also synchronizing these data consumed more power and processing time. To overcome such errors, generation of optical flow fields [6] and issues

Fig. 1 **a**, **b**, and **c** show the consecutive frames of a video shot by a hand-held camera

related with the robustness due to discontinuities were [15] studied. To enhance the optical flow structures in noisy image-sequence, a new anisotropic diffusion method [7] was designed with eigenvalues of the pre-recognized structure tensor. A realistic scenario for visual motion fields [16, 17] assumes a varying temporal constancy of brightness, for example, moving sources of lights. This affected the subsequent stability of robustness in egomotion estimation using optical flow fields.

The above drawbacks can be easily rectified by feature-based egomotion estimation, which has an excellent correspondence. It holds the key point for efficient egomotion detection. Here, the selection of features becomes a critical factor for obtaining optimal estimated results. Dense traffic conditions show a strategic challenge in real-time applications as they contain many background structures such as buildings, vehicles, and trees. Szeliski surveyed and presented the efficiency of pixel-based and feature-based models upon the selection of feature points [18]. The development of techniques that extracts and matches the feature using SIFT [19] and development of 3D pose estimation has given way for a proficient egomotion estimating system [20, 21] at a high complex computation. Scale invariant feature transform (SIFT) was used in feature tracking in trinocular systems by Se et al. [22]. Nister's defensive approach to RANSAC increased the efficiency of egomotion substantially [23]; later, he combined his five-point method [24] for deriving the system's egomotion parameters. But, this approach takes longer time to compute, and therefore, it is difficult to implement in real-time applications. Feature detectors, namely SURF (speed up robust features) [25], FAST (features from accelerated segment test) [26], and ORB [27], play an extensive role in feature detection based motion estimation. Pradeep presented a recovering algorithm for camera's motion using assorted features having point and line correspondences across stereo image pairs [28]. The feature-oriented estimation computed the motion with distinguished features that helped to overcome the aperture and illumination problem caused due to camera motion. Choosing an efficient feature detecting technique is an important factor as the number of feature points detected and matched directly disturbs the robustness of the successive steps. Procedure for feature extraction was initiated from deriving the gradient of the current frame to minimize the error in finding reliable singular points. Key-point detection in distorted images applied gradient compensation [29] to obtain a gain in computational efficiency. Similarly, gradient-based feature extraction was experimented in many works [30–32]. Gabor wavelet transform was applied to the singular points for further classification. A comparison study of Gabor coefficients with geometric distances was carried out by Jemaa and Khanfir, which substantiated the importance of wavelet components in automatic feature recognition [33]. Further, the generalized features and applications of 2D Gabor filter for various computer vision applications were reported in [34–37]. Subsequently, number of research attempts were reported in the literature [38–40] to discard the unwanted outliers and to estimate the rotational and translational motion of the camera using RANSAC. This paper is organized as follows: In Sect. 1, we have discussed about the basic algorithms used in this work; later in Sect. 2, we have elaborated methods and tools used for implementing the proposed

approach; Sect. 3 gives the detailed study of the results obtained from the proposed algorithm; and finally, Sect. 4 contains the concluding remarks and future work.

2 Algorithms

2.1 Gradient Projection Algorithm

Initially, the input video sequence was separated as frames for localizing the interesting key-points. In real-time scenarios, such key points from successive frames undergo drastic changes due to various environmental factors. To overcome this, gradient projection algorithm (GPA) was applied to the frames n and $n+1$ of the images I and I', respectively. Let I_x be the gradient along the x-axis and I_y be the gradient along the y-axis of the current frame. An image point that has a significant gradient magnitude greater than the noise level retains the corners of the features, whereas points with low magnitude remain as straight edges. By eliminating such straight edges, the gradient projection of the input frame results in reliable singular points of dominant feature in the current image frame.

The problem of $f: \mathbb{R}^n \rightarrow \mathbb{R}$ is a continuously differentiable mapping on C, a non-empty closed convex set of $\mathbb{R}^n$, with constrained minimization problem as described in Eq. (1).

$$\min_{x \in C} f(x) \tag{1}$$

where the object function $f(x)$ is a composite type convex function denoted by Eq. (2).

$$f(x) = F(x) + G(x) \tag{2}$$

The derived optimal solution of gradient projection problem is given as x^*, for step $k \in \mathbb{N}$, as given Eq. (3).

$$x^* = P_c[b - \lambda \eta(p_k, q_k)] \tag{3}$$

where P_c is the orthogonal projection operator on the set C, b is the observed noisy data, λ is the regularization parameter with $\lambda > 0$. The matrix pair $(p, q) \in P$, can be readily implemented [41].

2.2 Gabor Wavelet Transform

Gabor coefficients have more recognition rate when compared to geometric distances [33, 42]. The decomposition of the detected dominant feature with Gabor

wavelet transform resembles the primary visual cortex of a simple cell [43]. A complex sinusoidal plane wave modulated Gaussian kernel known as 2D Gabor filter in spatial domain is defined as Eq. (4) [44].

$$g(u, v; \lambda, \theta, \psi, \sigma, \gamma) = \exp\left[-(u'^2 + \gamma^2 v'^2)/2\sigma^2\right] \exp\{i(2\pi(u'/\lambda) + \psi)\} \quad (4)$$

$$u' = u \cos\theta + v \sin\theta \quad (5)$$

$$v' = -u \sin\theta + v \cos\theta \quad (6)$$

In Eq. (4), λ is the wavelength of the sinusoidal factor, θ denotes the orientation angle between normal and parallel strips. The ψ represents phase effect, and γ, σ are the spatial aspect ratio and sigma of Gaussian envelope, respectively. In this work, for efficient feature detection in the extracted frame images, the parameters θ, λ, ψ, γ and σ of Gabor filter are assigned the value as $\sigma = 4$, $\gamma = 0.5$, $\psi = \pi/2$, $\lambda = 50$ and $\theta = 0$. The true background information was derived by eliminating the freely moving objects (foreground information) with GWT.

2.3 Feature Matching

The features detected from consecutive frames are then matched for similarity measure. The difference in the similarity measure gives the motion vectors of the detected feature in the sequence. Motion vector fields (MVF) are used to denote the motion of objects or features within successive image frames. MVFs are derived by matching the above extracted singular point features. Let F_{fin}^{n} be a feature point in the nth frame and F_{fin}^{n+1} in the $n^{n+1\text{th}}$ frame. Let $\overrightarrow{\text{mv}_i}$ belongs to F_{fin}^{n} and $\overrightarrow{\text{mv}_j}$ to F_{fin}^{n+1}. The matches (M) between consecutive frames are represented by Eq. (7).

$$M(\overrightarrow{\text{mv}_i} \in F_{\text{fin}}^{n}) = \min_{\overrightarrow{mv_i} \in F_{\text{fin}}^{n+1}} \left\| \text{GV}_{\text{fin}}(\overrightarrow{\text{mv}_i}) - \text{GV}_{\text{fin}}(\overrightarrow{\text{mv}_j}) \right\| \quad (7)$$

In Eq. (7), GV is the normalized gradient value of the MVF's. Once the matches are extracted, the distance between each matched points are calculated. To get optimized results, a threshold value is checked with a condition of ignoring all matches which fails to satisfy $d_{\text{fm}} \geq 0.51 d_{\text{sm}}$. Here, d_{fm} and d_{sm} are the distance between first match and second match, respectively.

2.4 RANSAC

The rejection of outliers that move independent of the scene information is discarded using RANSAC technique. It randomly selects small sets of motion vectors

that gathers most support for observation and creates a hypothesis. It applies least mean square (LMS) to estimate the $\widehat{\mathrm{AT}}$. The hypothesis scoring a maximum number of consensus will be the resulting solution (inliers with higher probability) [45]. The total inliers are calculated using Eq. (8).

$$N_{\text{in}} = \left\| \overrightarrow{V_s} - \mathrm{AT}_B * \overrightarrow{V_e} \right\| \tag{8}$$

where N_{in} is number of inlier points, $\overrightarrow{V_s}$ and $\overrightarrow{V_e}$ are the starting and ending point of derived motion vector. The iteration of RANSAC model was continued till $N_{\text{in}} \geq 50\%$ of total $\overrightarrow{\text{mv}_i}$. The maximum iteration trails are limited according to the Eq. (9) [5].

$$N_{\text{iterations}} = \frac{\log(1 - P_s)}{\log[1 - (1 - \varepsilon^{N_{\text{mv}}})]} \tag{9}$$

The Eq. (9) ensures that N_{mv} vectors with a probability of P_s are free of outliers from the highest fraction of outliers ε.

Affine transformation (AT) [46] is a commonly used method for defining a camera's motion. In general, AT can be described as the mathematical form given in Eq. (10). The linear transformation parameters are a, b, d, and e with c and f as their horizontal and vertical translations, respectively. The pixel coordinates of images I and I' are denoted as (x^n, y^n) and (x^{n+1}, y^{n+1}).

$$\begin{bmatrix} x^n \\ y^n \\ 1 \end{bmatrix} = \begin{bmatrix} a & b & c \\ d & e & f \\ 0 & 0 & 1 \end{bmatrix} \begin{bmatrix} x^{n+1} \\ y^{n+1} \\ 1 \end{bmatrix} \tag{10}$$

3 Results and Discussion

The code for the proposed method was developed in OpenCV and performed using Intel core duo 3.0 GHz processor. Key feature points, which are lying at the background, hold the consistent static feature information with respect to the environment. By applying the gradient projection algorithm to the input sequence, the valuable noise-free information with high gradient values (singular points) was extracted. Another set of data was derived by implementing gradient projection in Gabor filtered image sequence. The later set gave the exact foreground information of all freely moving objects. Thus, subtracting this from the GPA applied image frame, the valuable noise-free background information with high gradient value (key singular points) was obtained. The extracted singular point features have high

accuracy with good precision that were used for further estimation process. A basic matching of features between consecutive frames generates the motion vectors of those key features. The main novelty of this proposed technique is that it yields a very good evenly distributed motion vectors over the image frame. Rotational and translational movements of the camera were computed using the motion vectors. To optimize the results, RANSAC-based elimination of outliers was performed to sort out remaining unwanted independently moving objects. To enhance the robustness of the proposed method, the motion is not only computed based on difference in successive frame, but also between the current frame and the long passed nth frame in order to provide stability in estimated egomotion.

Thus, the combination of Gabor with gradient and RANSAC allows egomotion estimation on pixel values present in the image alone without any need of 3D scene recovery. The average time taken for the whole estimation process was estimated to be around 74 ms, which is sufficient enough for the implementation of the proposed algorithm in real-time autonomous systems. Figure 2 explains the deduction of foreground objects (elephant and vehicle side view) from the image, which exhibits that all the estimated feature point vectors lies only on the background of the image scene. The effectiveness and practicability of the proposed method was evaluated by applying the real-time data recorded in an urban scenario. Different dataset with a resolution of *960* $\times$ *540* at a frame rate of *15–30* fps were tested, and the results showed a consistent output behavior.

Fig. 2 **a** Raw image frame from the video sequence, **b** gradient projection of (**a**), **c** Gabor + gradient of (**a**), and **d** detected motion vector points

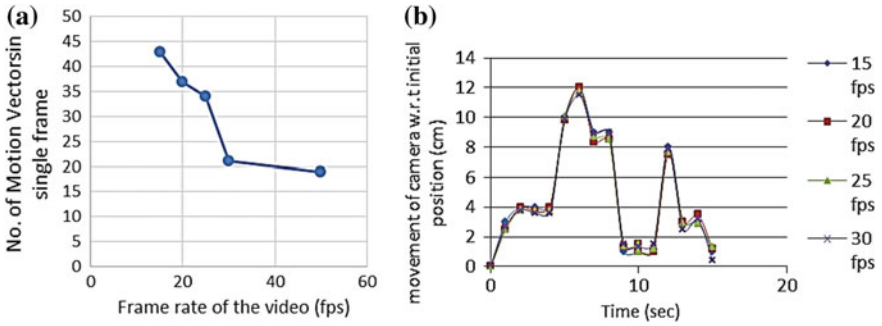

Fig. 3 **a** Detected motion vector plot for different fps of the video, **b** detected camera motion at different fps

Videos with different frame rate were also tested and the output data depending on fps and the number of motion vector detected as shown in Fig. 3. The number of motion vector is high for low frame rate, whereas it seems to be low for high frame rate; owing to the increase in frame rate, the interval between successive frames decreases resulting in low difference in motion of freely moving objects in the scene. These results elucidate that the number of detected motion vectors varies according to frame rate, even though the camera motion is almost the same. Further, this study helps in finding the motion vectors effectively for estimating the ego-motion in real-time applications.

4 Conclusions and Future Work

This study was motivated by autonomous motion control and video stabilization applications in real-time systems affected by egomotion of the camera. In the proposed work, the motion vectors of the input image sequence were used for the extraction of self-motion of the camera. Despite the freely moving features or objects present, the estimation was computed with high accuracy in real-time data. The trial results yielded a faster and robust estimation of egomotion at very low cost. Further, in future, a FPGA version of the proposed method will be attempted for reducing the processing time and for devising a fully automated embedded vision system for autonomous navigation, driving, motion control, video stabilization, and many more vision-based applications.

Acknowledgements The authors are grateful to the Department of Science and Technology for the award of a DST-INSPIRE Fellowship to carry out this research work.

References

1. Wolf W, Ozer B, Lv, T (2002) Smart cameras as embedded systems. Computer 35:48–53 (Long. Beach. Calif)
2. Borenstein J, Everett HR, Feng L, Wehe D (1997) Mobile robot positioning: sensors and techniques. J Robot Syst 14:231–249
3. Zanni L (2006) An improved gradient projection-based decomposition technique for support vector machines. Comput Manag Sci 3:131–145
4. Jiang W, Shen, TZ, Zhang J, Hu Y, Wang XY (2008) Gabor wavelets for image processing. In: Proceeding-ISECS international colloquium on computer, communication control, and management CCCM 2008, vol 1, pp 110–114
5. Fischler MA, Bolles, RC (1981) Random sample consensus: a paradigm for model fitting with applications to image analysis and automated cartography. Commun ACM 24:381–395
6. Beauchemin SS, Barron JL (1995) The computation of optical flow. ACM Comput Surv 27:433–466
7. Spies H, Scharr H (2001) Accurate optical flow in noisy image sequences. In: Eighth IEEE international conference on computer vision 1, vol 1, pp 587–592
8. Rutkowski AJ, Miller MM, Quinn RD, Willis MA (2011) Egomotion estimation with optic flow and air velocity sensors. Biol Cybern 104:351–367
9. Raudies F, Neumann H (2009) An efficient linear method for the estimation of ego-motion from optical flow. In: Lecture notes in computer science (including subseries lecture notes artificial intelligence Lecture Notes Bioinformatics), vol 5748 LNCS, pp 11–20
10. Grabe V, Bulthoff HH, Robuffo Giordano P (2012) Robust optical-flow based self-motion estimation for a quadrotor UAV. In: IEEE international conference on intelligent robots and systems, pp 2153–2159
11. Dahmen H, Franz M, Krapp H (2001) Extracting egomotion from optic flow: limits of accuracy and neural matched filters. In: Motion vision, pp 143–168
12. Brooks MJ, Baumela L, Chojnacki W (1997) Egomotion from optical flow with an uncalibrated camera. In: Proceeding SPIE-international society for optics engineering, vol 3024, pp 220–228
13. Scaramuzza D, Fraundorfer F (2011) Visual odometry part II. IEEE Robot Autom Mag 18:80–92
14. Nister D, Bergen J (2004) Visual odometry. In: Proceedings of the 2004 IEEE computer society conference on computer vision pattern recognition, CVPR 2004
15. Black MJ, Anandan P A framework for the robust estimation of optical flow. In: IEEE international conference on computer vision, pp 231–236
16. Wildes RP (1993) On the qualitative structure of temporally visual motion fields, pp 844–849
17. Gupta NC, Kanal LN (1995) 3-D motion estimation from motion field. J Artif Intel 78:45–86
18. Szeliski R (2006) Image alignment and stitching: a tutorial. Found Trends® Comput. Graph Vis 2:1–104
19. Lowe DG (1999) Object recognition from local scale-invariant features. In: Proceedings of the seventh IEEE international conference on computer vision, vol 2, pp 1150–1157
20. Nister D (2004) An efficient solution to the five-point relative pose problem. IEEE Trans Pattern Anal Mach Intell 26:756–770
21. Pollefeys M, Nistér D, Frahm J-M (2008) Detailed real-time urban 3D reconstruction from video. Int J Comput Vis 78:1–43
22. Se S, Lowe D, Little J (2002) Global localization using distinctive visual features. In: Intelligent robots and systems, IEEE/RSJ, pp 226–231
23. Nister D (2003) Preemptive RANSAC for live structure and motion estimation, Proc Ninth IEEE Intl Conf on Comput Vis 1:199–206
24. Nister D (2004) Automatic passive recovery of 3D from images and video. In: 3D data processing, visualization and transmission. 3DPVT 2004. Proceedings. 2nd international symposium, pp 438–445

25. Bay H, Ess A, Tuytelaars T, Van Gool L (2008) Speeded-up robust features (SURF). Comput Vis Image Underst 110:346–359
26. Trajkovii M, Hedley M, Trajkovic M, Hedley M (1998) Fast corner detection. Image Vis Comput 16:75–87
27. Rublee E, Bradski G (2011) ORB—an efficient alternative to SIFT or SURF, In: International Conference on Computer Vision (ICCV), pp 2564–2571
28. Pradeep V (2010) Egomotion using assorted features, Intl J Comput Vis 98(2):202-216
29. Lourenco M, Baretto JP, Malti A (2010) Feature detection and matching in images with radial distortion. In: IEEE International Conference on Robotics and Automation, pp 1028–1034
30. Kobayashi T, Hidaka A, Kurita T (2008) Selection of histograms of oriented gradients features for pedestrian detection. In: Lecture notes in computer science (including subseries lecture notes artificial intelligence lecture notes bioinformatics), 4985 LNCS, pp 598–607
31. Chen Y, Yeh T (2009) A method for extraction and recognition of isolated license plate characters. J Comput Sci 5:1–10
32. An Y, Rasheed W, Park S, Park J (2011) Feature extraction through generalization of histogram refinement technique for local region-based object attributes. Int J Imaging Syst Technol 21:298–306
33. Jemaa YB, Khanfir S (2009) Automatic local Gabor features extraction for face recognition. Int J Comput Sci Inform Secur 3(1):1–10
34. Kamarainen JK, Kyrki V, Kälviäinen H (2006) Invariance properties of Gabor filter-based features—overview and applications. IEEE Trans Image Process 15:1088–1099
35. Lee TS (1996) Image representation using 2D Gabor wavelets. IEEE Trans Pattern Anal Mach Intell 18:959–971
36. Pang WM (2010) Towards fast gabor wavelet feature extraction for texture segmentation by filter approximation. In: Proceeding-9th IEEE/ACIS international conference on computer and information science ICIS 2010, pp 252–257
37. Nestares O (1998) Efficient spatial-domain implementation of a multiscale image representation based on Gabor functions. J Electron Imaging 7:166
38. Yang S-W, Wang C-C (2009) Multiple-model RANSAC for ego-motion estimation in highly dynamic environments. In: IEEE international conference on robotics and automation, pp 3531–3538
39. Hong S, Ye C (2014) A fast egomotion estimation method based on visual feature tracking and iterative closest point. In: IEEE 11th international conference on networking, sensing and control (ICNSC), pp 114–119
40. Del-Blanco CR, Jaureguizar F, Salgad L, García N (2008) Motion estimation through efficient matching of a reduced number of reliable singular points. In: Proceeding, vol 6811, pp 68110 N–68110 N–12
41. Soman KP, Ramanathan R (2016) Digital signal and image processing. pp 408–416
42. Wei C, Li Y, Li C Effective extraction of Gabor features. IEEE International Conference on Multimedia and Expo. pp 1503–1506
43. Daugman JG (1985) Uncertainty relation for resolution in space, spatial frequency, and orientation optimized by two-dimensional visual cortical filters. J Opt Soc Am A 2:1160–1169
44. Amayeh G, Tavakkoli A, Bebis G (2009) Accurate and efficient computation of Gabor features in real-time applications. In: Lecture notes in computer science (including subseries lecture notes artificial intelligence lecture notes bioinformatics), vol 5875 LNCS, pp 243–252
45. Brown M, Lowe DG (2007) Automatic panoramic image stitching using invariant features. Int J Comput Vis 74:59–73
46. Wisetphanichkij S, Dejhan K (2005) Fast fourier transform technique and affine transform estimation-based high precision image registration method. GESTS Int Trans Comput Sci Eng 20:179–191

Performance Analysis of Wavelet Function Using Denoising for Clinical Database

Karthick Ganesan and Harikumar Rajaguru

Abstract Medical image processing plays a significant role in disease diagnosis and provides the details about tissues and organs. Image denoising techniques are used to restore the original information of the image and remove unwanted distortion. In this paper, denoising the clinical database image using discrete wavelet transform (DWT) is done and the performance is measured by considering the following quality metric parameters, namely peak signal-to-noise ratio, structural content, image fidelity, normalized correlation coefficient, structural similarity index, and universal quality index. We evaluate the performance of various wavelet filter coefficients for image denoising and which wavelet coefficient would be most reliable one on clinical dataset, and their efficiency is reported.

Keywords Denoising · Discrete wavelet transform · Clinical database image

1 Introduction

Image denoising is a basic operation to improve image analysis. In medical image processing, denoising is a necessary one and used to find out the abnormalities and to highlight some information about tissues contained in the image. The denoising process requires prior knowledge of the noise, otherwise it is not possible to get an ideal output image. Different types of images present different types of noises. Denoising process depends upon the problem, type of image, and noise model. While scanning irrespective of the sensor machines, some amount of noise will be added in scanned images and also physical phenomena properties of scanners are added with the image in noise form. Normally noise can be introduced by improper

K. Ganesan (✉)
Anna University, Chennai, Tamil Nadu, India
e-mail: karthick.sgs@gmail.com

H. Rajaguru
Bannari Amman Institute of Technology, Erode, Tamil Nadu, India
e-mail: harikumarrajaguru@gmail.com

M.C. Bhuvaneswari and J. Saxena (eds.), *Intelligent and Efficient Electrical Systems*, Lecture Notes in Electrical Engineering 446,
https://doi.org/10.1007/978-981-10-4852-4_23

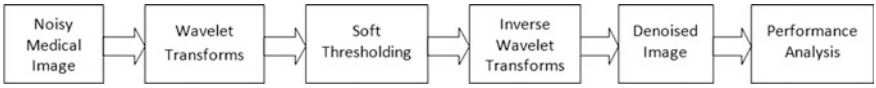

Fig. 1 Block diagram of image denoising using wavelet transform

machines, acquisition process, transmission, and compression processing. It is unwanted interference, and so the original image visual quality and information will be degraded. The denoising process involves in removing the noise in homogeneous (smooth) regions and to preserve edges, details, and texture [1]. It is challenging one because it causes blurring and corrupts the original image pixel values. Till now, lots of image denoising techniques have been designed but each technique has own advantages and drawbacks. Therefore, denoising process of clinical images is a very difficult task and crucial for a diagnosis. Normally, noise models are classified as additive and multiplicative noise models.

Spatial domain and Time domain filters are used in image denoising process to remove noise models. Spatial domain filters are efficient to remove the unwanted interference signal, but the sharp edges are blurred because of reducing the bridging gap of the pixels. It is not suitable for strong speckle noise. Hence, frequency domain filters are used to preserve the edges of the images. Wavelet techniques are one of the transform domain non-adaptive filtering techniques. Wavelet transform is suitable for denoising because of its properties such as sparsity, multi-resolution, and multi-scale nature [2]. Figure 1 represents outline of wavelet transform-based image denoising technique. Here a noisy clinical dataset is taken as the input. In the first stage, wavelet transformation is done on the given input using different wavelet functions. Soft thresholding takes place after the wavelet transform and provides smooth output image compare to the hard thresholding. After that, inverse wavelet transformation is done and the output of this stage is denoised image. Finally, quality metrics are evaluated for the output and input clinical dataset images.

2 Materials and Methods

The images are taken as a input such as T2-weighted contrast agents Magnetic Resonance (MR) brain tumor image, X-ray chest image, axial, non-enhanced computed tomography image at the level of the kidneys shows bilateral renal calculi, ultrasonic baby image, and mammogram right breast cancer image. The number of images taken for analysis is totally thirty clinical images (MRI–7, X-ray–7, CT–3, Ultrasonic–7, Mammogram–6) with different sizes and JPEG format. Here, we enhances the medical image based on the denoising process using different wavelet coefficients and evaluate the quality metrics.

3 Wavelet Transform

Wavelet transform is an efficient mathematical function tool. It is used for analyzing and synthesizing of one-dimensional and two-dimensional applications according to scale or resolution. It has advantages over the Fourier transform because they are localized in both time and frequency domain. It is analyzed based on basic functions called wavelets such as mother wavelets or analyzing wavelets [3, 4]. DWT is a discrete signal represented by a time-frequency method. It is used for the decomposition of the image signal into high- and low-frequency components. The wavelet coefficients are computed as a convolution of the image signal and the scaled wavelet functions. It is used to measure the frequency content similarity between the image signal and a chosen wavelet function. Image is decomposed into hieratical sub-band systems where sub-band systems are analyzed at different frequency bands with different resolutions.

Wavelet families can be split into two types such as orthogonal wavelets and Bi-orthogonal Wavelets. Orthogonal wavelets provide the non-redundancy representation, and symmetry characteristics provides linear phase. A bi-orthogonal wavelet is associated with invertible wavelet transform but not necessarily be orthogonal. The wavelet coefficient produces excellent output but is computationally much more complex and expensive. Here we illustrate the Haar Wavelets, Daubechies Wavelets, Symlets Wavelets, Coiflet Wavelets, Bi-orthogonal Wavelets, Reverse Bi-orthogonal, and Discrete FIR Meyer wavelet.

3.1 Haar Wavelets (haar)

Haar wavelet describes the basis and simplest orthogonal functions. They were introduced by Hungarian mathematician Alfred Haar and used in image denoising and image compression techniques effectively [5, 6]. It is represented by a uniformly and convergent series such as square-shaped functions which is similar to Fourier analysis, and it is also called as db1 wavelet. A discrete signal is decomposed into two sub-signals of half its length by using the Haar Wavelet. One sub-signal represents a running average or trend, and the other sub-signal represents a running difference or fluctuation, respectively. Advantages of Haar wavelets are faster, memory efficient, lower complexity, and simplest model [7]. The Haar wavelet's mother wavelet function $\psi(t)$ can be expressed as

$$\psi(t) = \begin{cases} 1 & 0 \le t \le 1/2 \\ -1 & 1/2 \le t \le 1 \\ 0 & \text{Otherwise} \end{cases} \tag{1}$$

Its scaling function $\phi(t)$ can be expressed as

$$\phi(t) = \begin{cases} 1 & 0 \leq t < 1 \\ 0 & \text{otherwise.} \end{cases} \tag{2}$$

3.2 Daubechies Wavelets (db)

The Daubechies wavelets are used as orthogonal function. It provides a dual representation of combining zero-crossings and local extrema. These are characterized by a maximal number of vanishing moments for some given support. In each type of Daubechies, there is a scaling function (called father wavelet) which generates an orthogonal multi-resolution analysis [8].

3.3 Symlets Wavelets (sym)

Symlets have the property of being closed to symmetric, and it can be defined by the scaling filter. They are based on least asymmetric and maximum number of vanishing moments. It is defined for any positive integer n. The scaling function (ϕ) and wavelet function (ψ) have compact support length of $2n$.

3.4 Coiflet Wavelet (coif)

Coiflet Wavelet is same as Daubechies wavelets and supported with highest number of vanishing moments for both phi and psi for a given support width. The wavelet function has $2N$ moments equal to 0, and the scaling function has $2N - 1$ moments equal to 0 [9]. The two functions have a support of length $6N - 1$.

3.5 Bi-Orthogonal Wavelets (biro)

There are families of compactly supported symmetric wavelets where the associated wavelet transform is invertible but not necessarily orthogonal. The symmetry of the filter coefficients is often desirable since it results in linear phase of the transfer function [10]. It is composed of the decomposition process and the reconstruction process.

3.6 Reverse Bi-Orthogonal (rbio)

Reverse Bi-orthogonal Wavelets family is found from the bi-orthogonal wavelet pairs, and both bi-orthogonal and reverse bi-orthogonal wavelet families are compactly supported bi-orthogonal spline wavelets. This wavelet has vanishing moments on decomposition for analysis and vanishing moment for the reconstruction of synthesis [11].

3.7 Discrete FIR Meyer Wavelet (dmey)

Yves Meyer constructed a smooth orthogonal wavelet basis. It is based on symmetric, orthogonal, and bi-orthogonal [11].

4 Results and Discussion

The performance analysis of different DWT coefficient functions is evaluated based on the following quality measures, which has been described by Avicibaset et al. [12], Mrak et al. [13], and Eskicioglu and Fisher [14].

4.1 Peak Signal-to-Noise Ratio (PSNR)

$$\mathrm{PSNR} = 10\log\frac{255 * 255}{\mathrm{MSE}}\mathrm{dB} \tag{3}$$

where MSE is mean square error [14, 15].

4.2 Average Difference (AD)

$$\mathrm{AD} = \sum_{j=1}^{M}\sum_{k=1}^{N}\frac{\left[X(j,k) - \widehat{X}(j,k)\right]}{\mathrm{MN}} \tag{4}$$

4.3 Structural Content (SC)

$$\mathrm{SC} = \sum_{j=1}^{M}\sum_{k=1}^{N}\frac{X(j,k)^2}{\sum_{j=1}^{M}\sum_{k=1}^{N}\widehat{X}(j,k)^2} \tag{5}$$

4.4 Image Fidelity (IF)

$$\mathrm{IF} = 1 - \sum_{j=1}^{M}\sum_{k=1}^{\mathrm{N}}\frac{\left[X(j,k) - \widehat{X}(j,k)^2\right]}{\sum_{j=1}^{M}\sum_{k=1}^{N}\left[X(j,k)^2\right]} \tag{6}$$

4.5 Normalized Correlation Coefficient (NK)

$$\mathrm{NK} = \sum_{j=1}^{M}\sum_{k=1}^{N}\frac{\left[X(j,k)\widehat{X}(j,k)\right]}{\sum_{j=1}^{M}\sum_{k=1}^{N}\left[X(j,k)^2\right].} \tag{7}$$

4.6 Structural Similarity Index (SSIM)

Zhou Wang et al. [16] proposed a mean structural similarity index and universal quality index (UQI). It compares local patterns of pixel intensities that have been normalized for luminance and contrast.

$$\mathrm{SSIM} = \frac{\left(2\mu_x\mu_y + C_1\right)\left(2\sigma_{xy} + C_2\right)}{\left(\mu_x^2 + \mu_y^2 + C_1\right)\left(\sigma_x^2 + \sigma_y^2 + C_2\right)} \tag{8}$$

where μ and σ are mean and variance, and x and y are noisy and denoisy images, respectively. The MSSIM is calculated by taking mean of SSIM, and UQI is calculated by substituting the values of C_1 and C_2 as zero. In this work, MRI, X-ray, CT, and ultrasonic images are taken for analysis. The experiments were carried out using MATLAB version R2010a. Here we used Haar wavelet, Daubechies wavelet, Symlets wavelet, Coiflet wavelet, Bi-orthogonal wavelet, Reverse bi-orthogonal, and Discrete FIR Meyer wavelet decomposition level at four for all the medical images. Tables 1, 2, 3, 4, and 5 show the performance analysis of different wavelet functions in five types of medical image such as MRI, X-ray, CT, ultrasonic, and mammogram images.

Table 1 Performance analysis for quality measures of MRI image

Wavelet functions	PSNR	AD	SC	NK	IF	SSIM	UQI
haar	43.3850	0.9903	0.9837	1.00	1.00	0.9996	0.9996
db4	43.0834	0.9882	0.9827	1.00	1.00	0.9995	0.9995
bior(2.8)	**43.7420**	0.9945	0.9817	1.00	1.00	0.9996	0.9996
coif(5)	42.8670	0.9917	0.9824	1.00	1.00	0.9995	0.9995
sym(2)	43.0370	0.9828	0.9825	1.00	1.00	0.9995	0.9995
rbio(2.8)	42.7200	0.9886	0.9826	1.00	1.00	0.9995	0.9995
dmey	42.6370	0.9906	0.9906	1.00	1.00	0.9995	0.9995

Table 2 Performance analysis for quality measures of X-ray image

Wavelet functions	PSNR	AD	SC	NK	IF	SSIM	UQI
haar	**44.0708**	0.9851	0.9860	1.00	1.00	0.9998	0.9998
db4	43.2657	0.9964	0.9859	1.00	1.00	0.9997	0.9997
bior(2.8)	43.9018	0.9978	0.9857	1.00	1.00	0.9998	0.9998
coif(5)	43.0869	1.0007	0.9858	1.00	1.00	0.9997	0.9997
sym(2)	43.5372	0.9997	0.9858	1.00	1.00	0.9997	0.9997
rbio(2.8)	42.9881	1.0029	0.9857	1.00	1.00	0.9997	0.9997
dmey	42.8749	0.9988	0.9858	1.00	1.00	0.9996	0.9996

Table 3 Performance analysis for quality measures of CT image

Wavelet functions	PSNR	AD	SC	NK	IF	SSIM	UQI
haar	44.4189	0.9787	0.9897	1.00	1.00	0.9997	0.9997
db4	**44.9355**	0.9842	0.9888	1.00	1.00	0.9997	0.9997
bior(2.8)	44.2911	0.9822	0.9895	1.00	1.00	0.9996	0.9996
coif(5)	44.4213	0.9804	0.9896	1.00	1.00	0.9997	0.9997
sym(2)	44.2305	0.9877	0.9894	1.00	1.00	0.9996	0.9996
rbio(2.8)	44.1320	0.9837	0.9895	1.00	1.00	0.9996	0.9996
dmey	44.6282	0.9863	0.9895	1.00	1.00	0.9997	0.9997

Table 4 Performance analysis for quality measures of ultrasonic image

Wavelet functions	PSNR	AD	SC	NK	IF	SSIM	UQI
haar	45.1736	0.6787	0.9963	1.00	1.00	0.9999	0.9999
db4	44.4798	0.6721	0.9962	1.00	1.00	0.9999	0.9999
bior(2.8)	45.1645	0.6749	0.9960	1.00	1.00	0.9999	0.9999
coif(5)	44.2664	0.6750	0.9962	1.00	1.00	0.9998	0.9998
sym(2)	**44.8522**	0.6763	0.9962	1.00	1.00	0.9999	0.9999
rbio(2.8)	44.2808	0.6699	0.9964	1.00	1.00	0.9998	0.9998
dmey	44.1832	0.6690	0.9963	1.00	1.00	0.9998	0.9998

Table 5 Performance analysis for quality measures of mammogram image

Wavelet functions	PSNR	AD	SC	NK	IF	SSIM	UQI
haar	**45.9464**	1.0049	0.9884	1.00	1.00	0.9999	0.9999
db4	44.9804	1.0032	0.9883	1.00	1.00	0.9999	0.9998
bior(2.8)	45.3498	0.9908	0.9882	1.00	1.00	0.9999	0.9999
coif(5)	44.6988	1.0090	0.9882	1.00	1.00	0.9998	0.9998
sym(2)	45.1446	1.0072	0.9881	1.00	1.00	0.9999	0.9999
rbio(2.8)	44.6837	1.0305	0.9878	1.00	1.00	0.9998	0.9998
dmey	44.6562	1.0016	0.9884	1.00	1.00	0.9998	0.9998

5 Conclusion

In medical image processing, denoising is one such an essential process which improves the visual quality of image. It is also to increase the accuracy of the segmentation and classification techniques. In this paper, we have enhanced the quality of images using DWT which is carried out for different types of clinical database images. The performance of different wavelet functions are compared using various quality metrics such as PSNR, structural content, image fidelity, normalized correlation coefficient, structural similarity index, and UQI. We have also highlighted the largest values of the PSNR for various clinical database images. From the above results, Haar wavelet provides better PSNR values for X-ray and mammogram images. Bi-orthogonal wavelets, Daubechies wavelets, and Symlets wavelets yield better values of MRI, CT, and ultrasonic images, respectively. In future work, we investigate that wavelet function-based image denoising process can provide better image classification results or not.

References

1. Oktem R, Egiazarian K, Lukin V, Ponomarenko N, Tsymbal O (2007) Locally adaptive DCT filtering for signal-dependent noise removal. EURASIP J Adv Signal Process 2007:1–10
2. Motwani MC, Gadiya MC, Motwani RC, Harris FC (2004) Survey of image denoising techniques. In: Proceedings of global signal processing expo and conference (GSPx '04), Santa Clara, California, USA
3. Graps A (1995) An introduction to wavelets. In: IEEE, signals and image processing, pp 50–61
4. Wang F, Liang S, Zhang Q (2011) Study on wavelet-based image denoising. In: IEEE international conference on multimedia technology (ICMT), pp 2629–2635
5. Stollniz EJ, DeRose TD, Salesin DH (1995) Wavelets for computer graphics: a primer, part 1. IEEE Comput Graph Appl 15(3):76–84
6. Porwik P, Lisowska A (2004) The Haar–wavelet transform in digital image processing: its status and achievements. Mach Graph Vis 13(1/2):79–98
7. Daubechies I (1988) Orthonormal bases of compactly supported wavelets. Commun Pure Appl Math 41:906–966

8. Dixit A, Majumdar S (2013) Comparative analysis of coiflet and daubechies wavelets using global threshold for image denoising. Int J Adv Eng Technol 6(5):2247–2252
9. Kaur S, Kaur G, Singh DD (2003) Comparative analysis of haar and coiflet wavelets using discrete wavelet transform in digital image compression. Int J Eng Res Appl 3(3):669–673
10. Jiang B, Yang A, Wang C, Hou Z (2013) Implementation of bi-orthogonal wavelet transform using discrete cosine sequency filter. Int J Signal Process Image Process Pattern Recognit 6(4): 179–190
11. Saini N, Sethy P (2015) Performance based analysis of wavelets family for image compression-a practical approach. Int J Comput Appl 129(9)
12. Avicibas I, Sankur B, Sayood K (2002) Statistical evaluation of image quality measures. J Electron Imaging 11:206–223
13. Mrak M, Grgic S, Grgic M (2003) Picture quality measures in image compression systems. In: EUROCON, Ljuijana, Slovenia
14. Eskicioglu AM, Fisher PS (1995) Image quality measures and their performance. IEEE Trans Commun 43:2959–2965
15. Kumari S, Vijay R (2011) Analysis of orthogonal and bi-orthogonal wavelet filters for image compression. Int J Comput Appl 21(5):17–19
16. Wang Z, Bovik AC, (2004) Image quality assessment: from error visibility to structural similarity. IEEE Trans Image Process 13:600–612

Influence of PWM Waveform on Breakdown in Twisted Pairs

S. Narasimha Rao and K. Elanseralathan

Abstract Issues in the life of stator winding of electrical motors fed by inverter drives have been concerned by researchers over the last two decades for obtaining adjustable speeds. The Power Electronic Converters using PWM (Pulse Width Modulation) technique produces pulsed waveforms having a very short rise and fall times due to the high switching frequency of IGBT's, causes premature failure of motor winding insulation. The life of such motor insulation is tested using twisted pair samples which are prepared using enamel wires. The enamel coating of Modified Polyester (non-corona resistant material) with different makes have the same thickness of 40 μ are used for this work. The breakdown tests were performed by applying a high frequency high voltage stress of PWM waveform with different frequency levels of 5, 15, and 25 kHz. The test results show that the breakdown strength of the various makes with the same thickness of same enamel material differs. Moreover, as the switching frequency is increased, the life of the motor insulation is reduced.

Keywords Twisted pair · Switching frequency · Primary insulation Breakdown · PWM waveform

1 Introduction

The use of inverter fed drive technology has been paved away for dramatic changes in industrial control of motors to achieve adjustable speeds with the help of Power Electronic Converters. But the PEC's using Pulse Width Modulation technique has a train of high frequency pulses due to the high frequency of IGBT's a and generates harmonic distortions towards the supply network side and the load side, and switching rates produced by these converters generate voltage, overshoots

S. Narasimha Rao (✉) · K. Elanseralathan
Department of EEE, Pondicherry Engineering College, Pillaichavadi, Puducherry, India
e-mail: snrinskit@pec.edu

K. Elanseralathan
e-mail: pecelan@pec.edu

M.C. Bhuvaneswari and J. Saxena (eds.), *Intelligent and Efficient Electrical Systems*, Lecture Notes in Electrical Engineering 446,
https://doi.org/10.1007/978-981-10-4852-4_24

which in turn lead to the premature failure of motor winding insulation [1–3]. The overvoltages would appear at the terminals of the phase-to-phase and turn-to-turn insulation of motor winding, generates voltage a double the input voltage due to reflection and resonance phenomenon due to impedance mismatching between the inverter, cable, and motor. These stresses are the responsible for leading to breakdown of motor insulation [4–8]. Further increasing of fast power electronic switching devices produces highly nonuniform voltage distribution among the turns and results in higher voltage stress in the first few turns of the coil, which is higher than the stress caused by a sinusoidal waveform [9–11]. The presence of these voltage overshoots can induce early inception of Partial discharges in the stator winding insulation. This PD activity, result in fast and continuous insulation degradation of organic materials. Therefore the life of enamel is extremely short [12, 13]. So it is noticed that one of the primary factors responsible for accelerated insulation degradation is the high switching frequency, and the motor winding insulation must be designed in such way that it should withstand these high stresses. In our experimental study, twisted pair specimen is used to investigate the life of the motor insulation. The work focuses here on testing that the primary insulation of different makes (Apple, Atlas, and RR Shramik) has same thickness made of modified polyester (Class-F insulation, noncorona-resistant material). All the breakdown tests performed with twisted pair samples are prepared by enamel wires. Breakdown tests were conducted on primary insulation with high voltage and high switching frequency of the PWM waveform with different frequency levels 5, 15, and 25 kHz. The test results also show that breakdown strength of Apple make is more than that of Atlas and RR Shramik. Apple and Atlas show almost same breakdown performance compared to RR Shramik with same thickness. Moreover, as the switching frequency is increased, the life of the motor insulation is reduced. The similar work was done by the Guastavino [14] who has shown that the breakdown voltage tested with switching frequency of 2.4 kHz is very less.

2 Experimental Setup

Figure 1 shows setup for inverter with PWM output waveform of high-voltage, high switching frequency variable for testing the samples. This block diagram shows that 220 V, 50 Hz source is fed to SMPS. The frequency and duty cycle is controlled by using the SMPS. An autotransformer is supplying for rectifier circuit. This circuit consists of EMI filter, bridge rectifier, and capacitor, whose output is given to inverter driver and power supply. This drive generates the pulses fed to H-bridge IGBT inverter. The output of the inverter is stepped up by means of a ferrite core transformer for high-frequency operation where twisted pair is stressed. The peak voltage is measured by a digital oscilloscope through 1:1000 capacitance voltage dividers.

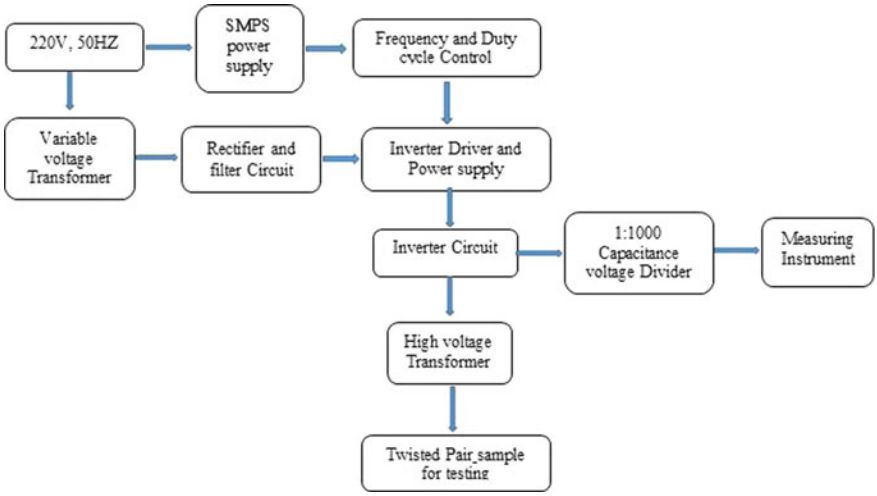

Fig. 1 Setup for inverter with PWM waveform of high voltage and high switching frequency

3 Sample Preparation

The life test of motor insulation is performed with twisted pair's samples composed by two-enamel-wire wound as a plait and prepared according to ASTM D 1676-03 standards. This specimen resembles a narrow contact between the first and last turns of the input coils of a motor with large voltage difference between the two coils.

So, number of twisting is required for this 16 gauge is '6' and the length of twisted pair is (12 ± 6) cm, and the tension maintained between the twisted pair is 1.35 kg. A 16-gauge (SWG) Class-F insulation is insulated by single-coated modified polyester enamel with a thickness of 40 μ (noncorona-resistant material) was used for testing.

4 Test Procedure

While performing the tests, care was taken that the voltage was not applied both the ends of the same wire and the breakdown test was done by applying the voltage gradually till the total breakdown of a twisted pair of sample. During conducting the breakdown test, one end of the twisted pair is connected to the high-voltage terminal and the other end connects ground terminal. While performing the breakdown test for modified polyester enamel wires with a PWM waveform of (duty cycle, 25%) high-voltage and high switching frequency levels of 5, 15, and 25 kHz were applied to the primary insulation. After the voltage is applied, the appearance

of initial spark is understood as insulation has failed and voltage at that point is noted which is reported here as breakdown voltage. Five samples per material were tested per each frequency, and average breakdown voltage was determined.

5 Results and Discussion

Table 1 shows that the breakdown voltage for the modified polyester of all the three makes stressed with PWM waveform at 5, 15, and 25 kHz. Figure 2 shows the variation in breakdown voltage, overfrequency for all the three makes. It can be seen from the graphs, the breakdown voltage of Apple and Atlas is almost same, though Apple make shows slightly higher breakdown voltage, whereas the breakdown strength of RR Shramik is much lower compared to other two makes. Moreover, when the frequency is increased from 5 to 15 kHz, RR Shramik shows the reduction in breakdown voltage with low slope and when increased from 15 to 25 kHz reduction in voltage with a slightly higher slope. Whereas Atlas make

Table 1 Breakdown voltages of modified polyester

High-voltage high-frequency stress (KV_{P-P})			
Make	Frequency		
	5 kHz	15 kHz	25 kHz
Modified polyester (Apple)	8.53	6.94	5.74
Modified polyester (Atlas)	8.52	6.76	5.72
Modified polyester (RR Shramik)	7.55	6.34	4.5

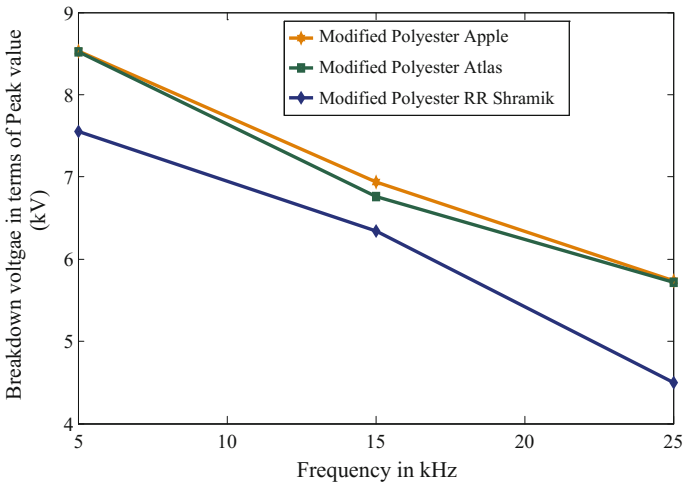

Fig. 2 Comparison of breakdown voltage with high switching frequency of modified polyester insulation of different makes

shows just the opposite, reduction in Apple make is almost linear. It is also obtained that reduction in voltage is 40% in RR Shramik whereas only 32% in Atlas and Apple.

6 Conclusions

Insulation degradation in electric drives is caused by PECs, in which high switching frequency is the major stress factor, which rapidly reduces the life of the motor insulation. In this work, we observed that the breakdown voltage of a PWM output waveform of high switching frequency of Apple make is more than that of Atlas and RR Shramik makes. Apple and Atlas show almost same breakdown performance compared to RR Shramik. Thus, when switching frequency is increased, the breakdown voltage decreased and the reduction in breakdown voltage in RR Shramik make is about 40% compared to other makes which are about 32%. Thus, it is concluded that as the switching frequency is increased, the life of the motor winding insulation is reduced and the winding wires available in the market claiming to have made with Indian standards with the same thickness does have a big difference in their breakdown voltages.

References

1. Oliver JA, Stone GC (1995) Implications for the application of adjustable speed drive electronics to motor stator winding insulation. IEEE Electr Insul Mag 11(4):32–36
2. Kaufhold M, Borner G, Eberhardt M, Speck J (1996) Failure mechanism of the interturn insulation of low voltage electric machines fed by pulse-controlled inverters. vol 12, no 5, Sept/Oct 1996
3. Yin W (1997) Failure mechanism of winding insulations in inverter-fed motors. IEEE Electr Insul Mag 13(6):18–23
4. Lawrence A, Skibinski GL, Evon ST, Kempkes DL (1996) Riding the reflected wave IGBT drive technology demands new motor and cable considerations, 23 Sept 1996
5. Kerkman RJ, Leggate D, Skibinski GL (1997) Interaction of drive modulation and cable parameters on AC motor transients. IEEE Trans Ind Appl 33:51–55
6. Melfi M, Sung AMJ, Bell S, Skibinski GL (1998) Effect of surge voltage rise time on the insulation of low-voltage machines fed by PWM converters. IEEE Trans Ind Appl 34: 766–775
7. Aoki N, Satoh K, Nabae A (1999) Damping circuit to suppress motor terminal overvoltage and ringing in PWM inverter-fed AC motor drive system with long motor leads. IEEE Trans Industr Appl 35(5):1014–1020
8. Cavallini A, Fabiani D, Montanari GC (2010) Power electronic insulation system-part1 phenomenology over view. vol 26, no 3
9. Rhudy R, Owen EL, Sharma DK, (1985) Voltage distribution among the coils and turns of a form wound AC rotating machine exposed to impulse voltage. In: IEEE PES winter meeting, 1985

10. Gubbala L, Von Jouanne A, Enjeti P, Singh C, Toliyat H (1995) Voltage distribution in the windings of an AC motor subjected to high dv = dt PWM voltages. In: Proceeding of PESC'95, pp 579–585 June 1995
11. Suresh G, Toliyat HA, Rendusara DA, Enjeti PN (1997) Predicting the transient effects of PWM voltage waveform on the stator windings of random wound induction motors. In: Proceeding of APEC'97, pp 135–141 Mar 1997
12. Fabiani D, Montanari GC, Cotin A (2001) Aging acceleration of insulating materials for electrical machine windings supplied by PWM in the presence and in absence of partial discharge. In: Proceeding of IEEEICSD'01, pp 283–286, June 2001
13. Fabiani D, Montanari GC (2001) The effects of voltage distortion on ageing acceleration of insulation system under partial discharge activity. IEEE Electr Insul Mag 17(3):24–33
14. Guastavino F, Dardano A (2012) Life tests on twisted pairs in presence of partial discharges: influence of the voltage waveform. IEEE Trans Dielectr Electr Insul 19(1):45–52

Diagnosis of Cardiovascular Diseases (CVD) Using Medical Images

R. Indumathi and M. Maheswari

Abstract Intima media thickness is the main indicator of the heart disease, and it is one of the major criteria for early screening and diagnosis of heart diseases. In the proposed work, left and right common carotid artery (CCA) intima media thickness is measured by taking ultrasound image of heart. A multistep algorithm is presented based on Otsu's thresholding to segment the carotid artery in the ultrasound image. The noises presented in the image are removed using filters such as Lee, Kuan, wavelet denoising, SRAD, and Kalman filters. Morphological operations enhance the carotid artery region, and it makes easy to measure the intima media thickness (IMT). Finally, the upper and lower intima media thickness range is measured accurately and the images are classified using the SVM and RBF classifiers which provide efficiency of 96 and 98%, respectively. The obtained efficiencies are more accurate compared to the existing one.

Keywords Ultrasound imaging · Common carotid artery
Cardiovascular diseases (CVD) · Intima media thickness (IMT)

1 Introduction

Cardiovascular disease is the main reason of death in the world. Blood flow to the heart or brain is blocked or reduced due to the blood clot or due to fat deposits on the walls of the heart or in the valves. Cardiovascular disease includes artery diseases such as angina and myocardial infarction. Atherosclerosis is artery wall thickness due to accretion of white blood cells and proliferation of intimal smooth muscle and creating plaque, which leads to heart disease. The foremost symptom is

R. Indumathi
K. Ramakrishnan College of Engineering, Tiruchirappalli 621112, India

M. Maheswari (✉)
Department of ECE, K. Ramakrishnan College of Engineering, Tiruchirappalli 621112, India
e-mail: kousi.rhithi@gmail.com

M.C. Bhuvaneswari and J. Saxena (eds.), *Intelligent and Efficient Electrical Systems*, Lecture Notes in Electrical Engineering 446,
https://doi.org/10.1007/978-981-10-4852-4_25

variation in the artery wall thickness [1]. Intima media thickness (IMT) is the measurement of artery walls. Increase in the IMT of the CCA creates high risk of heart diseases. These findings are helpful for the early diagnosis of cardiovascular diseases. Heart diseases can be identified using heart images (cardiac images) with accurate detection method. In the recent years, medical imaging has grown expressively. Cardiac images are obtained by (i) magnetic resonance imaging (MRI) (ii) echocardiogram (iii) tomography, and (iv) ultrasound images. These images are mainly used for clinical diagnosis, surgical preparation, postsurgical assessment, and abnormality detection. Echocardiography is a common clinical procedure for diagnosing heart disease. When digital echocardiographs are available, computer aid diagnosis may assist doctors to have more accurate decision. Ultrasound is one of the most modality in the medical imaging. The images are taken by using the sonogram. Here, ultrasound images are taken for analysis.

2 Existing Methods

In [2], the common carotid intima media thickness (IMT) is a trustworthy measure of initial atherosclerosis. The occurrence and tracking the progression of disease is done using accurate measurement. The goal of this work is to present a new computer-aided detection (CAD) process, that is, capable of identifying and measuring the IMT in 2D ultrasound images. This method depends on image processing algorithms that implants arithmetic model to categorize the two interfaces that form the IMT without any user involvement. In [3], the author proposed a method, by measuring the change in the diameter during the heart cycle by using ultrasound data in combination with the local pulse pressure, local stiffness of the superficial arteries can be estimated. Evaluation of carotid thickness can differentiate between healthy and hypertensive patients. Stiffness is not the suitable parameter, because it varies from person to person. In [4], automatic system for the measurement of carotid intima media thickness (IMT), that is, based on the digital processing of ultrasound images. Finally, systematic approach is used to estimate the fundamental accuracy of the system. Fundamental approach leads to mathematical difficulty. In [5] wavelet filtering is used to remove the speckle noise. Speckle noise is not completely removed. No accuracy in monitoring carotid wall evolution. In [6] they using the optimized values, the carotid artery was known in all the processed images in both multi-frame and single-frame data. Sometimes, the speckle noise is not effectively removed. In [7], they used structuring element is a function of local image to almost the same mathematical structure and properties as the conventional one. Morphological filters are used to eliminate the speckle noise, but it blurring in the edges. In the above-mentioned methods, no specific filters are used to take out the speckle noise which introduces inaccuracy in measurement of intima media thickness.

3 Methodology

3.1 Recording of Ultrasound Images

Ultrasound is a noninvasive diagnosis machine. It uses the high-frequency sound wave to capture the human inner body image. Unlike other imaging techniques, the sound wave that transmitted from the ultrasound machine probe is safe to human body. The sound wave goes through human body and reflects back to the probe again. After the probe receives the reflected signals, it will send to post processing system to create an image of human inner body. The gray scale image is obtained based on the difference of the reflected sound wave. Images were captured at the range of 576 × 768 pixels with 256 gray levels. There is no tissue damage due to ultrasound imaging. The frequency limit varies from 20 kHz to several MHz is used.

3.2 Proposed Methodology

3.2.1 Image Enhancement

First, the original image is converted into gray scale. The image enhancement is to increase the perception of images for human spectators and present better input for filtering. The resizing of gray scale image to standard pixel size of 512 × 512 is done with the help of bi-cubic spline interpolation. Bi-cubic interpolation is the efficient technique compared with other techniques. It requires neighborhood of 16 pixels and uses window processing. Bi-cubic interpolation does not suffer with step-like boundary problem, where other interpolations such as linear, nearest neighbor have the problem. Bi-cubic interpolation allows zooming but it preserves the fine details. Figure 1 refers the image chosen for processing, i.e., original image (Fig. 2).

3.3 De-speckling

Normally, the medical images are affected with speckle noise. The removal of speckle noise is challenging one. Speckle noise is the multiplicative noise or granular noise that disgraces the quality of ultrasound images. It is also referred to reflective noise, due to the reflections from transducers used in it. Several filtering techniques are used to take away the speckle noise. Mostly, adaptive and non-adaptive techniques are used. The adaptive filters include Lee filter and frost filter. Nonadaptive filters include mean and median filters.

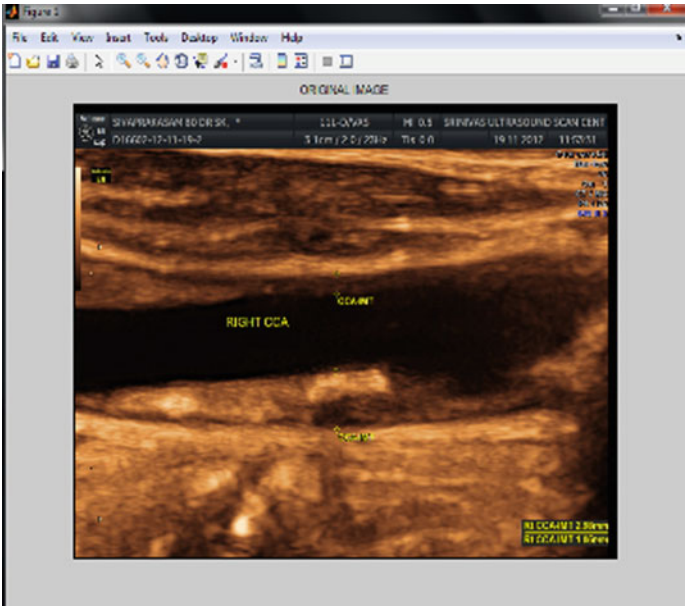

Fig. 1 Image taken for analysis

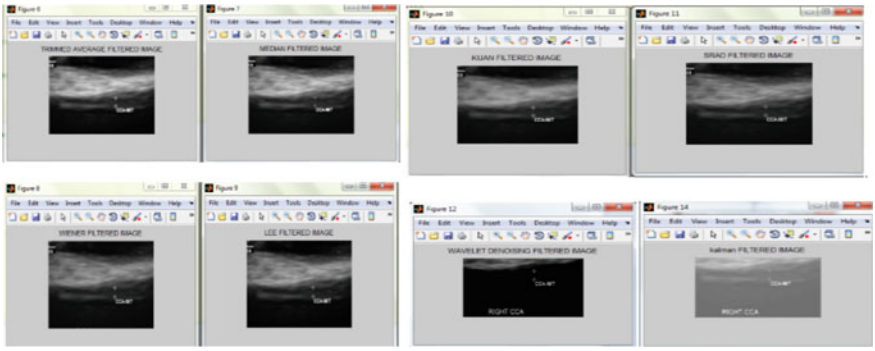

Fig. 2 Output of various filters

3.3.1 Trimmed Average Filter

It is based on the selection of appropriate inner and outer trimmed mean values based on the local measurement of impulse function of the noise product. It is type of order-statistics filter.

3.3.2 Median Filter

It is an example of a nonlinear filter, and it preserves image detail. This is the best known order-statistics filter, which substitutes the value of a pixel by the median value of the all gray levels in the neighbor of that pixel.

3.3.3 Wiener Filter

It is optimum linear filter which involves linear assessment of a preferred sequence from another associated sequence. The wiener filter is the optimal stationary linear filter used to remove noise and blur in the images degraded by noise and blurring.

3.3.4 Lee Filter

It is derived from the MMSE (minimum mean square error) by introducing the local statistics method, and it reduces the speckle noise while preserving the edges in the image.

$$\widehat{I}_S = \overline{I}_S + K_S(I_S - \overline{I}_S) \tag{1}$$

where I_S is the mean value of the intensity of the filter window ns and is the adaptive filter coefficient determined by

$$K_S = 1 - \frac{C_u^2}{C_s^2} \tag{2}$$

C_u and C_S are constant.

3.3.5 Kuan Filter

It is also derived from the MMSE criteria under the assumption of nonstationary mean and nonstationary variance. It is similar to Lee filter, but accurate than Lee filter due to no approximation is required in the total derivation.

3.3.6 SRAD Filter

Speckle reducing anisotropic diffusion filter uses partial differential equation. The partial differential equation-based speckle removal lets to generate an image scale space without bias due to filter window size and nature. SRAD not only preserves edges and but also enhances edges. This is done by inhibiting diffusion across edges

and allowing diffusion on either of the edges. Various parameters are used to remove the noise.

3.3.7 Kalman Filter

Kalman filter approximates the condition of a dynamic system, though the exact form of the system is indefinite. This filter is a great tool in the sense that it supports approximation of past, present, and even future states. It consists of two main steps, prediction and correction. The medical image considered here is two-dimensional image. For Kalman filter operation, there should be always exist on state vector. Hence, in order to produce this state vector, the image will be represented in one-dimensional array. The Kalman filter is a recursive algorithm used to compute optimal condition estimates given noisy observations and knowledge of the system dynamics and the relation between states and measurement vectors. It is also used to estimate the state of a system that provides the minimum expected mean squared error. The algorithm functions in a prediction-correction cycle.

3.4 Image Quality Assessment

Image quality assessment is done using PSNR, MSE, NAE, and SSIM. The obtained values for various filters are shown in Table 1.

$$\mathrm{MSE} = \frac{1}{M \times N} \sum_{i=1}^{M} \sum_{j=1}^{N} \left(a_{ij} - b_{ij}\right)^2 \tag{3}$$

$$\mathrm{PSNR} = 10 \log_{10} 255^2 / \mathrm{MSE} \tag{4}$$

Table 1 Comparison of filters

Filter types	PSNR (dB)	MSE (dB)	SSIM	NAE (dB)
Trimmed average filter	27.0402	4.07	0.9	1
Median filter	27.8402	106.9207	0.9641	0.0343
Wiener filter	46.5114	1.4519	0.9969	0.00174
Lee filter	37.4756	11.6285	0.9876	0.0232
Kuan filter	37.5829	11.3448	0.9864	0.0418
Wavelet denoising	12.0464	4.05	0.0016	0.9988
SRAD filter	47.7978	1.0797	0.9635	0.8616
Kalman filter	**71.2842**	**0.0048**	**0.9989**	**0.0073**

$$\mathrm{SSIM}(X,Y) = \frac{\left(2\mu_x\mu_y + C_1\right)}{\left(\mu_x^2 + \mu_y^2 + C_1\right)} \times \frac{(2\sigma_{xy} + C_2)}{(\sigma_x^2 + \sigma_y^2 + C_2)} \tag{5}$$

$$\mathrm{NAE} = \frac{\mathrm{AE}}{\frac{1}{M\times N}\sum_{i=1}^{M}\sum_{j=1}^{N}\left(a_{ij} - b_{ij}\right)^2} \tag{6}$$

$$\mathrm{AE} = \left(a_{ij} - b_{ij}\right) \tag{7}$$

Table 1 shows that the output of Kalman filter is better than other filters. So the output of Kalman is used for segmentation.

3.5 Segmentation

Image segmentation is performed using simple thresholding method. To develop an image thresholding algorithm, gray-level histogram of an image is usually considered as efficient tool. In thresholding technique, binary images are created from gray-level ones by changing all pixels below some threshold to zero and all pixels above that threshold to one. From a gray scale image, thresholding can be used to create binary images. Otsu's thresholding method includes reiterating through all the possible threshold values and calculating a measure of spread for the pixel levels each side of the threshold, i.e., the pixels that either falls in foreground or background. The threshold value is found where the sum of foreground and background spreads is at its minimum.

3.5.1 Otsu's Method

Otsu is a thresholding method in which it depends on only gray value of the image. The Otsu's method entails computing a gray-level histogram before running. However, the one-dimensional Otsu algorithm does not give better segmentation result as it only considers the gray-level information. Hence, to overcome the drawback two-dimensional Otsu algorithms have been proposed. This performs on both spatial correlation information of the neighborhood pixel and gray-level threshold of each pixel. Hence, Otsu algorithm can provide agreeable segmentation results for the noisy images. The output of Otsu thresholding is taken for further processing (Table 2).

Table 2 Various segmentation techniques

Segmentation type	PSNR	MSE
Snake segmentation	33.0606	3.213823
Otsu thresholding	34.0125	2.581229

3.6 Morphological Operations

Morphological operations create an output image based on comparison with the neighbor pixels by applying a structuring element to an input image. Erosion shrinks the object by etching away their boundaries. Dilation lets objects to expand thus possibly filling small holes and connecting disjoint objects. The ultrasound image has information such as patient's name, date, and name of the artery. These information in the segmented image appear to be in white in color. It leads to misidentification. So it is removed by morphological operation.

3.7 Classifier

3.7.1 SVM Classifier

SVM (support vector machine) has proven its competence and uses the linear separating hyper plane to separate two set of data in the feature space. It is produced by maximizing minimum boundary between the two data sets. In this, training and testing phase is done. The thickness of intima media is also measured and the classifier is applied. The obtained values are compared with default values that are provided by various researches. From the thickness itself, it is differentiated as normal or abnormal. The performance is calculated with mean and standard deviation. The efficiency obtained is 96%, so it is efficient than existing systems. Because the disease identification is done in [8] by back propagation classifier, the efficiency is 93%.

3.7.2 RBF Classifier

Radial basis function is one of the classes of single hidden layer feed forward neural networks. Radial basis function network consists of two layers. First one is the hidden radial basis layer of s1 neurons, and second one is the output linear layer of s2 neurons. The weighted input to each radial basis layer neuron is the distance between the two inputs and its weighted vector. The radial basis function network can be specified as a three-layer feed forward network. The input distributor to the hidden layer is the input layer. Each node in the hidden layer is a radial function of its dimensionality of the input data. The output is the weighted sum of the radial basis functions and the bias.

In order to use the RBF network, the specification of hidden unit activation, number of processing units, criteria for modeling a given task, and a training algorithm for finding parameters of the network is needed. Finding the RBF weight is known as network training. The set of input and output pair is called training set. The new parameters are optimized in order to fit the network output to the given

inputs. The neural network models the function of a certain mapping by providing training to the network. There are two types of training algorithms: (i) supervised and (ii) unsupervised. RBF networks are used mainly in supervised algorithm. RBF networks have very attractive properties such as localization, functional approximation, interpolation, cluster modeling, and quasi-orthogonality.

4 Results

The intima media thickness is varied from person to person. Figure 3 shows the carotid artery, from this the IMT values are measured. The normal thickness is about 0.7 ± 0.5, from these the conclusion is made. Within this, range is referred as normal person's image, otherwise it is diseased image. After the morphological processing, the intima media thickness is measured from the carotid artery (Figs. 4, 5 and 6; Table 3).

For this image, the intima media thickness is 0.476289 and it is classified as normal. Likewise, more number of images are stored in data set for analysis.

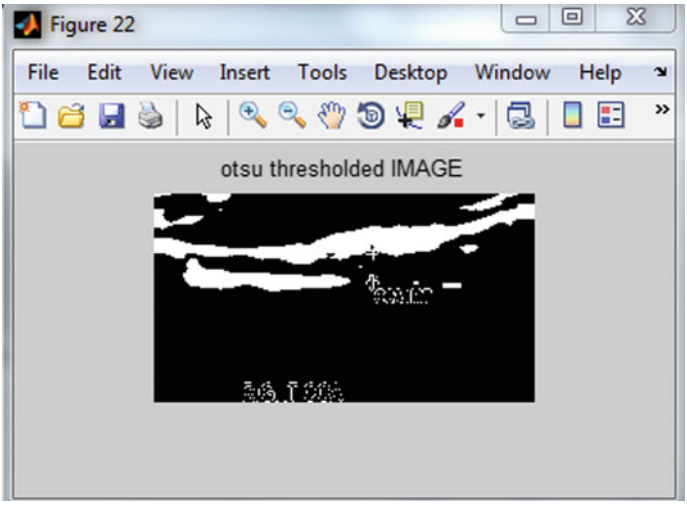

Fig. 3 Segmented image

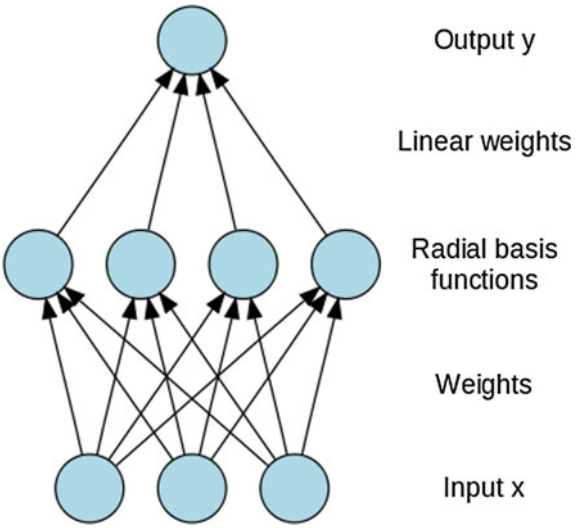

Fig. 4 Architecture of RBF

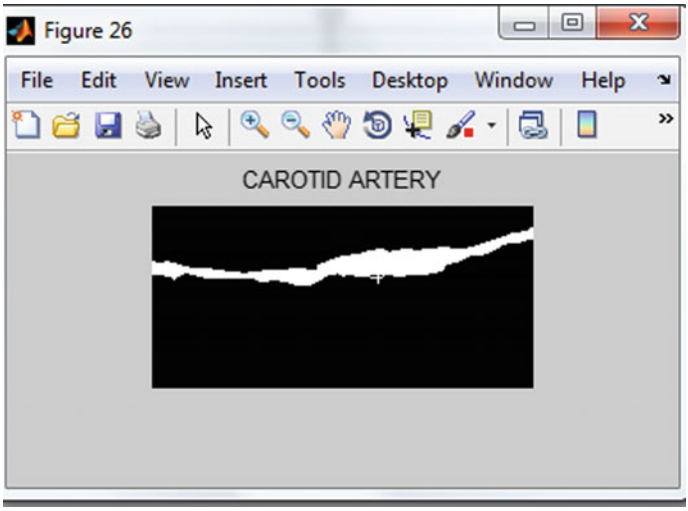

Fig. 5 Carotid artery

Fig. 6 Final output

Table 3 Comparison of classifiers

Classifier	Efficiency (%)
SVM	96
RBF	98

Table 4 Comparison of existing and proposed system

Techniques used	Existing system	Proposed system
Filtering	Gaussian filter, median filter	Lee, speckle reduction, anisotropic, diffusion, and Kalman filters
Segmentation	Snake segmentation	Otsu thresholding
Classifier	Back propagation classifier	SVM and RBF

5 Conclusion and Future Work

The shape of carotid artery is almost same like the muscle layer. Hence, it is very difficult for an inexperience doctors or radiologist to diagnose the ultrasound images. Hence, a carotid artery automatic detection method is proposed for the segmentation, and the measurement of the intima media thickness (IMT) is also proposed in this study. The de-speckling is done by using various filters such as Lee, Kuan, SRAD, and Kalman.

The Kalman filter provides the better result, so the output of Kalman filter is used for further processing such as segmentation and morphological operations. Finally, the disease classification is done by using classifiers such as support vector machine (SVM) and radial basis function (RBF) classifiers. The overall method of segmenting the carotid artery has been successfully developed using MATLAB to automatically detect the carotid artery from ultrasound images. The results will help the doctors and radiologist for further analysis. Besides that, the patient can get the correct earlier treatment and the chance of recovery is increased. This work can be extended by analyzing the same and to be implemented in reconfigurable device vertex **v** (FPGA) kit to develop a prototype model (Table 4).

References

1. Goyal P, Goyal K, Gupta V (2013) Calcification detection in coronary arteries using image processing. Int J Adv Res Comput Sci Softw Eng 3(8)
2. Mendis S, Puska P, Norrving B (2011) Global atlas on cardiovascular disease prevention and control. WHO
3. Loizou CP, Pattichis CS, Pantziaris M, Tyllis T, Nicolaides A (2007) Snakes based segmentation of the common carotid artery intima media. Med Biol Eng Comput 45(1):35–49
4. Loizou CP, Pattichis CS, Nicolaides AN, Pantziaris M (2009) Manual and automated media and intima thickness measurements of the common carotid artery. IEEE Trans Ultras Ferroel Freq Contr 56(5):983–994
5. Sifakis EG, Golemati S (2013) Robust carotid artery recognition in longitudinal B-mode ultrasound images. Medical Imaging-CAD 867031
6. Loizou CP, Pattichis CS, Georghiou N, Griffin M, Nicolaides A (2013) A comparison of ultrasound intima-media thickness measurements of the left and right common carotid artery. In: 12th international conference bioinformatics & bioengineering (BIBE), Chania, Crete, 11–13 Nov
7. Loizou CP, Pattichis CS, Christodoulou CI, Istepanian RSH, Pantziaris M, Nicolaides A (2005) Comparative evaluation of despeckle filtering in ultrasound imaging of the carotid artery. IEEE Trans Ultras Ferroel Freq Contr 52(10):1653–1669
8. Elalfi A, Eisa M, Ahmed H (2013) Artificial neural networks in medical images for diagnosis heart valse diseases. Int J Comput Sci Issues 10(5)